THE UNIVERSITY OF CHICAGO

UNDERSTANDING THE MAGNETIC ENVIRONMENT OF SPIN QUBITS FROM FIRST PRINCIPLES

A DISSERTATION SUBMITTED TO
THE FACULTY OF THE DIVISION OF THE PHYSICAL SCIENCES
IN CANDIDACY FOR THE DEGREE OF
DOCTOR OF PHILOSOPHY

DEPARTMENT OF CHEMISTRY

BY
MYKYTA ONIZHUK

CHICAGO, ILLINOIS
AUGUST 2023

For Oksana

TABLE OF CONTENTS

LIST OF FIGURES

LIST OF TABLES

ACKNOWLEDGMENTS

First and foremost, I want to thank my scientific advisor, Giulia Galli, for continuous support. An "Italian mom," as was coined by some members of our group, Giulia was there for all the good and the bad. I don't think I would be able to survive the treacherous waters of the graduate school without her deep care for my success.

But the grad school wouldn't be much of a school if I couldn't hang out with other students. And hang out we did. I thank Aritrajit Gupta for the ever present coffee breaks, each minute of I cherish wholeheartedly. I thank Siddhartha Sohoni for all the amazing chats we had together. I still wonder if I can deduct the dinners at Medici as a business expense on my tax return. And, of course, all the folks from our department — Kavya, Abhirup, Greg, Joe, Sasha, Andrii, Polina, Bogdan and everyone I met over the years, — thank you.

During my PhD, I had a rare chance to work with many, many brilliant scientists at the University of Chicago. My fellow labmates of the Galli group, I salute you. It was a great ride, and I will see you on the other side. The collaborations with the professor David Awschalom and his student became an integral part of my PhD, to the point of people being confused whether I was part of his group. I thank Paul Jerger, Jonathan Marcks, and Yuxin Wang from Clerk group for introducing me to the world of noise and how to sense it. Sam Bayliss, Pratiti Deb — thank you for letting me work on the molecules, as it was the only time I felt like an actual chemist. I owe everything I know about divacancies to the SiC guard of Chris Anderson, Alex Bourassa, and Kevin Miao. I am in even bigger dept to Kevin for giving me a glimpse of what the life is like outside the academia, which reinvigorated me with the drive for science in one of the most difficult periods of my life.

Speaking of which, the war in my home country Ukraine has been going on since early 2022, and at the time of writing this thesis, there is no end in sight. My mom, dad, and brother are still there, and I am deeply grateful for the sacrifices they have made for me, my country, and the whole democratic world.

And finally, I want to thank my wife, Oksana, for always being the person I needed the most.

ABSTRACT

The magnetic environment of spin qubits plays a key role in their applications in quantum information. For example, while the nuclear spin bath of material acts as a noise source for an electronic spin defect as qubit platforms, the spin-possessing nuclei can also be used as auxiliary quantum memories. They provide an excellent platform for long-term quantum information storage due to their low coupling to the magnetic environment.

This thesis aims to investigate the properties of the environmental spin bath in spin defects using first-principles simulations. We first build an efficient computational framework based on the cluster-correlation expansion (CCE) method to model the spin qubit interacting with the spin bath. We then combine theoretical predictions and detailed experimental validations to characterize the noisy environment of spin qubits in materials at the fundamental level. The spin qubits studied here exist in a wide variety of systems - defects in silicon carbide, diamond, oxides, and even in molecular crystals.

Over the last fifty years, computing evolved into a third pillar of science, alongside theory and experiment. As such, the first-principles simulations of spin qubits provide a rare opportunity to completely shift the paradigm of how we approach the characterization and interpretation of the experiments on spin qubits from the individual investigation towards the automation and an industrial scale.

PUBLISHED PAPERS

[1] Alexandre Bourassa, Christopher P Anderson, Kevin C Miao, **Mykyta Onizhuk**, He Ma, Alexander L Crook, Hiroshi Abe, Jawad Ul-Hassan, Takeshi Ohshima, Nguyen T Son, et al. Entanglement and control of single nuclear spins in isotopically engineered silicon carbide. *Nature Materials*, 19(12):1319–1325, 2020.

[2] **Mykyta Onizhuk**, Kevin C Miao, Joseph P Blanton, He Ma, Christopher P Anderson, Alexandre Bourassa, David D Awschalom, and Giulia Galli. Probing the coherence of solid-state qubits at avoided crossings. *PRX Quantum*, 2(1):010311, 2021.

[3] **Mykyta Onizhuk** and Giulia Galli. Substrate-controlled dynamics of spin qubits in low dimensional van der Waals materials. *Applied Physics Letters*, 118(15):154003, 2021.

[4] **Mykyta Onizhuk** and Giulia Galli. PyCCE: A python package for cluster correlation expansion simulations of spin qubit dynamics. *Advanced Theory and Simulations*, 4(11): 2100254, 2021.

[5] Yizhi Zhu, Berk Kovos, **Mykyta Onizhuk**, David Awschalom, and Giulia Galli. Theoretical and experimental study of the nitrogen-vacancy center in 4H-SiC. *Physical Review Materials*, 5(7):074602, 2021.

[6] Krishnendu Ghosh, He Ma, **Mykyta Onizhuk**, Vikram Gavini, and Giulia Galli. Spin-spin interactions in defects in solids from mixed all-electron and pseudopotential first-principles calculations. *npj Computational Materials*, 7(1):123, 2021.

[7] Shun Kanai, F Joseph Heremans, Hosung Seo, Gary Wolfowicz, Christopher P Anderson, Sean E Sullivan, **Mykyta Onizhuk**, Giulia Galli, David D Awschalom, and Hideo Ohno. Generalized scaling of spin qubit coherence in over 12,000 host materials. *Proceedings of the National Academy of Sciences*, 119(15):e2121808119, 2022.

[8] Sam L Bayliss, Pratiti Deb, Daniel W Laorenza, **Mykyta Onizhuk**, Giulia Galli, Danna E Freedman, and David D Awschalom. Enhancing spin coherence in optically addressable molecular qubits through host-matrix control. *Physical Review X*, 12(3): 031028, 2022.

[9] **Mykyta Onizhuk** and Giulia Galli. Bath-limited dynamics of nuclear spins in solid-state spin platforms. *arXiv preprint arXiv:2302.03257*, 2023.

[10] Paul C Jerger, Yu-Xin Wang, **Mykyta Onizhuk**, Benjamin S Soloway, Michael T Solomon, Christopher Egerstrom, F Joseph Heremans, Giulia Galli, Aashish A Clerk, and David D Awschalom. Detecting spin bath polarization with quantum quench phase shifts of single spins in diamond. *arXiv preprint arXiv:2303.02233*, 2023.

[11] Joel Davidsson, **Mykyta Onizhuk**, Christian Vorwerk, and Giulia Galli. Ab initio predictions of spin defects in simple oxides. *arXiv preprint arXiv:2302.07523*, 2023.

[12] Jonathan C. Marcks, **Mykyta Onizhuk**, Nazar Delegan, Yu-Xin Wang, Masaya Fukami, Maya Watts, Aashish A. Clerk, Giulia Galli, F. Joseph Heremans, and David D. Awschalom. Predictive methods for low-dimensional electron spin bath synthesis in diamond. *In preparation*, 2023.

During my PhD I also worked on Spatial Patterns of Light-Harvesting Antenna Complex Arrangements Tune the Transfer-to-Trap Efficiency of Excitons in Purple Bacteria, coauthored with Siddhartha Sohoni, Giulia Galli, and Gregory S. Engel (*Journal of Physical Chemistry Letters*, 12(29):6967, 2021) which is however not included in this dissertation.

CHAPTER 1

INTRODUCTION

"Nature never lets you win."

— Christopher P. Anderson

Quantum technologies are bound to fail. Even the most advanced quantum devices lose their quantum properties in mere seconds, as any interaction between a quantum system and its environment causes rapid deterioration of the delicate quantum state. Yet the quantum technologies' prompt breakdown is entirely by design; according to the principles of quantum mechanics, we cannot learn the state of a quantum system without affecting it. Both the quantum state's deterioration and its measurement come from the entanglement between the system and its surroundings. Thus, one needs to strike a delicate balance — make the system responsive just enough to control it in a timely manner while minimizing the effect of the environment.

In this thesis, I investigate a particular quantum platform of spin qubits in semiconductors. Many advantages make solid-state spins appealing for quantum pioneers: as a few-level quantum system, spin is a natural implementation of the quantum bit in quantum computing; a strong coupling but only to the magnetic environment allows one to use the spins as nanoscale quantum sensors to detect minuscule fluctuations in a microscopic magnetic field. And the optical addressability of a particular qubit type, color centers in semiconductors, makes them invaluable as the sources and receivers of quantum information encoded in single photons in quantum networks.

Using the first principles simulations as my main tool, I aim to find the balance between responsiveness and fallibility of the spin qubits by exploring the ways to shield the qubit from unwanted interactions and to leverage qubit's intrinsic environment for quantum applications.

This thesis is structured as follows. We begin by laying the theoretical groundwork to help understand the study presented here. As this work aims to bridge some distance between hardcore theorists, experimentalists, and my fellow computational connoisseurs, I will start with some very basic concepts of the open quantum systems. We begin with **Chapter 2**, where I provide the standard derivations of how one controls the a quantum two-level system, commonly referred to as qubit. One characterizes the detrimental effect of the environment by measuring the lifetimes, after which the quantum state ceases to exist. In **Chapter 3**, I introduce the theoretical framework of open quantum systems, interacting with the environment, and how one can predict the environment-limited characteristic decay (and thus lifetime) of the quantum states. **Chapter 4** concludes the first part of this thesis with the discussion on physical implementations of the spin qubits, what constitutes their environment, and how we can infer the coupling between the spin qubit and its environment.

Starting from **Chapter 5**, the major thrust of this thesis begins. In this chapter, I discuss in detail the theoretical framework I used in my research in the context of `PyCCE` — an open-sourced software to simulate central spin dynamics in a spin bath. **Chapters 6 and 7** discuss the first scientific advance — the investigation of the spin qubits' properties at optimal working points at which avoided crossings in the energy levels emerge and how we can use these avoided crossings to design spin qubits in rather unusual materials, such as molecules or oxides. **Chapter 8** presents the results of using spin dynamics simulations for the validation of the *ab initio* calculations of spin coupling parameters.

Next, in **Chapter 9** I discuss the utility of first principles simulations in designing the sensing experiments, and in **Chapter 10** I present the computational approach to guide the material synthesis. Finally, in **Chapters 11 and 12** I showcase the study of nuclear spins near electron spin defects from the first principles.

CHAPTER 2

QUANTUM 101

2.1 Density matrix formalism

> "In the beginning the Universe was created. This has made a lot of people very angry and been widely regarded as a bad move."
>
> — Douglas Adams

Let's start with simple things. Consider the evolution of the Universe over time. Assuming that the Universe is an isolated thermodynamic system, its evolution in a non-relativistic limit can be characterized with the Schrödinger equation (in the units of frequency, setting $\hbar = 1$):

$$i\frac{d}{dt}\left|\Psi(t)\right\rangle = \hat{H}_{\mathrm{u}}\left|\Psi(t)\right\rangle \tag{2.1}$$

Where I'm using the Dirac bracket notation, $\left|\Psi(t)\right\rangle$ is a state vector of the Universe at a time t, and $\hat{H}_{\mathrm{u}}$ is the Hamiltonian operator, which contains the interactions of everything. Note that $\hat{H}_{\mathrm{u}}$ is time-independent.

In principle, as long as we know all interactions present in the $\hat{H}_{\mathrm{u}}$, we can write a formal solution for the Schrödinger equation as:

$$\left|\Psi(t)\right\rangle = e^{-i\hat{H}_{\mathrm{u}}t}\left|\Psi(0)\right\rangle \tag{2.2}$$

And thus, knowing the state of the Universe at the beginning of time, we can predict the probability of anything happening in the world at any point in history (in the non-relativistic limit). However, the Universe is a tad too large to be tackled by a mere mortal me, so it is convenient to separate the Universe into two parts: the object we're interested in (the "System") and everything else (the "Environment"). The system exists in the Hilbert space

$\mathcal{H}_S$ and the environment in $\mathcal{H}_E$. The Hilbert space of the Universe then is given by the tensor product $\mathcal{H}_S \otimes \mathcal{H}_E$, and the total Hamiltonian $\hat{H}_u$ can be written as:

$$\hat{H}_u = \hat{H}_S \otimes \hat{I}_E + \hat{I}_S \otimes \hat{H}_E + \hat{H}_{SE} \tag{2.3}$$

where $\hat{H}_S$ is the system Hamiltonian in a Hilbert space $\mathcal{H}_S$, $\hat{H}_E$ determines the interactions inside the environment in a Hilbert space $\mathcal{H}_E$, and $\hat{H}_{SE}$ corresponds to the coupling between the system and the environment inseparable into corresponding Hilbert spaces. In the future, I will omit the identity operators $\hat{I}_S$ and $\hat{I}_E$, but they are always implied.

First, we want to answer how one defines the state of the system, assuming the total state of the Universe is known. We can deduce it from the *measurement* of the properties in the Hilbert space $\mathcal{H}_E$, given by some projectors $\hat{\Pi}_m$. The probability of an outcome m for the state of the Universe $|\Psi\rangle$ is given by:

$$p_m = \langle\Psi| \hat{\Pi}_m \otimes \hat{I}_E |\Psi\rangle \tag{2.4}$$

where $\hat{I}_E$ is the identity operator in the Hilbert space $\mathcal{H}_E$. using the fact that the inner product of the vector and the operator is equal to the trace, $\langle\psi| \hat{A} |\psi\rangle = \mathrm{Tr}\Big[\hat{A} |\psi\rangle \langle\psi|\Big]$, (see [6], p.76) and expanding Ψ in the product of basis states $\mathcal{H}_S$ and $\mathcal{H}_E$ as $\Psi = \sum_i \sum_j a_{ij} |s_i\rangle \otimes \big|e_j\big\rangle$ we obtain:

$$p_m = \mathrm{Tr}\Big[\hat{\Pi}_m \,\mathrm{Tr}_S |\Psi\rangle \langle\Psi|\Big] = \mathrm{Tr}\Big[\hat{\Pi}_m \hat{\rho}_S\Big] \tag{2.5}$$

Where we define the density matrix of a system $\hat{\rho}_S$ as a *partial trace* over the environment:

$$\hat{\rho}_S = \mathrm{Tr}_S |\Psi\rangle \langle\Psi| = \sum_j (\hat{I}_S \otimes \big\langle e_j\big|) |\psi\rangle \langle\psi| (\hat{I}_S \otimes \big|e_j\big\rangle). \tag{2.6}$$

The density matrix thus tells us all possible measurement probabilities that we can perform on a system but tells nothing about the measurements concerning the combined properties of

the system and the environment. Note that $\hat{\rho}_S$ will correspond to a density matrix of a *pure* state only if $|\Psi\rangle$ is a product state. The product state is the state which can be represented as a tensor product of the system and the environment $|\Psi\rangle = |\psi_S\rangle \otimes |\psi_E\rangle$). Then, and only then $\hat{\rho}_S = |\psi_S\rangle \langle\psi_S|$. Otherwise, $\hat{\rho}_S$ will be a sum of pure states with some probabilities $\hat{\rho}_S = \sum_i p_i |\psi_i\rangle \langle\psi_i|$ and represent a *mixed* state.

We can rewrite the Schrodinger equation (Eq. (2.1)) in the density matrix formalism:

$$i\frac{d}{dt}\hat{\rho}_{\mathrm{u}} = [\hat{H}_u, \hat{\rho}_u], \tag{2.7}$$

which is the so-called von Neumann equation, and $\rho_{\mathrm{u}} = |\Psi\rangle \langle\Psi|$ is the density matrix of the Universe. However, writing a similar equation for the reduced density matrix of the system $\hat{\rho}_S$ is significantly more challenging. In a trivial case, when $\hat{H}_{SE} = 0$ we can write:

$$i\frac{d}{dt}\hat{\rho}_{\mathrm{S}} = [\hat{H}_S, \hat{\rho}_S]. \tag{2.8}$$

The study of the system evolution in a general case $\hat{H}_{SE} \neq 0$ defines the whole field of the open quantum systems, a small subset of which I will present in Chapter 3.

2.2 What is a qubit, and how to control one

"In fact, the mere act of opening the box will determine the state of the cat, although in this case, there were three determinate states the cat could be in: these being Alive, Dead, and Bloody Furious."

— Terry Pratchett, Lords and Ladies

2.2.1 Qubit: a two-level quantum system

The system whose environment we are interested in is the qubit. Qubit is the most elementary quantum system with only two states, conventionally labeled as $|0\rangle$ and $|1\rangle$, separated by some energy difference ω. The Hamiltonian of any qubit can be then reduced to:

$$\hat{H}_q = \frac{\omega}{2}\hat{\sigma}_z, \tag{2.9}$$

where $\hat{\sigma}_z$ is one of the three Pauli matrices, defined as:

$$\hat{\sigma}_x = |1\rangle\langle 0| + |0\rangle\langle 1|, \tag{2.10}$$

$$\hat{\sigma}_y = i|1\rangle\langle 0| - i|0\rangle\langle 1|, \tag{2.11}$$

$$\hat{\sigma}_z = |1\rangle\langle 1| - |0\rangle\langle 0|, \tag{2.12}$$

which form a basis set for the space of 2×2 Hermitian matrices. Here $|i\rangle\langle j|$ defines the *outer* product of two vectors in the two-level Hilbert space (see [6], p. 67).

Similarly to the rather irritated feline, the predominant underlying physical systems used as a qubit contain more than two energy levels (such as superconducting qubits, Rydberg atoms, and even most of the spin qubits I focus on in this work), which might introduce a whole set of additional problems and/or opportunities. However, as long as the transition frequencies between the two energy levels and all other levels are well separated, one can

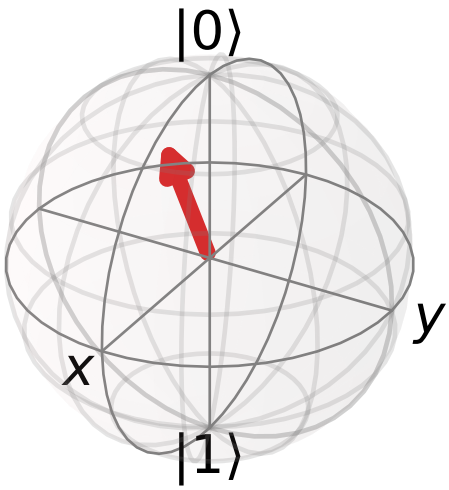

Figure 2.1: Representation of the quantum state $|\psi\rangle$ on a Bloch sphere. Cartesian axes match the directions in Eq. (2.13).

effectively isolate two energy levels and use them as a qubit. The population transfer to the remaining levels (so-called "leakage") is an important issue in superconducting qubit platforms, namely transmon qubits (See, for example, work by Google Quantum [7]), but thankfully the spin qubits are significantly less prone to this leakage.

Because the qubit has only two energy levels, we can uniquely map the state of the qubit on a 3D vector (in fancy words, this is explained by the equivalence between special unitary SU(2) and special orthogonal SO(3) Liu groups). The convenient way of visualizing quantum state is to represent the qubit as a vector on the so-called Bloch sphere, where the qubit with the density matrix $\hat{\rho}$ corresponds to a vector $\vec{a} = (a_x, a_y, a_z)$ in 3D space as:

$$\hat{\rho} = \frac{1}{2}\hat{\mathbb{1}} + \frac{1}{2}\vec{a} \cdot \vec{\sigma}, \tag{2.13}$$

where $\vec{\sigma} = (\hat{\sigma}_x, \hat{\sigma}_y, \hat{\sigma}_z)$ is a vector of Pauli matrices operators, and $\vec{a}$ is called Bloch vector. Figure (2.1) shows an example of such representation.

This representation has several interesting properties: the length of the vector $\vec{a}$ is equal to one for pure states of the qubit and is less than one for mixed states, and the expectation

values of the Pauli operators are connected to the Bloch vector components as $\langle\hat{\sigma}_i\rangle = a_i$.

Overall, any two quantum levels we can efficiently initialize, control, and measure can act as a qubit. In general, one uses the coupling between the qubit energy level and the oscillating electromagnetic fields to control the qubit state, as we discuss in the next section.

2.2.2 Rabi oscillations and Rotating Wave Approximation

To described the interactions between the qubit and the time-dependent oscillating field, it is convenient to use so-called rotating wave approximation (RWA), which allows one to treat the system as time-independent in some specific frame of reference. During the early days of my Ph.D. studies, I found it incredibly hard to follow the RWA derivation, so here I'm providing my own justification for this core concept in qubit control.

Consider a qubit interacting with an oscillating field, coupled to a qubit in xy plane:

$$\hat{H}(t) = \frac{\omega}{2}\hat{\sigma}_z + \Omega\cos(\omega_d t)\hat{\sigma}_x, \tag{2.14}$$

where Ω is a drive strength, ω_d is drive frequency. Think of it as an electric (magnetic) field oscillating in the xy plane, interacting with the electric (magnetic) dipole of a physical realization of a qubit.

For the next step, we apply unitary transformation $\hat{U}_0 = e^{i\hat{\sigma}_z\frac{\omega_d}{2}t}$ to the Hamiltonian, going into the so-called "rotating frame," defined by the frequency of the *drive* ω_d. The Hamiltonian changes as follows:

$$\hat{H}_I = \hat{U}_0\hat{H}\hat{U}_0^\dagger + i\frac{d\hat{U}_0}{dt}\hat{U}_0^\dagger, \tag{2.15}$$

with $\frac{d\hat{U}_0}{dt}\hat{U}^\dagger = i\frac{\omega_d}{2}\hat{\sigma}_z$. Then the Hamiltonian in the interaction picture is:

$$\hat{H}_I = \frac{\omega-\omega_d}{2}\sigma_z + \frac{\Omega}{2}(e^{i\omega_d t} + e^{-i\omega_d t})e^{i\hat{\sigma}_z\frac{\omega_d}{2}t}\hat{\sigma}_x e^{-i\hat{\sigma}_z\frac{\omega_d}{2}t} \tag{2.16}$$

It is convenient to write:

$$\hat{\sigma}_x = |0\rangle\langle 1| + |1\rangle\langle 0|. \tag{2.17}$$

Then, using the fact that $e^{-i\hat{\sigma}_z\frac{\omega_d}{2}t}|0\rangle = e^{i\frac{\omega_d}{2}t}|0\rangle$ and $e^{-i\hat{\sigma}_z\frac{\omega_d}{2}t}|1\rangle = e^{-i\frac{\omega_d}{2}t}|1\rangle$:

$$e^{i\hat{\sigma}_z\frac{\omega_d}{2}t}\hat{\sigma}_x e^{-i\hat{\sigma}_z\frac{\omega_d}{2}t} = e^{-i\omega_d t}|0\rangle\langle 1| + e^{i\omega_d t}|1\rangle\langle 0| = e^{-i\omega_d t}\hat{\sigma}_- + e^{i\omega_d t}\hat{\sigma}_+, \tag{2.18}$$

and plugging this result back into Eq. (2.16) we obtain:

$$\hat{H}_I = \frac{\delta}{2}\hat{\sigma}_z + \frac{\Omega}{2}(1 + e^{i2\omega_d t})\hat{\sigma}_+ + \frac{\Omega}{2}(1 + e^{-i2\omega_d t})\hat{\sigma}_-, \tag{2.19}$$

where $\delta = \omega - \omega_d$ is called detuning. So far, we haven't made any approximations – the Hamiltonian in Eq. (2.19) is still *exact*. Here is where the magic happens. As long as $\omega_d >> \Omega, \delta$ the time-dependent terms in the Eq. (2.19) oscillate significantly faster than the timescale of interest, then the effect of these time-dependent terms averages out, that is, $1 + e^{\pm i2\omega_d t} \approx 1$. Neglecting the fast-oscillating terms in the Hamiltonian is the core idea of RWA. Then the interaction Hamiltonian becomes:

$$\hat{H}_I = \frac{\delta}{2}\hat{\sigma}_z + \frac{\Omega}{2}\hat{\sigma}_x. \tag{2.20}$$

Now, one can wonder how we get the correct frame in more complicated systems and know which terms to neglect. Overall, the process is based on the researcher's intuition, which is rather disappointing. Quoting Daniel Sank's answer on Physics Stack Exchange, "The rotating wave approximation does not seem to be well-motivated in any book or paper that I know of." [8] Indeed, the exact boundaries where the rotating wave approximation stops being a good approximation are hard to pinpoint. However, when the energy scale of ω_d, ω is several orders of magnitudes higher than Ω, and the drive is near resonance, $\omega_d \approx \omega$, the RWA well reproduces the full numerical solution of the time-dependent Schrodinger

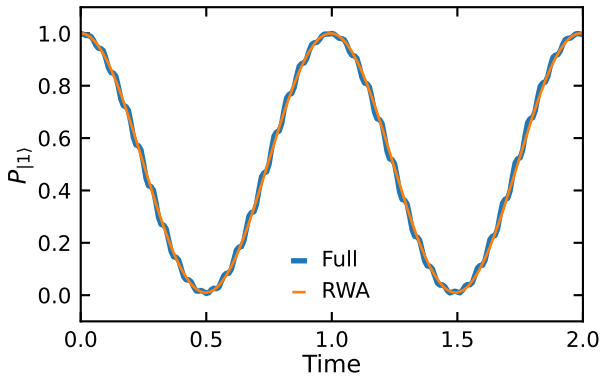

Figure 2.2: Example of Rabi oscillations, computed with (orange) and without (blue) rotating wave approximation. Time is in arbitrary units, $\delta/2\pi = 0.1$, $\Omega/2\pi = 2$, $\omega/2\pi = 10$.

equation.

The evolution of the state in the rotating frame then can easily be computed as:

$$|\psi_I(t)\rangle = \hat{U}_I(t)\,|\psi_I(0)\rangle\,, \tag{2.21}$$

where the RWA propagator $\hat{U}_I(t)$ is given as follows:

$$\hat{U}_I(t) = \exp\Big[-i\hat{H}_I t\Big] = \exp\Big[-i(\frac{\delta}{2}\hat{\sigma}_z + \frac{\Omega}{2}\hat{\sigma}_x)t\Big]. \tag{2.22}$$

This propagator acts as a *rotation* of the state about an axis, defined by δ and Ω relative amplitudes. If $\Omega >> \delta$, the rotation effectively happens about the x-axis. In this case, the qubit cycles between $|0\rangle$ and $|1\rangle$ states over time. This behavior is known as Rabi oscillations, named after an American physicist Isidor Isaac Rabi. The Rabi cycle is one of the most critical concepts in qubit control, as almost all single qubit gates are realized using these oscillations.

Figure 2.2 shows an example of Rabi oscillations. Even when ω is only five times larger than Ω, the RWA still agrees well with the exact calculation.

If necessary, one can easily recover the state in the lab frame by reversing the unitary

transformation $\hat{U}_0$:

$$|\psi(t)\rangle = \hat{U}_0^\dagger(t)\,|\psi_I(t)\rangle = \hat{U}_0^\dagger(t)\hat{U}_I(t)\,|\psi(0)\rangle \tag{2.23}$$

For many purposes, it is more convenient to consider the dynamics in the rotating frame (which is just a point of reference and not necessarily RWA itself), and we will primarily work in the rotating frame.

2.2.3 Control pulses

Assume that the Rabi oscillations happen significantly faster than the timescale of interactions between the qubit and the environment but significantly *slower* than the qubit frequency for RWA to hold. Then one can neglect the interactions during the time the oscillating field is turned on, and the qubit propagator in the rotating frame is equal to Eq. (2.22), or just a rotation about an axis by an angle $\phi = \frac{\sqrt{\delta^2+\Omega^2}}{2}t$. We call this rotation a *pulse*, specifying the angle and axis of rotation. For example, if $\delta = 0$ and the rotation happens about x axis (Eq. (2.20)) by the angle $\phi = \pi$ (180°), we will refer to such pulse as a π_x-pulse. Usually, if the axis is omitted, either the x or y axis is implied. For example, the effect of the π_x pulse on $|1\rangle$ qubit state is shown in Figure 2.3 on a Bloch sphere.

Here, however, one needs to take caution. The axes x or y are not defined by the geometrical considerations but by the *relative* phase of the oscillating field. For example, one can write the same Hamiltonian as in Eq. (2.14) but with an oscillating field shifted in phase by $\pi/2$:

$$\hat{H}(t) = \frac{\omega}{2}\hat{\sigma}_z + \Omega\sin(\omega_d t)\hat{\sigma}_x = \frac{\omega}{2}\hat{\sigma}_z + i\frac{\Omega}{2}(e^{-i\omega_d t} - e^{i\omega_d t})\hat{\sigma}_x, \tag{2.24}$$

which in the rotating frame (and under RWA) becomes:

$$\hat{H}_I = \frac{\omega-\omega_d}{2}\hat{\sigma}_z - i\frac{\Omega}{2}(1-e^{-i2\omega_d t})\hat{\sigma}_- + i\frac{\Omega}{2}(1-e^{i2\omega_d t})\hat{\sigma}_+ \approx \frac{\omega-\omega_d}{2}\hat{\sigma}_z - \frac{\Omega}{2}\hat{\sigma}_y. \tag{2.25}$$

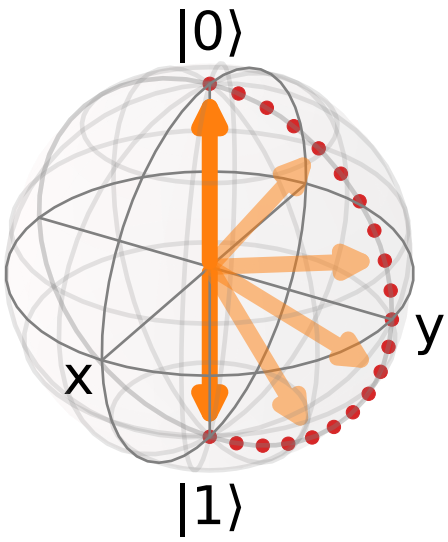

Figure 2.3: π_x-pulse acting on a $|1\rangle$ state. Orange lines represent the initial and final states of the qubit. Red points show the path of the qubit during the π_x-pulse.

Here we used the fact that:

$$\hat{\sigma}_y = i(|0\rangle\langle 1| - |1\rangle\langle 0|) = i\hat{\sigma}_- - i\hat{\sigma}_+ \tag{2.26}$$

So by merely adding a phase shift in the x drive, we changed the effective axis of rotation!

Therefore, in any pulse sequence, the first drive applied to the qubit "defines" the phase (locks the rotating frame), and every other pulse should be coherent with the first drive. That is, if the first drive, in general, is $\cos(\omega_d t + \alpha)$, all other drives to apply rotations about the same axis should have the phase offset $\cos(\omega_d t + \alpha)$ as well.

CHAPTER 3

A STORY OF A (QUBIT) LIFETIME

In this section, we discuss how we can treat the effect of the environment around the qubit. We aim to describe the environment as a source of the noise that leads to the eventual destruction of the precious quantum state.

3.1 Lindbladian Master Equation

If one wishes to write down a general equation of an open quantum system interacting with the environment contained only in the Hilbert space of the system, one is on quite a journey.

Let's step back and return to the Universe, described with the Hamiltonian (2.3). Moving to the frame defined by $e^{i(\hat{H}_E+\hat{H}_S)t}$ we can rewrite the von Neumann equation (2.7) as:

$$\frac{d}{dt}\hat{\rho}_I(t) = -i[\hat{H}_{SE}(t), \hat{\rho}_I(t)], \tag{3.1}$$

where $\hat{\rho}_I(t) = e^{i(\hat{H}_S+\hat{H}_E)}\hat{\rho}_u(t)e^{-i(\hat{H}_S+\hat{H}_E)}$ and $\hat{H}_{SE}(t) = e^{i(\hat{H}_S+\hat{H}_E)}\hat{H}_{SE}e^{-i(\hat{H}_S+\hat{H}_E)}$. We can formally integrate eq. (3.1), plug it into itself, and trace out the environment to arrive at the following monstrosity:

$$\frac{d}{dt}\hat{\rho}_{S,I}(t) = -i\,\mathrm{Tr}_E\left\{\left[\hat{H}_{SE}(t), \hat{\rho}_I(0)\right]\right\} - \mathrm{Tr}_E\left\{\int_0^t dt'\left[\hat{H}_{SE}(t), [\hat{H}_{SE}(t'), \hat{\rho}_I(t')]\right]\right\} \tag{3.2}$$

Now we have a closed equation that connects the state of the system at time 0 to a state at time t. It seems a bit pointless, as solving Eq. (3.2) still requires us to know the full quantum evolution of the environment, but now we have a clear order of the perturbation expansion. And under specific conditions, this form allows for a general treatment of the open quantum system in the way of master equations.

I will not give a complete derivation of the Lindbladian master equation in this work; for

a good description, see, for example, [9]. Here I will list the main approximations one needs to make to arrive at the final result:

- No initial correlations between the system and the environment, or the Universe is in the product state at the beginning of time, $\hat{\rho}_I(0) = \hat{\rho}_u(0) = \hat{\rho}_S(0) \otimes \hat{\rho}_E(0)$.

- Relaxation of the environment happens significantly faster than the timescale of the interaction between the system and the environment — so-called Born approximation (for my fellow chemists, this is similar as to when we assume that electronic structure instantaneously relaxes when nuclei move). Therefore we can write $\hat{\rho}_I(t) = \hat{\rho}_{S,I}(t) \otimes \hat{\rho}_E(0)$

- Bath correlations decay significantly faster than a change in the system's state. Therefore, one can substitute $\hat{\rho}_I(t')$ with $\hat{\rho}_I(t)$ in the R.H.S. of the eq. (3.2) and change the limits of integration from $(0, t)$ to $(0, +\infty)$. This assumption is the so-called Markovian approximation — the state of the system doesn't depend on the state of the system at earlier times.

- Rotating wave approximation (secular approximation) for the interactions between the system and the environment is used.

Under these assumptions, we can write the equation for the system dynamics, contained in the Hilbert space of the system as:

$$\frac{d}{dt}\hat{\rho}_S = \mathcal{L}[\hat{\rho}_S] = -i[\hat{H}_S, \hat{\rho}_S] + \sum_i \gamma_i \left(\hat{L}_i \hat{\rho}_S \hat{L}_i^\dagger - \frac{1}{2}\{\hat{L}_i \hat{L}_i^\dagger, \hat{\rho}_S\} \right), \tag{3.3}$$

where $\mathcal{L}$ is a Lindbladian superoperator, $\hat{L}_i$ are jump operators, and γ_i are the corresponding rates of the dissipation channels. In the following sections, we will use the Lindbladian description to connect different dissipative processes due to the interactions with the environment to the corresponding jump operators.

3.2 Types of dissipative processes in qubit

The master equations are a powerful tool to simulate the full dynamics of the system interacting with the Markovian environment. The number of approximations we need to account for, however, makes such an approach not applicable to many systems under study.

Instead of looking at the general case, I will separately focus on the possible dissipative processes relevant to the qubit system in this section.

Following [10], we consider a qubit weakly coupled to some environment:

$$\hat{H} = \frac{1}{2}\omega\hat{\sigma}_z + \frac{1}{2}\hat{\nu}_{\parallel}\hat{\sigma}_z + \frac{1}{2}\hat{\nu}_{\perp}\hat{\sigma}_x + \hat{H}_B, \tag{3.4}$$

where $\hat{\nu}_{\parallel}$ and $\hat{\nu}_{\perp}$ are environmental operators living in the Hilbert space of the environment, and $\hat{H}_B$ describes interactions inside the environment, not necessarily known. The important part is that $\hat{H}_B$ does not include interactions with the qubit. We can move into the frame, defined by $\hat{H}_B$ by applying unitary transformation $\hat{U}_{int} = e^{i\hat{H}_B t}$ (Eq. (2.15). As $\hat{H}_B$ commutes with $\hat{\sigma}_i$, the Hamiltonian in this frame becomes:

$$\hat{H}_I(t) = \frac{1}{2}\omega\hat{\sigma}_z + \frac{1}{2}\hat{\nu}_{\parallel}(t)\hat{\sigma}_z + \frac{1}{2}\hat{\nu}_{\perp}(t)\hat{\sigma}_x, \tag{3.5}$$

where we define effective time-dependent noise operators $\hat{\nu}_{\parallel}(t) = e^{i\hat{H}_B t}\hat{\nu}_{\parallel}e^{-i\hat{H}_B t}$ for the longitudinal noise and $\hat{\nu}_{\perp}(t) = e^{i\hat{H}_B t}\hat{\nu}_{\perp}e^{-i\hat{H}_B t}$ for the transverse noise.

We can then write a formal solution to the von Neumann equation (Eq. (2.7)) as:

$$\hat{\rho}_I(t) = \mathcal{T}\left\{e^{-i\int_0^t dt'\hat{H}_I(t)}\right\}\hat{\rho}_0\tilde{\mathcal{T}}\left\{e^{i\int_0^t dt'\hat{H}_I(t)}\right\}, \tag{3.6}$$

where $\mathcal{T}$ ($\tilde{\mathcal{T}}$) is an (anti) time-ordering operator, which ensures that the expression inside the curly brackets has only the products of operators (anti) ordered by the time coordinate.

To gain a heuristic understanding of relaxation and decoherence, in the following, we strip

$\nu_\parallel$ and $\nu_\perp$ of their hats and treat the environment as classical. This is what we refer to as a classical bath approximation when we treat the effect of the environment as some stochastic classical field and use the statistical properties of this field to uncover the limiting regimes of the qubit, losing its initial quantum state. Classical noise is not always a good description of the environment around the qubit, but as the most intuitive of the representations, many concepts (and corresponding measurements) in the field use classical picture as the starting point.

3.2.1 Dephasing

Let's assume that our qubit is initially in the pure $|\psi\rangle$ state. Then the total density matrix can be written as $\hat{\rho}_I(0) = |\psi\rangle\langle\psi| \otimes \hat{\rho}_E$. For simplicity, we assume that the noise is only longitudinal ($\hat{\nu}_\perp = 0$). In this section, we will write $\hat{\nu} \equiv \hat{\nu}_\parallel$ for clarity.

Without the transverse noise, the interactions with the environment cannot induce the transfer of the population between qubit energy levels. Therefore, all environment-induced dynamics will be reflected in the changes of the off-diagonal element of the density matrix $\rho_{10}(t)$. In general, the off-diagonal elements of any density matrix are often referred to as *coherences*, as they are equal to the relative phases between two states in the superposition. Analogous to the classical wave sources, the states can be considered coherent if that phase is well defined. If the average phase is zero, the two states are incoherent, and the density matrix represents a classical mixture of the states instead of the quantum superposition. The process in which qubit loses the well-defined phase between its levels is called *decoherence* or *dephasing*.

Using the definition of the partial trace (Eq. (2.6)), we can write $\rho_{10}(t)$ as:

$$\rho_{10}(t) = \sum_j \langle 1| \otimes \langle e_j| \, \mathcal{T}\left\{e^{-i\int_0^t dt' \hat{H}_I(t)}\right\} |\psi\rangle\langle\psi| \otimes \hat{\rho}_E \tilde{\mathcal{T}}\left\{e^{i\int_0^t dt' \hat{H}_I(t)}\right\} |0\rangle \otimes |e_j\rangle \,. \quad (3.7)$$

We can use the fact that qubit states are eigenstates of the $\hat{\sigma}_z$ to simplify the exponentials:

$$e^{\hat{\sigma}_z \otimes \hat{A}} \left|1/0\right\rangle = e^{\pm 1 \otimes \hat{A}} \left|1/0\right\rangle, \tag{3.8}$$

and insert in the Hamiltonian (3.5) into the exponential to write:

$$\exp\left[-i \int_0^t dt' \hat{H}_I(t)\right] = \exp\left[-i \left(\frac{1}{2}\omega\hat{\sigma}_z t + \frac{1}{2}\hat{\sigma}_z \otimes \int_0^t \hat{\nu}(t)dt\right)\right]. \tag{3.9}$$

Plugging it into Eq. (3.7) we obtain:

$$\rho_{10}(t) = \rho_{10}(0) \cdot e^{-i\omega t} \cdot L(t), \tag{3.10}$$

where we define coherence function $L(t)$ as:

$$L(t) = \sum_j \left\langle e_j \right| \mathcal{T}\left\{e^{-i\frac{1}{2}\int_0^t \hat{\nu}(t)dt}\right\} \hat{\rho}_E \tilde{\mathcal{T}}\left\{e^{-i\frac{1}{2}\int_0^t \hat{\nu}(t)dt}\right\} \left|e_j\right\rangle. \tag{3.11}$$

Formula (3.11) is still *exact*. Whatever environment we have, as long as the coupling between the qubit and the environment is purely longitudinal, we can recover the full dynamics of the qubit interacting with the environment from the coherence function $L(t)$. Quite profound, really, but still mostly useless. The operator $\hat{\nu}(t)$ exists in the Hilbert space of the bath and requires us to know the full dynamics of the environment.

This brings us to the hat stripping part. Assuming the noise is classical, the equation (3.11) is just an average of the random phase picked up by the qubit during the evolution:

$$L(t) = \langle e^{-i\int_0^t \nu(t)dt} \rangle = \langle e^{-i\phi(t)} \rangle, \tag{3.12}$$

with $\phi(t) = \int_0^t \nu(t)dt$. The neat approximation we make is we assume that the noise is Gaussian with mean $\langle \nu \rangle = 0$ and probability density function $P(\nu) = \frac{1}{\sigma\sqrt{2\pi}} e^{-\frac{\nu^2}{2\sigma^2}}$ with some

standard deviation σ. The Gaussian approximation means that *probability* of the value ν follows the normal distribution, but it doesn't tell us how it changes *over time*. It is still an instrumental observation as then we can do the following transformation:

$$L(t) = \langle e^{i\phi(t)} \rangle = e^{-\frac{1}{2}\langle \phi(t)^2 \rangle} = \exp\left[-\frac{1}{2} \int_0^t dt_1 \int_0^t dt_2 \langle \nu(t_1)\nu(t_2) \rangle \right] \tag{3.13}$$

Heuristically, equation (3.13) can be motivated because the Fourier transform of the Gaussian is still a Gaussian. More complete treatment depends on Wick's theorem, but the reader should look elsewhere for a rigorous derivation.

Then Equation (3.13) tells that if the noise is Gaussian, the decoherence of the qubit is determined solely by the noise correlation function $\langle \nu(t_1)\nu(t_2) \rangle$. Further, assuming that the noise is induced by a *stationary* process, i.e., the correlation function doesn't change with the shift in time, we can rewrite it as $\langle \nu(t_1)\nu(t_2) \rangle = \langle \nu(t_1 - t_2)\nu(0) \rangle$.

It is useful to introduce the *spectral density* of the noise $S[\omega] = \langle |\nu[\omega]|^2 \rangle$ (sometimes also known as noise spectrum), defined as a mean of a square of a windowed Fourier transform of the noise $\nu[\omega]$:

$$\nu[\omega] = \lim_{T \to \infty} \frac{1}{\sqrt{T}} \int_0^T \nu(t) e^{i\omega t} dt, \tag{3.14}$$

where normalization is chosen as $\frac{1}{\sqrt{T}}$ because at large T the integral is expected to grow as a $\sqrt{T}$ (see appendices of [11] for further reading). The Wiener-Khinchin Theorem ([11], appendix A) tells us that spectral density is directly related to the correlation function of the noise:

$$S[\omega] = \langle |\nu[\omega]|^2 \rangle = \int_{-\infty}^{\infty} \langle \nu(\tau)\nu(0) \rangle e^{i\omega\tau} d\tau. \tag{3.15}$$

Using the definition of the spectral density of the noise, we can rewrite the equation (3.13)

in a familiar way:

$$L(t) = \exp\left[-\frac{1}{2}\int_0^t dt_1 \int_0^t dt_2 \frac{1}{2\pi}\int_{-\infty}^{\infty} S[\omega] e^{-i\omega(t_1-t_2)} d\omega\right]$$
$$= \exp\left[-\frac{1}{4\pi}\int_{-\infty}^{\infty} S[\omega]\frac{4\sin^2\frac{\omega t}{2}}{\omega^2} d\omega\right] = \exp\left[-\frac{1}{4\pi}\int_{-\infty}^{\infty} S[\omega] F_{\mathrm{FID}}(\omega, t)\right], \quad (3.16)$$

where $F_{\mathrm{FID}}(\omega, t) = \frac{4\sin^2\frac{\omega t}{2}}{\omega^2}$ is the so-called filter function of the free induction decay (FID). The filter function determines which part of the noise spectrum $S[\omega]$ affects the decoherence of the qubit in a given experiment and will be discussed more in the dynamical decoupling part below (Sec. 3.2.1).

Inhomogeneous dephasing

The loss of coherence due to the noise that is constant throughout a single measurement, but varies between different measurements, is often called inhomogeneous dephasing or broadening. One can now exemplify the inhomogeneous broadening with both single qubit and ensemble experiments. In the ensemble measurement, every qubit might have a slightly different transition frequency due to static noise. But also, in the repeated measurement of a single qubit, its frequency might vary from measurement to measurement, leading to the same type of inhomogeneous broadening.

Consider the following toy model, where the spin governed by the Hamiltonian $\hat{H}_q$ interacts with the static longitudinal noise ν:

$$\hat{H} = \hat{H}_q + \nu\hat{\sigma}_z, \quad (3.17)$$

where ν is constant for each sample (measurement) but varies between different ones according to the Gaussian distribution $P_{\mathrm{inh}}(\nu) = \frac{1}{\sigma\sqrt{2\pi}} e^{-\frac{\nu^2}{2\sigma^2}}$ with standard deviation σ.

The autocorrelation of such noise is trivial, $\langle\nu(\tau)\nu(0)\rangle = \langle\nu(0)\nu(0)\rangle = \langle\nu^2\rangle = \sigma^2$, and

the spectral density is a delta function centered at zero, $S[\omega] = 2\pi\sigma^2\delta(\omega)$. Plugging in this autocorrelation function into the Eq. (3.13), we obtain the equation for the decay:

$$L_{\text{static}}(t) = e^{-\frac{\sigma^2}{2}t^2}. \tag{3.18}$$

We can define the characteristic *coherence time* $T_2^* = \frac{\sqrt{2}}{\sigma}$, after which the coherence decays to $1/e$ of the initial value in free induction decay. T_2^* is often called inhomogeneous dephasing time because it is mostly limited by the slow, static noise induced by the inhomogeneity of the qubit frequency in the ensemble.

It is useful to consider the opposite limit when the noise is so fast that the correlation decay much faster than the timescale of the experiment (Markovian noise). We write the autocorrelation function as exponential decay $\langle\nu(\tau)\nu(0)\rangle = \sigma^2 e^{-\frac{|t|}{\tau_c}}$ with correlation time $\tau_c << t$. Such an autocorrelation function can correspond to a variety of physical mechanisms behind the noise, but for the purpose of the current discussion, such details are omitted. This autocorrelation function corresponds to the Lorenzian spectral density $S[\omega] = \frac{1}{\pi}\frac{\tau_C^{-1}}{\omega^2+\tau_C^{-2}}$. Then the decay is computed as:

$$L(t) = \exp\left[-\frac{1}{2}\int_0^t\int_0^t \sigma^2 e^{-\frac{1}{\tau_c}|t_1-t_2|}dt_1dt_2\right] = \exp\left[-\sigma^2\tau_c t + \sigma^2\tau_c^2(1-e^{-\frac{t}{\tau_c}})\right]. \tag{3.19}$$

In the $\tau_c << t$ limit, we find the coherence function to be equal to $L(t) = e^{-\sigma^2\tau_c t}$ with characteristic time $T_2^* = \sigma^2\tau_c$ and strictly exponential decay. The exponential decay matches the predictions of the dephasing in the Lindbladian master equations (Eq. (3.3)). We can recover the same behavior by setting the jump operator to be equal to $\hat{L}_i = \hat{\sigma}_z$ and the corresponding rate to $\gamma_i = \frac{1}{2}S[0] = \frac{1}{\sigma^2\tau_c}$.

In the opposite limit of $\tau_c >> t$, we recover static noise decay (Eq. (3.17)). Equation (3.19), however, is more general and describes the free induction decay in the presence of any noise with the autocorrelation function that decays exponentially. It also brings up an

interesting point about the relative decay rates. The smaller the τ_c, the *slower* the decay is. This effect is called motional narrowing — the fast noise (i.e. autocorrelation of the noise decays rapidly) leads to the increase in coherence time.

Dephasing under dynamical decoupling

Under the dynamical decoupling train of pulses, a series of π pulses are applied to the qubit to mitigate the error introduced by the slow noise.

Consider the most basic dynamical decoupling sequence when a single π-pulse is applied at the middle point between the beginning of the experiment and the coherence readout. Such an experiment is known as Hahn echo [12], and the π pulses in the dynamical decoupling sequences are sometimes called "refocusing" pulses.

It is convenient to move to the frame defined by the π-pulse applied in the middle of the experiment:

$$\hat{U}(t) = e^{-i\theta(t-\tau)\hat{\sigma}_x \frac{\pi}{2}}, \tag{3.20}$$

where $\theta(t-\tau)$ is a Heaviside step function, and τ is the delay before the pulse. The coherence is read out at $t = 2\tau$. It's easy to see that $\hat{U}(t)\hat{\sigma}_z\hat{U}^\dagger(t) = y(t)\hat{\sigma}_z$ with $y(t)$ defined as[13]:

$$y(t) = \begin{cases} 1 & \text{if } t < \tau \\ -1 & \text{if } t \geq \tau \end{cases} \tag{3.21}$$

For more π-pulses in the dynamical decoupling sequence, the $y(t)$ will change the sign more times.

Then the Hamiltonian (Eq. (3.5)) in this toggled frame becomes:

$$\hat{H}_I = y(t)\hat{\sigma}_z(\omega + \hat{\nu}(t)). \tag{3.22}$$

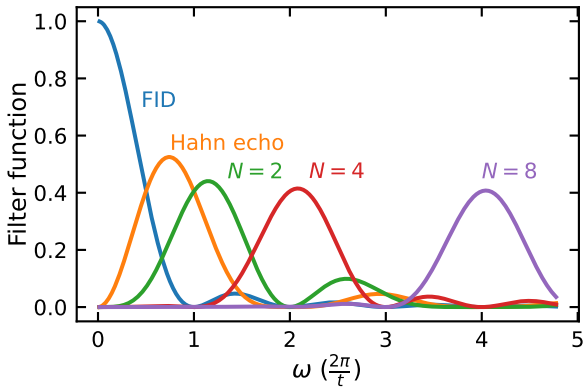

Figure 3.1: Filter functions for various types of experiments. N corresponds to the number of decoupling π-pulses in the given sequence.

Once again, we assume the absence of the transverse noise. We can rewrite the equation (3.13) as:

$$L(t) = \exp\left[-\frac{1}{2}\int_0^t dt_1 \int_0^t dt_2 \langle \nu(t_1)\nu(t_2)\rangle y(t_1)y(t_2)\right], \tag{3.23}$$

or in terms of the spectral density (Eq. (3.16)), the presence of the refocusing pulses modifies the filter function:

$$L(t) = \exp\left[-\frac{1}{4\pi}\int_{-\infty}^{\infty} S[\omega]F_{\mathrm{DD}}(\omega,t)\right], \tag{3.24}$$

where $F_{\mathrm{DD}}(\omega,t) = \int_0^t dt_1 \int_0^t dt_2 e^{-i\omega(t_1-t_2)} y(t_1)y(t_2)$ is a filter function for a specific dynamical decoupling pulse sequence. In the Hahn-echo experiment, $F_{\mathrm{DD}}(\omega,t) = \frac{8\sin^4(\frac{\omega t}{4})}{\omega^2}$. For the filter functions at a higher number of decoupling pulses, I refer the reader to look elsewhere, for example, [14].

Let's analyze how the change in the filter function affects what part of the noise spectrum qubit "sees." Figure 3.1 shows filter functions for different numbers of dynamical decoupling pulses and FID. We find that near zero frequency $\omega \to 0$ the filter function under dynamical decoupling protocol approaches 0, $F_{\mathrm{DD}}(\omega,t) \to 0$, while the FID filter function approaches unity, $F_{\mathrm{FID}}(\omega,t) \to 1$. So any low-frequency noise will be removed by the dynamical decoupling sequence!

The removal of the low-frequency noise is easy to see by considering only the static noise with $\langle \nu(t_1)\nu(t_2)\rangle = \sigma^2$. Then equation (3.23) becomes (the coherence is read out at $t = 2\tau$):

$$L(t) = \exp\left[-\frac{1}{2}\sigma^2 \int_0^t y(t_1)dt_1 \int_0^t y(t_2)dt_2\right] = \exp\left[-\frac{1}{2}\sigma^2(1\cdot(2\tau-\tau) - 1\cdot\tau)^2\right] = 1, \tag{3.25}$$

where the coherence function is now equal unity at all times.

In general, the noise is not static, and some coherence degradation will still occur. We characterize such decoherence phenomenologically by fitting the decay of the coherence into the general form $L(t) = \exp[-(t/T_2)^n]$ where T_2 is the Hahn-echo coherence time (if it's measured in the Hahn-echo dynamical decoupling sequence), and n is stretched, exponent.

There is confusion in the literature about the definition of T_2. The measured coherence time increases with the number of refocusing pulses in the dynamical decoupling sequence. If one then wants to compare coherence properties of two different systems one needs to define a single sequence as a reference. We use T_2 to refer only to Hahn-echo coherence time, and the coherence time measured in more sophisticated dynamical decoupling sequences will be correspondingly denoted.

3.2.2 Relaxation

In this section, we're interested in how the *population* of the qubit changes due to the interactions with the environment. Consider the case of the qubit interacting with classical transverse noise (3.5):

$$\hat{H}(t) = \frac{1}{2}\omega\hat{\sigma}_z + \frac{1}{2}\nu_\perp(t)\hat{\sigma}_x. \tag{3.26}$$

We can move into another rotating frame by applying the transformation $\hat{U}_I = e^{i\frac{\omega}{2}\hat{\sigma}_z t}$ to obtain:

$$\hat{H}_I(t) = \frac{1}{2}\nu_\perp(t)(e^{i\omega t}\hat{\sigma}_+ + e^{-i\omega t}\hat{\sigma}_-). \tag{3.27}$$

The Schrodinger equation in the interaction picture (rotating frame) for this system reads:

$$\frac{d}{dt}\left|\psi_I(t)\right\rangle = -i\hat{H}_I(t)\left|\psi_I(t)\right\rangle, \tag{3.28}$$

where $|\psi_I(t)\rangle$ is the state of the qubit at time t in the interaction picture, with simple transformation back to the Schrodinger picture (laboratory frame) as $|\psi(t)\rangle = e^{-i\frac{\omega}{2}\hat{\sigma}_z t}|\psi_I(t)\rangle$.

We next formally integrate the Schrodinger equation as a perturbative series:

$$|\psi_I(t)\rangle = |\psi(0)\rangle - i\int_0^t dt'\hat{H}_I(t')|\psi(0)\rangle + \int_0^t\int_0^t dt'dt''\hat{H}_I(t')\hat{H}_I(t'')|\psi(0)\rangle + ... \tag{3.29}$$

We will stop at the first order of perturbation theory and write the state of the qubit at time t as:

$$|\psi_I(t)\rangle \approx |\psi(0)\rangle - i\int_0^t dt\frac{1}{2}\nu_\perp(t')(e^{i\omega t'}\hat{\sigma}_+ + e^{-i\omega t'}\hat{\sigma}_-)|\psi(0)\rangle \tag{3.30}$$

Now assume the qubit is initially in the $|1\rangle$ state, and we're tracking the population of the $|0\rangle$ state. The probability of finding the qubit in $|\psi(0)\rangle = |0\rangle$ state can be computed as a square of the overlap of the wavefunction at time t with the $|0\rangle$ state $p_0(t) = |\langle 0|\psi_I(t)\rangle|^2$ with:

$$\langle 0|\psi_I(t)\rangle = 0 - i\int_0^t dt\frac{1}{2}\nu_\perp(t')\langle 0|(e^{i\omega t'}\hat{\sigma}_+ + e^{-i\omega t'}\hat{\sigma}_-)|\psi(0)\rangle \tag{3.31}$$

The average probability $\langle p_0(t)\rangle$ up to the first order of perturbation theory is equal to:

$$\begin{aligned}\langle p_0(t)\rangle &= \frac{1}{4}\langle\int_0^t dt_1\nu_\perp(t_1)e^{-i\omega t_1}\int_0^t dt_2\nu_\perp(t_2)e^{i\omega t_2}\rangle = \\ &= \frac{1}{4}\int_0^t dt_1\int_0^t dt_2\langle\nu_\perp(t_1)\nu_\perp(t_2)\rangle e^{-i\omega(t_1-t_2)}\end{aligned} \tag{3.32}$$

which is very reminiscent of the Eq. (3.13).

From the definition of the spectral density of the noise (Eq. (3.15), we can write:

$$S[\omega] = \langle |\nu_\perp[\omega]|^2 \rangle = \frac{1}{T} \lim_{T\to\infty} \int_0^T dt_1 \int_0^T dt_2 \langle \nu_\perp(t_1)\nu_\perp(t_2)\rangle e^{i\omega(t_1-t_2))} d\tau. \tag{3.33}$$

From equation (3.33), it is obvious that at "sufficiently large" time ($t \to \infty$), the probability of the transition to the $|0\rangle$ state is directly proportional to the spectral density at the qubit frequency:

$$\langle p_0(t)\rangle = \frac{1}{4} S[\omega] \cdot t = \Gamma_{10} \cdot t, \tag{3.34}$$

where we define the rate of transition as $\Gamma_{10} = \frac{1}{4}S[\omega]$ and find the probability to grow *linearly* in time. This result is the direct equivalent of the Fermi Golden Rule (FGR) for the noise spectrum save for normalization. However, applying the same logic to the probability of staying in $|1\rangle$ state, we find that it has constant amplitude, $\langle 1|\psi_I(t)\rangle = 1$ which does not match the reality.

To obtain the correct dynamics, we derive the dependency in the Markovian limit — the assumption that the qubit's state doesn't depend on all its previous states.

To achieve that, we rewrite the perturbative series, centered around $|\psi(t)\rangle$ instead:

$$|\psi_I(t)\rangle = |\psi(0)\rangle - i \int_0^t dt' \hat{H}_I(t') |\psi(t)\rangle + \int_0^t dt' \int_t^{t'} dt'' \hat{H}_I(t')\hat{H}_I(t'') |\psi(t)\rangle + ... \tag{3.35}$$

We use this definition to write the Schrodinger equation as follows:

$$\frac{d}{dt} |\psi_I(t)\rangle = -i\hat{H}_I(t) |\psi_I(0)\rangle - \hat{H}_I(t) \int_0^t \hat{H}_I(t') |\psi_I(t)\rangle . \tag{3.36}$$

We then find the amplitude $c_1(t) = \langle 1|\psi_I(t)\rangle$ from the following equation:

$$\frac{d}{dt} c_1(t) = -\frac{1}{2}\nu_\perp(t) \int_0^t dt' \frac{1}{2}\nu_\perp(t') e^{-i\omega(t'-t)} c_1(t). \tag{3.37}$$

To get mean amplitude change, we get an average of the left-hand side and right-hand side:

$$\frac{d}{dt}\langle c_1(t)\rangle = -\frac{1}{4}\int_0^t dt' \langle \nu_\perp(t)\nu_\perp(t')\rangle e^{-i\omega(t'-t)}\langle c_1(t)\rangle, \tag{3.38}$$

where we imply that the amplitudes of the qubit are not correlated with the noise $\nu_\perp(t)$.

By assuming a long-term limit $t \to \infty$ and by changing the variables $\tau = t - t'$, we can connect the emerging noise autocorrelation function in equation (3.38) with the spectral density:

$$\begin{aligned} \int_0^t dt' \langle \nu_\perp(t)\nu_\perp(t')\rangle e^{-i\omega(t'-t)} = \int_0^t d\tau \langle \nu_\perp(t)\nu_\perp(t-\tau)\rangle e^{i\omega\tau} = \\ = \int_0^t d\tau \langle \nu_\perp(t)\nu_\perp(t-\tau)\rangle e^{i\omega\tau} = \frac{1}{2}\int_{-t}^t d\tau \langle \nu_\perp(\tau)\nu_\perp(0)\rangle e^{i\omega\tau} = \frac{1}{2}S[\omega]. \end{aligned} \tag{3.39}$$

We then recover the change of the amplitude with time to be proportional to the amplitude itself:

$$\frac{d}{dt}\langle c_1(t)\rangle = -\frac{1}{8}S[\omega]\langle c_1(t)\rangle = -\frac{1}{2}\Gamma_{10}\langle c_1(t)\rangle, \tag{3.40}$$

which has a simple solution in the form of the exponential decay:

$$\langle c_1(t)\rangle = c_1(0)e^{-\frac{1}{2}\Gamma_{10}t}, \tag{3.41}$$

and we can finally write the probability as (assuming $c_1(0) = 1$):

$$\langle p_1(t)\rangle = \langle c_1(t)\rangle^2 = e^{-\Gamma_{10}t}, \tag{3.42}$$

with Γ_{10} given by the Fermi golden rule (Eq. (3.34)). We define the characteristic decay time $T_1 = 1/\Gamma_{10}$ as a time after which the system will decay to the $1/e$ population from the initial state.

As the population change is induced by the high-frequency noise, the Markovian approx-

imation usually works well for the relaxation (or T_1) processes, and Fermi golden rule is widely used in simulations to predict the relaxation rate.

The same behavior is recovered in the Lindbladian master equation with $\hat{L}_i = \hat{\sigma}_-$ and the rate $\gamma_i = \Gamma_{10}$. Notice, however, that we derived the decay of only one of the states; doing the same procedure for the lower state (and assuming a large temperature limit of $S[\omega] = S[-\omega]$), we find that the system should equilibrate to the equal populations in both states. In the limit of low temperature, the system will equilibrate into the lowest state instead.

The other question, then, is how does the coherence decay when there is a transverse source of the noise? This is easier to explain using the Lindbladian equation (Eq. (3.3) with jump operator $\hat{\sigma}_-$ and the rate γ_i:

$$\frac{d}{dt}\langle 0|\,\hat{\rho}_I(t)\,|1\rangle = \gamma_i \langle 0|\,\hat{\sigma}_-\hat{\rho}_I(t)\hat{\sigma}_+ - \frac{1}{2}\{\hat{\sigma}_-\hat{\sigma}_+, \hat{\rho}_I(t)\}\,|1\rangle = -\frac{\gamma_i}{2}\langle 0|\,\hat{\rho}_I(t)\,|1\rangle\,, \tag{3.43}$$

where the rate of decoherence ($1/T_2$) is one-half of the rate of the relaxation ($1/T_1$). Thus, the famous relation between the two characteristic times emerges $T_2 \leq 2T_1$. Note that by T_2 here we mean *any* dephasing coherence time, as no dynamical decoupling sequence can recover the loss of population.

However, in most systems of interest of this work the relaxation is significantly slower than dephasing, $T_1 \gg T_2$. Thus, for simplicity we assume the limit of the $T_1 \to \infty$ and do not consider the relaxation in considerable detail here.

3.2.3 Relevant experimental measurements of the qubit dissipation

Finally, I briefly summarize how one measures the previously described dissipative processes affecting qubits.

The inhomogeneous broadening of the qubit (T_2^* coherence time) is measured in the free

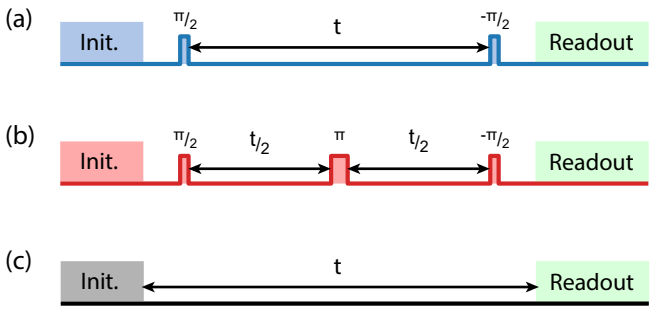

Figure 3.2: The pulse sequences are used to measure characteristic qubit coherence times. **Init.** stands for initialization of the qubit in the $|0\rangle$ state, and **Readout** means measurement of the population in $|0\rangle$ state. (a) Ramsey pulse sequence (b) Hahn-echo pulse sequence (c) Relaxometry.

induction decay (FID). In this measurement, one prepares qubit in $|+X\rangle = \frac{1}{2}(|0\rangle + |1\rangle)$ state, waits for time t, and measures the final magnetization along x ($\langle\hat{\sigma}_x\rangle$) or y-axes ($\langle\hat{\sigma}_y\rangle$).

Experimentally, however, the magnetization in xy-plane is measurable in only a small number of physical realization of qubits. Thus, the inhomogeneous broadening experimentally is usually recovered in the Ramsey experiment (Fig. 3.2a). In this experiment, one prepares qubit in $|0\rangle$ state, applies $\pi_x/2$ pulse, lets the qubit evolve for a time t, applies $-\pi_x/2$ (or $-\pi_y/2$) pulse, and measures population in the $|0\rangle$ state. Depending on the axis of the final $\pi/2$-pulse, one can recover either ($\langle\hat{\sigma}_x\rangle$) or ($\langle\hat{\sigma}_y\rangle$) in this way. The coherence is recovered from the compressed exponential decay of the envelope, $p_0 = e^{-(\frac{t}{T_2^*})^n}$.

Compared to the FID, where the magnetization is measured in the laboratory frame, the Ramsey experiment locks the frame determined by the detuning in the drive, used to apply $\pi/2$ pulses.

Finally, the Fourier transform of the Ramsey measurement gives us the frequency spectrum, with the broadening around central frequency (centered at the detuning between the drive and the qubit frequency) proportional to $1/T_2^*$. This is the reason why T_2^* corresponds to broadening.

Next, the Hahn-echo coherence time T_2 is measured in, well, the Hahn-echo experiment.

To perform Hahn echo, one prepares a qubit in $|0\rangle$ state, applies $\pi_x/2$ pulse, lets the qubit evolve for a time $t/2$, applies $\pi_{x(y)}$ pulse, lets the qubit evolve for a time $t/2$ again, applies another $-\pi_x/2$ pulse, and measures population in the $|0\rangle$ state (Fig. 3.2b). In the dynamical-decoupling sequences (CPMG, UDD, you name it), the number of the *pi*-pulses is larger than one. The coherence time T_2 is obtained by fitting the population of $|0\rangle$ to the compressed exponent $p_0 = e^{-(\frac{t}{T_2})^n}$.

The relaxation time T_1 is measured in the relaxometry by initializing qubit in the $|0\rangle$ state, waiting time t, and measuring population in the $|1\rangle$ state, and vise versa (Fig 3.2c). The T_1 is recovered from the exponential decay $p(1) = e^{-\frac{t}{T_1}}$.

3.3 Quantum bath approach to qubit decoherence

"That is not only not right; it is not even wrong." — Wolfgang Pauli

As one can notice, the approximations in 3.2 are relatively strong and require some *ad hoc* assumptions about the nature of the environment. The primary violation of the classicality of the bath can be introduced when the state of the qubit significantly impacts the state of the environment — so-called "backaction" of the qubit [15]. This happens when the interactions between the qubit and the environment are much stronger than the interactions within the environment itself.

I adopt a conceptually different approach to the finite-size bath approximation in my work. Here, we assume that only a small part of the environment (bath) is sufficiently strongly coupled to the system, and the coupling between the bath and the rest of the environment can be neglected. This approximation already reduces the size of the environment from the rest of the Universe to a few hundred particles, which is nice. The goal is then to compute the coherence function (Eq. (3.11)) directly from the quantum evolution of this finite-sized bath.

However, the number of particles in such a finite-sized bath can still routinely exceed hundreds in realistic systems, especially in the problems concerning the Hahn-echo signal. The full Hilbert space then includes at least 2^{100} degrees of freedom, and a naive approach to evolving the bath will not cut it in the problems of our interest.

The approximation I utilize the most is so-called cluster correlation expansion (CCE). The core idea of the CCE method is to factorize the bath-induced decoherence into a product of cluster contributions. Each cluster is defined in real space, and their contribution to the decoherence is computed by evolving the separate clusters in time. The cluster expansion approach is discussed in detail in a separate chapter (Chapter 5) in the context of the software I developed to target the central spin qubit in a spin bath problem. But first, we will introduce the physical implementations of the spin-based qubits.

CHAPTER 4

SPIN QUBITS AND WHERE TO FIND THEM

"This will be great!" — David D. Awschalom

It's time to finally define what the physical systems we investigate are. Specifically, we discuss how one can map the qubit onto spin levels of the particles in the solid state and what constitutes the environment of such qubits.

Note that here I describe only spin-based qubits, but there are a lot more quantum systems widely used as qubits. For example, there are superconducting qubits, neutral atoms, trapped ions, and others. The reader should look elsewhere to seek information about those (e.g., book [6] is a good start).

4.1 Spin in the solid state

There are a plethora of physical realizations of spin-based qubit platforms. In this section, I briefly summarize existing solid-state hosts of electron and nuclear spins for quantum information applications and my own (completely unbiased) opinion about the feasibility of describing each of the systems from the first principles.

4.1.1 Quantum dots

To manufacture quantum dots in semiconductors, one uses the static electric field bias to confine a single or a few electronic spins to 0D (hence the name, quantum dots) [17]. Such electrostatic engineering is achieved by restricting the electron density to the interfaces and controlling the electric field with metallic gates. The device based on spin qubit quantum dots is schematically shown in Figure 4.1c. The exemplary structure of the device is adapted from the recent work on a three-qubit array in silicon (ref. [16]).

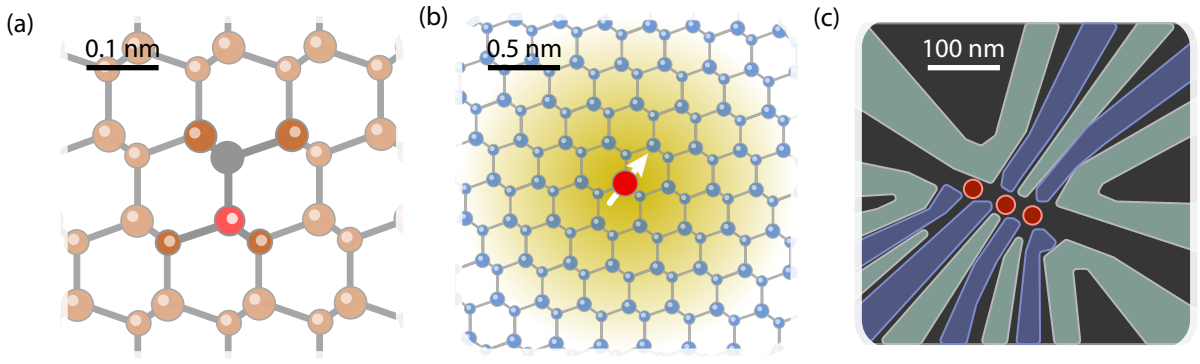

Figure 4.1: The semiconductor spin qubits. (c) An array of three quantum dots spins qubits in silicon (schematically represented as red circles). The structure of the quantum dot device is adapted from [16].

The Quantum dot-based technologies are operated at millikelvin temperatures to control thermal excitations.

The first quantum dots in semiconductors were created at the interface of GaAs/AlGaAs, but the field has thankfully moved towards mostly Si-based quantum dots. The readout is usually achieved via the spin-to-charge conversion. There are many various implementations of quantum dots-based spin qubits (single spin qubits, exchange qubits, singlet-triplet qubits, etc.), and for a more extensive overview, see the works [18] and [17].

The first-principles characterization of such systems is virtually impossible, as the size of the confined electron gas lies within tens of nanometers (Fig. 4.1c). The theoretical description usually relies on simplified semi-empirical models.

4.1.2 Shallow donors

Shallow donors are created by adding an atom of a group-V element, such as phosphorus or arsenic, to a group-IV crystal, usually silicon. The donor atom replaces a host atom in the crystal, and its extra electron is loosely bound to the donor nucleus in a hydrogen-like orbital. The most widely used system is ^{31}P donor in Si. [19]. The ^{31}P-dopants in silicon have an energy level of only 45 meV below the conduction band; thus, all applications require

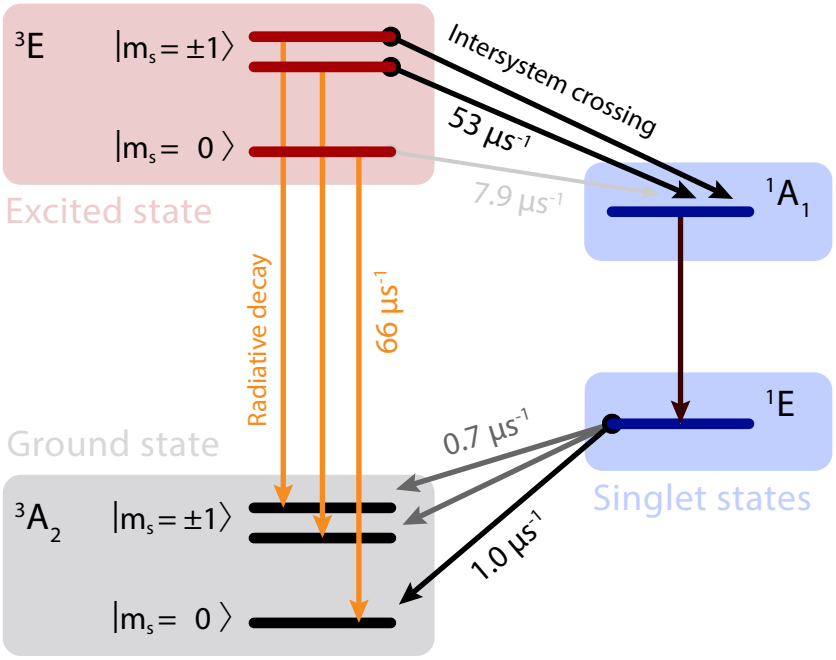

Figure 4.2: Energy levels of the NV^- center in diamond. The rates of transition are taken from [23].

cryogenic temperatures.

In quantum technologies, both the nuclear spin-½ of ^{31}P and bounded electron spin-½ play an important role. The control and readout of the nuclear spin are achieved only through the bound electron spin. See the work by [20] for a good overview of the donor-based qubits.

The electronic structure of the shallow defects is significantly delocalized in space, and the electron wavefunction spans several nanometers in size (Fig. 4.1b). Usually, one would adopt the Kohn-Luttinger model to estimate dopant wavefunction by treating the donor potential as a perturbation to the band structure of the pristine silicon (see, for example, [21]). However, recently there has been an effort to characterize the shallow donor electronic structure completely from the first principles [22].

4.1.3 Spin defects

Point defects are elementary substitutions in the crystal lattice of the material. A small subset of such defects can possess an attached electron spin in wide bandgap semiconductors, such as diamond or silicon carbide (SiC). Another subset of these defects will have both ground energy level and excited energy level inside the band gap of the material. Such defects are known as *color centers* as they absorb light at a frequency smaller than the band gap, commonly in the visible region. We're interested in the overlap of these two subsets of defects, commonly referred to as *optically active spin defects*. The qubit is mapped on different spin states of the ground electronic state.

The ground state optical properties are spin-dependent in these defects, i.e., the amount of light the defect emits depends on the magnetic state of the electron spin. Therefore, we can detect the spin states of the defects using their fluorescence in the method called *optical detected magnetic resonance*, providing a convenient way to readout (and initialize, as will be discussed below) the qubit. The spin-depended optical cycle between excited and ground states allows for optical readout and state preparation even at room temperature.

Consider the most well-studied point defect system, the negatively charged Nitrogen-Vacancy center in a diamond (Fig. 4.1a). It consists of the nitrogen substitution of the carbon atom located next to a vacant lattice site. The energy structure of the negatively charged NV^- center is shown in Figure 4.2. NV has a ground triplet state ($^3A_2$), an excited triplet state ((^3E)) and two intermediate singlet states ($^1A_1$ and $^1E_1$). The triplet states have three sublevels, different by a projection of the spin m_s. Two of these sublevels are used as qubit states. The intersystem crossing from triplet to singlet state is spin-dependent, with the states $m_s = \pm 1$ preferred. Thus, optically exciting the NV center, one can effectively reset the qubit into $|m_s = 0\rangle$ state within microseconds. Such unique properties allow one to use the NV^- center even at room temperature.

For further reading, see a great review by G. Wolfowics et al. [24] or an outstanding

doctoral thesis by C. P. Anderson [25].

The localization in the band gap leads to another important property of the spin defects. The *spatial extent* of such systems is also confined within only a few unit cells of the material. The highly localized nature of the point defects allows one to treat them as small molecules encapsulated in a solid state. Such behavior opens up many opportunities for first-principles studies, as the size of the computational system necessary to obtain converged results is tractable with existing hardware. For example, the quantum defect embedding theory (QDET) treats the defects using a high level of theory while accounting for the semiconductor environment around them using simpler DFT functionals [26]. The theoretical investigation of spin defects remains an active area of research to this day.

4.2 Spin environment around the qubit

Independent of the physical system type, quantum spin as a magnetic moment will strongly interact with other magnetic moments around it. Of course, that's not the only kind of interaction (for example, the interactions with electric field charges can induce both relaxation and dephasing in the spin defect systems: see recent work by Denis R. Candido and Michael E. Flatté [27]), and understanding the effect of all other factors is an area of research in itself. Here, however, we focus primarily on the magnetic noise as the most dominating effect on the quantum evolution of the spin qubits.

The magnetic environment consists mainly of nuclear spins (nuclear spin bath) and other paramagnetic impurities (electron spin bath). Figure 4.3 gives the general overview of the spin baths.

A nuclear spin bath is inherent to the host material of the defect and is usually determined by the natural concentration of spinful isotopes of the elements constituting the crystal lattice. For example, the diamond contains 98.9% of the ^{12}C isotope with spin zero, and 1.1% of the ^{13}C nuclei with spin-$1/2$. Therefore, the nuclear spin bath of the diamond is by

far dominated by ^{13}C nuclei. However, because carbon possesses naturally abundant spinless ^{12}C isotope as well, one can isotopically purify the diamond host to obtain a virtually nuclear spin-free environment.

But not every material is that lucky. For example, hexagonal boron nitride (hBN), a promising 2D platform for quantum technologies, contains a near 100% concentration of spinful isotopes of both nitrogen and boron, making the nuclear spin bath a dominating source of decoherence in any regime.

The electron spin bath consists of the electron spin-possessing defects in the host material or on its surface. These defects include defects of the same type as a central spin and other defects. Usually, these defects are introduced during the growth of the material and can be almost unavoidable as their presence is required to create the desired spin qubit. For example, consider the negatively charged NV center of a diamond. To grow NV centers, one needs to have a high enough concentration of nitrogen in the diamond, as well as introduce some vacancies into the lattice structure. The vacancies migrate during the high-temperature annealing and for NV centers upon meeting the nitrogen. But both vacancies and substitutional nitrogen possess electron magnetic moment. The substitutional nitrogen is known as the P1 center, and we will discuss this type of electron spin bath in more detail in Chapter 10.

The interactions between central qubit spin and the spin bath can be represented with effective Hamiltonian, discussed in detail in the next section.

4.2.1 Effective Hamiltonian

The non relativistic electronic Hamiltonian of the system in the Born-Oppenheimer approximation doesn't include terms which depend on the spin degree of freedom. Yet precisely these interactions give rise to all various and unique phenomena responsible for energy splitting of non-zero spin levels and spin dynamics. Interactions among spins can be inferred from

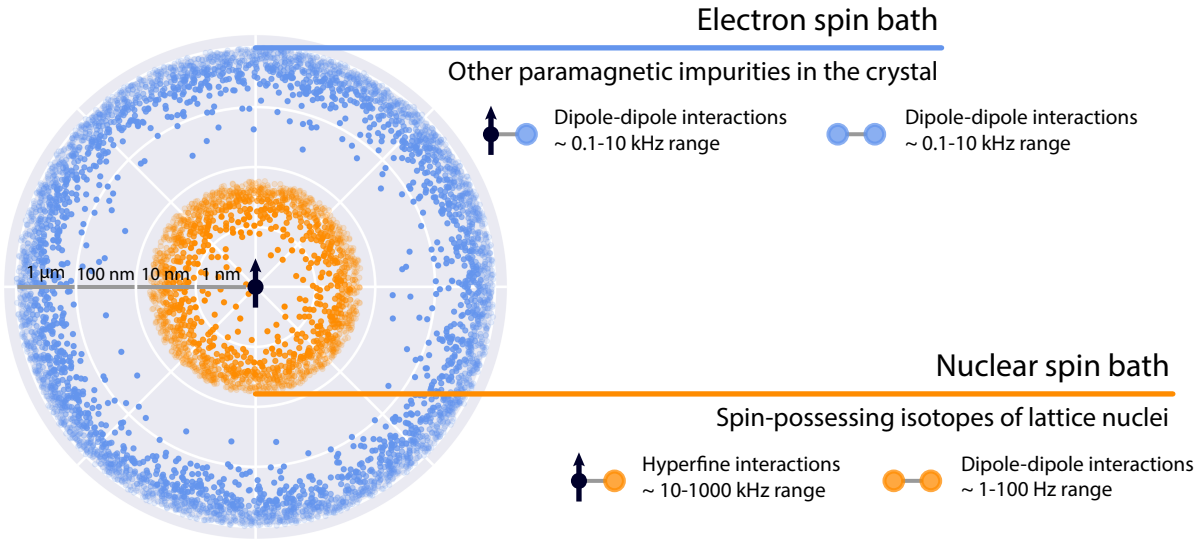

Figure 4.3: Spin environment around the qubit. The picture shows the relative spatial scale of the electron and nuclear spin baths on the example of the diamond with the electronic defect concentration of a few parts per million.

the relativistic Dirac equation, and involve an infinite series of terms (see, for example[28]).

Unfortunately, for any realistic system it is impossible to diagonalize exactly the Hamiltonian, even if we limit the number of spin terms. It is easier to use an effective Hamiltonian, which contains only spin-variables of a "fictious" electron spins $\mathbf{S}_e$ and the nuclear spins $\mathbf{I}_n$. It describes a model system in a Hilbert space of electron and nuclear spins, while keeping the correct energy splitting of the true Hamiltonian of the system.

Phenomenologically, the leading terms of spin interactions, mentioned above, can be expressed as products of spin operators with external field and coupling constants (parameters). All reference to the "true" many electron wavefunction, geometry, and other structural parameters are implicitly contained in these coupling parameters.

As an example, we consider electron with spin-1 in an external magnetic field and in the presence of the bath spins. In this system the spin Hamiltonian is given by:

$$\hat{H} = \mu_B \mathbf{BgS} + \mathbf{SDS} + \sum_n \mathbf{SA}_n\mathbf{I}_n + \sum_n \gamma_n[1+\sigma_n]\,\mathbf{BI}_n + \sum_{i<j} \mathbf{I}_i\mathbf{J}_{ij}\mathbf{I}_j + \sum_n \mathbf{I}_n\mathbf{P}_n\mathbf{I}_n, \quad (4.1)$$

Wwere $\mathbf{S} = (\hat{S}_x, \hat{S}_y, \hat{S}_z)$ and $\mathbf{I} = (\hat{I}_x, \hat{I}_y, \hat{I}_z)$ are central spin and bath spins operators respectively, $\mathbf{B} = (B_x, B_y, B_z)$ is an external magnetic field, and all other terms are coupling parameters. In the following discussion we will discuss how one can compute each parameter of the spin Hamiltonian, focusing on the most relevant terms for this research.

Zeeman tensor

The magnetic field-electron interaction can be expressed as one term:

$$\hat{H}_Z = \mu_B \mathbf{BgS}, \tag{4.2}$$

where μ_B is Bohr magneton, equal to a magnetic moment of an electron, and $\mathbf{g}$ is the dimensionless tensor, describing the interactions between central spin and magnetic field, The $\mathbf{g}$ tensor contains contribution from the spin-field interactions, and orbital momentum-field interactions. The terms of $\mathbf{g}$ tensor can be written as:

$$g_{rs} = g_e \delta_{rs} + \Delta g^{RMC} \delta_{rs} + \Delta g_{rs}^{GC} + \Delta g_{rs}^{OZ/SOC}, \tag{4.3}$$

where $g_e \approx 2.002318$ is the free electron value (dominating contribution), Δg^{RMC} is due to the relativistic mass correction, the term Δg_{rs}^{GC} is a diamagnetic correction, and the fourth term arises from orbital Zeeman and spin orbital interactions [29].

In the presence of only axial magnetic field B_z, the product $\omega_e = \mu_B g_{zz} B_z$ defines the Larmor frequency ω_i of the electron spin. The gyromagnetic ratio of the electron is equal to $\mu_B g_{zz}$.

Zero field splitting

We can express the electron-electron (for spin-1) interactions as one term, known as zero field splitting, given by the product:

$$\hat{H}_{ZFS} = \mathbf{SDS}, \tag{4.4}$$

where $\mathbf{S}$ is the effective electronic spin of the system. The tensor $\mathbf{D}$ completely describes interactions between the electron spins. To the first order of perturbation theory, $\mathbf{D}$ is given by spin dipole-dipole interactions, and at the second order spin-orbit coupling arises [30]. For higher electron spins one might need higher order operators, usually represented as a set of Stevens operators (see for example [31]).

Hyperfine interaction

Interactions between effective electron spin and n-th bath spin can be expressed phenomenologically as:

$$\hat{H}_{HFI} = \mathbf{SA}_n\mathbf{I}_n. \tag{4.5}$$

In the case of electron bath spins, $\mathbf{A}$ tensor corresponds to only dipole-dipole interaction (Eq. (4.8)). For the nuclear bath spins, $\mathbf{A}$ is known as hyperfine coupling. Let's consider the hyperfine tensor in more detail, which should be calculated for each nuclear spin. It consists of three different components: isotropic (contact), anisotropic (dipolar), and spin-orbital coupling parts:

$$\mathbf{A} = \mathbf{A}^{iso} + \mathbf{A}^{dip} + \mathbf{A}^{SO}, \tag{4.6}$$

where first two parts are given by:

$$A^{iso}_{ab} = -\delta_{ab}\frac{1}{3S}\mu_0\gamma_e\gamma_n\hbar^2 n_s(\mathbf{R}_n) \tag{4.7}$$

$$A_{ab}^{dipole} = \frac{1}{2S}\frac{\mu_0}{4\pi}\gamma_e\gamma_n\hbar^2 \int \frac{|\mathbf{r}-\mathbf{R}_n|\delta_{ab} - 3(\mathbf{r}-\mathbf{R}_n)_a(\mathbf{r}-\mathbf{R}_n)_b}{|\mathbf{r}-\mathbf{R}_n|^5} n_s(\mathbf{r})d\mathbf{r} \tag{4.8}$$

where γ_e and γ_n are gyromagnetic ratios of the central spin and bath spin respectively, n_s is the spin density [32]. The third term arises from spin-orbital interactions.

Zeeman interaction

Similar to the electron spin, each of the bath spins interacts with the external magnetic field as follows:

$$\hat{H}_{nz} = \gamma_n[1+\sigma_n]\mathbf{B}\mathbf{I}_n \tag{4.9}$$

where $\sigma_\mathbf{N}$ is a chemical shift tensor, which shows the local change in the magnetic field due to the electronic structure [33]. We adopt the notation for nuclear spins; for electron spins the same information is usually represented using the effective **g**-tensor (Eq. (4.2)). Chemical shift is usually very small relative to the total Zeeman interaction, of the order of few parts per million (ppm). Thus, for the purposes of this study it can be safely ignored.

J-coupling and dipolar coupling

The interaction between two bath spins i and j can be expressed by the following term:

$$\hat{H}_{nn} = \mathbf{I}_i\mathbf{J}_{ij}\mathbf{I}_j, \tag{4.10}$$

where $\mathbf{J_{ij}}$ will have two main components: dipolar coupling (for both electron and nuclear spin baths) and J-coupling (nuclear spin bath only).

The direct dipolar coupling represents interactions of two bath spins as point dipoles and can be computed as:

$$\hat{H}_{dd} = \frac{\mu_0}{4\pi}\gamma_i\gamma_j\hbar^2\left(\frac{\mathbf{I}_i\mathbf{I}_j}{r_{ij}^3} - \frac{3(\mathbf{I}_i\cdot\mathbf{r}_{ij})(\mathbf{I}_j\cdot\mathbf{r}_{ij})}{r_{ij}^5}\right). \tag{4.11}$$

J-coupling represents indirect interactions of nuclei through the electron cloud. These interactions require two nuclei to be connected through a small number of chemical bonds and thus decay rapidly with distance [34].

Quadrupole interaction

The nuclear spin Hamiltonian contains terms that describe the orientation dependence of the electronic interactions of nuclei. Nuclei do not possess an electric dipole moment [34], and electric multipoles of the nuclei are equal to zero starting from $2I$ ($\mathbb{C}^{(n)} = 0$ for $n > 2I$). Therefore, for $I = 1/2$ no additional electronic interactions appear between nuclei and the electronic field. But for any higher spins there are interactions of the quadrupoles order or higher.

The quadrupole interactions with the electronic field are given by:

$$\hat{H}_Q = \mathbf{I}_n \mathbf{P}_n \mathbf{I}_n = \frac{eQ}{6I(2I-1)} \sum_{a,b \in x,y,z} V_{ab} \left[\frac{3}{2}(I_a I_b + I_b I_a) - \delta_{ab} I(I+1) \right], \tag{4.12}$$

where V_{ab} is the second derivative of the electrostatic potential at the nucleus, e is the electronic charge and Q is the nuclear quadrupole moment.

4.2.2 Note on secular approximation and its correspondence to RWA

In the NMR community, one can often encounter the so-called "secular approximation": in the presence of large magnetic fields along the z-axis, we can neglect all terms in the effective spin-spin Hamiltonian except for the ones that commute with the Zeeman term ($\hat{S}_{z,1}\hat{S}_{z,2}$ type of interactions, where two operators correspond to different spins) or conserve the total magnetization of the system ($\hat{S}_{+,1}\hat{S}_{-,2} + h.c.$). It turns out we have already encountered this approximation and denoted it as the rotating wave approximation (RWA, see Section 2.2.2). To see that the two approximations are the same, consider the two spins interacting

with a full dipole-dipole tensor:

$$\hat{H} = \omega_1 \hat{S}_{z,1} + \omega_2 \hat{S}_{z,2} + \mathbf{S}_1 \mathbf{A} \mathbf{S}_2, \tag{4.13}$$

where $\mathbf{S}_1 \mathbf{A} \mathbf{S}_2 = \sum_{i=x,y,z} \sum_{j=x,y,z} \hat{S}_{i,1} A_{ij} \hat{S}_{j,2}$ is a sum over all possible interactions.

Let's move into the rotating frame, defined by the Zeeman term in the Hamiltonian: $\hat{U} = e^{i(\omega_1 \hat{S}_{z,1} + \omega_2 \hat{S}_{z,2})t}$. The Hamiltonian in the interaction picture becomes:

$$\hat{H}_I(t) = \sum_{i=x,y,z} \sum_{j=x,y,z} e^{i\omega_1 \hat{S}_{z,1}} \hat{S}_{i,1} e^{-i\omega_1 \hat{S}_{z,1}} A_{ij} e^{i\omega_2 \hat{S}_{z,2}} \hat{S}_{j,2} e^{-i\omega_2 \hat{S}_{z,2}}. \tag{4.14}$$

Now we need to find which terms are slowly oscillating in this summation. Assuming $\omega_1 \approx \omega_2$ we find that following terms survive:

$$\tilde{S}_{z,1}(t) \tilde{S}_{z,2}(t) = \hat{S}_{z,1} \hat{S}_{z,2}, \tag{4.15}$$

$$\tilde{S}_{+,1}(t) \tilde{S}_{-,2}(t) = e^{i(\omega_1 - \omega_2)t} \hat{S}_{+,1} \hat{S}_{-,2}, \tag{4.16}$$

$$\tilde{S}_{-,1}(t) \tilde{S}_{+,2}(t) = e^{-i(\omega_1 - \omega_2)t} \hat{S}_{-,1} \hat{S}_{+,2}. \tag{4.17}$$

Here for clarity we define $\tilde{S}_{a,i}(t) = e^{i[\omega_i \hat{S}_{z,i} t]} \hat{S}_{a,i} e^{-i[\omega_i \hat{S}_{z,i} t]}$. Every other term will oscillate at the Larmor frequency of one of the spins or faster. For example:

$$\tilde{S}_{z,1}(t) \tilde{S}_{+,2}(t) = e^{i\omega_2 t} \hat{S}_{z,1} \hat{S}_{+,2}, \tag{4.18}$$

$$\tilde{S}_{-,1}(t) \tilde{S}_{z,2}(t) = e^{-i\omega_1 t} \hat{S}_{-,1} \hat{S}_{z,2}, \tag{4.19}$$

$$\tilde{S}_{+,1}(t) \tilde{S}_{+,2}(t) = e^{i(\omega_1 + \omega_2)t} \hat{S}_{+,1} \hat{S}_{+,2}, \tag{4.20}$$

and so on. Using the RWA, we can neglect the fast oscillating terms, keeping only the terms defined in the equations (4.15, 4.16, 4.17). If two spins have sufficiently different Larmor frequencies, the terms in the equations (4.16) and (4.17) can be discarded as well.

However, note that some nonsecular interactions cannot be discarded in the case of the electron spin and nuclear spin in the intermediate magnetic field regimes. Specifically, if hyperfine coupling A is of the same order of magnitude as the nuclear Larmor frequency ω_n, the $\tilde{S}_z(t)\tilde{I}_+(t) = e^{i\omega_n t}\hat{S}_z\hat{I}_+$ and $\tilde{S}_z(t)\tilde{I}_-(t) = e^{-i\omega_n t}\hat{S}_z\hat{I}_-$ interactions will oscillate at a comparable frequency as the strength of the hyperfine interaction; thus they cannot be safely ignored. Indeed, the $A_\perp = \sqrt{A_{zx}^2 + A_{zy}^2}$ hyperfine interaction, also known as perpendicular hyperfine interaction, is of particular interest as it allows the control of a nuclear spin state with electron spin at ambient magnetic fields (see Section 11 for more details).

Overall, this note concludes the theoretical background necessary to understand the following chapters of this thesis, describing the application of the first principles simulations in probing the magnetic environment of spin qubits.

CHAPTER 5

LET ME FIND MY HAMMER... PYCCE

"If the only tool you have is a hammer, it is tempting to treat everything as if it were a nail." — Abraham Maslow

This chapter is adapted from the published work [4].

In this chapter we present PyCCE, an open-source Python library for simulating the dynamics of spin qubits in a spin bath, using the cluster-correlation expansion (CCE) method. PyCCE includes modules to generate realistic spin baths, employing coupling parameters computed from first principles with electronic structure codes, and enables the user to run simulations with either the conventional or generalized CCE method. We illustrate three use cases of the Python library: the calculation of the Hahn-echo coherence time of the nitrogen-vacancy in diamond; the calculation of the coherence time of the basal divacancy in silicon carbide at avoided crossings; and the calculation for magnetic field orientation-dependent dynamics of a shallow donor in silicon.

The complete documentation, downloadable tutorials, and installation instructions are available at `https://pycce.readthedocs.io/en/latest/`.

5.1 Introduction

In solid-state systems, the spin of electrons is one of the leading platforms for quantum information applications [20, 24, 35]. Examples include but are not limited to quantum dot spin qubits [36–39], shallow donors in Si [40–42], and localized spin defects in semiconductors [4, 43, 44].

These systems share an important attribute: the time evolution of the spin qubit, at least in part, is controlled by its magnetic environment, consisting of nuclear and other

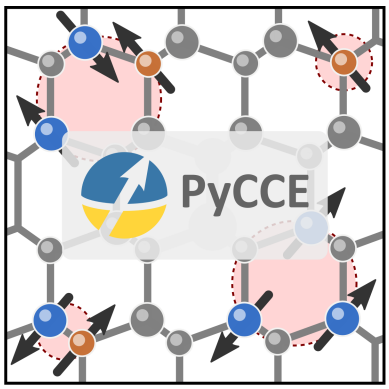

Figure 5.1: We present `PyCCE` - an open source Python library to simulate the dynamics of a spin qubit interacting with a spin bath using the cluster-correlation expansion (CCE) method.

electronic spins. This environment can hinder the applications of spin-based technologies by imposing limits on the spin qubits' coherence times [15] but can also advance applications where nuclear spins may act as memory units in quantum networks [45, 46]. First principles predictions of the spin bath dynamics in materials are critical to the design and realization of solid-state spin technologies.

The cluster correlation expansion (CCE) method [47, 48] is one of the most widely used approaches to simulate the quantum decoherence dynamics of spin qubits in a finite spin bath [15]. The approach reproduces the correct dynamics for a variety of physical realizations of spin qubits. For example, results of the CCE method show excellent agreement with experiments for bismuth [49, 50] and phosphorous [51] donors in Si, the nitrogen-vacancy (NV) center in diamond [52], and divacancies in 4H-SiC, both axial [3, 5] and basal [53]. The CCE method has also been used to predict properties of novel materials, such as 2D platforms for spin qubits [54, 55], and to conduct a general screening of potential qubit hosts over a wide range of materials [56]. However, software implementations of the CCE method are not readily accessible and hinge on in-house developments, which lack openness and transferability.

To overcome these challenges, we developed `PyCCE` - an open-source python-based library

for carrying out CCE calculations. This module is the first public implementation of the CCE code, available as an open-source package with high integration within the existing scientific Python ecosystem. Here we describe the theoretical framework of the CCE method and its implementation in the `PyCCE` library. We then highlight the application of the `PyCCE` module to several physical systems and verify and validate our implementation with theoretical and experimental data.

5.2 Theoretical framework

We begin by discussing the theoretical background of the model used in the CCE.

5.2.1 Hamiltonian of system

The Hamiltonian for the central spin in a spin bath includes the following terms:

$$\hat{H} = \hat{H}_S + \hat{H}_{SB} + \hat{H}_B \tag{5.1}$$

where $\hat{H}_S$ is the Hamiltonian of the free central spin, $\hat{H}_{SB}$ denotes interactions between the central spin and a spin belonging to the bath, and $\hat{H}_B$ describes intrinsic bath spin interactions. These terms are written as:

$$\hat{H}_S = \mathbf{SDS} + \mathbf{B}\gamma_S\mathbf{S} \tag{5.2}$$

$$\hat{H}_{SB} = \sum_i \mathbf{S}\mathbf{A}_i\mathbf{I}_i \tag{5.3}$$

$$\hat{H}_B = \sum_i \mathbf{I}_i\mathbf{P}_i\mathbf{I}_i + \mathbf{B}\gamma_i\mathbf{I}_i + \sum_{i>j} \mathbf{I}_i\mathbf{J}_{ij}\mathbf{I}_j \tag{5.4}$$

where $\mathbf{S} = (\hat{S}_x, \hat{S}_y, \hat{S}_z)$ are the components of spin operators of the central spin, and $\mathbf{I} = (\hat{I}_x, \hat{I}_y, \hat{I}_z)$ are the components of the bath spin operators. The following tensors describe

the interactions:

- **D** (**P**) is the self-interaction tensor of the central spin (bath spin). For the electron spin, the tensor corresponds to the zero-field splitting (ZFS) tensor. For nuclear spins, the tensor corresponds to the quadrupole interactions tensor.

- γ_i is the magnetic field interaction tensor of the i-th spin describing the interaction between the spin and the external magnetic field **B**. We assume that for the bath spins, it is isotropic. This assumption is justified for both the nuclear spin bath and the electron spin bath, which consists of light elements (s- and p-elements).

- **A** is the interaction tensor between central and bath spins. In the case of the nuclear spin bath, it corresponds to the hyperfine couplings.

- **J** is the interaction tensor between bath spins.

5.2.2 Qubit coherence

Two coherence times are commonly measured to characterize the loss of a qubit's coherence - T_1 and T_2. T_1 defines the timescale over which the qubit population is thermalized; T_2 describes a purely quantum phenomenon - the loss of the phase of the qubit's superposition state.

In the pure dephasing regime ($T_1 >> T_2$), the decoherence of the central spin is completely determined by the decay of the off-diagonal element of the qubit's density matrix. Namely, if the qubit is initially prepared in the $|\psi\rangle = \frac{1}{\sqrt{2}}(|0\rangle + e^{i\phi}|1\rangle)$ state, the coherence function $\mathcal{L}(t)$ characterizes the loss of the relative phase of the $|0\rangle$ and $|1\rangle$ levels:

$$\mathcal{L}(t) = \frac{\langle 1|\hat{\rho}_S(t)|0\rangle}{\langle 1|\hat{\rho}_S(0)|0\rangle} = \frac{\langle \hat{\sigma}_-(t)\rangle}{\langle \hat{\sigma}_-(0)\rangle} \tag{5.5}$$

where $\hat{\rho}_S(t)$ is the density matrix of the central spin, and $|0\rangle$ and $|1\rangle$ are qubit levels.

In general, one could potentially obtain the qubit's coherence function by directly solving the Schrodinger equation of the total system and tracing out the bath degrees of freedom. However, the complexity of such computations grows exponentially with the bath size, and for any meaningful system (bath of several hundred spins), the problem is impossible to solve computationally.

The core idea of the CCE approach is that the spin bath-induced decoherence can be factorized into a set of irreducible contributions from the bath spin clusters. We can rewrite the factorized coherence function as:

$$\mathcal{L}(t) = \prod_{C} \tilde{L}_C(t) = \prod_{i} \tilde{L}_{\{i\}}(t) \prod_{i,j} \tilde{L}_{\{ij\}}(t)... \tag{5.6}$$

where $\tilde{L}_{\{i\}}(t)$ is the contribution of the single bath spin i and $\tilde{L}_{\{ij\}}(t)$ is the irreducible contribution of the spin pair i, j. The maximum size of the cluster included in the expansion determines the order of the CCE approximation. For example, in the CCE2 approximation only contributions up to spin pairs are included, in CCE3 only cluster contributions up to triplets of bath spins are included, and so on. Each cluster contribution is defined recursively as:

$$\tilde{L}_C = \frac{L_C}{\prod_{C'} \tilde{L}_{C' \subset C}}, \tag{5.7}$$

where time dependence is implied; L_C is the coherence function of the qubit, including only interactions with the bath spins in a given cluster C, and $\tilde{L}_{C'}$ are contributions of subcluster C' of C.

The first element of the cluster expansion $\tilde{L}_{\{0\}} = L_{\{0\}}$ is the phase factor of the free evolution of the central spin. The contribution of each single bath spin i is computed as:

$$\tilde{L}_{\{i\}} = \frac{L_{\{i\}}}{\tilde{L}_{\{0\}}}. \tag{5.8}$$

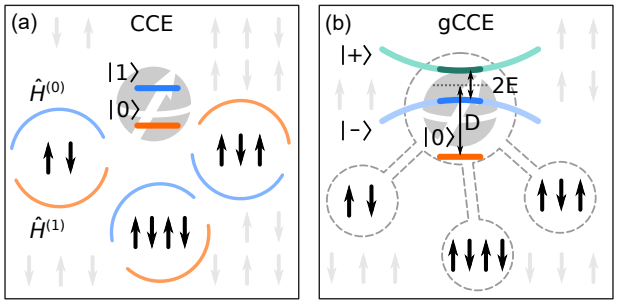

Figure 5.2: CCE Formulations. (a) Conventional CCE, where the cluster Hamiltonian is reduced to the sum of two effective Hamiltonians $\hat{H}^{(0)}$ and $\hat{H}^{(1)}$. (b) Generalized CCE, where each cluster Hamiltonian includes all central spin levels.

Next, the contribution of spin pairs is computed as:

$$\tilde{L}_{\{ij\}} = \frac{L_{\{ij\}}}{\tilde{L}_{\{0\}}\tilde{L}_{\{i\}}\tilde{L}_{\{j\}}} \tag{5.9}$$

and so on.

The workload of this iterative evaluation of correlation functions grows polynomially instead of exponentially as a function of the number of bath spins, hence computations for thousands of bath spins are trivial.

Within the CCE formalism, one assumes that the bath-induced relaxation is significantly slower than the dephasing, thus such relaxation is ignored. This approximation is justified when the central spin energy splitting and the spin-bath interaction energies are substantially different, which is usually the case for nuclear spin baths. However, several studies have shown that the CCE method is also applicable to cases where the central electron spin interacts with the electron spin bath [3], or even the resonant bath, where central spin flips can occur [57].

5.2.3 Conventional CCE

In the original formulation of the CCE method (Fig. 5.2a), the total Hamiltonian of the system (Eq. 5.1) is reduced to the sum of two effective Hamiltonians, conditioned on the qubit levels of the central spin:

$$\hat{H} = |0\rangle\langle 0| \otimes \hat{H}^{(0)} + |1\rangle\langle 1| \otimes \hat{H}^{(1)} \tag{5.10}$$

where $\hat{H}^{(\alpha)}$ is an effective Hamiltonian acting on the bath when the central qubit is in the $|\alpha\rangle$ state ($|\alpha\rangle = |0\rangle, |1\rangle$ is one of the two eigenstates of the $\hat{H}_S$ that are chosen as qubit levels):

$$\hat{H}^{(\alpha)} = E_\alpha + \langle\alpha| \hat{H}_{SB} |\alpha\rangle + \hat{H}_B + \hat{H}^{(\alpha)}_{PT} \tag{5.11}$$

and $\hat{H}^{(\alpha)}_{PT}$ are higher order perturbations to the effective Hamiltonian $\hat{H}^{(\alpha)}$. Up to the second order, we can write:

$$\hat{H}^{(\alpha)}_{PT} = \sum_{i,j} \sum_{\beta\neq\alpha} \frac{(\langle\alpha| \mathbf{S} |\beta\rangle \mathbf{A}_i\mathbf{I}_i)\left(\langle\beta| \mathbf{S} |\alpha\rangle \mathbf{A}_j\mathbf{I}_j\right)}{E_\alpha - E_\beta} = \sum_{i,j} \mathbf{I}_i\mathbf{T_{ij}}\mathbf{I}_j. \tag{5.12}$$

Here the summation is over all $|\beta\rangle$ eigenstates of the central spin Hamiltonian $\hat{H}_S$.

For each cluster C, the Hamiltonian $\hat{H}^{(\alpha)}_C$ is obtained by tracing out the degrees of freedom of the bath spins, not included in the cluster:

$$\begin{aligned}\hat{H}^{(\alpha)}_C = &\sum_{i\in C} \langle\alpha| \mathbf{S} |\alpha\rangle \mathbf{A}_i\mathbf{I}_i + \sum_{i\in C} \mathbf{I}_i\mathbf{P}_i\mathbf{I}_i + \mathbf{B}\gamma_i\mathbf{I}_i + \\ &\sum_{i,j\in C} \mathbf{I}_i(\mathbf{J}_{ij} + \mathbf{T}_{ij})\mathbf{I}_j + \sum_{i\in C,\ a\notin C} \mathbf{I}_i(\mathbf{J}_{ia} + \mathbf{T}_{ia})\langle\mathbf{I}_a\rangle\end{aligned} \tag{5.13}$$

where $\langle\mathbf{I}_a\rangle = \mathrm{Tr}\{\hat{\rho}_a\mathbf{I}_a\}$ is an average value of each bath spin outside of a given cluster, and ρ_a is the initial density matrix of the bath spin.

In most systems of interest, it is justified to assume that the state of each bath spin i with

spin s,is purely random ($\hat{\rho}_i = \frac{1}{2s+1}\mathbb{1}$, where $\mathbb{1}$ is the identity). As a result, the spin operator expectation values in Eq. (5.13) are nullified, $\langle \mathbf{I}_a \rangle = 0$. However, this approximation is not always valid and may lead to incorrect results, as we discuss below.

Given an initial qubit state $|\psi\rangle = \frac{1}{\sqrt{2}}(|0\rangle + e^{i\phi}|1\rangle)$ and an initial state of the bath spin cluster C characterized by the density matrix $\hat{\rho}_C$, the coherence function of the qubit interacting with the cluster C can be computed as:

$$L_C(t) = Tr[\hat{U}_C^{(0)}(t)\hat{\rho}_C\hat{U}_C^{(1)\dagger}(t)] \tag{5.14}$$

where $\hat{U}_C^{(\alpha)}(t)$ is the time propagator defined in terms of the effective Hamiltonian $\hat{H}_C^{(\alpha)}$ and the number of decoupling pulses. For free induction decay (FID) the time propagators are trivial:

$$\hat{U}_C^{(0)} = e^{-\frac{i}{\hbar}\hat{H}_C^{(0)}t};\ \hat{U}_C^{(1)} = e^{-\frac{i}{\hbar}\hat{H}_C^{(1)}t}. \tag{5.15}$$

Each applied π-pulse flips the state of the central spin and therefore changes the evolution of the bath. For the Hahn-echo sequence (where a single π-pulse is applied halfway between the initialization and the measurement of the qubit) we can write the propagators as:

$$\hat{U}^{(0)} = e^{-\frac{i}{\hbar}\hat{H}_C^{(1)}\frac{t}{2}}e^{-\frac{i}{\hbar}\hat{H}_C^{(0)}\frac{t}{2}} \tag{5.16}$$

$$\hat{U}^{(1)} = e^{-\frac{i}{\hbar}\hat{H}_C^{(0)}\frac{t}{2}}e^{-\frac{i}{\hbar}\hat{H}_C^{(1)}\frac{t}{2}} \tag{5.17}$$

For the generic decoupling sequence with N (even) decoupling pulses applied at $t_1, t_2 ... t_N$, we write:

$$\hat{U}^{(\alpha)}(t) = e^{-\frac{i}{\hbar}\hat{H}_C^{(\alpha)}\Delta t_N}e^{-\frac{i}{\hbar}\hat{H}_C^{(\beta)}\Delta t_{N-1}}...e^{-\frac{i}{\hbar}\hat{H}_C^{(\alpha)}\Delta t_1} \tag{5.18}$$

Where $|\alpha\rangle = |0\rangle, |1\rangle$ and $|\beta\rangle = |1\rangle, |0\rangle$, respectively, $\Delta t_n = t_n - t_{n-1}$ is the time difference between consecutive pulses and $t = \sum_i t_i$ is the total evolution time. In sequences with odd number of pulses N, the leftmost propagator is the exponent of $\hat{H}_C^{(\beta)}$. For further details,

we refer the readers to the seminal papers on CCE [47, 48].

5.2.4 Generalized CCE (gCCE)

Instead of projecting the total Hamiltonian on the qubit levels, one may directly include the central spin degrees of freedom to each clusters. This approach is particularly well-suited to study the coherence of spin qubits at clock transitions [50, 53]. We refer to such formulation as gCCE (Fig. 5.2b). In this case, we write the cluster Hamiltonian as:

$$\begin{aligned}\hat{H}_C = \mathbf{SDS} + \mathbf{B}\gamma_{\mathbf{S}}\mathbf{S} + \sum_{i\in C}\mathbf{S}\mathbf{A}_i\mathbf{I}_i + \sum_{i\in C}\mathbf{I}_i\mathbf{P}_i\mathbf{I}_i + \mathbf{B}\gamma_i\mathbf{I}_i + \\ \sum_{i<j\in C}\mathbf{I}_i\mathbf{J}_{ij}\mathbf{I}_j + \sum_{a\notin C}\mathbf{S}\mathbf{A}_a\langle\mathbf{I}_a\rangle + \sum_{i\in C,\ a\notin C}\mathbf{I}_i\mathbf{J}_{ia}\langle\mathbf{I}_a\rangle.\end{aligned} \tag{5.19}$$

The coherence function of the cluster $L_C(t)$ is computed as:

$$L_C(t) = \langle 0|\, \hat{U}_C(t)\hat{\rho}_{C+S}\hat{U}_C^{\dagger}(t)\,|1\rangle\,, \tag{5.20}$$

where $\hat{\rho}_{C+S} = \hat{\rho}_C \otimes \hat{\rho}_S$ is the combined initial density matrix of the bath spins' cluster and central spin.

Similar to the conventional CCE, we define the time propagator in terms of the number of decoupling π-pulses and the cluster Hamiltonian (Eq. 5.19). The FID propagator is given as:

$$\hat{U}_C(t) = e^{-\frac{i}{\hbar}\hat{H}_C t}. \tag{5.21}$$

For an arbitrary set of decoupling pulses, we can write the propagator as follows:

$$\hat{U}_C(t) = \mathcal{T}\left[e^{-\frac{i}{\hbar}\hat{H}_C\tau}e^{-\frac{i}{\hbar}\hat{\sigma}_{\{x,y,z\}}\frac{\phi}{2}}e^{-\frac{i}{\hbar}\hat{H}_C\tau}\right]^N \tag{5.22}$$

where $\hat{\sigma}_{\{x,y,z\}}$ are the Pauli matrices of the qubit, τ is the delay between pulses, ϕ is the

rotational angle, and N is the number of pulses. For Hahn-echo experiments with a π rotation about the x axis, the propagator is given by:

$$\hat{U}_C^{HE}(t) = e^{-\frac{i}{\hbar}\hat{H}_C\frac{t}{2}}e^{-\frac{i}{\hbar}\hat{\sigma}_x\frac{\pi}{2}}e^{-\frac{i}{\hbar}\hat{H}_C\frac{t}{2}}. \tag{5.23}$$

For further details, see Chapter 6 of this thesis or the reference [53].

5.2.5 Monte Carlo bath state sampling

To improve the convergence of the cluster expansion for some particularly challenging systems, we can directly sample the pure states of the bath to predict the random state of the bath. Then, the coherence can be computed as:

$$\mathcal{L}(t) = \sum_i p_i \mathcal{L}_i(t) \tag{5.24}$$

where $\mathcal{L}_i(t)$ is the coherence function, computed for the pure bath state i, and p_i is the probability of such state (for the completely mixed bath state, all p_i are equal).

5.2.6 Correlation Function

A cluster expansion similar to the one described above may be applied to the autocorrelation of the Overhauser field upon the central spin. The autocorrelation in secular approximation is given by:

$$\mathcal{C}_{AA}(t) = \left\langle \sum_{\{I\}} A_{zz}\hat{I}_z(t) \sum_{\{I\}} A_{zz}\hat{I}_z(0) \right\rangle \tag{5.25}$$

where the $\hat{I}_z(t)$ is the spin operator in the Heisenberg picture $\hat{I}_z(t) = \hat{U}^\dagger(t)\hat{I}_z\hat{U}(t)$. Under the CCE approximation, we can write the autocorrelation function as a sum of the spin

cluster contributions:

$$\mathcal{C}_{AA}(t) = \sum_{C} \tilde{C}_{AA,\,C} \tag{5.26}$$

where cluster contributions are defined recursively, in a fashion similar to coherence function contributions:

$$\tilde{C}_{AA,\,C} = C_{AA,\,C} - \sum_{C'} \tilde{C}_{AA,\,C' \subset C}. \tag{5.27}$$

The noise autocorrelation function for each cluster is computed using Eq. 5.25 for the bath spins within the cluster. Further details are available in ref. [58, 59].

5.3 Code implementation

In the `PyCCE` library, we provide a convenient way to simulate the dynamics of the central spin interacting with a realistic spin bath.

The general workflow of running simulations with `PyCCE` includes the following steps (Fig. 5.3):

- Generate the spin bath as an instance of `BathArray` class.
- Input the properties of the central spin to the instance of the `Simulator` class - a central object used for CCE simulations.
- Calculate the desired properties using the `Simulator` object.

Generation of the spin bath. The `BathCell` class enables one to initialize the structure of the material, populate it with spins, and generate a large supercell. The procedure assumes a random distribution of spins over the lattice positions of a given type (e.g., ^{13}C nuclear spins are distributed randomly over the lattice sites occupied by Carbon atoms), which can be fixed by setting the seed of the random number generator. The supercell with bath spins is stored in the `BathArray` format. The same object stores the properties of

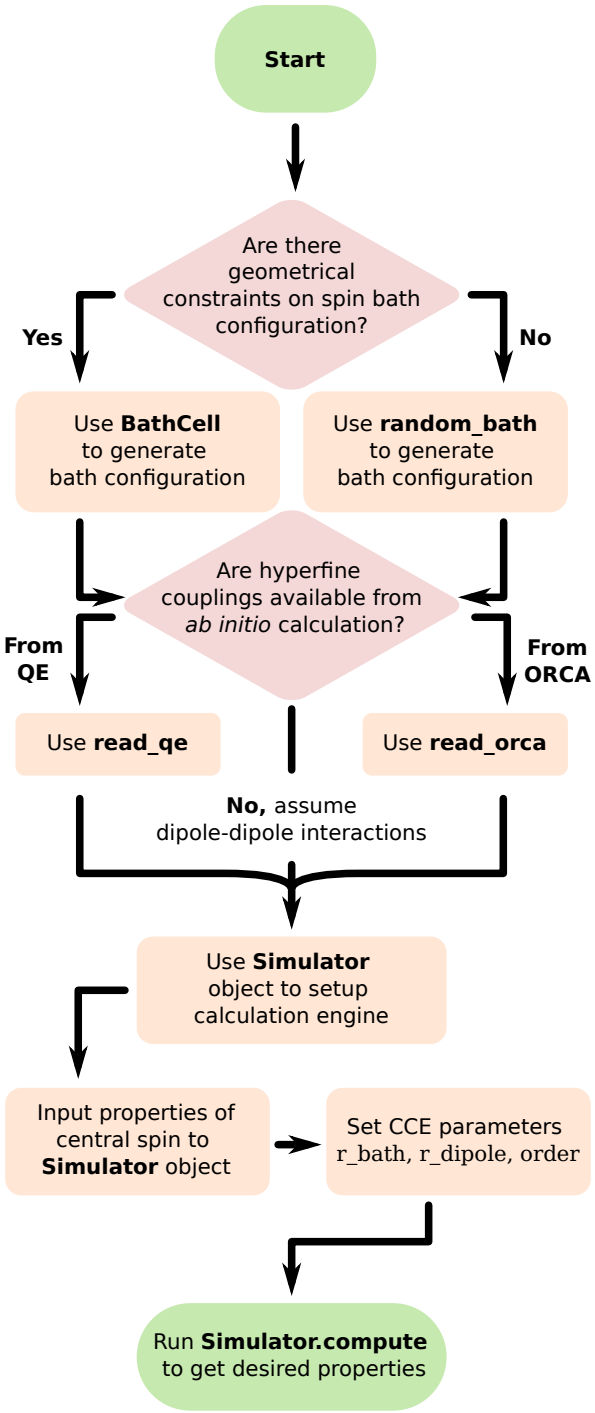

Figure 5.3: General workflow of the `PyCCE` module. Top to bottom: generate the spin bath; determine the properties of the central and cluster composition; run CCE simulations.

the bath spins (hyperfine couplings, quadrupole interactions, gyromagnetic ratios). Most of the properties of the nuclear spins (e.g., gyromagnetic ratio, concentrations) are already available in the `PyCCE` library using the EasySpin [31] database.

The `BathCell` supports an interface with the Atomic Simulations Environment (ASE) package [60], a well-developed tool to initialize the structure of many solid-state materials.

Setting up the `Simulator` object. In this step, a user should provide properties of the central spin, including zero-field splitting, magnetic field interaction tensor, and the amplitude of the external magnetic field.

Next, one chooses the size of the "active" bath spins by imposing a cutoff radius, `r_bath` (Fig. 5.4), defined as the maximum distance from the central spin to the bath spin to be considered in the calculation.

The hyperfine couplings entering Eq. (5.1) are either:

- Approximated using the point dipole-dipole approximation as:

$$\mathbf{A} = -\gamma_{\mathbf{S}}\gamma_i \frac{\mu_0 \hbar^2}{4\pi |\vec{r}|^5} \left[3 \cdot \vec{r} \otimes \vec{r} - \mathbb{1} \cdot |\vec{r}|^2\right] \tag{5.28}$$

  Where $\mathbb{1}$ is 3×3 identity matrix, and the γ_i tensors are assumed to be isotropic.

- Computed using the spin density distribution of the central spin. The `PyCCE` package supports input of the spin density of the central spin in the Gaussian cube format [61] and can integrate it to obtain dipolar hyperfine couplings.

- Obtained from first-principles calculations using quantum chemistry or solid-state simulation packages. As of now, an interface with ORCA [62] and Quantum Espresso [63] packages is provided in the `PyCCE` implementation.

- Set manually by user.

The hyperfine couplings are required for each bath spin within the "active" region.

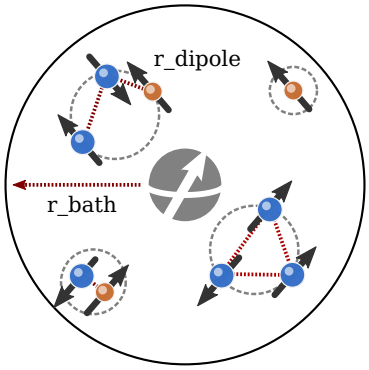

Figure 5.4: Illustration of the parameters `r_bath` and `r_dipole`. `r_bath` defines maximum allowed distance from the central spin to the bath spin, and `r_dipole` sets the maximum distance at which two bath spins form an "edge".

The interaction tensors between two bath spins $\mathbf{J}_{ij}$ are assumed from the point dipole-dipole interaction or can be set by the user.

Finally, the clusters entering the cluster expansion are determined. We followed the procedure of Ref. [5, 15] to obtain the clusters entering Eq. (5.6). We define a cutoff radius, `r_dipole`, that sets the maximum distance at which two bath spins form an "edge" (Fig. 5.4). Bath spins i and j form a cluster of two if there is an edge between them (distance $d_{ij} <$ `r_dipole`). Bath spins i, j, and k form a cluster of three if enough edges are found connecting them (e.g., there are two edges ij and jk) and so on. In general, we assume that spins $\{i..n\}$ form clusters if they form a connected graph. Imposing a spatial cutoff on the cluster connectivity reduces the scaling from polynomial to almost linear, in the case of sparse baths. Only clusters up to the size imposed by the `order` parameter (equal to the CCE order) are included.

Running CCE simulations. Once all parameters of the Hamiltonian are set, the `Simulator` object can be used to compute the coherence function of the central spin and the autocorrelation function of the bath spin noise using both the conventional CCE and gCCE.

Full documentation is available online at [64].

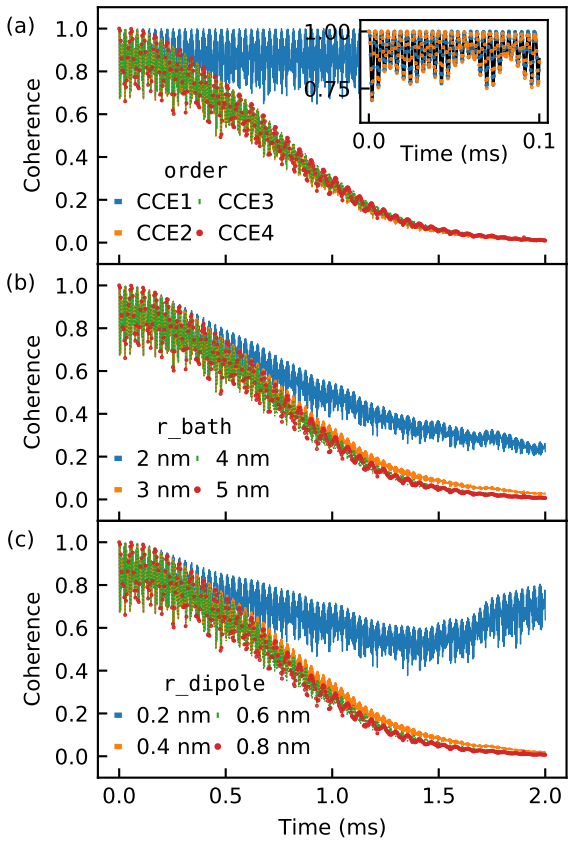

Figure 5.5: Convergence of the Hahn-echo coherence curve for NV^- Center in diamond. (a) Convergence with respect to the CCE order. Inset shows CCE1 (blue) and CCE2 (orange) curves against the exact solution for the isolated nuclear spins. (b) Convergence with respect to the size of the bath in nm. (c) Convergence with respect to the connectivity distance in nm.

5.4 Showcasing capabilities

All scripts used to generate the data below, along with the reference data, are available at the Qresp repository of this paper at `https://paperstack.uchicago.edu/paperdetails/613244e96381b275e8ec9928?server=https%3A%2F%2Fpaperstack.uchicago.edu`.

5.4.1 NV Center in diamond

First, we use `PyCCE` to highlight the application of the CCE method to a well-known physical system, the negatively charged nitrogen-vacancy (NV^-) center in diamond. For this example,

we compute hyperfine couplings using the point dipole approximation. In Figure 5.5 we present the convergence of the ensemble-averaged decay of the Hahn-echo coherence function, computed using the conventional CCE method. We averaged the coherence function over 100 different spatial realizations of nuclear spins to obtain an ensemble average. The calculations take several seconds on one processor core for each spatial realization.

The coherence function has two distinct elements: the fast electron spin echo envelope modulations (ESEEM) and the slow decay of the envelope. The calculations at the CCE1 level already reproduce the ESEEMs for short timescales and exactly follow the analytical solutions for the bath of the isolated nuclear spins [5, 65] (inset of Fig. 5.5a, black):

$$\mathcal{L}^{\text{exact}}(t) = \prod_i 1 - 2k_i \sin^2\left(w_i^{(0)}\frac{t}{4}\right)\sin^2\left(w_i^{(+1)}\frac{t}{4}\right) \tag{5.29}$$

where $w_i^{(0)} = w_L$ and $w^{(1)} = \sqrt{(w_L + A_{||})^2 + A_\perp^2}$ are conditioned Larmor frequencies and $k_i = \frac{A_\perp^2}{(w_L+A_{||})^2+A_\perp^2}$. Perpendicular and parallel hyperfine couplings are given as $A_\perp^2 = A_{zx}^2 + A_{zy}^2$ and $A_{||} = A_{zz}$, and the free Larmor frequency is $w_L = \gamma_i B_z$ for nuclear spin i. The decay of the coherence function can be seen at the CCE2 level and higher orders of CCE.

We find that the coherence time T_2, obtained from the fit of the coherence function envelope to the compressed exponent $\exp[-(t/T_2)^n]$, is about 0.92 ms, in line with previously reported theoretical predictions [52, 66]. Finally, we confirm that CCE calculations converge at second order, size of the bath of ≈ 4 nm, and connectivity distance in the clusters of ≈ 0.6 nm, consistent with the supplementary information of ref. [5].

5.4.2 Basal VV in SiC

Next, we highlight the importance of the bath state sampling to converge the dynamics of the localized spin defects at avoided crossings. As an example, we consider the basal

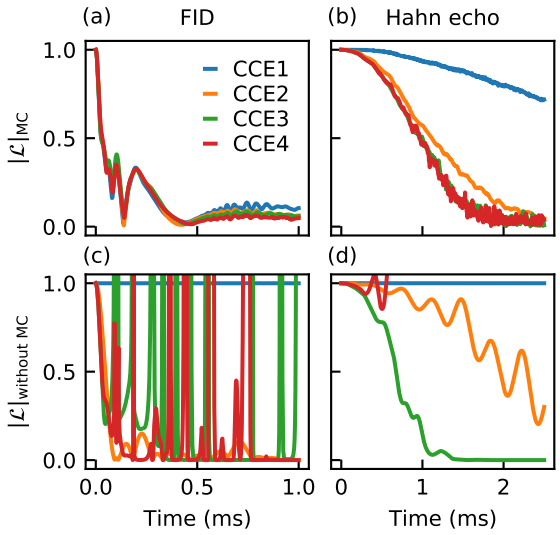

Figure 5.6: Coherence function of the basal kh-divacancy in 4H-SiC at avoided crossing of energy levels, computed with ($\mathcal{L}_{\mathrm{MC}}$) or without ($\mathcal{L}_{\mathrm{without\ MC}}$) bath state sampling for free induction decay ((a), (c)) and Hahn echo ((b), (d)) experiments at different CCE orders.

kh-divacancy in 4H-SiC. In this system, both nonzero axial D and transverse E zero-field splitting are non-zero, leading to an anisotropic $\mathbf{D}$ tensor in Eq. (5.1). The presence of the anisotropy in the $\mathbf{D}$ tensor allows for avoided crossing to emerge at zero applied magnetic field. When operating the qubit at this avoided crossing, one may significantly prolong the spin coherence.

We consider one random nuclear spin configuration and compute the coherence function corresponding to the free induction decay (FID), and Hahn echo experiments, using the gCCE method with and without Monte Carlo state sampling (Fig. 5.6a-d). We use *ab initio* hyperfine couplings for the inner shell (at distances $\leq$ 1 nm from the defect), computed with the GIPAW [67] module of the Quantum Espresso package [63]. We used a plane-wave basis with a kinetic energy cutoff of 40 Ry and the Perdew-Burke-Ernzerhof (PBE) in DFT calculations. We employed a point dipole approximation for the outer shell (distances $\geq$ 1 nm).

We find that the bath state sampling is crucial for the convergence of the coherence

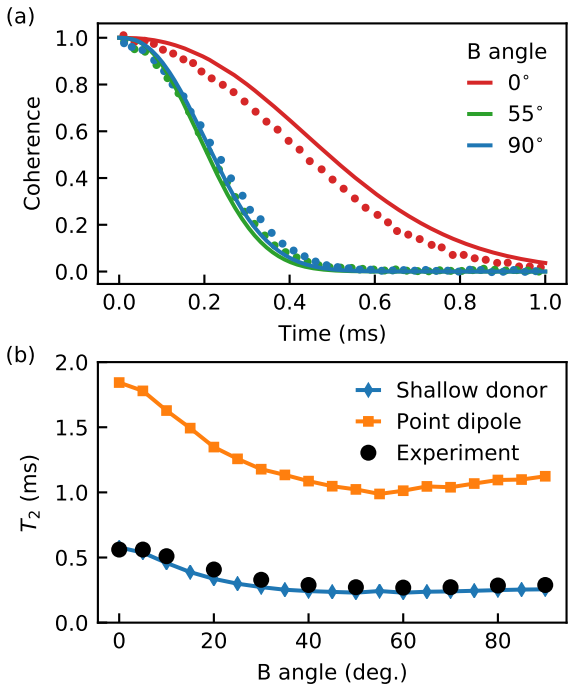

Figure 5.7: Coherence of the P donor in Si as a function of the magnetic field orientation, where $0B \parallel [001]$, $55B \parallel [111]$ and $90B \parallel [110]$. (a) The coherence at three representative angles. Solid lines show the coherence computed with `PyCCE`, and points show experimental data. (b) Computed coherence time T_2 as a function of the magnetic field rotation about $[1\bar{1}1]$ axis for P shallow donor (blue) and for the hypothetical localized electron spin with the same nuclear spin bath (orange) against experimental results (black). Experimental data are taken from [68].

function for both free induction and Hahn-echo experiments. The coherence function is well-converged at the second order for both cases. The decay of the coherence function is highly dependent on the specific nuclear spin configuration, as discussed in Ref.[53]. The calculations with the bath state sampling becomes $\sim m$ times more expensive, where m is the number of states sampled.

5.4.3 Shallow P donor in Si

Finally, we use `PyCCE` to compute the coherence decay of a shallow donor in Si induced by the nuclear spin bath. In this system, the contact Fermi terms dominate the hyperfine

interactions. The contact hyperfine couplings for ^{29}Si nuclear spins can be approximated using the Kohn-Luttinger wave function as:

$$A_F = \frac{16\pi}{9}\gamma_S\gamma_{^{29}Si}\eta[F_1(\vec{r})\cos k_0 x + F_3(\vec{r})\cos k_0 y + F_5(\vec{r})\cos k_0 z]^2 \tag{5.30}$$

where the envelope functions F_j are given as:

$$F_1 = \frac{\exp\left\{\left[\sqrt{\frac{x^2}{(nb)^2} + \frac{y^2+z^2}{(na)^2}}\right]\right\}}{\sqrt{\pi(na)^2(nb)}}. \tag{5.31}$$

Here $\vec{r} = x\vec{i} + y\vec{j} + z\vec{k}$ is the position of the nuclear spin, $k_0 = 0.85\frac{2\pi}{a_{Si}}$, $a_{Si} = 0.543$ nm is the lattice parameter, $n = 0.81$ for a phosphorus impurity, $\eta = 186$ is the charge density at Si lattice site, and $a = 2.509$ nm, $b = 1.443$ nm are characteristic lengths for hydrogenic impurities in Si [69].

The dipolar interaction is assumed to be equal to the one of point dipole at distances $\geq na \approx 2$ nm and zero otherwise [51].

The computed coherence for different alignments of the applied magnetic field is shown in Figure 5.7 along with the experimental results of Eisuke Abe et al. [68].

We find excellent agreement with the reported experiments as a function of the angle of the magnetic field. It is interesting to note that for a localized electron spin, such as a T-center [70], we predict the coherence time for naturally abundant Si to be more than twice as that of the shallow donor (Fig. 5.7b).

5.5 Conclusion

In this work, we presented an open-source python library to perform CCE calculations of a central spin interacting with a multitude of bath spins, including localized spin defects and

shallow donors, as well as to perform CCE calculations for novel emerging platforms, such as molecular spin qubits [71, 72].

We verified the implementation of the method using theoretical data from previous studies and validated several of our results with experiments. In the future, we will extend the framework to include an arbitrary number of central spins. Implementation of the so-called "hybrid CCE" [15, 57] formulation, which allows one to study systems with the same type of bath spins as central spin, is also underway.

The open-source nature of our module allows for broad collaborations within the scientific community and will facilitate rapid advances in first principle predictions of the coherence dynamics of the spin qubits.

CHAPTER 6

SPIN QUBIT COHERENCE AT AVOIDED CROSSINGS

This chapter is adapted from the published work [2].

Optically addressable paramagnetic defects in wide-band-gap semiconductors are promising platforms for quantum communications and sensing. The presence of avoided crossings between the electronic levels of these defects can substantially alter their quantum dynamics and be both detrimental and beneficial for quantum information applications.

Here we present a joint theoretical and experimental study of the quantum dynamics of paramagnetic defects interacting with a nuclear spin bath at avoided crossings. We find that we can condition the clock transition of the divacancies in SiC on multiple adjacent nuclear spins states. We suppress the effects of fluctuating charge impurities and demonstrate an increased coherence time at clock transition, which is limited purely by magnetic noise. Our results pave the way to designing single defect quantum devices operating at avoided crossings.

6.1 Introduction

In search of solid-state qubits, electron spin defects in wide-band-gap semiconductors have been extensively explored as robust quantum systems offering both long coherence times [73] and optical read-out [74] capabilities for quantum information [75] and quantum sensing [10] applications. In order to design optimal qubits, it is critical to understand and control the interaction between the central electronic spin and the nuclear spin bath. The latter determines, at least in part, the coherence time of qubits, as observed in many solid-state color centers [5, 41, 76, 77], but it also offers a platform for robust multiqubit registers for the development of quantum networks [3, 78–80].

The description of the interaction between a central spin and the nuclear bath can be particularly challenging when avoided crossings between energy levels of the central spin occur. Avoided crossings give rise to regimes that can be both beneficial and deleterious to the qubit's coherence. For example, operating at the minimum of the spin transition frequency can significantly increase the coherence time when clock transitions arise [40, 81, 82]. On the other hand, spin ground state level anticrossings may lead to an undesired increase in longitudinal relaxation rates [83, 84] of spin defects.

Here we investigate the adiabatic dynamics of a qubit interacting with nuclear baths at clock transitions and near ground state level anti-crossings (GSLAC) both theoretically and experimentally. Further, we suggest ways to design and optimize the electron-nuclear spin interactions in clock-transition-based quantum devices.

We focus on neutral divacancies ($V_C V_{Si}$) in silicon carbide (SiC), which are promising spin qubit candidates [4, 85–87]. In particular, the axial divacancy (Fig. 6.1b) is one of the most commonly studied defect qubits in SiC [88, 89], with purely axial zero field splitting. The basal divacancy (Fig. 6.1c), on the other hand, exhibits both an axial and transverse crystal field splitting component, giving rise to clock transitions at zero magnetic field [82, 90]. We validate our predictions, obtained using cluster-correlation expansion (CCE) technique, by carrying out Ramsey and Hahn-echo experiments on the basal divacancy, as well as by comparing our theoretical results to previous measurements [5]. Using theory and experiment we show that in the presence of strongly coupled nuclear spins, multiple clock transition conditioned on the nuclear spin state may occur. Importantly, we identify the dominant causes of decoherence at avoided crossings and clock transitions, and we discuss the nature of the noise as a function of the magnetic field. Finally, we show experimentally that the impact of the nuclear bath on the qubit dynamics can be isolated by employing a charge depletion technique, which leads to an increase of spin coherence time of clock transition qubits by suppressing electric noise.

6.2 Spin defect Hamiltonian

We investigate the dynamics of a spin qubit by studying the evolution of the central spin interacting with the nuclear spin bath. The Hamiltonian of a given system in an external magnetic field can be written as a sum of the central spin Hamiltonian $\hat{H}_e$, and nuclear Zeeman splitting, hyperfine coupling, and nuclear dipolar coupling terms:

$$\hat{H} = \hat{H}_e - \sum_i \gamma_{n,i} B_z \hat{I}_{z,i} + \sum_i \mathbf{S}\mathbf{A}\mathbf{I}_i + \sum_{i \neq j} \mathbf{I}_i \mathbf{P} \mathbf{I}_j \tag{6.1}$$

Here B_z is the magnetic field oriented along the z axis, $\gamma_{n,i}$ is the gyromagnetic ratio of the i-th nuclear spin, $\mathbf{S} = (\hat{S}_x, \hat{S}_y, \hat{S}_z)$ and $\mathbf{I}_i = (\hat{I}_{x,i}, \hat{I}_{y,i}, \hat{I}_{z,i})$ denote electron and the i-th nuclear spin operators respectively, $\mathbf{A}_i$ is the hyperfine coupling tensor of the i-th nuclear spin, and $\mathbf{P}_{ij}$ is the dipole-dipole coupling between spins i and j.

The electron Hamiltonian $\hat{H}_e$ includes the Zeeman interaction with the external magnetic field and a zero field splitting (ZFS) term with longitudinal (D) and transverse (E) components:

$$\hat{H}_e = -\gamma_e B_z \hat{S}_z + D\left(\hat{S}_z^2 - \frac{1}{3}S(S+1)\right) + E(\hat{S}_x^2 - \hat{S}_y^2) \tag{6.2}$$

6.2.1 Calculations of hyperfine coupling of nuclear spins

The inhomogeneous coherence time T_2^* is directly related to the hyperfine couplings. Under weak magnetic fields, the nuclear spin flips can be induced by both the hyperfine coupling and dipolar-dipolar interactions between nuclear spins [52]; hence accurate predictions of the hyperfine parameters are necessary to correctly compute the Hahn-echo coherence time as well.

We performed *ab initio* Density Functional Theory (DFT) calculations to predict hyperfine coupling constants for nuclear spins at distances up to 1 nm from the defect and we

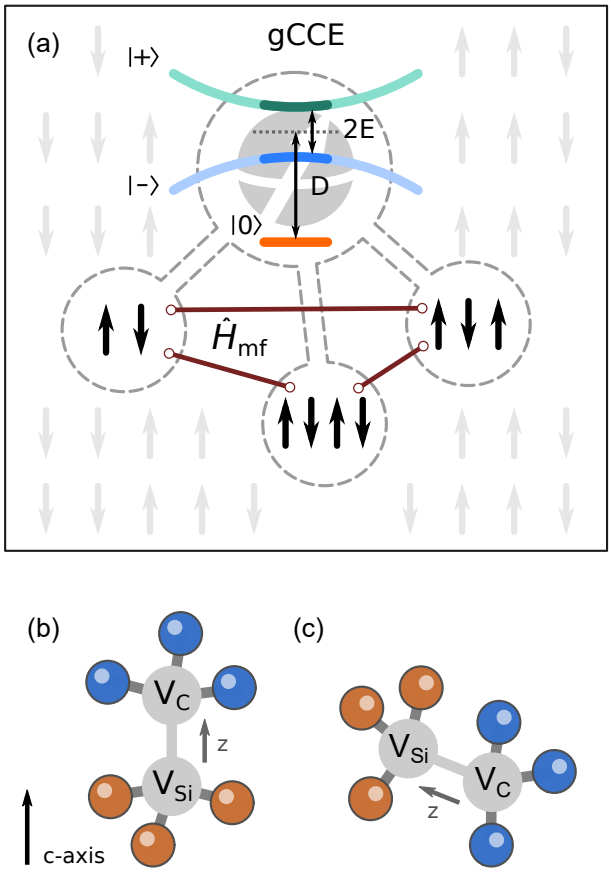

Figure 6.1: (a) Schematic representation of the Cluster-Correlation Expansion method used in this work (denoted as gCCE). Each cluster includes the central spin levels (denoted as $|+\rangle$, $|-\rangle$, and $|0\rangle$ for spin-1 with nonzero longitudinal D and transverse E zero field splitting (ZFS)). The interactions between clusters are treated at the mean field level ($\hat{H}_{\mathrm{mf}}$), using Monte-Carlo sampling of bath states. (b) Schematic representation of the axial kk-divacancy. (c) Schematic representation of the basal kh-divacancy.

used the point dipole approximation for spins at larger distances. DFT calculations using the PBE functional were carried out with the GIPAW code [67] using single-particle wavefunctions obtained with the Quantum Espresso code [63]. Wavefunctions are represented on a plane-wave basis with a kinetic energy cutoff of 40 Ry. GIPAW pseudopotentials [91] are used to model electron-ion interactions. Divancancies are modeled with $9 \times 5 \times 2$ orthorhombic supercells containing 1438 atoms and the Brillouin zone is sampled with the Γ point only.

We define a weakly coupled bath as a bath in which the nuclear spins do not change the energy splitting of the defect. We impose a cutoff of the hyperfine couplings of $A_{zz} < 1$ MHz present in the weakly coupled bath, which is of typical order of magnitude compared to strongly coupled nuclear spins in NV center [92, 93]. The ensemble dynamics throughout the text is shown for the weakly coupled bath.

6.3 Cluster-correlation expansion method for avoided crossings

The CCE method is one of the leading approaches for the simulation of quantum dynamics of spin-qubits interacting with a multitude of bath spins [5, 15, 47, 55]. The method approximates the off-diagonal elements of the qubit density matrix as a product of contributions from independent nuclear spin clusters. Recently, the CCE technique was successfully applied to study clock transitions of bismuth spin qubits in silicon (Si:Bi) with an explicit diagonalization of central spin energy levels within each cluster [49, 50].

In a similar fashion, in this work we adopt the generalized CCE formulation [94] to compute both the population change and coherence of the central spin at avoided crossings (gCCE, Fig. 6.1a). The generalized CCE is distinct from the "pseudospin" model conventionally used in CCE calculations [5, 51, 55, 59] as it includes the full central spin Hamiltonian in each cluster. In particular, here we compute elements of the density matrix of the central spin $\rho_{ab} = \langle a| \hat{\rho} |b\rangle$ as the product of cluster contributions, where a, b denote

different spin states (e.g. $m_s = 1, 0, -1$ states for spin 1 systems):

$$\rho_{ab} = \tilde{\rho}_{ab}^{\{0\}} \prod_i \tilde{\rho}_{ab}^{\{i\}} \prod_{i,j} \tilde{\rho}_{ab}^{\{ij\}} ... \tag{6.3}$$

Where $\{0\}$ denotes a cluster consisting of a free central spin, $\{i\}$ a cluster including the central spin and nuclear spin i, and so on. The maximum size of the cluster in Eq. (6.3) defines the order of the approximation. For example, at first order (gCCE1), only isolated nuclear spins ($\rho^{\{i\}}$) are included in the expansion. At second order (gCCE2), contributions from pairs of nuclear spins ($\rho^{\{i,j\}}$) are added, etc.

We note that at clock transitions previously studied in the Si:Bi system [50], the large splitting at avoided crossings induced by the interaction between electron spin and Bi nuclear spin leads to a pure dephasing regime of the qubit decoherence. S. J. Balian *et al* established that in such systems the inhomogeneous magnetic noise can be treated macroscopically. Instead, for qubits with small energy splittings at zero applied magnetic field, we found that a careful microscopic treatment of Overhauser fields is required for each spatial configuration of nuclear spins, consistent with the conclusion of recent work by G.-L. Zhang, *et al* [95] (see Section 6.5.2).

Therefore, we performed calculations with randomly sampled pure states of the spin bath, and for each pure state we include the mean-field effect of all the nuclear spins outside a chosen cluster $\hat{H}_{\text{mf}}$ (Fig. 6.1a). Such treatment also allows for different energy splittings of spins within a cluster, improving the numerical convergence of cluster dynamic simulations [57].

6.3.1 Calculation of cluster contributions in the gCCE

The cluster contributions are defined recursively:

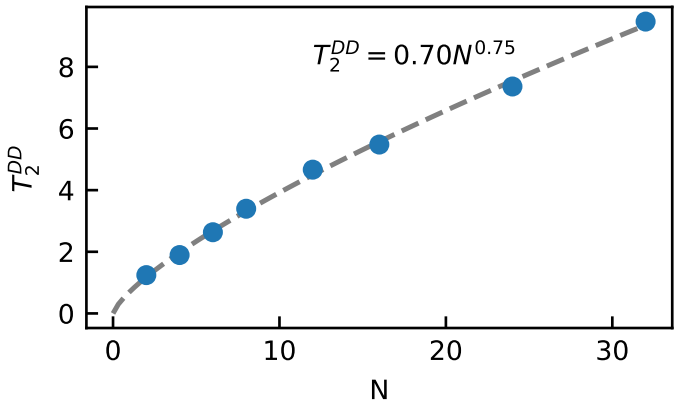

Figure 6.2: Coherence time of the basal divacancy at zero magnetic field as a function of number of decoupling pulses N.

$$\tilde{\rho}_{ab}^{\{C\}} = \frac{\langle a| \hat{\rho}_C(t) |b\rangle}{\prod_{C'} \tilde{\rho}_{ab}^{\{C' \subset C\}}} \tag{6.4}$$

Where $\rho_C(t)$ is the density matrix of the cluster C, the superscript $\{C'\}$ indicates all sub-clusters of C, including the free central spin sub-cluster $\{0\}$. The density matrix $\rho_C(t)$ is computed using the time ordered propagator:

$$\hat{U}_C(t) = \mathcal{T}\left[e^{-i\int_0^t \hat{H}(\tau)d\tau}\right] \tag{6.5}$$

where the $\mathcal{T}$ is the time ordering operator, and $\hat{H}(\tau)$ is the time dependent Hamiltonian, which includes only the interactions within a given cluster.

In order to evaluate the density matrix $\rho_C(t)$ in equation (6.4) we compute the evolution of the initial density matrix of a given cluster as:

$$\hat{\rho}_C(t) = \hat{U}_C \hat{\rho}_C(0) \hat{U}_C^\dagger \tag{6.6}$$

Using time ordered propagator $\hat{U}_C$ (6.5). The Hamiltonian used to model Ramsey experiments does not depend on time $\hat{H}(\tau) = \hat{H}_C$, and the propagator is trivial:

$$\hat{U}_C(t) = e^{-i\hat{H}_C t} \tag{6.7}$$

The Hamiltonian $\hat{H}_C$ is equal to the system Hamiltonian (6.1), which contains only the central spin and a given cluster of nuclear spins:

$$\hat{H}_C = \hat{H}_e + \sum_{i \subset C} \mathbf{SAI}_i - \sum_{i \subset C} \gamma_n B_z \hat{I}_{z,i} + \sum_{i \neq j \subset C} \mathbf{I}_i \mathbf{PI}_j \tag{6.8}$$

Under the dynamical decoupling to the qubit, by assuming ideal instantaneous control pulses, we can write the propagator as follows:

$$\hat{U}_C(t) = \mathcal{T}\left[e^{-i\hat{H}_C\tau} e^{-i\sigma_{\{x,y,z\}}\frac{\phi}{2}} e^{-i\hat{H}_C\tau}\right]^N \tag{6.9}$$

where $\sigma_{\{x,y,z\}}$ is one of the Pauli matrices (depending on the type of the pulse), spanned by two qubit levels, τ is the delay between pulses, ϕ is the angle of rotation (equal to π for CPMG, XY4 sequences [96]; it may be varied to represent more complicated schemes [97]) and N is number of pulses. For example, the propagator used to model Hahn-echo experiments with a π rotation about the x axis is defined as follows:

$$\hat{U}_C^{HE}(t) = e^{-i\hat{H}_C\tau} e^{-i\sigma_x\frac{\pi}{2}} e^{-i\hat{H}_C\tau} \tag{6.10}$$

The Pauli matricies for qubit levels $|0\rangle$ and $|1\rangle$ are defined as:

$$\sigma_x = (\,|0\rangle\langle 1| + |1\rangle\langle 0|) \tag{6.11}$$

$$\sigma_y = i(\,|1\rangle\langle 0| - |0\rangle\langle 1|) \tag{6.12}$$

$$\sigma_z = (\,|0\rangle\langle 0| - |1\rangle\langle 1|) \tag{6.13}$$

When using Monte-Carlo sampling of the bath states, we perform the CCE calculations for each pure bath state separately. In the pure bath state, each nucleus is initialized in the spin up or spin down state, and in the mixed state each nuclear spin has a classical probability of being in one of the two states. We define the density matrix elements of the central spin as follows:

$$\hat{\rho}_{ab}(t) = \sum_{B} p_J \hat{\rho}^J_{ab}(t) \tag{6.14}$$

where the elements of the density matrix $\hat{\rho}_{ab}$ are written as a summation over pure bath states J, with elements $\hat{\rho}^J_{ab}$ and probability p_J. In the case of a completely randomized bath (the density matrix of each nuclear spin is equal to $I/2$), the probability p_J is the same for all pure bath states. At the typical temperatures of the experiment ($\geq$ 4 K) the nuclear bath can be considered completely randomized.

The procedure used to evaluate the density matrix elements is the following. First, we generate a set of random pure bath states. For each bath state we perform CCE calculations to obtain the electron spin density matrix. Finally, we compute the density matrix elements for the mixed bath state from equation (6.14), and verify the convergence of density matrix elements $\rho_{ab}(t)$ with respect to the number of generated bath states (see Supplementary Information).

We add the mean field effect of the bath spins outside a given cluster, by adding the $\hat{H}_{\text{mf}}$ term into the cluster Hamiltonian (6.8). The mean field term is defined as:

$$\hat{H}_{\text{mf}} = \sum_{i \not\subset C} \left[A_{zz} \langle I_{z,i} \rangle \hat{S}_z + \sum_{j \subset C} P_{zz} \langle I_{z,i} \rangle \hat{I}_{z,j} \right] \tag{6.15}$$

where $\langle I_{z,i} \rangle = \pm 1/2$, is the projection of the nuclear spin in the z direction. The sign depends on the initial state of the nuclei i in the given random bath state.

For a specific bath state at the given time step the contribution of some clusters can be

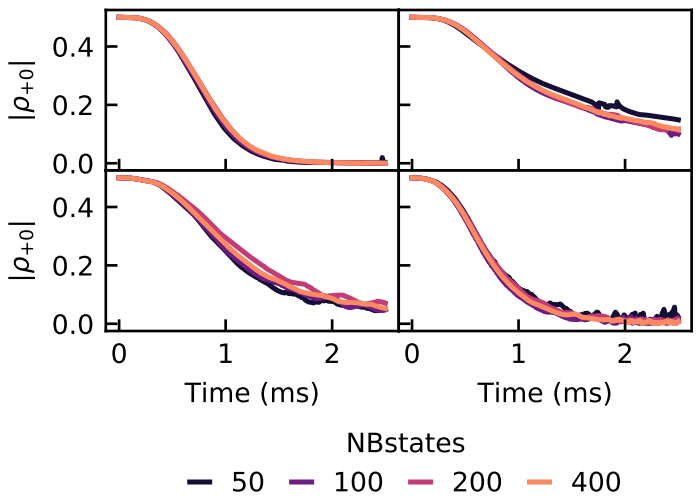

Figure 6.3: The convergence of the off-diagonal element ρ_{+0} of the density matrix in Hahn-echo measurement of kh-$V_C V_{Si}$ as a function of the number of random bath states (NBstates).

very close to 0, leading to the numerically unstable value of the density matrix elements. We identify such points when the elements of the density matrix are higher than one, and remove them from computing the average density matrix at the given time.

The off-diagonal element of density matrix of the basal divacancy converges quickly with the number of random bath states (Fig. 6.3).

At the same time, the diagonal elements are predicted with significant amount of noise (Fig. 6.4). The noise in computed diagonal elements due to the random states is more significant than the effect of other parameters. Therefore, we consider the changes in the population on the qualitative level, while we use off-diagonal elements for quantitative predictions of the entanglement with nuclear bath.

In the presence of the strongly coupled nuclear spins at the nonzero magnetic field, the results converge only when the exact averaging over the states of the strongly coupled spin is followed. In such systems, the modified sampling procedure can be implemented. For each state of the strongly coupled nuclear spins, we sample the same number of random bath states to obtain a density matrix element. The resulting matrix element for the randomized

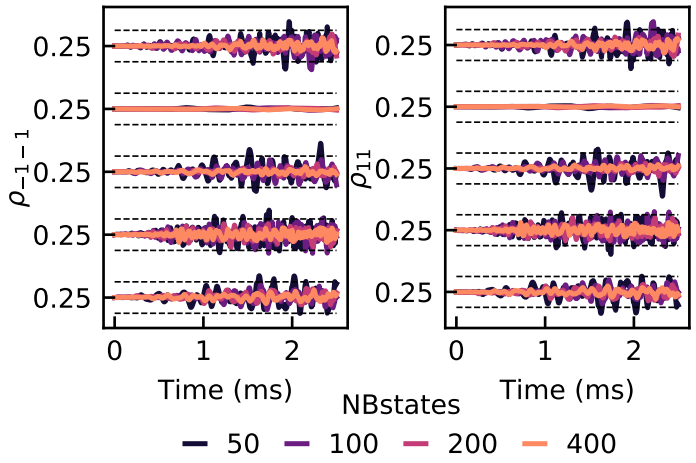

Figure 6.4: The convergence of diagonal elements ρ_{-1-1} and ρ_{11} of the density matrix of kh-$V_C V_{Si}$ in Hahn-echo measurement as a function of the number of random bath states (NBstates). Calculations are performed for 5 random nuclear spin configurations at zero magnetic field. Grey dashed lines correspond to the $\pm 10\%$ range. $\rho_{00} = 0$ for all calculations.

bath is an average of the elements, computed for each pure state of strongly coupled nuclear spins.

Computing the diagonal elements of the density matrix we renormalize the changing diagonal elements of the density matrix for each time step, to ensure that the total population is equal to 1.

6.4 Decoherence at ground state level anticrossings

We start by investigating the dynamics of the axial *kk*-$V_C V_{Si}$ defect in 4H-SiC near its GSLAC. The measured ensemble-averaged Hahn-echo coherence times (T_2) of this defect reaches 1.3 ms in samples with natural isotopic concentration [5]. Due to its C_{3v} symmetry, the ZFS entering (6.2) has only a longitudinal component $D = 1.305$ GHz [98], and the qubit levels may be chosen as the $|-1_z\rangle$ and $|0_z\rangle$ eigenstates of S_z, where z is the spin quantization axis.

The coherence time of the *kk*-$V_C V_{Si}$ divacancy was successfully predicted with the con-

ventional CCE for a wide range of magnetic fields, and the homo-nuclear pair-wise spin flips were found to be the main source of decoherence at strong fields [5]. However, a significant decrease in the coherence time was observed in experiments when the magnetic field approaches $\sim$ 45 mT; such a decrease is not captured by conventional CCE calculations with a "pseudospin" model (Fig. 6.5a), suggesting a decoherence mechanism beyond pure dephasing.

We performed gCCE calculations with Monte Carlo sampling of bath states (Fig. 6.5d) and we correctly obtained a local minimum in $T_2(B)$ for $B_z = 46.6$ mT, while reproducing the results of conventional CCE calculations for other values of B_z. We note that while previous CCE results [5] were obtained using a point dipole approximation, here we used accurate hyperfine couplings predicted by *ab initio* calculations (see Section 6.2.1). This difference in hyperfine couplings accounts for the small discrepancy between CCE and gCCE results observed at small fields.

The origin of the minimum in $T_2(B)$ can be understood by analyzing the populations of different spin levels (Fig. 6.5c). For most values of B, the population of the electron spin levels is constant. However, there are values of B for which the energy difference between the $|1\rangle$ and $|0\rangle$ levels is of the same order of magnitude as the hyperfine interaction with nuclear spins. We note that when the energy splitting falls below $\sim$ 100 MHz, significant deviations from pure dephasing occur (Fig. 6.5b). In this case, the electron spin experiences large population fluctuations which lead to a significant decrease in coherence time near the GSLAC. Therefore, we conclude that at a GSLAC, the longitudinal relaxation process substantially contributes to decreasing the Hahn-echo coherence time, as observed experimentally.

6.5 Decoherence at clock transitions

As mentioned earlier, the basal divacancy *kh*-$V_C V_{Si}$ exhibits a clock transition at zero magnetic field, which arises from ZFS interactions, unlike the one in the Bi:Si donor qubits

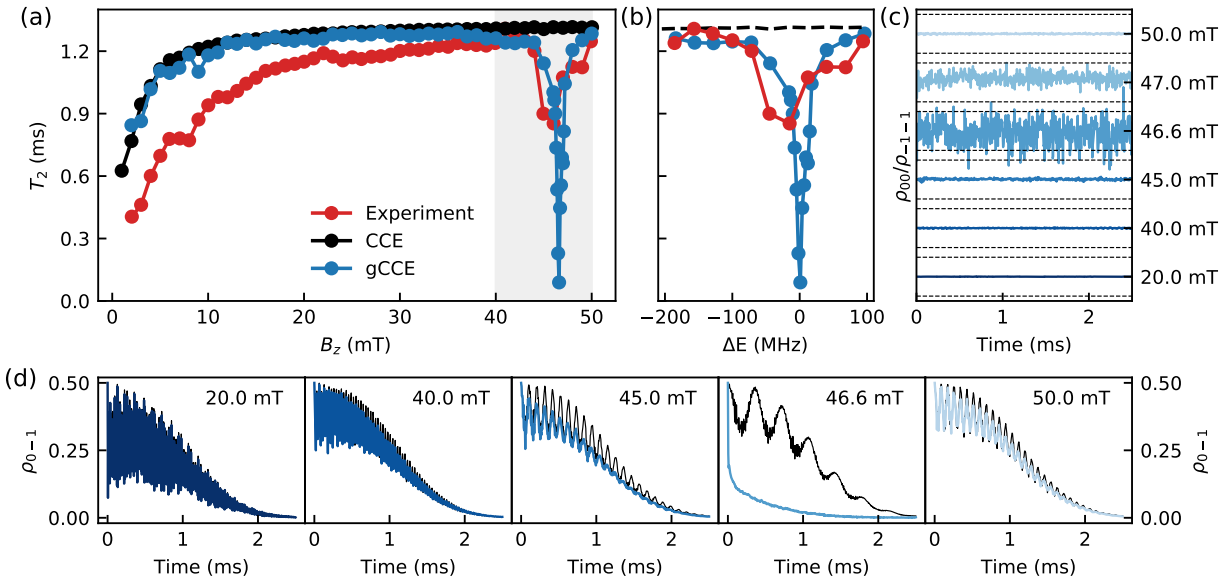

Figure 6.5: Ensemble Hahn-echo coherence of the axial kk-divacancy in 4H-SiC.(a) Coherence time T_2 (blue dots) as a function of the magnetic field B_z. The experimental results (red dots) and conventional CCE predictions (black dots) are from [5]. Grey shading denotes the range of T_2 shown in (b). (b) Experimental (red dots) and predicted (blue dots) coherence time T_2 as a function of energy splitting between qubit levels. Black line shows pure dephasing results. (c) The oscillations in the ratio of the diagonal elements of the density matrix of the divacancy as a function of time for various values of the magnetic field. The dashed lines show the $\pm 2\%$ range. (d) The off-diagonal elements of the density matrix for different magnetic fields computed using the gCCE method with Monte-Carlo sampling of the bath states (color) and using the conventional CCE (black).

studied in Ref.[49, 59]. *kh*-$V_C V_{Si}$ defect has C_{1h} symmetry, leading to a nonzero transverse component of the ZFS: $E = 18.4$ MHz [90]. Combined with a strong longitudinal splitting ($D = 1.334$ GHz), the ZFS tensor leads to an avoided crossing of electron spin levels at zero magnetic field from which a clock transition emerges. The qubit levels at the clock transition correspond to $|+\rangle = \frac{1}{\sqrt{2}}(|1_z\rangle + |-1_z\rangle)$ and $|0\rangle = |0_z\rangle$. The frequency of clock transitions is insensitive to magnetic fields to first order, thus increasing protection from the nuclear bath induced decoherence [81].

6.5.1 Experimental Measurements of the kh-$V_C V_{Si}$ coherence properties

Our 4H-SiC sample consists of a 20 μm high-purity i-type SiC layer epitaxially grown on a 4° off-axis miscut of the Si face of a high-purity semi-insulating SiC substrate (serial number A3177-14, Norstel AB). Neutral divacancies are uniformly produced throughout the epitaxial i-type 4H-SiC by electron irradiation with 2-MeV electrons at a dose of 3×10^{12} e/cm^2 followed by annealing at 850 °C for 30 min in Ar. A coplanar capacitor structure with a 10 μm gap width and a wire with 10 μm width made of Ti/Au are then patterned on the sample surface using electron beam lithography. Samples are cooled to 5 K in a closed-cycle cryostat (Cryostation s100, Montana Instruments).

The confocal microscope consists of a 905 nm excitation laser (QFLD-905-200S, QPhotonics) for off-resonant spin initialization, as well as a narrow-line tunable laser (DL pro, TOPTICA Photonics) for resonant spin readout. We focus these excitation beams through a microscope objective (LCPLN100XIR, Olympus). We detect the filtered optical signal with >80% quantum efficiency using a low-jitter, low-dark count superconducting nanowire single-photon detector (SNSPD; Opus One, Quantum Opus). Electrical pulses from the SNSPD are counted using a data acquisition module (PCI-6259, National Instruments).

We drive the spin transition $|0\rangle \leftrightarrow |+\rangle$ using signal generators (SG396, Stanford Research Systems) modulated by an arbitrary waveform generator (HDAWG8, Zurich Instruments).

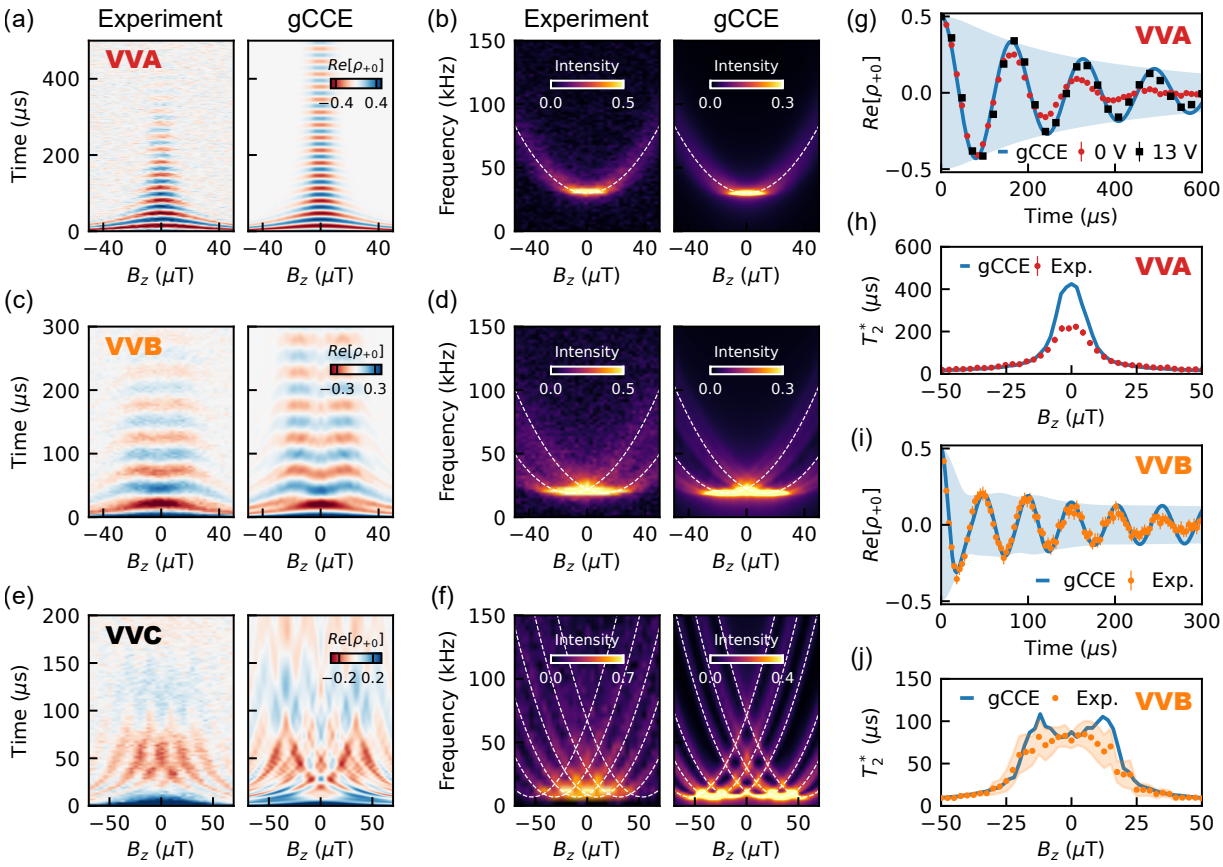

Figure 6.6: Ramsey interferometry for three experimental kh-$V_C V_{Si}$ systems. (a-f) Ramsey precession and frequency spectrum for a defect with only weakly coupled nuclear spins (VVA, a, b), with one (VVB, c, d), and with three strongly coupled nuclear spins (VVC, e, f). For each defect we show theoretical predictions and experimental results. White dashed lines show the positions of the hyperbolae (see Eq. 6.16). (g) Measured Ramsey precession of VVA at zero field with (black) or without (red) charge depletion (see text), compared to the theoretical prediction (blue). The shaded area corresponds to the theoretically predicted decay. (h, j) Distribution of T_2^* for VVA (h) and VVB (j) as a function of the magnetic field (B_z). Shaded area in (j) shows the error of the fit. (i) Measured Ramsey precession of VVB at weak applied magnetic field compared to the theoretical prediction. Error bars correspond to 2SD.

The output of the signal generator is routed to the on-chip wire, which produces ac magnetic fields. Vector control of the magnetic field is obtained using a three-axis electromagnet outside the cryostat.

6.5.2 Convergence of the gCCE calculations at avoided crossings with respect to cluster size

We applied the gCCE method with and without Monte Carlo bath state sampling to reveal the qubit dynamics at clock transition of the basal divacancy, observed in the Ramsey and Hahn-echo experiments. Figure 6.7 shows the time evolution of the off-diagonal element of the density matrix of the qubit for one random spatial configuration of nuclear spins.

We emphasize that considering mean-field effects of nuclear interactions is crucial in order to obtain the correct dynamics of the coherent state in the system studied here. The results without mean-field corrections (Fig. 6.7 on the left) may significantly underestimate the coherence on longer timescales, and high order corrections may lead to divergence of the results.

We found that the decay of the observed central spin Ramsey envelope can be accurately described by performing calculations at the gCCE1 level with Monte Carlo bath state sampling (Fig. 6.7a). Since gCCE1 simulations do not explicitly include nuclear-nuclear interactions, our results suggest that in the Ramsey experiment the dominant decoherence mechanism is the static Overhauser field generated by nuclear spins, in agreement with Ref. [95].

On the other hand, we found that for most configurations, gCCE2 is necessary and sufficient to converge the value of the Hahn-echo coherence (Fig. 6.7b) time, confirming the significant contribution of nuclear-nuclear interactions. This result differs from that of calculations for Si:Bi [50] where convergence is achieved only with the inclusion of 3-spin clusters. These differences suggest that accounting for the Overhauser field at microscopic

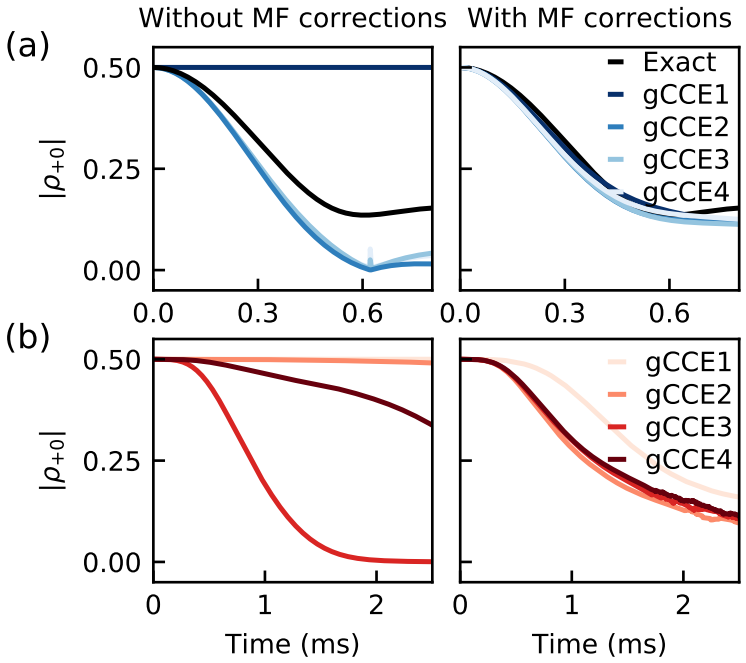

Figure 6.7: Single defect coherence of the basal *kh*-divacancy in 4H-SiC predicted by different theoretical approximations. (a, b) The absolute value of the off-diagonal elements of the density matrix $|\rho_{0+}| = |\langle 0|\hat{\rho}|+\rangle|$ for one random nuclear configuration corresponding to Ramsey (b) and Hahn-echo (c) experiments. The results of the gCCE at different orders (from 1 to 3) without mean field (MF) interactions are shown on the left hand side, with mean field corrections are on the right hand side. The exact solution for a bath of 9 nuclear spins for the Ramsey decay is shown as a black line.

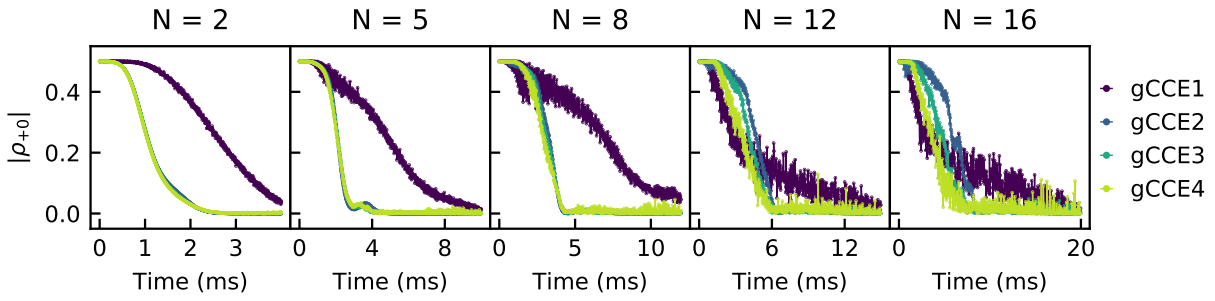

Figure 6.8: Off-diagonal element of the density matrix of the qubit at zero magnetic field for the various number of decoupling pulses N.

level, as proposed in our work, may effectively decreases the order necessary to converge the calculations presented in Ref. [50]; however further in-depth study is necessary to reach a definitive conclusion.

Finally, we note that we observed the convergence of coherence times at avoided crossings at the gCCE2 level even for more complicated CPMG sequences (Fig. 6.8), with number of decoupling pulses $2 \leq N \geq 8$. Higher number of pulses requires the inclusion of higher order cluster contributions. The coherence time T_2^{DD} (Fig, 6.2) scales sublinearly in the range of considered number of pulses.

6.5.3 Impact of nuclear spin coupling

In order to understand how the coupling strength between the central spin and the nuclear spins affects clock transitions, we experimentally investigated three different single kh-$\mathrm{V_C V_{Si}}$ divacancy qubits (see Section 6.5.1 for the experimental procedure). They are labeled VVA, VVB, and VVC, and they represent configurations with weakly (VVA) and strongly interacting (VVB and VVC) nuclear spins. We obtained theoretical configurations directly comparable with the experimental ones by generating a set of random nuclear spin configurations in the SiC lattice with the same number of strongly interacting nuclear spins as observed in the measured Ramsey fringes. Out of this set, we then selected the configurations with a computed value of T_2^* at $B_z = 50$ μT similar to the measured one (see Section

6.8 for details).

We first analyze the VVA configuration, which contains only weakly coupled nuclear spins. Its frequency spectrum, obtained as a Fourier transform of Ramsey fringe oscillations, can be simply represented by one hyperbola (Fig. 6.6a, b). In the absence of a nuclear bath, the frequency of the clock transition is given by:

$$\omega - \omega_0 = \sqrt{\gamma_e^2 B_z^2 + E^2} \tag{6.16}$$

We obtain good agreement between theoretical predictions and the measured Ramsey fringes at small fields, but in the zero field regime the experimentally observed decoherence is significantly faster (Fig. 6.6h). We found that this apparent discrepancy is due to the electric noise affecting the qubit state, as we explain below.

When operated near a clock transition, the basal divacancy spin becomes first-order insensitive to magnetic fluctuations. However, a first-order sensitivity to electric field fluctuations emerges, due to the linear dependence of the ZFS tensor components on the local electric field [99]. Therefore, the electron spin dephasing time becomes limited by the electric field noise [3, 82, 99]. In SiC divacancies, the electric noise is primarily caused by charge state fluctuations of photoactive impurities, which may undergo charge state transitions under optical excitation [100, 101], leading to a variation of local electric fields.

In our experiments, we used charge depletion [90, 100] to deactivate photoactive impurities within the optical excitation region, thus substantially reducing the electric field contributions to the ground-state spin dephasing. We applied 13 V across a lithographically patterned capacitor with a 10 μm gap width. The applied electric field acting on a divacancy located between the capacitor plates ionizes the undesired charge carriers and removes them from photoactive impurities in the proximity of the divacancy. This technique allowed us to isolate the contributions of the magnetic field noise near the clock transition (Fig. 6.6g) and to perform a meaningful comparison with our theoretical model.

We found that under charge depleted conditions, the measured coherence time is substantially increased and the experimentally observed Ramsey precession at zero field agrees well with the theoretical prediction of the gCCE. Interestingly, in the presence of a weak magnetic field, an agreement between theory and experiment is obtained without applying any charge depletion, indicating that the decoherence rate in this case is not limited by electric noise.

We now turn to lattice configurations with strongly coupled nuclear spins. We first consider the defect labeled VVB, for which we observe a splitting in the frequency spectrum due to the presence of one strongly coupled nuclear spin (Fig. 6.6c, d). Each of the hyperbolae shown in the figure corresponds to the oscillation frequency of Ramsey fringes of the divacancy, coupled to either the spin-up or spin-down nuclear state. The minimum of each hyperbola occurs when the magnetic field is equal to the hyperfine field of the strongly coupled nuclear spin, $\left|\frac{A_{iz}}{2\gamma_e}\right| = |B_z|$ where $A_{iz} = \sqrt{A_{xz}^2 + A_{yz}^2 + A_{zz}^2}$ [90]. By solving this equation, we obtain the hyperfine parameter of the strongly coupled nuclear spin in VVB: $A_{iz} \approx 0.6$ MHz.

In Fig. 6.6c, d we compare with experiments our theoretical results for a nuclear configuration for which the computed A_{iz} is 0.75 MHz. We find an excellent agreement for the time evolution and the frequency spectrum. We note that due to the presence of the strongly coupled spin, the Ramsey precession exhibits a fast and a slow decay mode (Fig. 6.6i), and the full dynamics of the decoherence process may not be described by a single T_2^* (Fig. 6.6j). However, by initializing the strongly coupled nuclear spin so that it is antiparallel to the external magnetic field, one can eliminate the fast decay mode, and, together with the charge depletion strategy outlined above, one may achieve a substantial increase (by a factor of 5) in the coherence time (see Section 6.8).

In the presence of several strongly coupled nuclear spins, further splitting of the frequency

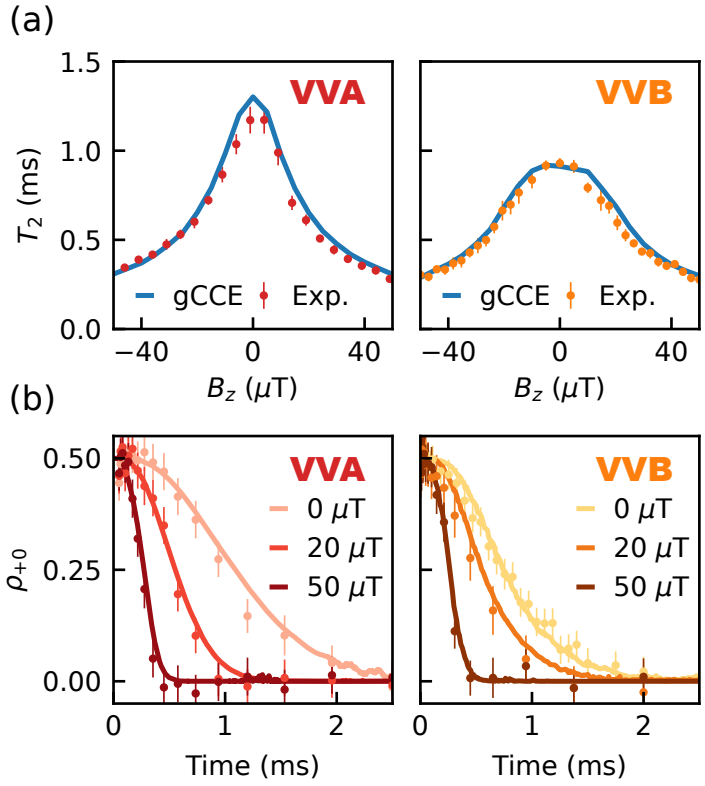

Figure 6.9: Single defect Hahn-echo coherence time of *kh*-$V_C V_{Si}$. (a) Distribution of T_2 for VVA (left) and VVB (right) as a function of the magnetic field B_z (VVA and VVB are the same defects represented in Fig. 6.6). (b) The Hahn echo decay for three different values of the magnetic field. Solid lines correspond to theoretical predictions, points to experimental measurements. Error bars correspond to 2SD.

spectrum may occur. In this case, the minimum of each hyperbola is located at:

$$B_z = \sum_{\text{strong}} \pm \frac{A_{iz}}{2\gamma_e} \tag{6.17}$$

The measured frequency spectrum of the defect labeled VVC contains six separate hyperbolae, suggesting the presence of three strongly coupled nuclear spins with two of them having similar hyperfine parameters (Fig. 6.6e, f). We identify one nuclear spin with $A_{iz} \approx 1.7$ MHz and two nuclear spins with $A_{iz} \approx 0.6$ MHz.

Hence, we compare theory and experiment using calculations for a nuclear configuration which contains 3 strongly coupled nuclear spins with similar values of the hyperfine constants: $A_{iz} = 1.92,\ 0.65,\ 0.49$ MHz. We obtain a good agreement in both the time and frequency domains. However, due to the complexity of the dynamics, a simple exponential decay cannot reliably characterize the decoherence time of VVC; nevertheless the decoherence occurs on a timescale of 200-300 μs, both in theory and experiment.

Furthermore, we carried out a study of the Hahn-echo decoherence time for the VVA and VVB defects (Fig. 6.9a, b) and again found excellent agreement between experimental values and theoretical predictions. In VVB, the presence of the strongly coupled nuclear spin leads to a broadening of the coherence time peak compared to VVA, and to a decrease in the maximum of T_2 (0.930(14) ms for VVB vs. 1.17(4) ms for VVA). We note that the measured and computed zero-field Hahn-echo coherence times agree even without applying any charge depletion to the sample, suggesting that the electric noise has a minor impact on T_2.

6.6 Nature of nuclear noise in solid-state qubits

Having validated the predictions of the gCCE with several experiments, we can now analyze the nature of the nuclear noise in the decoherence processes of the *kh*-$V_C V_{Si}$.

We computed the coherence time of the *kh*-$V_C V_{Si}$ at zero field (0 T), where a clock transition occurs, and at $B_z = 0.1$ T where we expect the basal and axial divacancies to exhibit similar coherence properties. We considered eigenstates of $\hat{S}_z$ as qubit levels at 0.1 T. We find that at both zero and strong magnetic fields, the Ramsey decay is limited by static thermal noise arising from the entanglement of the qubit with pure states of the bath, which remain unchanged in time [15]:

$$\hat{\rho}(0) \otimes \sum_B p_B \left|B\right\rangle \left\langle B\right| \rightarrow \sum_B p_B \hat{\rho}_B(t) \otimes \left|B\right\rangle \left\langle B\right| \tag{6.18}$$

Indeed our calculations of T_2^* for the *kh*-$V_C V_{Si}$ in the weakly-coupled bath (Fig. 6.10a, b) show that the inhomogeneous coherence time depends on the hyperfine parameters only through the average bath coupling ($\sqrt{\sum_i A_{iz}^2}$), as expected in the case of static thermal noise. [102].

The nature of noise is different in Hahn-echo experiments, where the π-pulse removes the static part of the noise dominating the Ramsey decay, and T_2 depends only on the dynamical fluctuations of the magnetic field due to nuclear spins flips [15]. If the flips are completely random, the decay rates originate primarily from the accumulation of random phases due to dynamical fluctuations; in this case the noise is by definition classical and the variance of the noise distribution is given by $\sum_i A_{iz}^2$ [103]. Therefore we expect the coherence time to vary linearly as a function of $\sqrt{\sum_i A_{iz}^2}$ in systems where the noise is classical[104]. On the other hand, when the back action of the central spin is dominant (i.e. the dynamics of the nuclear bath is strongly influenced by the electron spin state [15]), the coherence dynamics deviates from that predicted using classical approximations [105]. Fig. 6.10c shows T_2 of *kk*-$V_C V_{Si}$ as a function of $\sqrt{\sum_i A_{iz}^2}$ in the zero and strong field regimes. At zero field, T_2 varies as $\sqrt{\sum_i A_{iz}^2}$, with more than an order of magnitude difference in $\sqrt{\sum_i A_{iz}^2}$ between the different configurations. This dependence suggests a stochastic nature of the noise at clock transitions and is consistent with the results reported for bismuth qubits in silicon [59].

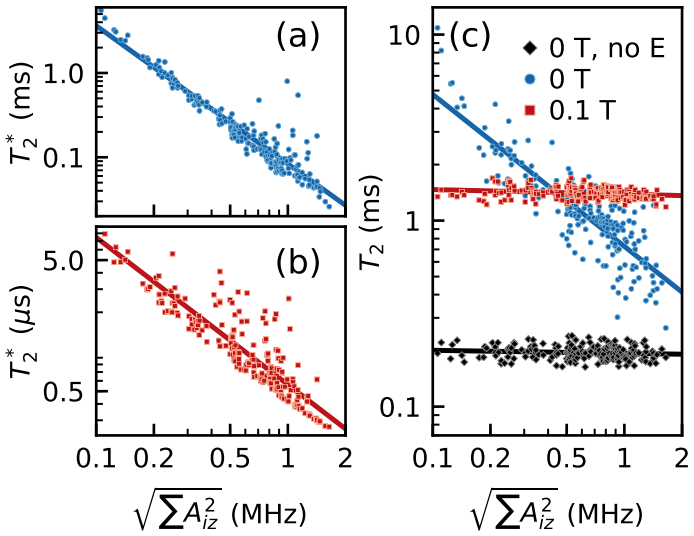

Figure 6.10: Single defect coherence times T_2^* and T_2 of the kh-$V_C V_{Si}$ at zero and high magnetic field for different bath coupling. (a, b) T^* for zero (a) and high (b) field as a function of the square root of the sum of squares of the hyperfine couplings with the bath spins $\sqrt{\sum_i A_{iz}^2}$. Significant deviations from the least squares fit (solid lines) are present for systems containing single nuclear spins with high hyperfine coupling, and the coherence decay may not be approximated by a single exponential [52]. (c) T_2 for zero (blue) and high (red) magnetic fields, and for an hypothetical system with $E = 0$ MHz at zero field (black). All calculations are performed for SiC with natural isotope concentration for the weakly coupled nuclear bath.

At strong fields, T_2 is instead independent on the average coupling to the bath, consistent with the quantum nature of the noise, expected in this regime. These results show that the noise affecting Hahn-echo experiments is different at clock transitions and in the strong field regime, and the transition from classical to quantum noise may be tuned by simply varying the applied magnetic field.

We note that the differences in the nature of the noise is not sufficient to explain why the average value of T_2 at the clock transition of the basal divacancy is similar to the one at strong field (1.15 ms vs 1.4 ms). This similarity arises from the combination of two competing effects: strong electron spin back-action, leading in principle to a reduction in coherence time, and the Zeeman splitting of nuclear spins, having instead the opposite effect. We can isolate the effect of the electron spin's strong back-action on coherence time, by considering a hypothetical *kh*-$V_C V_{Si}$ with $E = 0$ MHz at zero magnetic field (Fig. 6.10c, 0 T, no E). We found that the T_2 of this system is independent from $\sqrt{\sum_i A_{iz}^2}$, and the ensemble average T_2 is 0.2 ms, significantly smaller than the one obtained for the clock transition, confirming that the electron back-action is indeed responsible for an increase in the decoherence rate. At strong magnetic field, the Zeeman splitting of the nuclear spins is instead responsible for a decrease in decoherence rates. The splitting can be larger than both the interaction strength between nuclear spins and the hyperfine coupling, leading to the suppression of spin non-conserving flips [52]. Only the secular pairwise flip-flops of nuclear spins with the same gyromagnetic ratio ($\uparrow\downarrow \leftrightarrow \downarrow\uparrow$) are possible in this regime [5, 106], thus greatly reducing the number of possible spin flips and decreasing the decoherence rate. (Fig. 6.5b).

6.7 Engineering qubit protection at a clock transition

It is interesting to analyze in detail the effect of the magnitude of the transverse component of the ZFS on coherence protection. In order to do so, we investigated how coherence times vary as a function of a hypothetical change in E for the *kh*-$V_C V_{Si}$, within a weakly coupled

nuclear bath (Fig. 6.11(a)). We find that the ensemble averaged coherence time scales sublinearly as a function of the transverse ZFS ($T_2 \approx 0.34E^{0.43}$, $T_2^* \approx 0.03E^{0.61}$; see Section 6.8 for the distribution of single defect coherence times). Our calculations show that defects with large transverse ZFS will exhibit substantially higher protection from magnetic noise.

In particular, we predict the coherence time of the hk-V_CV_{Si} basal divacancy. hk-V_CV_{Si} has significantly higher transverse ZFS than kh-V_CV_{Si} ($E = 82.0$ MHz), and similar longitudinal ZFS ($D = 1.222$ GHz) [98]. The total distribution of the T_2 and T_2^* as a function of the magnetic field for different spatial configurations of the weakly coupled nuclear bath is shown in Fig. 6.11(b, c) for both basal defects. We can see that there is a significant variability in the value of the coherence time at $B = 0$. The increase in the transverse ZFS leads both to a significant increase in the maximum value of the coherence time and to an increased robustness towards the external magnetic field. The ensemble average zero field $T_2^* = 380$ μs of hk-V_CV_{Si} is predicted to be 2.3 times higher than the one of kh-V_CV_{Si}, and the $T_2 = 2.12$ ms is found to be increased by a factor of 1.8, in a good agreement with Fig. 6.11a. In the presence of a strong field (0.1 T) the ensemble average coherence time for both basal divacancies is the same: $T_2^* = 0.7$ μs, $T_2 = 1.4$ ms, which confirms that the large transverse ZFS is the main driving force for an increased coherence protection in the hk-V_CV_{Si}.

Our results for the different basal divacancies show that by engineering high zero field splitting either by selecting different defects, or applying the strain to the system [107], one can achieve substantial increase in the coherence time.

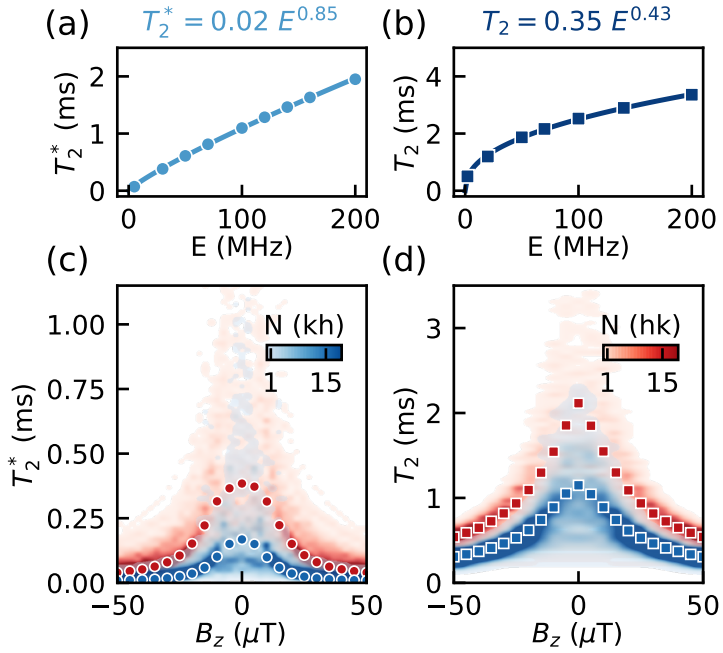

Figure 6.11: Dependence of the coherence time on the transverse zero-field-splitting (ZFS). (a, b) Coherence times T_2^* (a) and T_2 (b) of kh-$V_C V_{Si}$ with different hypothetical values of transverse ZFS E. (c, d) The heat map of the single defect T_2^* (T_2) for 120 different nuclear spin configurations of both hk-$V_C V_{Si}$ (red) and kh-$V_C V_{Si}$ (blue) as a function of magnetic field. The color corresponds to the number of configurations with a given T_2^* (T_2) at the given magnetic field. The circles (squares) indicate the ensemble averaged coherence time.

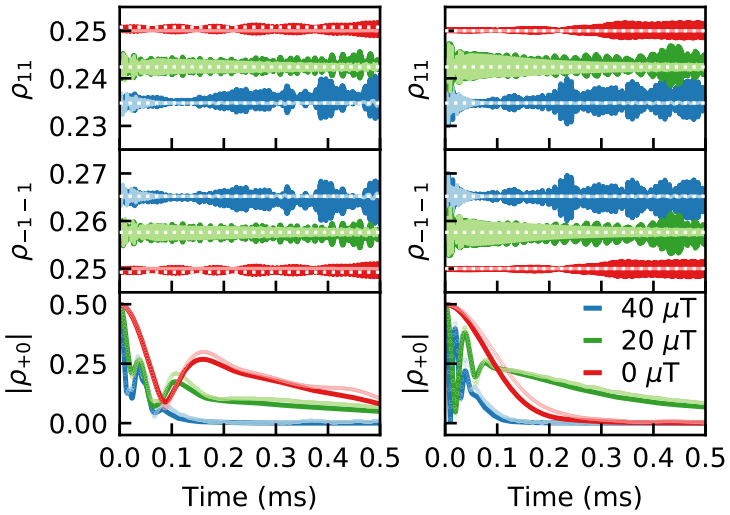

Figure 6.12: Density matrix elements of kh-$V_C V_{Si}$ for two random nuclear spin spatial configurations of weakly coupled nuclear bath (in columns) as a function of the magnetic field. The lines with brighter color correspond to the exact solution for smaller bath (9 nuclear spins). The dotted white line corresponds to the initial value of ρ_{ii}. $\rho_{00} = 0$ for all calculations.

6.8 Additional properties of basal divacancies in the presence of nuclear spins

6.8.1 Impact of the magnetic field on initial qubit state of basal divacancy

For the nonzero magnetic field the general qubit states are defined as $|+\rangle = a\,|1_z\rangle + b\,|-1_z\rangle$ and $|0\rangle = |0_z\rangle$. Amplitudes a and b are different for varied magnetic field. E.g., at the $B_z = 0$ mT the amplitudes are equal $|a| = |b| = \frac{1}{\sqrt{2}}$, and at $B_z = 0.5$ mT the ratio between amplitudes is $|a| : |b| \approx 2 : 1$. In the presence of nuclear spins, when the qubit is prepared in the $|\psi\rangle$ state, the transition occurs for all possible bath states. For the weakly coupled nuclear bath the Overhauser field for each bath state is compensated by randomization of the bath ($\sum_n A_{iz} I_n \approx 0$, $I_n = \pm 1/2$). Then, the interactions between central qubit and nuclei do not impose significant changes in the qubit level structures compared to the isolated defect in the external magnetic field. This can be seen by detecting the evolution of the diagonal

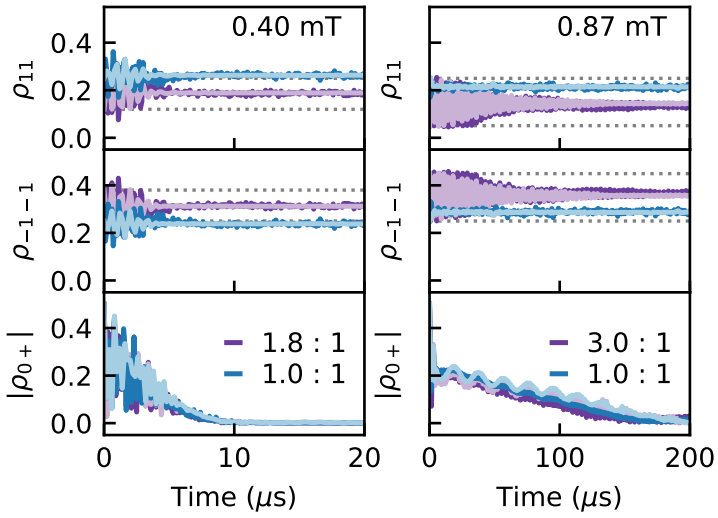

Figure 6.13: Density matrix elements of kh-$V_C V_{Si}$ for nuclear configuration containing strongly coupled nuclear spin with $A_{iz} = 8.93$ MHz at low magnetic fields. The color indicates ratio of $|a|$ and $|b|$ in the initial $|+\rangle = a\,|-1_z\rangle + b\,|+1_z\rangle$ state of the qubit. In each case, the qubit was initially prepared in the state $|\psi\rangle = \frac{1}{\sqrt{2}}(|+\rangle + |0\rangle)$. The lines with brighter color correspond to the exact solution with the same initial state for smaller bath (9 nuclear spins). The dotted grey line corresponds to the initial value of the density matrix diagonal element. $\rho_{00} = 0$ for all calculations.

elements of the density matrix of the qubit (Fig. 6.12). Therefore, for the weakly coupled bath we consider initial qubit states as eigenstates of $\hat{H}_e$.

In the presence of the strongly coupled nuclear spins, the Overhauser field from these nuclear spins cannot be compensated by other nuclei ($A_{iz}^{\text{strong}} \gg \sum_{\text{weak}} A_{iz}^{\text{weak}}$), and can shift the qubit levels substantially.

As an example we consider the most extreme case, when Hyperfine coupling $A_{iz} = 50.96$ MHz is higher than the transverse ZFS (Fig. 6.13). The initial nuclear spins states are completely randomized. The initial adiabatic change in the qubit $|+\rangle$ state occurs significantly faster than the following decoherence, and the rate of decoherence is mostly independent of the initial qubit state.

For the given nuclear spin bath, in both initial states of the qubit, the off-diagonal elements of the density matrix decay an order of magnitude slower at 0.87 mT compared

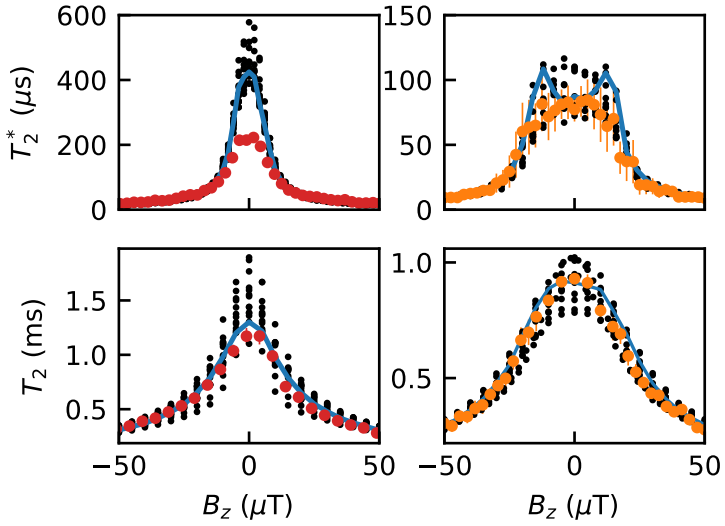

Figure 6.14: The distribution of coherence time T_2^* (top) and T_2 (bottom) for theoretical nuclear configurations obtained for VVA (red) and VVB (orange). Blue line correspond to configurations shown in the main text.

to 0.4 mT. This allows us to use the initial qubit state $|\psi\rangle$ with $|+\rangle = \frac{1}{\sqrt{2}}(|-1\rangle + |+1\rangle)$ for systems with strongly coupled nuclear spins, and allow it to evolve adiabatically even at relatively high magnetic fields to correctly predict FID decoherence.

6.8.2 Determining the experimental configurations

To find the theoretical nuclear configurations which correspond to the experimentally measured basal divacancies, we applied the following procedure.

First, we generated a large set of random nuclear spin configurations. Out of this set, we identified the ones with or without strongly coupled nuclear spins. For each experimental divacancy, we determined the subsets of configurations with the same number of identifiable strongly coupled nuclear spins. For VVA we determined a subset of random nuclear spin configurations with no identifiable strongly coupled nuclear spins, for VVB - configurations containing one strongly coupled nuclear spin with $A_{iz} \sim 0.6$ MHz, for VVC - configurations containing three strongly coupled nuclear spins with $\sum A_{iz} \sim 3$ MHz.

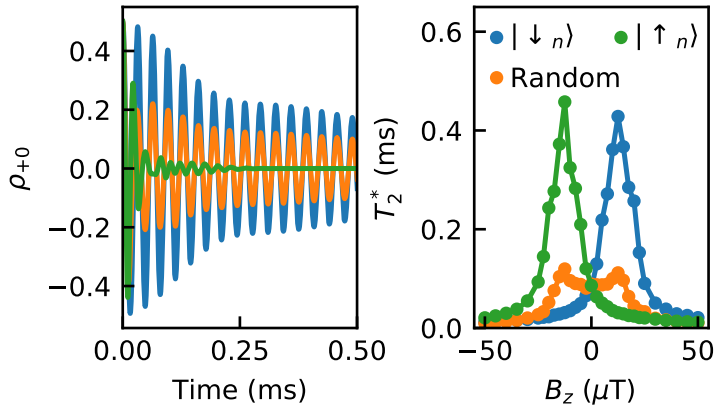

Figure 6.15: FID with the strongly coupled nuclear spin. Left: ρ_{0+} at the magnetic field of 12.5 μT in the presence of the nuclear spin with $A_{iz} = 0.75$ MHz initialized in spin up ($\langle\uparrow_n|$, orange), spin down ($\langle\downarrow_n|$, blue) or thermalized (green) state. Right: T_2^* against magnetic field for system with differently initiallized strongly coupled nuclear spin. All other nuclear spins are completely randomized.

For VVC we identify the configurations, containing 6 minima in the frequency spectrum. For VVA and VVB we identify the nuclear configurations that have a similar value of T_2^* at the applied magnetic field of 50 μT to the corresponding experimental system. This value is instrumental to find the configurations with a similar total coupling of the bath and allows us to choose the configurations with the coupling of the nuclear bath to the electron spin closest to the experimental system. One such configuration for each divacancy is shown in the main text. All of the configurations for VVA and VVB are shown in Fig. 6.14.

6.8.3 Initialization of strongly coupled nuclear spins

We show the theoretical nuclear configuration with the strongly coupled nucleus of $A_{iz} = 0.75$ MHz present, compared in the main text to VVB (Fig. 6.15) and study the effect of its initial state. If the strongly coupled nuclear spin is initially in the thermalized state, the decay of the off-diagonal element contains two components: the fast initial decay due to the fast entanglement with the bath states, containing the strongly coupled nuclear spin parallel to the magnetic field, and the slow decay due to the entanglement with the bath states with

Table 6.1: Highest five hyperfine coupling A_{iz} of the configurations, shown in Fig. 6.16. The nuclear couplings giving rise to the peak splitting are highlighted in bold.

No,	A_{iz}, MHz				
1	**1.97**	0.46	0.17	0.12	0.11
2	**2.09**	**1.34**	**0.48**	0.06	0.04
3	**2.04**	**1.97**	**1.01**	0.12	0.12
4	**4.19**	0.09	0.04	0.04	0.04
5	**8.93**	0.13	0.09	0.05	0.05
6	2.04	1.97	1.93	1.21	0.72
7	**10.39**	0.53	0.12	0.04	0.03
8	**10.39**	0.46	0.13	0.09	0.09
9	**10.39**	0.15	0.12	0.07	0.05
10	**10.39**	**4.83**	0.15	0.11	0.07
11	**8.93**	**8.23**	**2.09**	0.19	0.17
12	**50.95**	0.09	0.07	0.04	0.03

strongly coupled spin down. When we initialize the strongly coupled nuclei in one specific state, only one mode of the decay is observed. The initialization of strongly coupled nuclear spin antiparallel to the magnetic field (Fig. 6.15 left, blue) significantly prolongs coherence, while the antiparallel orientation shortens coherence time.

6.8.4 Nuclear bath with strongly coupled nuclear spins

Here, we theoretically study the coherence time of several additional configurations with strongly coupled nuclear spins. The coherence time of the basal divacancy can have several resonances as a function of the magnetic field if strongly coupled nuclei are present. The main reason for the appearance of the maxima is due to completely negated interactions with the strongly coupled nuclear spins in spin up or spin down states.

When hyperfine couplings for several nuclei is significantly higher than the coupling to the remaining bath, the number of peaks can be higher than two (Fig. 6.16 and table 6.1). For each pure bath state the resonance occurs at the magnetic field $B_z = \sum_{\text{strong}} \pm \frac{A_{iz}}{2\gamma_e}$. The resulting coherence time dependence for the thermalized bath will show peaks either aligned with the peaks of pure bath states (Fig. 6.16(9)), or at the overlap of two peaks

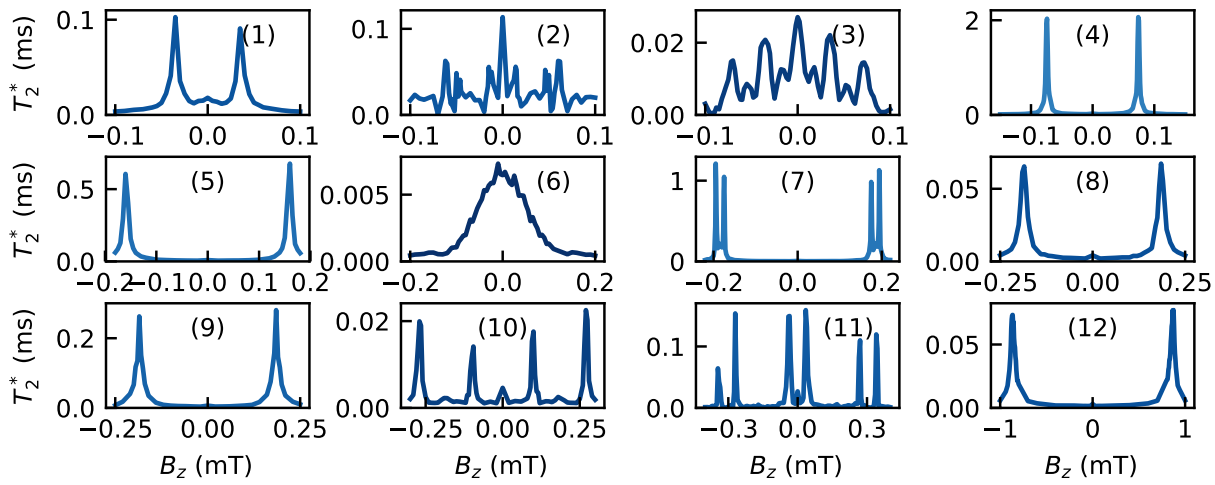

Figure 6.16: Coherence time against the magnetic field for the theoretical configurations, containing strongly coupled nuclear spins.

(Fig. 6.16(3)). In the presence of many strongly coupled nuclear spins the peaks can become indistinguishable (Fig. 6.16(6)).

6.8.5 Single defect coherence time at different transverse ZFS

In figure 6.17 we show the coherence time of basal divacancy as a function of the transverse ZFS E. We can see that a single defect T_2 scales sublinearly with E, while T_2^* scales linearly. We note significant variability in values of the single defect coherence times at zero magnetic field.

6.9 Conclusions

Understanding the relation between the electronic structure of spin defects and their coherence properties is pivotal to optimizing the conditions for solid-state qubit applications. In this work, we carried out a series of calculations to investigate the effect of the nuclear spin bath at avoided crossings on the quantum dynamics of divacancies in SiC. We validated our results with measurements of Ramsey fringes and Hahn-echo coherence times and found

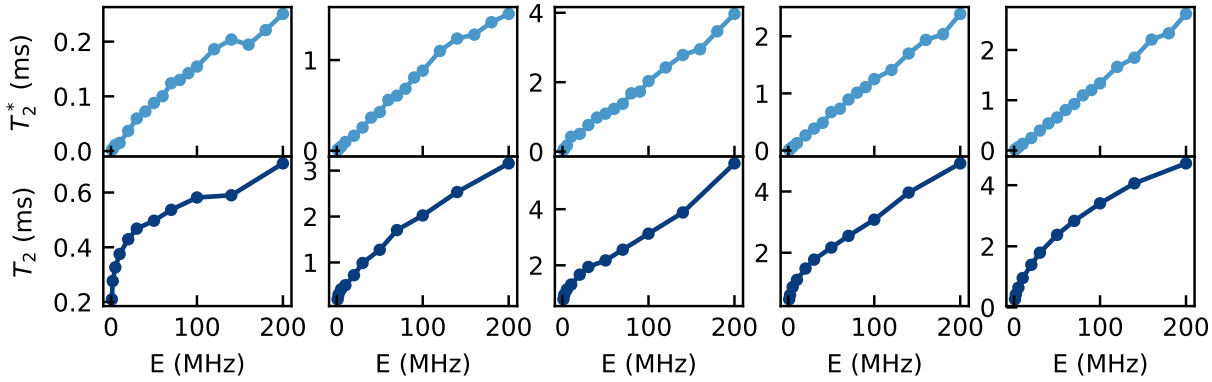

Figure 6.17: Coherence time of kh-$V_C V_{Si}$ for FID (top) and Hahn-echo (bottom) as a function of transverse ZFS E for five random nuclear spin configurations without strongly coupled nuclear spins.

excellent agreement between theory and experiments. Our work provides a robust strategy to uncover the effect of the interaction of nuclear spins on solid-state qubits' decoherence over a wide range of applied magnetic fields.

Applying charge depletion [100] to electrically improve coherence, we were able to experimentally isolate and elucidate the duality of the nuclear bath impact on clock transitions' dynamics. We discovered that in the presence of strongly coupled nuclear spins, multiple clock transitions in the frequency spectrum of the spin qubit can emerge. We identified and characterized the nuclei with high hyperfine coupling in these systems; the initialization of these nuclear spins should allow one to achieve significantly higher coherence times under applied magnetic fields, while the nuclear-spin dependent spectral features provides guidance for the development of a new class of electron-nuclear two-qubit gates. We found that the effect of weakly coupled nuclear spins can be treated as a stochastic classical noise at the clock transition, and that the total amplitude of the coupling is a good descriptor of the coherence time. We further probed the classical-to-quantum transition of the noise and showed how a tunable back action of the electronic spin emerges with applied magnetic fields.

In sum, the joint computational and experimental study allowed us to probe the nuclear environment around divacancies in SiC at avoided crossings down to the single nuclear spin

level. The experimental validation of the predictions made here paves the way to optimize and eventually design the coherence properties of spin qubits yet to be explored experimentally.

CHAPTER 7

DESIGNING ATOMIC CLOCKS IN EXOTIC SYSTEMS

This chapter is adapted from the published works [8, 11].

7.1 Enhancing Spin Coherence in Optically Addressable Molecular Qubits through Host-Matrix Control

Optically addressable spins are a promising platform for quantum information science due to their combination of a long-lived qubit with a spin-optical interface for external qubit control and read out. The ability to chemically synthesize such systems — to generate optically addressable molecular spins — offers a modular qubit architecture which can be transported across different environments, and atomistically tailored for targeted applications through bottom-up design and synthesis. In this section, we demonstrate how the spin coherence in such optically addressable molecular qubits can be controlled through engineering their host environment. By inserting chromium (IV)-based molecular qubits into a non-isostructural host matrix, we generate noise-insensitive clock transitions, through a transverse zero-field splitting, that are not present when using an isostructural host. This host-matrix engineering leads to spin-coherence times of more than 10 μs for optically addressable molecular spin qubits in a nuclear and electron-spin rich environment. We model the dependence of spin coherence on transverse zero-field splitting from first principles and experimentally verify the theoretical predictions with four distinct molecular systems. Finally, we explore how to further enhance optical-spin interfaces in molecular qubits by investigating the key parameters of optical linewidth and spin-lattice relaxation time. Our results demonstrate the ability to test qubit structure-function relationships through a tunable molecular platform and highlight opportunities for using molecular qubits for nanoscale quantum sensing in noisy environments.

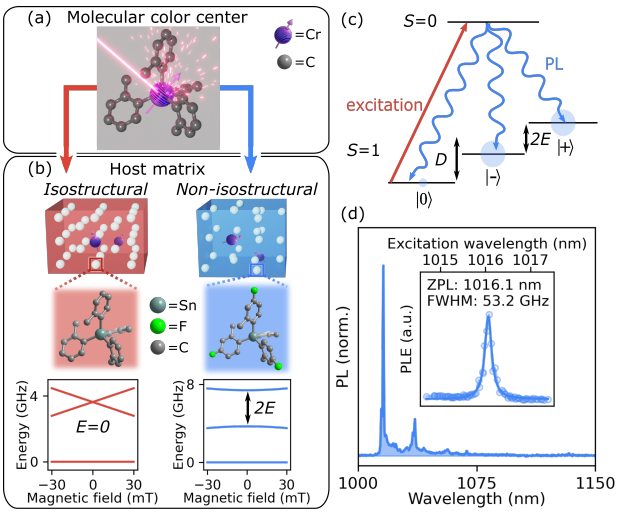

Figure 7.1: Host-matrix engineering of optically addressable molecular qubits. (a) Molecular structure of **1-Cr** (determined from single crystal X-ray diffraction) with laser excitation and emission outlined. Hydrogen atoms are omitted for clarity. (b) Single crystal packing diagram of **1-Cr** in its isostructural host, **1-Sn** (red, left), and non-isostructural host, **2-Sn** (blue, right), showing only positions of metal centers. The cell volumes for the representations of **1-Sn** and **2-Sn** are 9 and 10 nm^3, respectively. Below each cell, we show the molecular structures of the tin host, with hydrogen atoms are omitted for clarity. The resulting ground-state spin structures (bottom) show the clock transition ($E > 0$) induced in **2**. (c) Energy level diagram of chromium molecular color centers, highlighting resonant excitation to, and photoluminescence (PL) from, the S=0 excited state, and zero-field splitting of the ground-state spin sublevels. (d) PL and photoluminescence excitation (PLE) spectra of 2 at 4 K.

7.1.1 Host-matrix enhanced spin coherence

We create clock transitions in optically addressable molecular spin qubits through host-matrix induced symmetry control. We use the chromium-based molecular color center — Cr(IV)(o-tolyl)$_4$, **1-Cr** [Fig. 7.1(a)] — to demonstrate the impact of the host environment on the ground state spin structure. The crystallographic symmetry of **1-Cr** and its isostructural, diamagnetic host, Sn(IV)(o-tolyl)$_4$, **1-Sn**, yields ground-state spin transitions that are first-order sensitive to magnetic-field fluctuations [72]. In contrast, and as we outline below, inserting **1-Cr** into a non-isostructural, lower symmetry host matrix — Sn(IV)(4-fluoro-2-methylphenyl)$_4$, **2-Sn** [Fig. 7.1(b)] — induces clock transitions as a result of the creation of a significant transverse zero-field splitting. These host-induced clock transitions significantly enhance the spin coherence of **1-Cr** in **2-Sn** (which we refer to as **2**) compared to **1-Cr** in the isostructural **1-Sn** host (which we refer to as **1**). We model this behavior from first principles using generalized cluster-correlation expansion methods, and further experimentally demonstrate enhanced optical contrast and spin-lattice relaxation times for these host-matrix engineered molecular color centers. Remarkably, the host modification to achieve this coherence enhancement comprises interchange of just one hydrogen atom on the host ligands with a fluorine atom. In fact, the nuclear spin densities of **1-Sn** and **2-Sn** are 51.7 and 46.9 N/nm^3, where N is the number of nuclear spin-bearing atoms. Thus, the coherence enhancement arises primarily from symmetry control by the host—without requiring control of the nuclear spin bath—offering a pathway for coherence-protected quantum sensing (e.g., of electric fields and strain) in intrinsically noisy environments (e.g., biological systems), all within a versatile molecular platform.

We now illustrate how this behavior significantly enhances the spin coherence (T_2) in **2** compared to **1**. At zero magnetic field, we measure a ground state spin coherence time $T2 = 10.6 \pm 0.2 mu$s, despite the nuclear spin rich environment, and the relatively high Cr concentration ($\sim 1\%$, $\simeq 1 - 2 \times 10^{19}$ $\mathrm{Cr}^{4+}/\mathrm{cm}^3$). In contrast, we measure a significantly

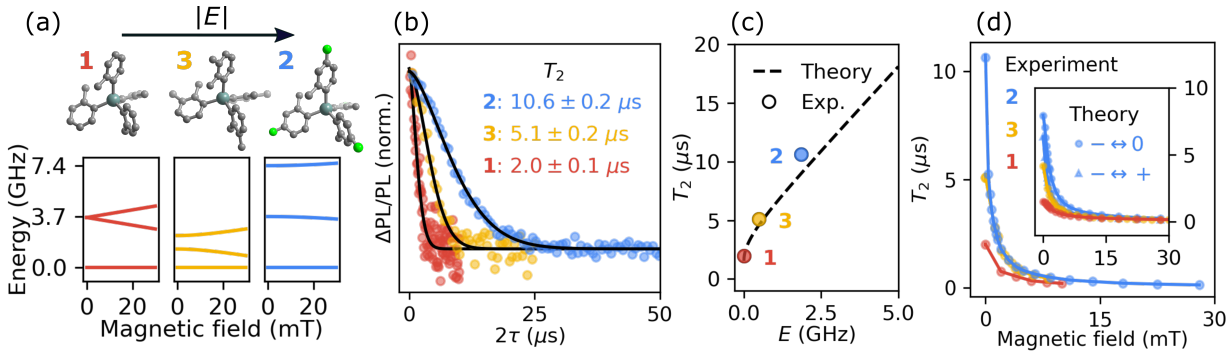

Figure 7.2: Host and chemical tuning of transverse zero-field splitting to enhance coherence. (a) Molecular structures of the host matrix for 1, 2, and 3 with their simulated spin energy levels as a function of magnetic field. (b) Hahn echo traces for single crystals of 1, 2, and 3 at zero magnetic field. (c) Zero-field spin coherence as a function of transverse zero-field splitting along with theoretical dependence calculated from first-principles gCCE methods (using large D limit, see Supplemental Material). (d) Experimental and calculated T2 as a function of magnetic field.

shorter $T_2 = 2.0 \pm 0.1 \mu$s for **1** at zero-magnetic field, indicating the effectiveness of the clock transition in **2** for enhancing spin coherence.

To further understand the dependence of zero-field spin coherence on the transverse zero-field splitting, we investigated two other molecular systems: Cr(IV)(2,3-dimethylphenyl)$_4$ diluted in Sn(2,3-dimethylphenyl)$_4$ (**3**), and Cr(IV)(2,4-dimethylphenyl)$_4$ diluted in Sn(2,4-dimethylphenyl)$_4$ (**4**). The additional methyl group on the ligands of these compounds induces lower symmetry crystal packing than **1**, and consequently, $E \simeq 0.5$ GHz in both cases [72], providing additional testbeds of the role of the transverse zero-field splitting in enhancing spin coherence, here from tuning the qubit rather than the host matrix. Fig. 7.2(c) plots the zero-field coherence time for **1**, **2**, and **3** showing that T_2 increases with increasing E. **4** shows a similar T_2 as **3** due to its very similar E value. Generally, these four systems highlight paths to engineer even longer coherence times through independently optimizing both the host matrix and the chemical composition of the qubit.

To investigate the spin coherence of these molecular color centers interacting with their nuclear spin bath we used first principles generalized cluster correlation expansion (gCCE)

calculations with Monte Carlo bath state sampling using the PyCCE package [108]. Starting from the crystal structure for these compounds, we calculated the electron-nuclear hyperfine couplings of the Cr-containing molecule using density functional theory (DFT) with SCAN functional. Using DFT-computed spin densities, we calculate the interactions between the Cr center and nuclear spins in the host matrix and use point dipole-dipole interactions between nuclear spins. The calculated zero-field T_2 as a function of transverse zero-field splitting E shows good agreement with the experimental values [Fig. 7.2(c)]. Since the calculations only consider the nuclear spin bath, they highlight that Cr electronic spins or electric-field/strain-induced noise are not a major limitation on the coherence in our experiments. Interestingly, the calculations also allow us to determine the distance at which nuclear spins play a significant role in determining the coherence. By varying the number of nearest-neighbor molecules included in the calculations, we found T_2 converges when 3-4 nearest neighbors are included, corresponding to a radius of approximately 1.5 nm around the Cr center.

To the best of our knowledge, the behavior of ground-state electronic spin coherence in the low magnetic field regime (from 0 to $\sim$ 100 mT) has largely been unexplored in molecular systems, but, as demonstrated in solid-state color centers, is an important domain for applications in quantum information science [44, 109]. To explore this regime in molecular color centers, we measured T_2 as a function of magnetic field for **1**, **2**, and **3**. In each case, T2 decreases with increasing magnetic field between 0 and 30 mT [Fig. 7.2(d)]. The good agreement between the experimental data and the gCCE calculations indicates this behavior arises from the magnetic-field dependent dynamics of the nuclear spin bath, combined with moving away from the clock transitions of **2** and **3**. A similar drop in T_2 with field due to nuclear spin bath dynamics—albeit at a lower field scale—has been studied in the nitrogen-vacancy center in diamond (which has $E = 0$) [52]. In this case, T_2 drops with magnetic field to a minimum at $\sim$ 0.1 mT due to nuclear spin bath dynamics, before recovering at $\sim$ 10

mT, when the nuclear Zeeman splitting dominates over the electron-nuclear and nuclear-nuclear spin interactions [52]. Our observations in molecular color centers can be assigned to a similar mechanism—albeit with a larger characteristic field scale due to the stronger spin interactions [110] — combined with the increased noise sensitivity for **2** and **3** as they shift from their zero-field clock transitions. Due to the higher field scale involved for these molecular color centers, we only see a reduction in T2 in the measured field range. We note, however, that electron spin resonance measurements performed on **1** at higher magnetic fields ($\simeq$ 400 mT) yield $T_2 \simeq 2.5\mu$s [111], consistent with the theoretical prediction of a high-field recovery in T_2 [52].

7.2 Discovery of atomic clock-like spin defects in simple oxides from first principles

Virtually noiseless due to the scarcity of spinful nuclei in the lattice, simple oxides hold promise as hosts of solid-state spin qubits. However, no suitable spin defect has yet been found in these systems. Using high-throughput first-principles calculations, we predict spin defects in calcium oxide with electronic properties remarkably similar to those of the NV center in diamond. These defects are charged complexes where a dopant atom — Sb, Bi, or I — occupies the volume vacated by adjacent cation and anion vacancies. The predicted zero phonon line shows that the Bi complex emits in the telecommunication range, and the computed many-body energy levels suggest a viable optical cycle required for qubit initialization. Notably, the high-spin nucleus of each dopant strongly couples to the electron spin, leading to many controllable quantum levels and the emergence of atomic clock-like transitions that are well protected from environmental noise. Specifically, the Hanh-echo coherence time increases beyond seconds at the clock-like transition in the defect with ^{209}Bi. Our results pave the way to designing quantum states with long coherence times in simple oxides, making them attractive platforms for quantum technologies.

7.2.1 Structure of the defects

The geometrical configuration of the NV-like defects identified here has C_{4v} symmetry (see Figure 7.3) and gives rise to four states within the band gap in both spin channels. One is close to the valence band maximum; the other three are mid-gap states. For example, for X from group 15, the mid-gap states originate from the single substitutional X_O^- that has O_h symmetry and a threefold degenerate state (T_{1u}). As mentioned above, the most stable position of the X dopant in $X_{Ca}V_O$, in the absence of the adjacent Ca, is between the Ca and O vacancy sites (Figure 7.3a). This geometrical configuration lowers the O_h symmetry of the

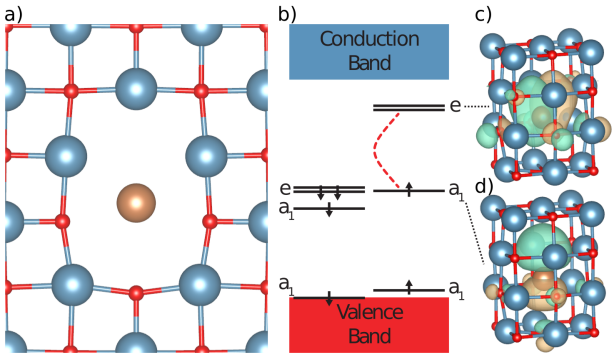

Figure 7.3: (a) Atomic configuration of the $X_{Ca}V_O$ defects identified in our search, where X = Sb, Bi, I is located between the missing cation and anion sites. For X=Sb or Bi, the defect is negatively charged; for X = I, it is positively charged. All defects have C_{4v} symmetry. Red, blue and brown spheres denote oxygen, calcium and dopant atoms, respectively. (b) Electronic structure of the $X_{Ca}V_O$ complexes, where we have indicated the zero-phonon line excitation between the a_1 and e states. States are labeled following the representation of the C_{4v} group. c) and d) show the iso-surfaces of the sum of e_x and e_y defect orbitals, and of the a_1 defect orbital, respectively, both with a value of 10^{-4}Å$^{3/2}$.

complex to C_{4v}, leading to a split of the T_{1u} into a_1 and e states; as shown in Figure 7.3c), these states are highly localized.

7.2.2 Coherence properties of the defects

CaO is an almost noiseless host of spin-defects, removing the need for any isotopic engineering. Natural-abundant CaO contains only about 0.13% of magnetic nuclei ^{43}Ca with spin-7/2 and about 0.04% of spin-5/2 ^{17}O. As a result, the nuclear-spin limited Hahn-echo T_2 of the localized electron spin in CaO is 34 ms, an order of magnitude higher than of naturally abundant diamond (0.89 ms) [56]. A significant additional advantage of the defect centers discovered here is that each of them contains a *single* nuclear spin that strongly couples to the electron spin of the defect. For example, ^{209}Bi is a spin-9/2 particle with nearly 100% natural abundance. The parallel component of the hyperfine coupling between the electron and Bi nuclear spins, 1.27 GHz, is similar to Bi donors in Si [40]. Hence, the combined electron-nuclear system exhibits 30 energy levels (see Fig 7.4a) that are separately addressable in

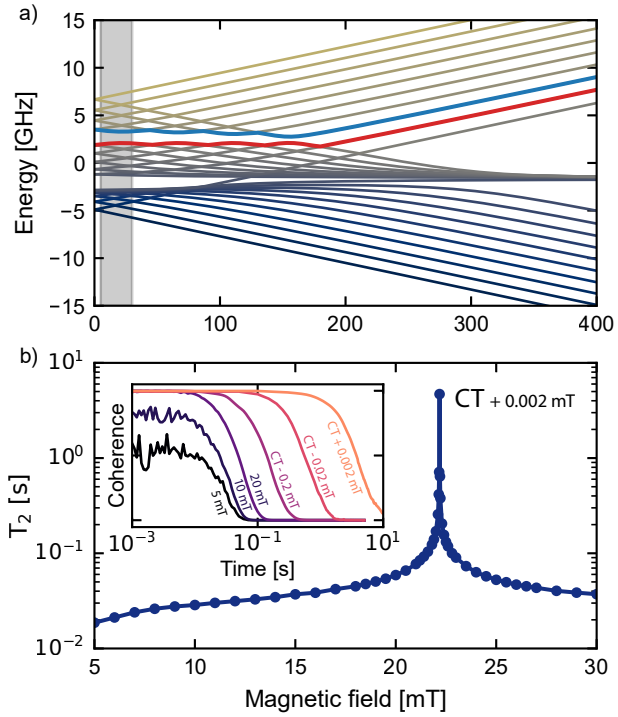

Figure 7.4: (a) Spin energy levels of the $Bi_{Ca}V_O^-$ defect. Levels chosen as qubit levels are marked with red and blue. Grey shaded area represents the range of magnetic fields shown in (b). (b) Nuclear spin-limited T_2 of the electron spin near a clock transition (CT), as computed using the CCE method. The inset shows actual computed coherence signal near a clock transition.

experiments, providing a broad space of spin states accessible for the design of quantum technologies.

The strong electron-nuclear spin coupling in $Bi_{Ca}V_O^-$ leads to a set of avoided crossings between energy levels as a function of the magnetic field. The spin transitions between these levels, known as "clock transitions" (CT) [40], are remarkably robust to external perturbations, and thus the coherence time of qubits operating at a CT can be substantially increased [49, 53]. Using the cluster-correlation expansion method (CCE), implemented in the PyCCE code [108], we computed the coherence of the spin qubit $Bi_{Ca}V_O^-$ near CTs (see Fig. 7.4b). We find that at the magnetic field of 22.18 mT (2 μT from a clock transition), the T_2 is already increased by two orders of magnitude (4.7 seconds) compared to that of a qubit operating away from CTs (34 ms).

In summary, several simple oxides, particularly CaO, have been predicted to be promising hosts of spin defects with long coherence times. Using a high-throughput search based on first principles calculations, we predicted a class of spin defects in CaO with properties remarkably similar to those of the NV center in diamond. Such NV-like defects ($X_{Ca}V_O$) consist of a missing Ca-O pair and a dopant X=Sb, Bi, and I; they are stable, with a triplet ground state, in their negatively charged (Sb, Bi) and positively charged (I) states. They also exhibit two singlet excited states between the ground and first triplet excited states, as explicitly verified in the case of Bi, suggesting the possibility of an optical cycle similar to that of the NV center. Importantly, the $X_{Ca}V_O$ complexes have a detectable zero phonon line close to the telecommunication range and exhibit a zero-field splitting similar to the NV center in diamond. In particular, we predict that the $Bi_{Ca}V_O^-$ complex has a bright emission in the L-band. In addition, the presence of a high spin nucleus, strongly coupled to the electron spin, leads to many spin levels addressable in experiments and to the emergence of avoided crossings in the spin energy spectrum. We showed that when operating at these avoided crossings, the spin coherence of the $Bi_{Ca}V_O^-$ complex is increased by at least two orders of magnitude, exceeding seconds.

Experimental verification of our results should be relatively straightforward, given the ease of growth of CaO and our estimate of the propensity of the defects identified here to be implanted in the material. Overall, our results show that CaO, and other simple oxides, are promising emerging materials for quantum applications.

CHAPTER 8

ACCURATE PREDICTION OF SPIN HAMILTONIAN PARAMETERS

This chapter is adapted from the published works [5, 6].

In this section, we use coherence calculations to benchmark the results of the *ab initio* DFT calculations of spin Hamiltonian parameters and test the sensitivity of the dynamical spin properties on the accuracy of the DFT predictions.

8.1 Theoretical and experimental study of the nitrogen-vacancy center in 4H-SiC

Using first principles calculations and magnetic resonance experiments, we investigated the physical properties of the negatively charged NV center in 4H-SiC, a promising spin qubit. Our predictive theoretical model in conjunction with experimental measurements reveal a large sensitivity to strain and symmetry. The measured and computed zero phonon lines (ZPLs) are in agreement and show a consistent trend as a function of the defect location in the crystal. The computed ZPLs are extremely sensitive to the geometrical configurations of the ground and excited states, and large supercells with more than 2000 atoms are required to obtain accurate numerical results. We find that the computed decoherence time of the basal NV centers at zero magnetic field is substantially larger than that of the axial configurations. Furthermore, at natural nuclear spin abundance and zero field, the Hahn-echo coherence time of one of the basal configurations is similar to that of the axial divacancy in isotopically purified SiC.

Table 8.1: Value (MHz) of the components of the zero field splitting tensor (D;E) obtained in this and previous works. The values reported in Ref.[1, 2] are the same.

Config.	Exp. [1, 2]	Exp. [this work]	Th. [2]	Th. [this work]
hh	1331; 0	1339; 0	1427; 0	1513;∼0
kk	1282; 0	1288; 0	1377; 0	1454; 0
hk	1193;104	1232;111	1331;110	1409;110
kh	1328; 15	1355; 15	1404; 44	1489; 45

8.1.1 Spin Hamiltonian parameters and coherence times

We now turn to discussing coherence times of the NV in 4H-SiC. One of the advantages of SiC based qubits compared to diamond spin qubits is the presence of the binary lattice, which leads to a significant enhancement of the coherence time of divacancies in SiC even at the natural isotopic concentration of nuclear spins [5] [3]. We show below that axial NV centers in SiC exhibits the same coherence properties as the VV in SiC and that the theoretical limit of T_2 is similar to that of the axial divacancy (Table 8.2).

Compared to axial NV centers, basal configurations exhibit a lower symmetry and hence a substantial transverse zero-field splitting E. The lower symmetry allows for clock transitions to emerge at zero applied magnetic field. The frequency of clock transitions is insensitive to the magnetic field fluctuations up to first order [90], thus significantly improving protection from the nuclear spin noise.

Our calculations predict a substantially larger T_2^* for the basal NV centers at zero magnetic field compared to that of the axial ones. We note the importance of the amplitude of the transverse ZFS in determining the value of T_2^* at clock transitions. The coherence times for the kh NV center at zero magnetic field, computed using the theoretical value of the ZFS is larger than the one obtained with the experimental E value by a factor of two. This significant difference points at the necessity (Table 8.1) of accurate predictions of spin Hamiltonian parameters [112].

Finally, we investigated the dependence of the Hahn-echo coherence time T_2 on the magnetic field (B_z), shown in Fig.8.1 computed using measured E values[1, 2]. At low

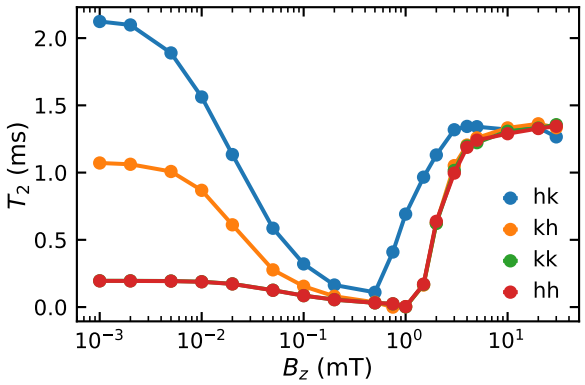

Figure 8.1: Computed coherence time T_2 as a function of the strength of the applied magnetic field (B_z) for four configurations of the NV center in 4H-SiC. Note that the T_2 of the hh and kk configurations is similar, especially in the the lower B_z range.

magnetic fields the hyperfine couplings are stronger or on par with the energy splitting arising from the external magnetic field. The increase of the magnetic field leads to an increase in the speed of precession of single nuclear spins, which in turn leads to faster fluctuations of the magnetic noise and to a decrease in coherence time in this regime. For the basal defects with clock transition, the decrease in coherence time is further exacerbated by the removal of the qubit energy levels from the avoided crossing, at which the additional protection from the magnetic noise is achieved [52]. We note that the clock transition in basal configurations leads to a substantial increase in T_2 at $B_z = 0$, relative to that of axial configurations. At strong magnetic fields all configurations exhibit the same coherence time of ~ 1.3 ms as the Zeeman splitting plays a major role in this regime, leading to only secular pairwise nuclear spin flips being allowed and thus to an increase of T_2 in this regime. For the hk case at natural abundance of nuclear spins, the predicted Hahn-echo coherence time at zero field is similar to those of the divacancies in isotopically purified SiC [3]. Furthermore, the high amplitude of the transverse ZFS affects the coherence time also for intermediate values of the magnetic fields ($B_z = 10 - 50$ G): interestingly, we found that the T_2 of the hk NV center is higher than those of other NV and divacancy configurations.

In sum, we have predicted coherence times of the NV in basal and axial configurations

Table 8.2: Nuclear spin bath-limited coherence time. For the kh configuration, we show coherence times computed using both the experimental ([1, 2]) and our theoretical value of the E component of the zero field splitting tensor (see Table 8.1). The experimental data for the kk divacancy (kk-VV) are from [3],[4], and[5].

For the axial NV centers the coherence time is computed at magnetic field of 200 G and for the basal centers at zero applied magnetic field.

Config.	T_2^* (μs)	T_2 (ms)
hh	0.64 (1.0^1)	1.32 (0.017^1)
kk	0.85 (0.4^2)	1.31
hk	520	2.2
kh (exp. E)	150	0.99
kh (th. E)	340	1.68
kk-VV	1.1	1.2

and found a substantially larger T_2^* of the basal NV centers at zero magnetic field, compared to that of the axial configurations. Interestingly our calculations show that at natural nuclear spin abundance the Hahn-echo coherence time at zero field of one of the basal configurations is similar that of the divacancies in isotopically purified SiC. Given the readily accessible ^{14}N nuclear registers and the availability of universal dressing schemes at clock transitions [82] to protect qubit states, we expect the basal NV centers to provide robust platforms for the next generation of defect qubits in SiC.

8.2 Spin-spin interactions in defects in solids from mixed all-electron and pseudopotential first- principles calculations.

Understanding the quantum dynamics of spin defects and their coherence properties requires an accurate modeling of spin-spin interaction in solids and molecules, for example by using spin Hamiltonians with parameters obtained from first-principles calculations. We present a real-space approach based on density functional theory for the calculation of spin-Hamiltonian parameters, where only selected atoms are treated at the all-electron level, while the rest of the system is described with the pseudopotential approximation. Our approach permits calculations for systems containing more than 1000 atoms, as demonstrated for defects in diamond and silicon carbide. We show that only a small number of atoms surrounding the defect needs to be treated at the all-electron level, in order to obtain an overall all-electron accuracy for hyperfine and zero-field splitting tensors. We also present results for coherence times, computed with the cluster correlation expansion method, highlighting the importance of accurate spin-Hamiltonian parameters for quantitative predictions of spin dynamics.

8.2.1 Finite Element DFT Predictions of the Spin Hamiltonian parameters

The spin Hamiltonian parameters can be determined from first-principles electronic structure calculations [115–127], the majority of which are based on plane-wave pseudopotential (PW-PP) approaches. DFT calculations of SH parameters using basis sets different from PW have been proposed (e.g. numerical atomic orbitals [128], linearized augmented plane-wave [129], linear muffin-tin orbitals [117, 130], and Gaussian orbitals [131]), but they are often limited to smaller systems than those accessible to PW calculations. In the PW-PP method, pseudopotentials (PP) are used to describe the interaction between valence and core electrons, and single-particle wavefunctions of core electrons in the solid are not explicitly

evaluated. All-electron wavefunctions may be reconstructed, for example using the projected augmented wave (PAW) procedure [132], and then used to compute the parameters of the SH. Recently, we proposed and benchmarked a real-space all-electron DFT framework [133] using a finite-element (FE) basis sets [134] for accurate predictions of SH parameters in molecules and solids, which does not require any reconstruction of core-wavefunctions. This framework allows one to systematically convergence the results of SH parameters with respect to the basis set size and hence to establish robust results to compare with experiments for a chosen level of first-principles theory. However, the method is computationally rather demanding and it only permitted the investigation of systems with tens of atoms.

Here we propose a computational scheme where only selected atoms are treated at the all-electron (AE) level, while the rest of the system is described within the PP approximation. We show that in order to obtain accurate SH parameters for spin-defects, only a small number of atoms surrounding the defect (of the order of 10) needs to be treated at the AE level. Our approach permits calculations for cells with hundreds of atoms, as shown for the NV center in diamond and the VV in 4H-SiC, for which we used cells with up to 1022 atoms. In addition, using the cluster correlation expansion (CCE) [47] method, we demonstrate the importance of accurate SH parameters for precise predictions of coherence times of spin defects in semiconductors.

8.2.2 Coherence time in weakly coupled nuclear spin baths: the need for all-electron descriptions

In general, there are two ways to control nuclear spins in defect systems. The strongly coupled nuclear spins (with hyperfine coupling of order ~ 1 MHz) can be directly accessed via radio frequency radiation. Here we define nuclear spins as strongly coupled when their hyperfine parameter is larger than the linewidth of the optically detected magnetic resonance (ODMR) [87] and separate oscillations in the Ramsey sequence due to the nuclear spin are

observed [3]. These nuclear spins can be controlled with short gate times but they are highly susceptible to electron spin induced noise.

The second type of nuclear spins, weakly coupled to the electron spin ($A \ll 1$ MHz) are controlled by dynamical decoupling schemes [135]. Applying refocusing pulses to the central spin may be used to not only increase the coherence time of the defect but also to isolate and control weakly coupled nuclear spins. These spins provide significantly longer coherence times than strongly coupled spins, and the number of weakly coupled nuclear spins is not limited by the short distance to the central spin which is required for strong coupling.

The strength of the nuclear-spin induced dephasing mechanism, limiting coherence time T_2^* in spin defects is directly related to the $\boldsymbol{A}$-tensor [136], which therefore requires accurate calculations. Here, we first estimate the sensitivity of the inhomogeneous dephasing time T_2^* and the Hahn-echo coherence time T_2 on the values of the $\boldsymbol{A}$-tensor by carrying out CCE calculations (Fig. 8.2); T_2 determines the stability of the qubit under dynamical decoupling schemes. We used two sets of hyperfine coupling computed for $4 \times 4 \times 4$ supercell of the NV center in diamond: one set for which the $\boldsymbol{A}$-tensor is calculated using the PAW reconstructed spin densities, and a second one based on the $\boldsymbol{A}$-tensor calculated using FE-AE calculations. Fig. 8.2 b shows a histogram of the calculated $A_{||}$ (A_{zz} in the defect reference frame) obtained using the two methods. We found that for large hyperfine coupling values, the relative difference is rather minor compared to the one for the smaller coupling terms. In order to see the impact of these differences on the dephasing of the electron spin, first we compute the ensemble-averaged dephasing time, T_2^*, by considering the decay of the coherence function averaged over a set of nuclear spin configurations. The difference in the ensemble averages dephasing time was found not to be significant (1.35 (FE-AE) μs vs 1.37 (PAW) μs). We note that the predicted value is close to the generally accepted value of nuclear-spin-limited T_2^* in diamond of ~ 1 μs [137]. The dynamical decoupling changes the sensitivity of the qubit to the static noise, and the resulting Hahn-echo coherence time

T_2 is found to be insensitive to the choice of hyperfine couplings and equal to 0.89 ms, in agreement with previously reported CCE predictions [5].

Next, we focus on the single-defect dephasing time in the weakly coupled nuclear spin bath considering the example to NV center in diamond (Fig. 8.2(a)). We select nuclear configurations whose Fourier transform of the free induction decay (FID) contains only one peak. This procedure ensures that the coherence function of the defects in the chosen subset of nuclear configurations does not contain any oscillations due to the nuclear spins with high hyperfine coupling. Hence the procedure guarantees that the nuclear baths contain only weakly coupled nuclear spins and we can thus use an exponential decay fit to obtain the value of T_2^*. Fig. 8.2(c) shows the T_2^* for the chosen subset of nuclear configurations. In these systems, the difference between PAW and FE-AE results is significant as the dephasing time differs by a factor of 2 for certain nuclear configurations. We note that in general for weakly coupled spins, the hyperfine coupling computed with PAW are higher (as can be seen in Fig. 8.2(b) compared to their FE-AE counterpart, leading to significant differences in the predictions of the dephasing time. At the same time the Hahn-echo coherence time (Fig. 8.2(c), right pane) does not depend on the choice of hyperfine couplings, as the main dephasing mechanism under dynamical decoupling is pairwise spin flip of distant spin pairs [5].

However, in the emerging qubit systems based on the clock transitions at avoided crossings of spin levels [40, 82, 138], the sensitivity of the coherence time to the magnetic noise from the nearby nuclear spins is different. As an example, we consider the basal *kh* divacancy in 4H-SiC (Fig. 8.2(d)). Compared to *kk*-VV, the basal divacancy has a lower symmetry and ZFS tensor contains both axial splitting D_3 and basal splitting $E = D_2 - D_1 = 18.4$ MHz [90], leading to emergence of avoided crossing in spin levels at zero magnetic field. Using hyperfine couplings computed with PAW and FE-AE in $6 \times 3 \times 2$ orthorhombic supercell containing 574 atoms (Fig. 8.2(e)) we predict the ensemble average $T_{2\,\mathrm{PAW}}^* = 0.13$ ms, $T_{2\,\mathrm{FE}}^* = 0.14$

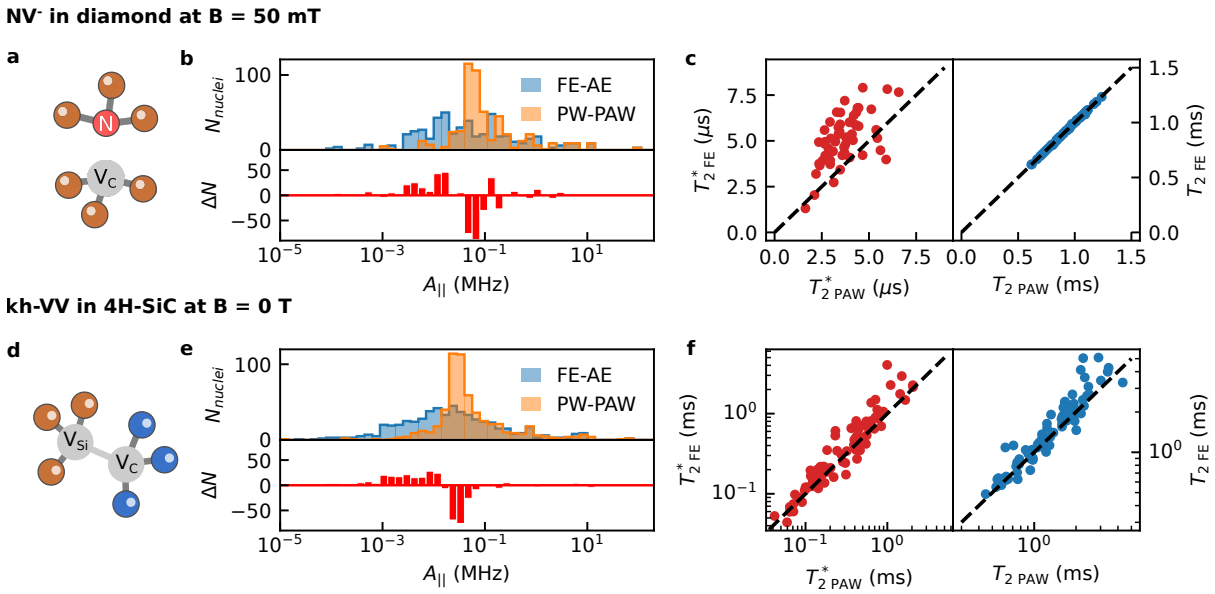

Figure 8.2: (a) Structure of the NV center in diamond (b) Histogram of $A_{||}$ (see text) for carbon atoms in a 4×4×4 NV-diamond supercell calculated using PAW and FE-AE methods. (c) Comparison of coherence times T_2^* and T_2 induced by weakly coupled nuclear spin baths, predicted with hyperfine values from PAW ($T_{2\ \mathrm{PAW}}$) and FE-AE ($T_{2\ \mathrm{FE}}$) calculations. (d) Structure of the basal kh-VV in 4H-SiC. (e) Histogram of $A_{||}$ (see text) for silicon and carbon atoms in a $6 \times 3 \times 2$ 4H-SiC supercell with kh-VV in the middle calculated using PAW and FE-AE methods. (f) Comparison of coherence times T_2^* and T_2 of the basal divacancy at clock transition.

ms and $T_{2\ \mathrm{PAW}} = 1.04$ ms, $T^*_{2\ \mathrm{FE}} = 1.11$ ms using generalization of CCE method [53]. The PW-PAW results consistently overestimate the hyperfine couplings of the weakly coupled nuclear spins, which leads to notable differences even in the ensemble averaged coherence times of this system. Both values are smaller than the ones, reported in the previous work ($T_2^* = 0.16$ ms, $T_2 = 1.15$ ms)[53] where we used larger $9 \times 5 \times 2$ orthorhombic supercell containing 1438 atoms to compute hyperfines with PW-PAW approach, which confirms the importance of larger supercell for precise calculations of hyperfine couplings. Finally, we analyze the coherence times of basal divacancy at clock transition in the single nuclear spin spatial configurations (Fig. 8.2(f)). We find that both T_2^* *and* T_2 depend significantly on the approximation used to obtain hyperfine couplings of the nearby nuclear spins, leading to

significant differences in predicted coherence times.

Overall, we computed hyperfine constants for both strongly and weakly coupled nuclei spins from AE calculations in two systems, NV in diamond and kh-VV in SiC, followed by coherence times estimation in those two systems. This shows that the *relative* difference between AE and PP predictions of hyperfine tensors for strongly coupled nuclear spins (those for which $A \geq 1$ MHz) is small. However, *absolute* differences in hyperfine tensors predicted with PW-PP and AE methods for weakly coupled spins ($A \ll 1$ MHz), even when similar in magnitude to those found for strongly coupled spins, may dramatically impact the prediction of T_2^* of the NV center, with differences up to a factor of 2 for certain nuclear spin configurations. In the case of the clock transitions of the basal kh-VV in SiC, the variance in the predictions is even more drastic, with relative difference up to a factor of 4. In this case, the choice of the approximation affects both T_2 and T_2^* coherence times. We note that, in addition to coherence time calculations, accurate predictions of zero-field splitting and hyperfine tensors for strongly-coupled nuclear spins are important to identify the atomistic structure of spin-defects [139]; furthermore, accurate predictions of hyperfine tensors for weakly coupled nuclear spins are key for the spatial mapping of experimental multinuclear registers [140] and the prediction of plausible memory units in spin centers [3].

CHAPTER 9

FIRST PRINCIPLES SIMULATIONS IN QUANTUM SENSING

9.1 Sensing dynamics of spin qubits in low dimensional van der Waals materials.

This section is adapted from the published work [3].

We report a theoretical study of the coherence dynamics of spin qubits in two-dimensional materials (2DMs) and van-der-Waals heterostructures, as a function of the host thickness and the composition of the surrounding environment. We focus on MoS_2 and WS_2, two promising systems for quantum technology applications, and we consider the decoherence arising from the interaction of the spin qubit with nuclear spins. We show that the Hahn-echo coherence time is determined by a complex interplay between the source of decoherence in the qubit host and in the environment, which in turn determines whether the noise evolution is in a classical or quantum mechanical regime. We suggest that the composition and thickness of van-der-Waals heterostructures encapsulating a qubit host can be engineered to maximize coherence times. Finally, we discuss how quantum sensors may be able to probe the dynamics of the nuclear bath in 2DMs.

9.1.1 Introduction

In the last few years, two-dimensional materials (2DMs) have attracted widespread attention in the field of quantum technologies[141], with potential applications as spin quantum dot qubits [142, 143] and single-photon emitters [144–146]. Recently, the coherent control of atomic defects in a 2DM has been reported for a boron vacancy in hexagonal boron nitride (h-BN) [147, 148], with the room temperature coherence time (T_2) of 2 μs [149]. Moreover, theoretical studies have predicted a significant increase in T_2 of defect-based qubits in

monolayers compared to their bulk counterparts [55].

However, the presence of the environment may change the properties of the 2D host and hence those of the qubit; therefore environmental effects are expected to play an important role in the control and design of spin defects in two dimensions. For example, the nature of the substrate significantly alters the photoluminescence of WS_2 [150], and the band gap of a MoS_2 monolayer, with variations of more than 1 eV (1.23-2.65 eV)[151]. In some cases, the presence of the environment may be beneficial for 2DM applications: combining several layers of 2DMs leads to materials with interesting properties for nanoelectronics[152, 153], including atomic-scale transistors [154] and memory units [155].

In this work, we present a theoretical investigation of the impact of the environment on the quantum dynamics of defect-based qubits in 2DMs and van-der-Waals heterostructures. We consider spin defects in wide-band-gap transition metal dichalcogenides WS_2 and MoS_2, which are promising platforms for optoelectronic applications[156] and quantum emitters [157]. We focus on a single source of decoherence, the interaction of the spin-defect with the surrounding nuclear spin bath, known to be the limiting factor for the coherence time of many solid-state qubits[15, 158].

Assuming a pure dephasing regime, we model the spin dynamics of the qubit using the cluster correlation expansion (CCE) method[47, 48], which has been shown to yield accurate results for numerous systems [5, 49, 51, 53]. We model Hahn-echo experiments, and the coherence time is obtained from the decay of the coherence function $L(t)$, defined as a normalized off-diagonal element of the density matrix $\hat{\rho}$ of the qubit:

$$L(t) = \left| \frac{\langle 0| \hat{\rho}(t) |1\rangle}{\langle 0| \hat{\rho}(0) |1\rangle} \right| \tag{9.1}$$

The structure of suitable spin defects in WS_2 and MoS_2 is still an open question[159]. Hence we simply consider a model defect with spin-1 and $|0\rangle$ and $|-1\rangle$ as qubit levels, similar to those of optically addressable qubits in 3D materials, e.g. the NV^- center in diamond

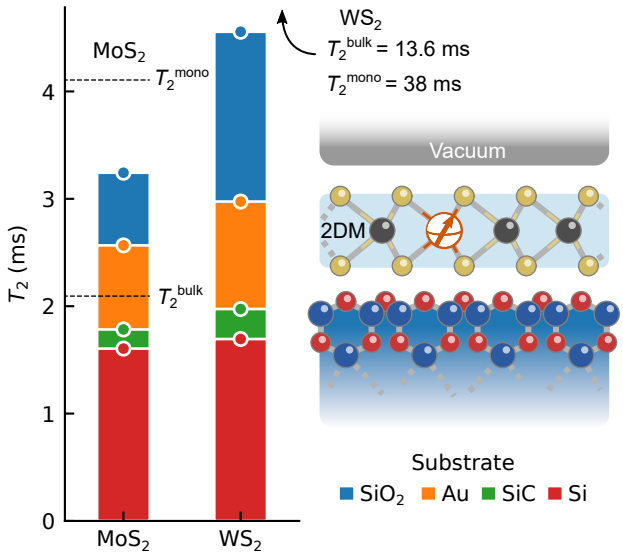

Figure 9.1: Left: Computed Hahn-echo coherence time (T_2) of 2DMs as a function of different substrates listed on the right. Distance between 2DM and the surface is ~ 0.3 nm [162–164]. Applied magnetic field is perpendicular to the surface. Right: Representation of the model system.

[160] or the divacancy in SiC [3]. Furthermore, we assume that the electronic energy levels associated with the defect are localized within one unit cell, and the spin defect interacts with the nuclear bath as a magnetic point dipole. We compute the quadrupole tensors for the nuclei with spin ≥ 1 using density functional theory with the PBE functional [161], and the GIPAW module [67] of the Quantum Espresso code [63]. We assume that for sparse baths the quadrupole interactions between nuclear spins and the electric field gradient are the same as those in the pristine material.

9.1.2 Substrate effect on the Qubit Coherence in 2D Materials

We start by discussing our results for the MoS_2 and WS_2 2DMs. Both materials contain a significantly lower concentration of nuclear spins than h-BN – the only experimentally characterized 2D host so far – thus allowing for significantly longer coherence times. For isolated 2D systems in vacuum, Ye et al. [55] predicted that the T_2 of a spin qubit in MoS_2

increases by a factor of $\simeq 2$ ($T_2^{\text{mono}} = 2.2$, $T_2^{\text{bulk}} = 1.2$ ms) when the nuclear bath of the host is reduced from 3D to 2D. The calculations of Ref.[55] neglected the quadrupole term in the spin Hamiltonian. When including such term, we find that T_2 further increases ($T_2^{\text{mono}} = 4.1$ ms), while the ratio between T_2 in 2D and 3D remains the same as previously reported. In natural WS_2, the nuclear bath contains a smaller number of nuclear spins than in MoS_2, with a relatively small gyromagnetic ratio. Hence the nuclear spin-induced decoherence in WS_2 is an order of magnitude slower than in MoS_2, and the increase in coherence time with reduced dimensionality becomes more significant: $T_2^{\text{mono}} = 38$ ms, 3 times higher than $T_2^{\text{bulk}} = 13.6$ ms.

Next, we investigate how coherence times vary when MoS_2 and WS_2 are deposited on a substrate. We consider Au (111), Si (111) and SiO_2 (ideal siloxane-terminated surface) [165–168]. These substrates have been used in spectroscopic measurements [166], and applications of 2DMs in catalysis[165, 167] and electronics [168]. We neglect the reconstruction of the surface of the substrate and we assume that the quadrupole couplings are the same as those of the pristine material in vacuum. Because the quadrupole splittings are large in the systems considered here, the interface-induced variations in their amplitude are unlikely to substantially alter the coherence dynamics at strong magnetic fields.

Under an applied magnetic field, the contributions to coherence times of the different species of the nuclear bath are decoupled [5]; hence:

$$L = L^S L^{2DM} \tag{9.2}$$

where L^S and L^{2DM} are the contributions of the substrate (S) and of the 2DM host, respectively. We find that the nuclear baths of both the 2DM and the substrate may act as limiting factors to the qubit coherence. In particular, in WS_2 the qubit dynamics is completely determined by the substrate nuclear bath, and T_2 is significantly smaller than the one of the qubits in bulk WS_2 (Fig. 9.1). The coherence time depends on the nature of

the substrate. The longest and shortest coherence times are obtained for SiO_2 and the Si (111) surface, respectively. These results can be understood by noticing that the Si substrate has the highest concentrations of ^{29}Si spins, compared to SiO_2 and SiC; the latter exhibits however an additional source of decoherence given by the ^{13}C bath. We also note that while gold contains the highest concentration of nuclear spins (100% ^{197}Au with $s = 3/2$), the small gyromagnetic ratio and large separation of the nuclei lead to a moderate influence of the substrate on the coherence time of the 2D material, with $T_2 = 3$ ms.

In MoS_2, on the other hand, both the substrate and host contribute significantly to the qubit decoherence. We find that an enhancement of T_2 from the reduced dimensionality persists only for the SiO_2 and gold substrates. In the presence of a Si (111) surface, the T_2 of a qubit in MoS_2 and WS_2 is almost identical.

The presence of paramagnetic defects both on the surface of the substrate and in the 2DM itself may significantly impact decoherence rates and limit the value of T_2. To decrease the number of paramagnetic impurities in the 2D host, advanced experimental techniques are being developed [169]. In general, to eliminate surface charges, it is desirable to reduce interfacial reconstructions as much as possible, e.g. by using van-der-Waals bonded materials as substrates. [169, 170].

9.1.3 Qubit Dynamics in van-der-Waals Heterostructures

Hence we turn to consider heterostructures of van-der-Waals bonded materials, which are emerging as promising platforms for 2D-based photonics. For example, a heterostructure of layered graphene and WS_2 was recently used to realize atomic defect-based photon emitters [173]. To simulate the qubit dynamics in van-der-Waals bonded integrated systems, we focus on layered heterostructures with the spin qubit located in an inner layer, as shown in Fig. 9.2a.

We investigated the effect of the decoherence arising from the presence of a substrate

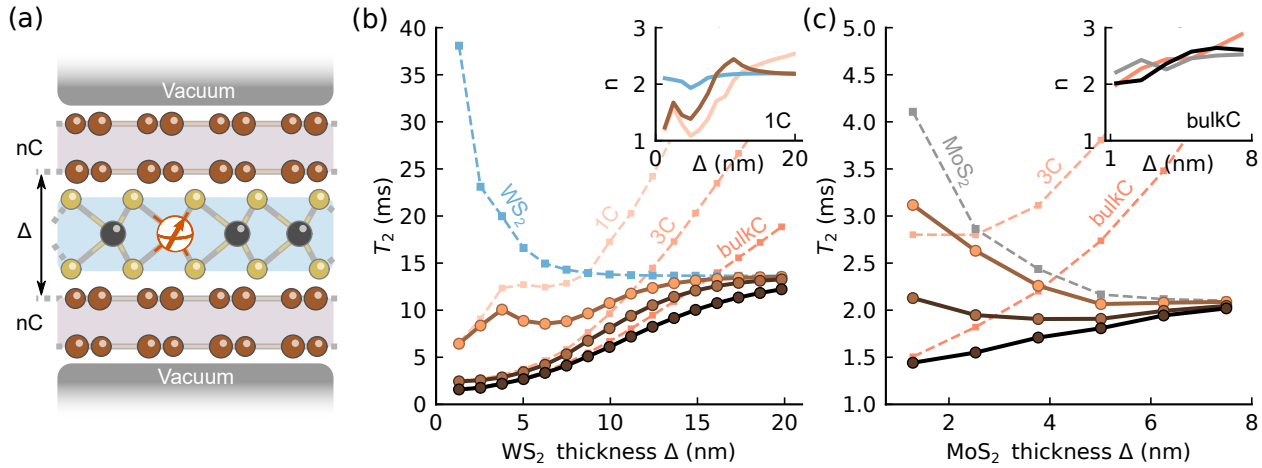

Figure 9.2: Computed Hahn-echo coherence time (T_2) of qubit located in low-dimensional heterostructure. (a) Schematic representation of the model system used in calculations. The qubit is located in the middle of the inner layer of thickness Δ (b), (c) T_2 of the C/WS$_2$/C (C/MoS$_2$/C) heterostructure depicted with solid lines. Dotted lines show the contributions of the host WS$_2$ (MoS$_2$) and graphite substrate with different numbers of layers. The insets show the compressed exponential factor n for host contribution in blue (grey), graphene (bulk graphite) substrate in orange, and the whole system in brown (black) as a function of Δ. Graphite-host distances available from refs. [171, 172].

(outer layer) and from the host (inner layer) of thickness Δ; the coherence time is obtained by fitting the coherence function contribution (Eq. 9.2) to the compressed exponential function, $L^M = \exp\{[-(t/T_2^M)^n]\}$, where M denotes either the substrate (S) or the host 2DM. We found that as Δ increases, the rate of the decoherence induced by the host bath increases (see Fig. 9.2(b) and Fig. 9.2(c) for WS$_2$ and MoS$_2$, respectively). Instead the decoherence rate originating from the substrate nuclear bath decreases with the distance of the qubit from the substrate (see Fig. 9.2a and 9.2b, where mC denotes the number of Carbon layers). The combination of these two factors may result in a non-monotonic behavior of the total coherence time of the heterostructure as a function of Δ.

Fig. 9.2(b) shows our results for C/WS$_2$/C heterostructures. For $\Delta \leq 3$ nm, the effect of the substrate completely supersedes the effect of the host nuclear bath. With increasing Δ, $T_2^{WS_2}$ decreases, but T_2^C increases. We find that for $\Delta \geq 5$ nm, T_2^C is proportional to Δ^α,

where α depends on the thickness of the outer layer; in particular $\alpha = 1.67$ for bulk graphite and 2.5 for graphene. The interplay between the host- and substrate-induced decoherence leads to a local maximum in the coherence time. When the thicknesses of the host material exceeds ~ 15 nm, the decoherence is essentially limited by that of the WS_2 bath.

Our results show that depending on the number of graphite layers in the substrate, the coherence time of monolayer MoS_2-based qubits can be either smaller or larger than T_2 in bulk MoS_2 (Fig 9.2(c)). The presence of two similar sources of decoherence arising from the host and the graphite/3C substrates leads to a minimum of the total coherence time around 4 nm.

As the distance from the graphite substrate increases, the nature of the substrate-induced decoherence process changes. In particular, the graphene-induced decoherence as a function of Δ exhibits the most complex behavior: we observe a transition from a Gaussian ($n = 2$) to an exponential decay ($n = 1$) of the coherence function, near the local maximum in T_2^C and in T_2 of the $C/WS_2/C$ heterostructure. For large Δ, n approaches 3 for both graphene and bulk graphite environments (insets of Fig. 9.2b and c).

Fig. 9.3 shows the decoherence induced by graphene monolayers in ensemble dynamics and for individual bath configurations. Our calculations show that the ensemble-averaged decay induced by the graphene nuclear bath has a smaller compressed exponent n than the mean of the individual fitted decays (Fig. 9.3(a)), consistent with the predictions of stochastic noise models[174, 175]. However, we find that n of the ensemble is not reduced by a factor of two, but only by $\sim 17\%$. Both ensemble and single spin dynamics show a non-monotonic variation of the coherence time with increased distance from the graphene substrate. We analyze below in detail the noise regimes of the Hahn-echo decay depending on the host thickness.

For $\Delta \geq 10$ nm, the dipolar coupling between nuclear spins in graphene is larger than the coupling of the graphene layer to the central spin. Therefore, the magnetic noise from

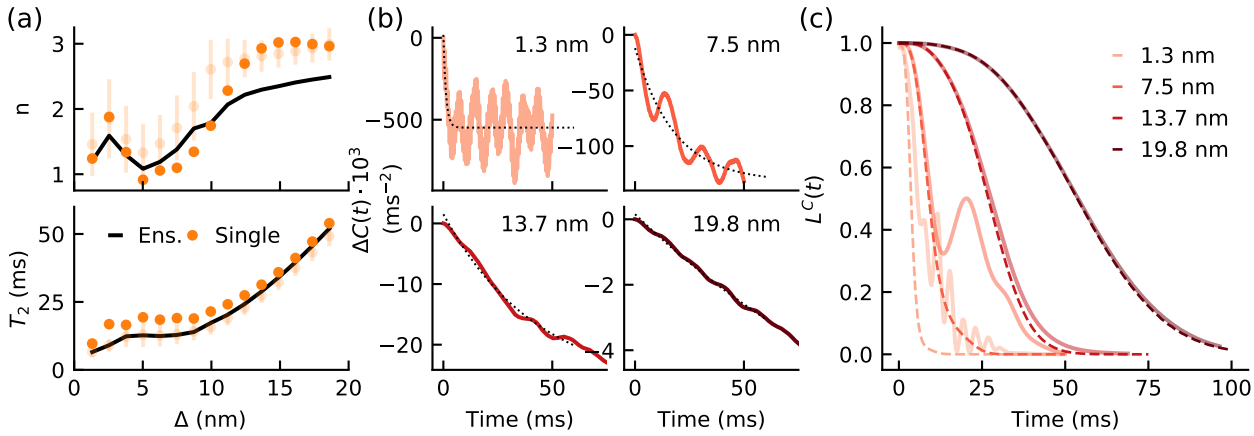

Figure 9.3: Graphene nuclear bath contribution to the qubit dynamics in the model heterostructures (Fig. 9.2). (a) Compressed exponential n and coherence time T_2^C as a function of the host thickness Δ for ensemble (black), mean value of single measurements ± 1 SD (light orange with error bars), and values for one specific configuration (orange). (b) Correlation function of the noise at different Δ. Dotted lines show an exponential fit. (c) Graphene contribution L^C at different Δ computed directly with the CCE method (solid lines) and reconstructed from correlation functions (dashed lines).

the spin bath can be approximated with a classical stochastic variable. In this framework, the evolution of the central spin is governed by the Hamiltonian:

$$\hat{H}^{\text{classical}}(t) = y(t)\eta(t)\hat{S}_z \tag{9.3}$$

where $\hat{S}_z$ is the spin operator of the qubit electron spin, and $y(t) = \pm 1$ changes its sign each time a π pulse is applied [58]. $\eta(t)$ is a stochastic variable, corresponding to the magnetic noise. Assuming Gaussian noise, the coherence function can be computed as [13]:

$$L(t) = \exp\left[\int_0^t C(u)F_t(u)du\right] \tag{9.4}$$

Where $C(t) = \langle \hat{\eta}_{\text{eff}}(t)\hat{\eta}_{\text{eff}}(0)\rangle$ is the correlation of the Overhauser field of the nuclear

bath. $F_t(u)$ is a correlation filter function, defined as [13]:

$$F_t(u) = \int_u^{2t-u} y\left(\frac{v-u}{2}\right) y\left(\frac{v+u}{2}\right) dv \tag{9.5}$$

We compute the noise correlation function with the CCE method [58, 59] from the autocorrelation function of the Overhauser field operator $\hat{\eta}_{\text{eff}}(t) = \sum_i A_{||} \hat{I}_z^i(t)$ where $A_{||}$ is the hyperfine coupling. The correlation function for one random nuclear spin configuration is shown in Fig. 9.3(b) for different separations of graphene layers from the qubit. The dotted black lines show the exponential fit $\Delta C(t) = b^2(e^{-t/\tau_C} - 1)$, where τ_C is the correlation time of the bath. We observe that τ_C increases with thickness from 1.2 ms to 150 ms for the largest separation considered here. The long correlation time at large Δ and the coherence decay of $L^C \approx \exp\left[-(t/T_2)^3\right]$ agree well with stochastic model predictions for the slow evolution of the bath[176, 177].

We further observe the emergence of a classical regime by reconstructing the coherence function from the noise correlation using Eq. 9.4 (Fig. 9.3(c)). We find that the semiclassical approach correctly reproduces the complete quantum mechanical evolution of the bath at separations between graphene layers larger than 10 nm.

For $\Delta \leq 10$ nm, however, the hyperfine coupling is on a par or significantly larger than the average dipolar coupling between nuclear spins. Thus, the evolution of the nuclear spin bath is conditioned on the electron state, and the decoherence of the central spin cannot be correctly reproduced with a classical treatment of the noise[15]. In this case, a complex decay of the coherence function is observed (Fig. 9.3c), which is not captured by Eq. 9.4.

An insight into this complex dynamics can be gained by analyzing the evolution of a single pair of spins i and j. At sufficiently strong magnetic fields, only pairwise spin flip-flops are allowed ($|\uparrow\downarrow\rangle \leftrightarrow |\downarrow\uparrow\rangle$), and their dynamics can be mapped on a 2-level "pseudospin",

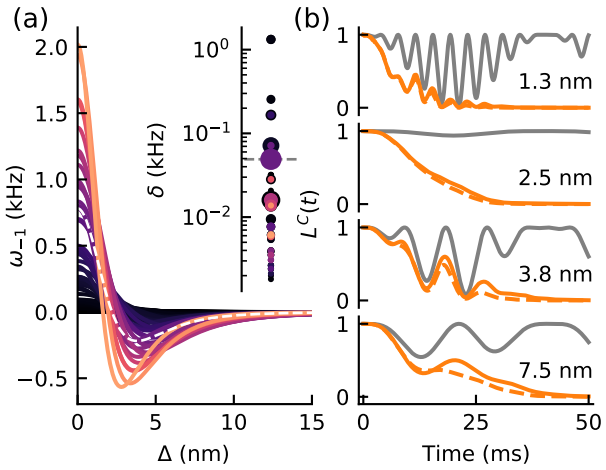

Figure 9.4: Dynamics of the pseudospins in a graphene nuclear bath. (a) Pseudospin frequency ω_{-1} for 100 spin pairs contributing to $L^C(t)$ as a function of the host thickness Δ. Inset shows the corresponding flip rate δ for the given spin pairs. The symbol represents the maximum value of ω_{-1}, and its size represents relative contribution. The dashed line corresponds to the pseudospin shown in (b). (b) Graphene contribution L^C to the decoherence as a function of Δ computed with the CCE method (orange solid lines) and reconstructed from the pseudospin approximation (dashed lines). The grey solid lines show a single pseudospin contribution.

governed by the Hamiltonian:

$$\hat{H}^{\text{pseudo}} = \frac{\omega(t)}{2}\hat{\sigma}_z + \frac{\delta}{2}\hat{\sigma_x} \tag{9.6}$$

where the frequency of the pseudospin, $\omega(t) = \omega_{-1} = \Delta A_{||}$, is given by the difference in hyperfine coupling, if the central spin is in the $|-1\rangle$ state, or $\omega(t) = \omega_0 = 0$ if the central spin is in the $|0\rangle$ state. σ_i are Pauli matrices for spin-½. $\delta = \frac{\hbar\gamma_i\gamma_j}{2r_{ij}^3}(3\cos^2\theta - 1)$ is obtained from the dipolar coupling of i, j nuclear spins, where θ is the angle between the vector r_{ij} connecting two nuclear spins and the external magnetic field.

The total coherence function can be obtained analytically [5, 178] as a product of the contributions of all spin pairs ij:

$$L(t) = \prod_{ij} \left[1 - \kappa \cdot \sin^2(\sqrt{\omega_{-1}^2 + \delta^2}\frac{t}{4}) \sin^2(\delta\frac{t}{4}) \right] \tag{9.7}$$

where $\kappa = \frac{\omega_{-1}^2}{\omega_{-1}^2+\delta^2}$. Due to the reduced dimensionality of graphene and the sparse concentration of nuclear spins, only a small number of spin pairs exists in close proximity of the qubit and thus contributes to determining the coherence decay. (Fig. 9.4).

The dependence of ω_{-1} on the distance from the graphene layer can be computed from the hyperfine couplings of nuclear spins and is quite complex (Fig. 9.4(a)). As Δ increases, the frequency of pseudospins changes its sign and exhibits a local extremum. At $\omega_{-1} = 0$, the hyperfine couplings of two nuclear spins are the same, and the contribution of the spin pair to the coherence function becomes negligible (Fig. 9.4(b)). When the amplitude ω_{-1} reaches a local maximum, the spin pair's dynamics again significantly impacts the coherence function.

This unique behavior of the hyperfine couplings determines the non-monotonic dependence of T_2^C and of the compressed exponent n on the distance between the graphene layers and the qubit. We note the good agreement between the pseudospin prediction and the exact solution at small distances. For large values of Δ, the pseudospin model gives an underestimation of the coherence time, due to the longer correlation time τ_C and to higher-order effects playing a dominant role.

Finally, we note that there are cases in which the choice of the substrate in van-der-Waals structures can completely suppress the effect of the host at any host thickness of interest. As an example, we consider h-BN as a substrate, whose nuclear spin bath contains 100% concentration of spins with a high gyromagnetic ratio. Using CCE calculations up to the second order, without quadrupole tensors included, we estimated the thickness of the qubit host at which the coherence time is determined purely by the host spin bath. We found a lower bound of ≈ 20 nm for MoS_2 and ≈ 80 nm for WS_2, respectively.

9.1.4 Conclusions

In sum, we presented a theoretical study of the influence of the environment on the coherence time of spin qubits in 2D materials. We found that both the nuclear spins of the substrate and those of the host 2DM can act as sources of decoherence for the qubit. Our results show that the composition of van-der-Waals heterostructures encapsulating the qubit may be engineered to obtain longer coherence times.

Our calculations also revealed a complex behavior of the Hahn-echo coherence time as a function of the thickness of the 2D material hosting the qubit. For thin hosts ($\Delta \leq 5$ nm) it is possible to identify specifically which pairs of spins give rise to the oscillations observed in the Hahn-echo decay time. This result points at the possibility of using the electron spin of the qubit as a sensor of dipolar couplings within the 2D nuclear bath[140, 179]. For thicker hosts ($\Delta \geq 10$ nm), we observed a transition from a quantum to a classical regime of the induced decoherence, which might be revealed experimentally by using. e.g. a NV center in diamond as a quantum sensor[180, 181].

Finally we note that for the 2DMs investigated here, other decoherence channels (spin-orbit, spin-phonon interactions [182–184]) exist, which may play a significant role at nonzero temperatures. Their contribution to decoherence needs to be carefully assessed in the future. Although we focused only on the interaction of the spin defect with the nuclear spin bath, our results point at the importance of the substrate and its composition in the design of 2DMs and van-der-Waals heterostructures for quantum applications.

9.2 Detecting spin bath polarization with quantum quench phase shifts of single spins in diamond

This section is adapted from the submitted work [10].

Single-qubit sensing protocols can be used to measure qubit-bath coupling parameters. However, for sufficiently large coupling, the sensing protocol itself perturbs the bath, which is predicted to result in a characteristic response in the sensing measurements. Here, we observe this bath perturbation, also known as a quantum quench, by preparing the nuclear spin bath of a nitrogen-vacancy (NV) center in polarized initial states and performing phase-resolved spin echo measurements on the NV electron spin. These measurements reveal a time-dependent phase determined by the initial state of the bath. We derive the relationship between sensor phase and Gaussian spin bath polarization, and apply it to reconstruct both the axial and transverse polarization components. Using this insight, we optimize the transfer efficiency of our dynamic nuclear polarization sequence. This technique for directly measuring bath polarization may assist in preparing high-fidelity quantum memory states, improving nanoscale NMR methods, and investigating non-Gaussian quantum baths.

9.2.1 NV Center Characterization and Polarization

To experimentally investigate the quantum quench-induced phase shift (QPS), we study single NV centers in natural isotope abundance IIa diamond at room temperature.

In order to study Gaussian bath dynamics, we identify single NV centers with suitably weak hyperfine couplings. In a perturbative treatment, the Gaussian approximation holds for $\tau < |A_{\parallel,j}|^{-1}, (A_{\perp,j})^{-1}$ for all spins, and when $\max_j |A_{\parallel(\perp),j}| \ll \omega_L$. Due to the stochastic distribution of ^{13}C spins around each NV center, some defects have strongly coupled nuclei, which is unfavorable for these criteria. Ideally, a spin-free volume surrounds the NV center, as in Fig. 9.5(a). Ref. [185] calculated a minimum spin-free radius of 0.5 nm for the bath

to appear Gaussian at moderate magnetic fields. We filter candidate NVs based on narrow optically detected magnetic resonance (ODMR) spectra, as in Fig. 9.5(b), which indicates relatively weak total bath interactions and an absence of individual couplings larger than the linewidth.

We select two NV centers with suitable local spin baths, NV A (FWHM linewidth 221(6) kHz) and NV B (284(14) kHz). To fully characterize the respective nuclear spin environments, we apply the XY8 pulse sequence to each NV center to map out hyperfine coupling parameters. Specifically, the XY8-2 sequence with 16 total π pulses isolates resonant features in the coherence envelope of the NV center corresponding to the hyperfine interaction with distinct nuclear spins [186, 187]. Fig. 9.5(c) shows the coherence data for NV A, and the best-fit parameters for both NVs are displayed in Table 9.1. The data show that both NVs are sufficiently distant from the closest nuclear spins to make the Gaussian approximation reliable for roughly one nuclear Larmor period $T_L = 2\pi\omega_L^{-1}$. Using the fit parameters for individual hyperfine couplings, we can compute ϵ for each NV based on Eq. (9.18), and find estimated $\tilde{\epsilon}_A = 0.094$ and $\tilde{\epsilon}_B = 0.77$. Using NVs A and B, we investigate the appearance of phase shifts during spin echo experiments. Since the QPS is only predicted to arise with nonzero bath polarization, each measurement involves preparing the initial state of the bath.

The nuclear hyperfine parameters were extracted as follows. First, using the PyCCE [108] package we generated 10^4 random nuclear spin configurations and computed their expected XY8 signal. For each of the experimentally available NVs, we found a closest matching random nuclear spin configuration and used it as an initial guess for the fitting procedure. We then fit the experimental coherence to the analytical expression [186]:

$$\langle X \rangle = \prod_i 1 - \left(1 - \hat{n}_0^{(i)} \hat{n}_{-1}^{(i)}\right) \sin^2 \frac{N\phi_i}{2}, \tag{9.8}$$

where

$$\cos\phi_i = \cos\alpha_i \cos\beta_i - m_z^{(i)} \sin\alpha_i \sin\beta_i, \tag{9.9}$$

$$1 - \hat{n}_0^{(i)} \hat{n}_{-1}^{(i)} = \left(m_x^{(i)}\right)^2 \frac{(1-\cos\alpha_i)(1-\cos\beta_i)}{1+\cos\phi_i}. \tag{9.10}$$

Here, $m_x^{(i)} = \frac{a_\perp^{(i)}}{\tilde{w}^{(i)}}$ and $m_z^{(i)} = \frac{a_\parallel^{(i)} + w_L}{\tilde{w}^{(i)}}$ using $\tilde{w}^{(i)} = \sqrt{(a_\parallel^{(i)} + w_L)^2 + (a_\perp^{(i)})^2}$; angles are $\alpha_i = \tilde{w}^{(i)}\tau$, $\beta_i = w_L\tau$ for each ith nuclear spin.

Starting from one nuclear spin, we increase number of spins by one in the fitting procedure until the fit deviation from the experimental data stops decreasing. We then check the robustness of the fit by removing each of the identified nuclear spins in turn, and for all remaining nuclear spins we check whether the identified parameters have shifted. Only the nuclear spins which are validated with the leave-one-out procedure are reported.

9.2.2 Origin of the NV Center Quench Phase Shift

First, we describe how a quantum quench phase arises in NV center spin echo experiments. The NV center has a spin-1 electronic ground state, and an external magnetic field is applied along its quantization axis. The NV's ^{14}N nucleus is also spin-1, but is polarized when the applied field is well-aligned [188], as in this work, and does not affect the electron spin dynamics. In natural isotopic samples, each NV is also surrounded by a 1.1%-abundant bath of spin-$\frac{1}{2}$ ^{13}C nuclear spins. The relevant combined NV-bath spin Hamiltonian can be

written in terms of NV electron spin $\hat{S}_\alpha$ and nuclear spin $\hat{I}_{\alpha,j}$ ($\alpha = x, y, z$) operators as

$$\hat{H} = \hat{H}_{NV} + \hat{H}_{bath} + \hat{H}_{int}, \tag{9.11}$$

$$\hat{H}_{NV} = D\hat{S}_z^2 + \gamma_e B_0 \hat{S}_z, \tag{9.12}$$

$$\hat{H}_{bath} = \gamma_n B_0 \sum_j \hat{I}_{z,j}, \tag{9.13}$$

$$\hat{H}_{int} = \sum_j \hat{\mathbf{S}} \cdot A_j \cdot \hat{\mathbf{I}}_j, \tag{9.14}$$

where $D = 2\pi \times 2.87\,\text{GHz}$ is the zero-field splitting, γ_e and γ_n are the electron and nuclear gyromagnetic ratios, and A_j is the hyperfine tensor for the jth nuclear spin. Nuclear-nuclear interactions are relatively weak ($\propto \gamma_n^2$) and can be neglected on the timescales of our experiments. In this work, the electron level splitting dominates all energy scales, so the secular approximation can be applied to recast the hyperfine terms into parallel (axial) and perpendicular (transverse) terms for each nuclear spin as

$$\hat{H}_{int} = \hat{S}_z \left(\sum_j A_{\parallel,j} \hat{I}_{z,j} + A_{\perp,j} \hat{I}_{x,j} \right). \tag{9.15}$$

From the perspective of bath spins, $\hat{H}_{int}$ is often described as the NV-state-dependent hyperfine field. With $\hat{H}_{int} \propto \hat{S}_z$, the system is well approximated by pure dephasing models. To simplify the problem further, we focus on nuclear spin environments that can be well approximated as Gaussian baths. This limit is best satisfied for baths with many spins, each weakly coupled to the central NV spin. For a given NV center and ^{13}C distribution, the Gaussian approximation holds for a time $\tau \lesssim \left(\max_j |A_{\parallel(\perp),j}|\right)^{-1}$. Operating in a pure-dephasing, Gaussian bath regime enables the application of analytic QPS calculations for our system.

Eq. (9.15) makes clear that an NV spin echo sequence produces an effective quantum quench on the nuclear spin environment. At initialization and as long as the NV remains

in $|0\rangle$, $\hat{H}_{int}$ vanishes, and the bath evolves purely under $\hat{H}_{bath}$. However, when the NV is rotated to a superposition state, $\hat{H}_{int}$ once again contributes to bath dynamics. While the consequences of Eq. (9.15) have been studied and used for nuclear spin sensing and control, the quench dynamics which follow from the sudden activation of $\hat{H}_{int}$ have only recently been explored. As shown in Ref. [189], a quench will occur whenever $[\hat{\rho}_{b,i}, \hat{H}_{bath} + \mathrm{Tr}_{NV}(\hat{H}_{int})/2] \neq 0$, with initial bath density matrix $\hat{\rho}_{b,i}$ and Tr_{NV} denoting partial trace over the NV degrees of freedom. The principal consequence of this quench for spin echo measurements is an additional phase on the final state. Conceptually, this phase arises because the change in bath dynamics conditional on the qubit state creates a net average field from the bath. Concretely, in the NV-bath system, any bath spins initially oriented along the z axis are stationary while the NV state is $|0\rangle$. When the NV state changes, the bath spins begin precessing around a tilted axis due to the $A_{\perp,j}\hat{S}_z\hat{I}_{x,j}$ terms. The precessing bath spins can then induce phase accumulation on an NV superposition state.

Spin echo spectroscopy experiments typically investigate a system by mapping out its coherence function. We can rewrite a generic coherence function $W(\tau)$ as

$$\begin{aligned} W(\tau) &\equiv \frac{\langle\hat{\sigma}_-(\tau)\rangle}{\langle\hat{\sigma}_-(0)\rangle} \equiv \langle X\rangle - i\langle Y\rangle \\ &= e^{-\chi(\tau)-i\Phi(\tau)}. \end{aligned} \tag{9.16}$$

Here, $\hat{\sigma}_- \equiv (\hat{\sigma}_x - i\hat{\sigma}_y)/2$ denotes the spin lowering operator, X/Y are Bloch vector components, and χ and Φ parameterize qubit coherence and phase evolution, respectively. The physical processes which determine $\langle X\rangle = e^{-\chi}\cos\Phi$ have been thoroughly examined in previous studies, finding χ to be a function of the bath noise spectral density and the filter function of the echo sequence. In the case where the NV undergoes a single (Hahn) spin echo in the presence of a Gaussian spin bath described by Eq. (9.11), this has a simple analytic

formula,

$$\chi(\tau) = 2\epsilon \sin^4\left(\frac{\omega_L \tau}{4}\right), \tag{9.17}$$

where ω_L is the Larmor frequency of the bath spins. The strength of the qubit-bath coupling is parameterized with the dimensionless quantity

$$\epsilon \equiv \frac{\sum_j A_{\perp,j}^2}{\omega_L^2}. \tag{9.18}$$

Note that χ is independent of the bath state. The corresponding oscillations in $\langle X \rangle$ have been observed in numerous experiments. In contrast, Φ is usually found to vanish, reflected in an absence of signal when measuring $\langle Y \rangle = e^{-\chi} \sin \Phi$. We show that nonzero Φ can provide extensive information on the bath state.

We derive two contributions to Φ, one being the QPS, and both attributable to bath spin polarization. The QPS, denoted Φ_q, can be derived using a linear response approach to be

$$\Phi_q(\tau) = \bar{p}_z \epsilon \sin^2\left(\frac{\omega_L \tau}{4}\right) \sin\left(\frac{\omega_L \tau}{2}\right). \tag{9.19}$$

Here, $\bar{p}_z$ is the coupling-weighted axial polarization of the bath,

$$\bar{p}_z \equiv \frac{\sum_j p_{z,j} A_{\perp,j}^2}{\sum_j A_{\perp,j}^2}, \tag{9.20}$$

where $p_{z,j} \in [-1, 1]$ is the axial polarization of the jth nuclear spin. If ω_L is known or the τ-dependence is characterized, Φ_q is determined by only $\bar{p}_z$ and ϵ. Since ϵ can be characterized independently via Eq. (9.17), measuring Φ_q provides a direct readout of the axial spin polarization in the local bath.

A second contribution to Φ originates from transverse bath spin polarization. Analogous to a phase generated by nearby precessing classical magnetic moments, we label this term Φ_m. Defining $p_{x,j}$ and $p_{y,j}$ in accordance with $p_{z,j}$, Φ_m enters to first order with hyperfine

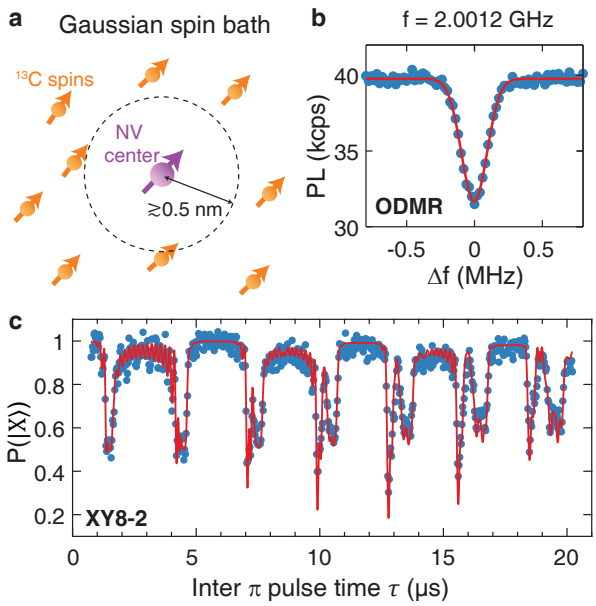

Figure 9.5: (a) The ^{13}C spin bath surrounding a nitrogen-vacancy (NV) center in diamond can act as a Gaussian bath if no spins are closer than $\approx 0.5\,\text{nm}$ to the NV center. By polarizing the bath spins, a polarization-dependent phase appears in NV spin echo measurements, which we observe and analyze under a Gaussian framework. (b) Optically detected magnetic resonance of the NV center corresponding to the $m_I = 1$ nitrogen nuclear spin state. The FWHM is $2\pi\times$ 221(6) kHz, and the single resonance indicates an absence of strongly coupled spins. PL: photoluminescence. (c) Coherence revivals for NV A during an XY8-2 sequence (16 pulses). Fits to the data are used to extract nearby spin coupling parameters, collected in Table 1, and confirm the environment is sufficiently Gaussian.

couplings:

$$\Phi_m(\tau) = \frac{2\sin^2\left(\frac{\omega_L\tau}{4}\right)}{\omega_L}\times \sum_j A_{\perp,j}\left(p_{x,j}\sin\left(\frac{\omega_L\tau}{2}\right) + p_{y,j}\cos\left(\frac{\omega_L\tau}{2}\right)\right). \tag{9.21}$$

Here, we calculate Φ_m for a single sensor spin coupled to a Gaussian spin bath. A key step in measuring the QPS is distinguishing Φ_q from Φ_m, since Φ_m features leading-order hyperfine terms while Φ_q is second-order in the couplings, and in general experimental systems exhibit nonzero transverse polarization. As we later show, the distinct physical sources of phase allow us to separate them and extract information about the bath.

NV	^{13}C #	$A_{\parallel}$ (kHz)	$A_{\perp}$ (kHz)	θ (deg)	r (nm)
	1	28.7(3)	81(1)	71	0.77
	2	29.0(1)	46.9(9)	77	0.83
A	3	-9.8(2)	27.1(7)	35	1.27
	4	0.3(4)	23(1)	55	1.34
	5	11.4(4)	20.2(9)	76	1.13
	1	-0.1(7)	177(1)	55	0.68
	2	-39.4(7)	148(1)	40	0.73
	3	87.9(4)	122(1)	102	0.58
B	4	-30.0(2)	80.5(9)	34	0.88
	5	-16.0(3)	72(1)	42	0.94
	6	51.7(7)	58(2)	100	0.71
	7	-0.1(6)	45(1)	55	1.08

Table 9.1: Parallel ($A_{\parallel}$) and perpendicular ($A_{\perp}$) ^{13}C hyperfine parameters obtained from XY8 measurements as in Fig. 9.5(c). Approximate values of θ (azimuthal angle) and r (NV-nuclear displacement) are calculated assuming pure dipole-dipole interactions.

9.2.3 Spin Echoes with Polarized Nuclear Baths

We use the Nuclear Orientation Via Electron spin-Locking (NOVEL) sequence [190] to polarize the nearby nuclear spins. The NV is optically polarized to $|0\rangle$ and rotated to $|\pm X\rangle = (|0\rangle \pm |-1\rangle)/2$ prior to a spin-locking pulse of duration t_{SL}. When the Rabi frequency of the spin-locking pulse, Ω_{SL}, matches ω_L, resonant exchange occurs between the NV and coupled ^{13}C nuclei. This exchange is shown in Fig. 9.6(b), where the $|X\rangle$ state is measured after a single NOVEL pulse. The electron-nuclear resonance appears at the expected $\gamma_n B_0 = 2\pi\times$ 335 kHz. By repeating the NOVEL subsequence, polarization accumulates in the bath and persists for much longer than the spin echo timescale of tens of microseconds. The sign of the polarization transfer is determined by the choice of initial NV center state ($|\pm X\rangle$), providing a simple means to invert the bath polarization.

With a polarized bath, NV spin echo measurements exhibit additional oscillations. The basic measurement framework is illustrated in Fig. 9.6(a), and consists of alternating steps

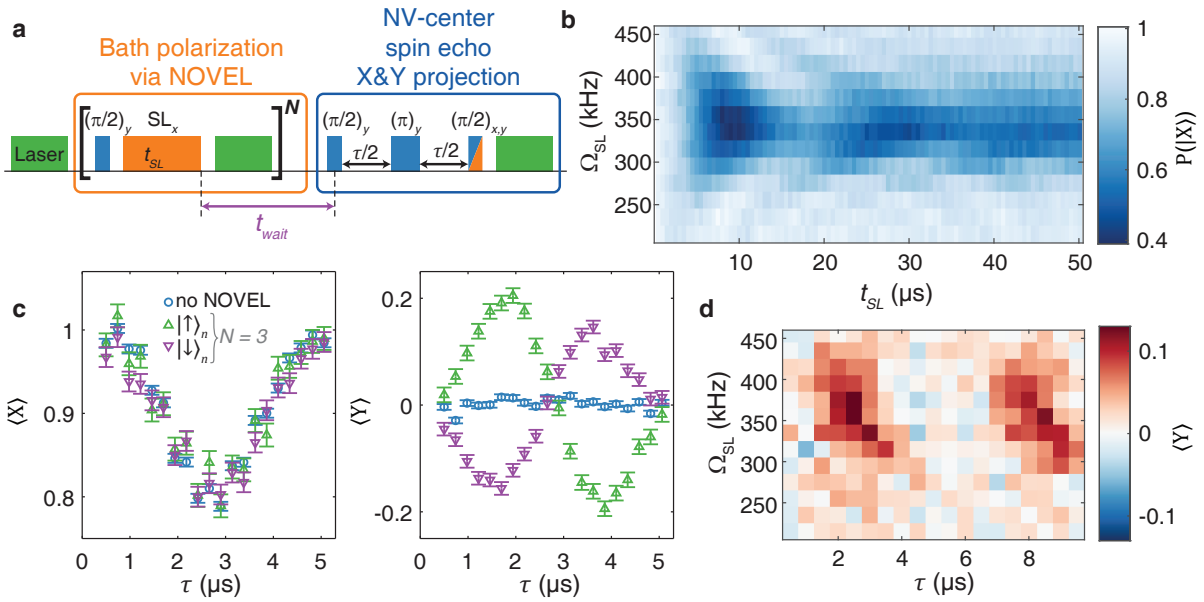

Figure 9.6: NV center phase shifts appear when the bath is polarized. (a) Initial bath preparation and measurement sequence. N NOVEL repetitions transfer polarization from the NV center to nearby nuclear spins, followed by phase-resolved spin echoes (PSE) to measure both $\langle X\rangle$ and $\langle Y\rangle$ components of the NV electron spin. (b) NV-bath oscillations during a single NOVEL pulse, after the NV is initialized to $|X\rangle$. Maximal polarization transfer is observed when $\Omega_{SL} = \omega_L = 2\pi\times$ 335 kHz. (c) On resonance, no discernible difference is observed in $\langle X\rangle$ (left), but $\langle Y\rangle$ (right) shows bath-polarization-dependent oscillations. (d) Using $t_{SL} = 4\,\mu$s, $N = 3$, and preparing the bath into $|\uparrow\rangle$, a phase appears with nuclear Larmor periodicity, but only near resonance. All data shown is taken on NV A.

that polarize the bath to a steady state and perform spin echo measurements. After N repetitions of NOVEL re-establish steady-state polarization, we reinitialize the NV to $|0\rangle$ and initiate the spin echo after a delay of t_{wait}. Using different phases for the spin echo readout pulse, we measure the $\pm X$ and $\pm Y$ components of the final state to reconstruct the amplitude and phase – a phase-resolved spin echo (PSE). The combined NOVEL+PSE sequence is then repeated 10^6-10^7 times to record average statistics. Conventionally, only $\langle X\rangle$ is measured in an echo experiment, with NV-bath interactions producing coherence oscillations resembling the blue data of Fig. 9.6(c). With a high-temperature bath, $\langle Y\rangle$ provides no additional information. However, when the bath is polarized ($N = 3$, green/purple curves), clear oscillations in $\langle Y\rangle$ appear on the timescale of the Larmor period. These phase oscillations

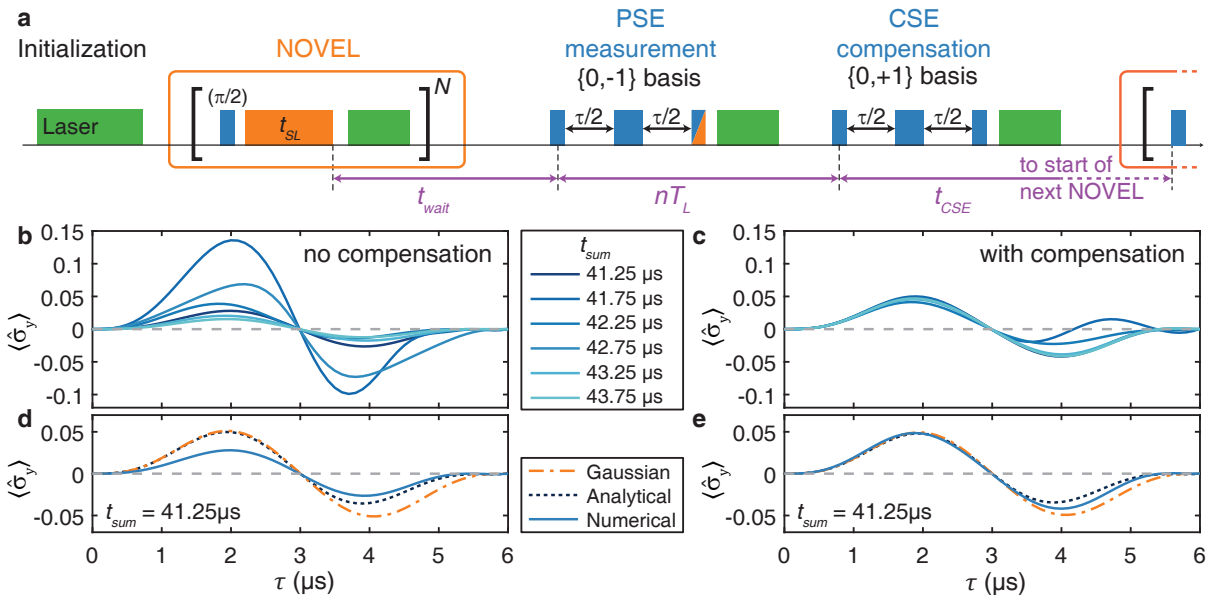

Figure 9.7: Compensated measurement sequences ensure robust QPS detection. (a) Over many repetitions, the NV-bath coupling during PSE measurement alters the equilibrium bath polarization, but this effect can be minimized by following it with a non-measurement, compensating spin echo (CSE) in the opposite triplet basis. The CSE begins a multiple of the Larmor period (T_L) after the start of the PSE. (b) Without CSE pulses, numerical simulations of NV A show the equilibrium bath polarization and resulting PSE signal $\langle\hat{\sigma}_y\rangle$ are strongly affected by $t_{sum} = t_{wait} + nT_L + t_{CSE}$, obscuring the quench phase shift Φ_q. (c) When CSE is included, the bath polarization is robust against changing sequence parameters. Deviations only become significant when the Gaussian approximation falters at longer τ, approximately 3 μs for NV A. (d,e) Without CSE pulses, the PSE may not capture Φ_q accurately, even within the valid Gaussian approximation regime. With CSE pulses, the exact numerical results agree with the Gaussian approximation until the approximation begins to deviate from analytical expectations. For the measurements in this work, $\langle Y\rangle = \langle\hat{\sigma}_y\rangle$.

follow the sign of the bath polarization (Fig. 9.6(c)) and are correlated with the spin-locking resonance (Fig. 9.6(d)), clearly linking their origin to the polarized bath spins. Note that $\langle X\rangle$ shows no difference regardless of bath polarization; for Gaussian baths, polarization has an imperceptible effect on this projection. Since ϵ is independent of the bath state, we fit the $\langle X\rangle$ data for each NV to Eq. (9.17), resulting in measured values $\epsilon_A = 0.110(9)$ and $\epsilon_B = 0.68(5)$. These values are in good agreement with the estimations $\tilde{\epsilon}_A$ and $\tilde{\epsilon}_B$ from Sec. 9.2.1, increasing confidence in the extracted hyperfine parameters.

Before quantifying and further investigating the spin echo dynamics, we refine the measurement protocol to robustly extract the QPS. Since the combined measurement sequence modifies the spin bath by design, the PSE sequence necessarily alters the bath preparation entering the next repetition of the experiment. This can produce a confounding effect when sweeping a spin echo or NOVEL parameter, as we demonstrate through numerical simulations. In Fig. 9.7, we simulate the exact spin dynamics of NV A and its nearby ^{13}C spins, using the measured hyperfine parameters, while evolving under the preparation and measurement sequence of Fig. 9.7(a). The simulated sequence is repeated until the bath reaches a steady state. We calculate $\langle\hat{\sigma}_y\rangle$, which is equal to $\langle Y\rangle$ for our measurements. Each trace is an average over a range of t_{wait} to reduce the effects of nuclear precession, which isolates the Φ_q component, as will be addressed in more detail in Section 9.2.5. In Fig. 9.7(b), we begin by incorporating only the NOVEL and PSE elements, followed by a variable wait period. We define t_{sum} as the interval between the Nth NOVEL pulse and the first NOVEL pulse of the next repetition. Despite only changing t_{sum}, i.e., varying the wait time between repetitions, we note dramatic changes in the behavior of $\langle\hat{\sigma}_y\rangle$. This indicates the steady-state bath polarization can strongly depend on the measurement parameters in addition to the NOVEL parameters.

To mitigate this effect, we introduce a second, non-measurement spin echo performed on the $\{0,+1\}$ basis following the PSE in the $\{0,-1\}$ basis, which we refer to as a compensating spin echo (CSE). Because of the symmetry between the $|\pm1\rangle$ states, the net effect of the CSE is to reverse the PSE's perturbation on the bath state to lowest order. Importantly, for the most effective compensation, the initial pulses of the PSE and CSE are separated by a multiple of T_L, so that the bath spins are close to their state at the beginning of the PSE. The benefit of compensation is shown in Fig. 9.7(c), where the simulations are repeated including the CSE. The echo signal is observed to be robust, indicating a bath state which is not sensitive to parameters in the measurement sequence. At large τ, the computed $\langle\hat{\sigma}_y\rangle$

does eventually exhibit noticeable difference for different t_{sum}, but only after the Gaussian approximation begins to break down. Heuristically, the PSE and CSE can each be viewed as performing a 'pulse' on the surrounding bath. While the effect of the first such pulse may be complicated in general, the bath can be restored to approximately its initial state by performing an inverse pulse with appropriate timing.

In addition to establishing the robustness of the augmented measurement protocol, we confirm that it accurately quantifies the QPS. Figs. 9.7(d) and 9.7(e) show three separate calculations of $\langle\hat{\sigma}_y\rangle$ for $t_{sum} = 41.25\,\mu s$. These calculations each stem from the same simulation of the NV A spin cluster, but incorporate the steady-state bath polarization components $\bar{p}_z$ and $p_\perp = \sqrt{p_x^2 + p_y^2}$ (at the start of the PSE) in different ways, as follows:

(i) The Gaussian curve (dashed orange) plots the QPS signal for a Gaussian bath with $\epsilon = \epsilon_A$ and $\bar{p}_z$ only.

(ii) The analytical curve (dotted black) plots the exact dynamics for $\bar{p}_z$ only.

(iii) The numerical curve (solid blue) plots the exact dynamics including both $\bar{p}_z$ and $p_\perp$.

Without the CSE (Fig. 9.7(d)), the $\langle\hat{\sigma}_y\rangle$ signal is biased by $p_\perp$ contributions and differs from Φ_q by roughly a factor of 2. Including the CSE (Fig. 9.7(e)) eliminates the bias, indicating that Φ_q can be extracted by averaging over t_{wait}. These simulations also confirm that the Gaussian approximation is reliable for $\tau \lesssim 3\,\mu s$. In ensuing experiments, we use the full compensated PSE sequence to quantify Φ_m and Φ_q.

9.2.4 Simulations details

All simulations were carried out by numerically diagonalizing the time-independent model Hamiltonian and computing the corresponding propagators for each of the parts of the pulse sequence. Control pulses on the NV and NV reinitialization via laser pulse were assumed

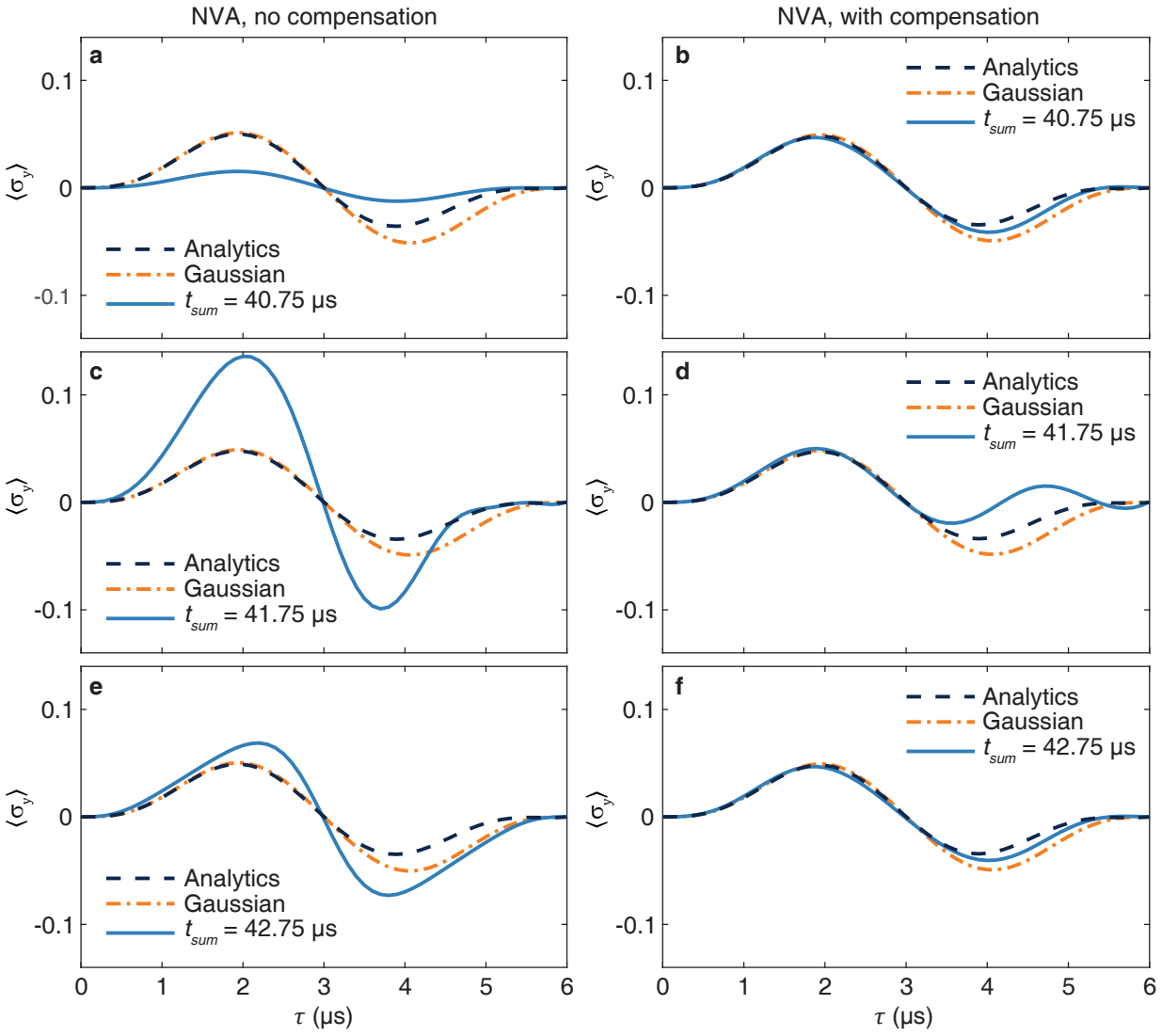

Figure 9.8: Simulations comparing the analytics, Gaussian, and numerics for the uncompensated (a,c,e) and compensated pulses (c,d,f) at three different values of t_{sum}

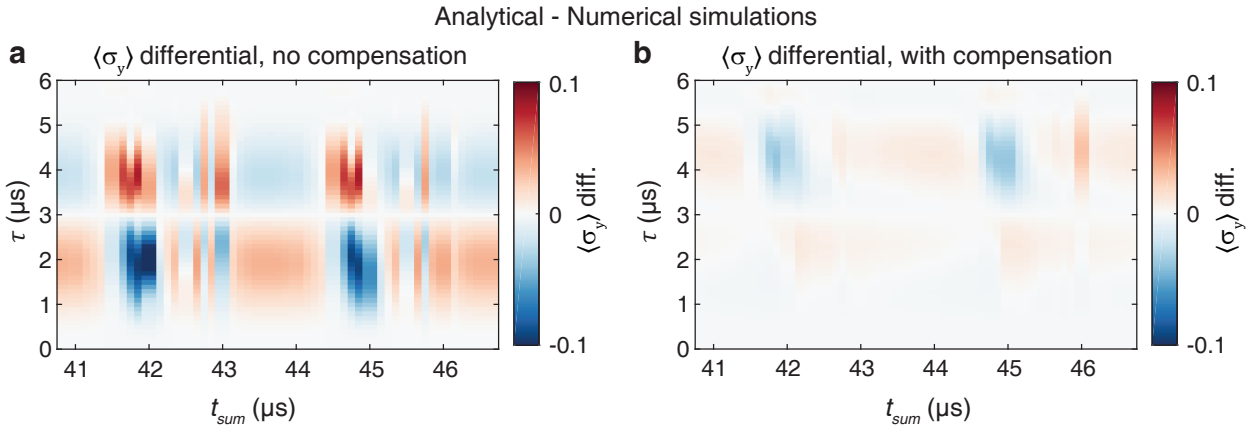

Figure 9.9: Colormap showing the $\langle \hat{\sigma}_y \rangle$ differential between analytical and numerical simulations for the uncompensated (a) and compensated (b) sequence.

to be instantaneous, and rotating wave approximation was used for the NOVEL sequence. Interactions between nuclear spins were neglected.

To recover the steady-state polarization, each simulation included 50 cycles of the full experiment (5 NOVEL periods, PSE sequence, and CSE sequence when applicable). The nuclear and electron states, used in Figure 3, are recorded at the last cycle. The simulation included the following parameters: t_{wait} was varied between 5 and 20.6 μs, $t_{SL} = 3$ μs, $nT_L = 6$ μs.

Figures 9.8 and 9.9 show additional numerical data for the effect of compensating pulse at the phase signal of NV A. We observe a great match between numerical predictions using the whole sequence and analytical equations using the quench phase only when compensating pulse is applied. In the absence of compensating pulse, the behavior of the numerical curve deviates from the analytical expressions and thus cannot be used to recover the properties of the bath.

9.2.5 Phase Shift Measurements

Using the measurement sequence of Fig. 9.7(a), we observe phase shifts on our single NV centers which correspond to the polarization and precession of the nuclear spin bath. In

Fig. 9.10(a) (NV A) and 9.10(b) (NV B), we vary t_{wait} while holding all other sequence parameters constant. We choose $\tau = \pi/\omega_L = 1.5\,\mu s$, which maintains large signal while simplifying Eqs. (9.19) and (9.21) to

$$\Phi_q\left(\tau = \frac{\pi}{\omega_L}\right) = \frac{\bar{p}_z \epsilon}{2}, \tag{9.22}$$

$$\Phi_m\left(\tau = \frac{\pi}{\omega_L}\right) = \frac{1}{\omega_L}\sum_j A_{\perp,j}\; p_{x,j}. \tag{9.23}$$

The resulting oscillations match ω_L and arise from the precession of the nuclear spin state after the final NOVEL pulse. The NOVEL preparation gives rise to $p_\perp > 0$ through two mechanisms: appreciable $A_\parallel$ components relative to ω_L, and spin-locking in the asymmetric $\{|0\rangle, |-1\rangle\}$ basis. The latter is particularly easy to overlook for the NV center, since its triplet structure is often reduced to a two-level system to simplify calculations. As described by Eq. (9.21), any transverse polarization produces a $\langle Y \rangle$ signal. After the final NOVEL pulse, the initial transverse polarization will precess during t_{wait} between p_x and p_y:

$$\begin{aligned} p_{x,j} &= p_{\perp,j} \cos\left(\omega_L t_{wait} + \varphi_j\right), \\ p_{y,j} &= p_{\perp,j} \sin\left(\omega_L t_{wait} + \varphi_j\right). \end{aligned} \tag{9.24}$$

φ is the initial phase of the transverse polarization. Previously, related oscillations have been detected in ensemble experiments [191, 192], but are observed here at the single-NV level and quantified in a Gaussian framework. Combining Eq. (9.23) with the parameters in Table 9.1, and assuming a uniform initial bath polarization via $p_{\perp,j} = \tilde{p}_\perp$, $\varphi_j = \varphi$, we can estimate the mean transverse polarization $\tilde{p}_\perp$. By fitting the oscillations, we find $\tilde{p}_\perp = 0.32(1)$ for NV A using $t_{SL} = 3.75\,\mu s$, and $0.107(5)$ for NV B using $t_{SL} = 4.5\,\mu s$ (purple data sets of Figs. 9.10(a) and 9.10(b)). By tuning t_{SL}, we minimize $\tilde{p}_\perp$ (Fig. 9.10(d)), achieving $\tilde{p}_\perp = 0.003(15)$ for NV A and $0.004(4)$ for NV B. These measurements do not suffice to uniquely determine the transverse polarization of each nearby nuclear spin, but do

provide a means of rapidly estimating it with a single quantity – the oscillation amplitude – to adjust for nonideal behavior in polarization sequences. Even without quantifying the bath's hyperfine constants, this metric provides qualitative feedback when optimizing bath preparation sequence parameters.

Within the same PSE data set, we observe the QPS and use it to quantify $\bar{p}_z$. In addition to the oscillating Φ_m component, we detect a constant phase offset as a function of t_{wait}. Φ_q is independent of t_{wait}, since decay of nuclear polarization is negligible on the timescale of t_{wait}. The Φ_m component of Φ can be canceled by averaging $\langle Y \rangle$ over t_{wait} or, equivalently, fitting the $\langle Y \rangle$ oscillations to an offset. Thus, both Φ_m and $\Phi_q \propto \bar{p}_z \epsilon$ can be fit simultaneously to $\langle Y \rangle = e^{-\chi} \sin \Phi$, using the previously measured ϵ. For the optimal values of t_{SL} (green data sets), we measure $\bar{p}_{(z,A)} = 1.00(11)$ and $\bar{p}_{(z,B)} = 0.77(2)$.

The observed Φ_q exhibits the predicted QPS characteristics. Φ_q is sensitive to the direction of bath polarization, as in Fig. 9.10a, where the offset inverts along with the bath state. When transverse polarization is present, sweeping t_{wait} is necessary to confirm the sign of the offset, since $|\Phi_m|$ can exceed $|\Phi_q|$. Alternatively, with fixed t_{wait}, τ can be swept to map the $\Phi(\tau)$. Both $\langle X \rangle$ and $\langle Y \rangle$ are needed to correctly calculate $|W| \equiv e^{-\chi}$ and Φ. In Figs. 9.10(e) and 9.10(f), the fits to Φ_q for both NVs with minimized $\tilde{p}_\perp$ show that Φ_q closely matches the predicted dynamics of Eqs. (9.17) and (9.19).

As with $\tilde{p}_\perp$, we examine the dependence of $\bar{p}_z$ on t_{SL}. In Fig. 9.10(c), both NVs exhibit similar trends: $\bar{p}_z$ improves where $t_{SL} \sim T_L$, and is reduced where $\tilde{p}_\perp$ is largest. While predicting t_{SL} dependence in general requires knowledge of the spin bath, PSE measurements offer a simple method to investigate parameter sensitivity without exhaustively characterizing the bath. $\bar{p}_z$ exceeding unity is observed for NV A, and can be attributed to uncertainty in ϵ_A, which is used as a constant for calculating all $\bar{p}_{z,A}$ values. The confidence intervals for NV A are larger than NV B since the QPS is smaller for A, leading to larger fractional uncertainty.

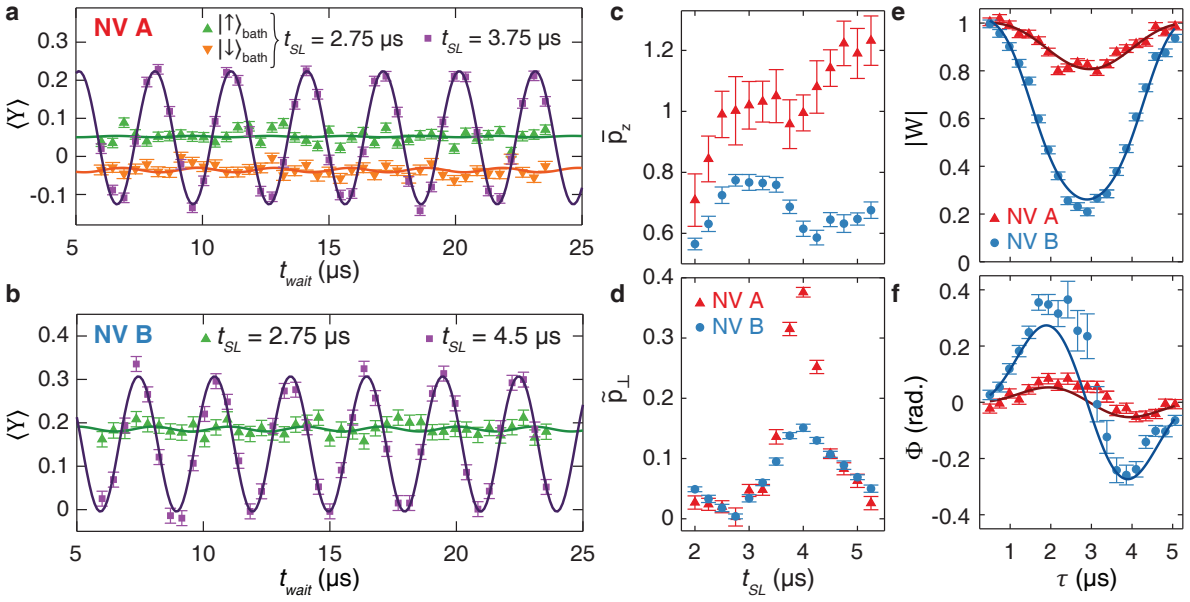

Figure 9.10: Observation of quench phase shifts and corresponding polarization measurements. (a,b) Phase evolution with τ =1.5 µs on NVs A (a) and B (b) with respect to t_{wait}, and for several t_{SL}. The oscillations correspond to the precession of transverse nuclear polarization, manifesting in an oscillating Φ_m as described in Eqs. (9.21) and (9.24). The constant offset is $\Phi_q \propto \bar{p}_z$. NV B, with stronger hyperfine couplings, exhibits both larger Φ_m and Φ_q. (c,d) The bath polarization state is optimized by tuning t_{SL}. Each point is determined by fitting a sweep of t_{wait}, as in (a,b), to the combined Eqs. (9.19), (9.21), and (9.24). (e,f) The time evolution of the coherence magnitude $|W|$ and Φ, fit to Eq. (9.19), with $\tilde{p}_\perp$ minimized for each NV using t_{SL} =2.75 µs.

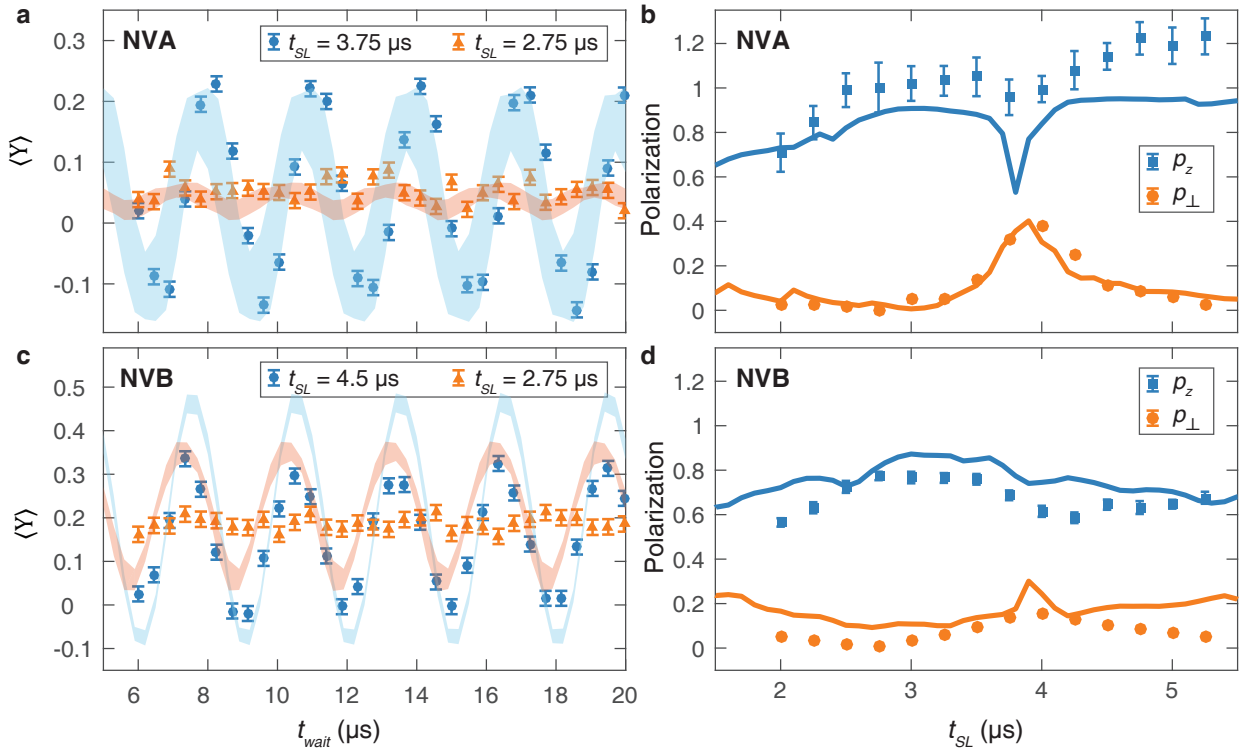

Figure 9.11: Simulations for the experiments in the Figure 9.10. Phase evolution with τ =1.5 μs on NVs A (a) and B (c) as with respect to t_{wait}, and for several t_{SL}. Points represent experimental results, shaded areas - calculations for varied t_{sum}. Bath polarization for NVs A (b) and B (d). Solid lines represent numerical simulations, points represent experimental data.

Figure 9.11 shows numerical simulations in comparison with the results from Fig. 9.10. We observe an excellent agreement for NV A in both the observed signal ($\langle Y \rangle$) and derived quantities ($\tilde{p}_\perp$ and $\bar{p}_z$.). Still, we note that the parallel polarization seems to be overestimated in the experiment by about 20%, at all data points. The overestimation stems likely from the uncertainty in the value of ϵ.

NV B shows worse agreement with the theory in the $\langle Y \rangle$ simulations, hinting that not all relevant nuclear spins were determined with dynamical decoupling spectroscopy, or the internuclear interactions play non-negligible role.

Overall, we have used single NV centers in diamond to observe a periodic phase shift which arises in spin echo measurements due to axial polarization of surrounding nuclear

bath spins. This quantum quench phase shift has been predicted previously through linear response calculations of Gaussian spin baths, and arises due to the bath Hamiltonian's dependence on the qubit state. We have extended the existing theory by calculating the effects of transverse polarization and multiple spin echo pulses, which are relevant to experimental implementations. A critical step in observing the quench phase was introducing a pulse sequence to minimize changes to the bath polarization due to many repetitions of the measurement protocol.

CHAPTER 10

PREDICTIVE METHODS FOR LOW-DIMENSIONAL ELECTRON SPIN BATH SYNTHESIS IN DIAMOND.

This chapter is adapted from the early draft of [12].

The nitrogen vacancy (NV) center in diamond, a well-studied, optically active spin defect, is the prototypical system in many state-of-the-art quantum sensing and communication applications. In addition to the enticing properties intrinsic to the NV center, its diamond host's nuclear and electronic spin baths can be leveraged as resources for quantum information, rather than allowed to act solely as decoherence sources. However, current synthesis approaches result in stochastic defect spin positions, reducing the technology's potential for deterministic control and yield of NV-spin bath systems, as well as scalability and integration with other technologies. In this chapter, we demonstrate the use of theoretical calculations of central spin decoherence as an integral part of an NV-spin bath synthesis workflow, providing a path forward for the quantitative design of NV center-based quantum sensing systems. We use computationally generated coherence data to characterize the properties of single NV qubits across relevant growth parameters to find general trends in coherence time distributions dependent on spin bath dimensionality and density. We then build a maximum likelihood estimator with our theoretical model, enabling the characterization of a test sample through NV T_2^* measurements. Finally, we explore the impact of dimensionality on the yield of strongly coupled electron spin systems. The methods presented herein are general and applicable to other qubit platforms that can be appropriately simulated.

10.1 Introduction

Defect color centers in diamond [193, 194] have been demonstrated as quantum magnetometers [195–203] and nodes in quantum communication networks [46, 204–207]. Quantum

applications of the nitrogen vacancy (NV) center, with a spin-photon interface and coherent operation up to and above room temperature [141, 193, 208, 209], will benefit from interfacing the central NV spin qubit with accessible dark spins in the diamond lattice for quantum memories [210–212] and many-body metrological states [213, 214]. These applications could enable national-scale quantum networks and quantum sensing beyond the standard quantum limit. Explorations of such multi-spin systems have relied on NV centers that are either naturally occurring [46, 207, 211, 212, 215, 216], precluding scalability, or that are formed via nitrogen implantation [217–224], introducing qubit decoherence sources, associated with crystal damage [225].

Diamond-based quantum applications benefit greatly from the ongoing optimization of bottom-up color center synthesis via plasma-enhanced chemical vapor deposition (PECVD) [226–229]. Delta(δ)-doping studies [230, 231] have demonstrated vacancy diffusion-limited spatially localized NV centers, while avoiding the crystal damage and processing inherent to aperture mask or focused implantation [232–238]. PECVD of diamond quantum systems has enabled engineering of NV center spin environments via isotopic purification [230, 239, 240], dimensionality control [230, 241, 242], and co-doping techniques [73, 243, 244]. However, the development of these techniques has outpaced computational efforts to model spin bath-induced decoherence [174, 245], and theoretical approaches have not yet been applied to investigate diamond qubit synthesis. Cluster Correlation Expansion (CCE) methods provide an accurate tool to model decoherence in varied and tailored electron and nuclear spin bath environments [54]. Such approaches have recently been applied to study material systems relevant for quantum applications [56, 72, 108, 245], indicating that CCE may indeed be a powerful tool to enable more efficient synthesis procedures, which are crucial for the design of quantum materials [246].

In this work, we apply CCE methods, as implemented in the open source framework PyCCE [108], to predict and characterize bottom-up solid state spin qubit synthesis. We first

introduce the computation and materials growth techniques. We then explore a common defect created during NV center synthesis: the neutrally charged substitutional nitrogen N_s^0 with electron spin $S = 1/2$ (P1 center). Using theoretical predictions, we investigate the P1 center spin bath-induced decoherence [174, 247] of NV centers in diamond across the parameter space of our growth regime (P1 density and layer thickness). Obtained dependencies enable us to use the coherence time as descriptors of these systems for determining the parameters of the growth. For that we develop a maximum likelihood estimation (MLE) model based on Ramsey T_2^* coherence times and apply it to characterize nitrogen incorporation in a experimental test sample. We then study low-dimensional electron spin baths as hosts to strongly coupled electron spin systems, demonstrating how our computational techniques can help improve the yield of future quantum devices and aid in experimental design.

In Fig. 10.1 we show the strategy adopted in this work to improve upon the current NV synthesis process. The blue boxes show the commonly adopted process for generating single NV centers. After identifying a desired sample density and geometry, iterations of growth and secondary ion mass spectroscopy (SIMS) are necessary to confirm the nitrogen doping density. In practice, we have observed large variations in SIMS results that reduce the efficacy of this approach, as discussed in Sec. 10.2.2. Here we show that it is beneficial to incorporate theoretical spin bath predictions as well as an *in-situ* density characterization tool into our workflow (green boxes). The understanding of low-dimensional spin bath decoherence obtained through theory and computation improves initial experiment design, and the local density feedback enabled by the MLE model circumvents the need for SIMS characterizations of doping density.

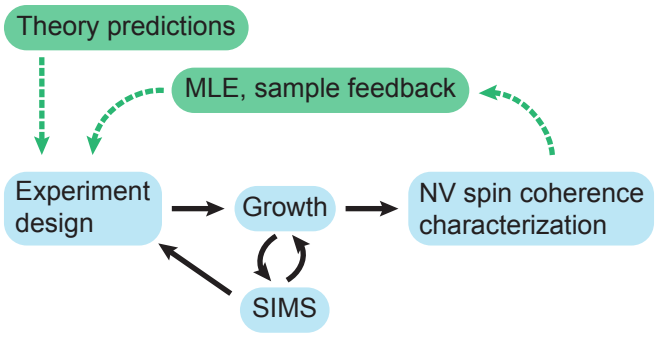

Figure 10.1: Growth process workflow. The current process steps (blue) for synthesizing a diamond NV sample. Iterations of growth and SIMS analysis are required to confirm nitrogen doping densities. The theoretical predictions and density maximum likelihood estimation model in this work (green) enable a non-destructive feedback process to circumvent SIMS and allow for an efficient experimental design.

10.2 Results

10.2.1 Validation of theoretical calculations

Within the CCE approach [47, 48] the coherence function $\mathcal{L}(t) = \frac{\langle 0|\hat{\rho}(t)|1\rangle}{\langle 0|\hat{\rho}(0)|1\rangle}$, defined as the normalized off-diagonal element of the density matrix of the qubit $\hat{\rho}(t)$, is approximated as a product of irreducible contributions of bath spin clusters, where the maximum size of the cluster n corresponds to the order n of the CCEn approximation (Fig. 10.2(a)). We converge the calculations with respect to the size of the bath, and the order of CCE approximation. We find that the Ramsey signal of the electron spin in the electron spin bath is converged at first order (CCE1), when each P1 is treated as isolated spin. We can thus solve the P1-limited Ramsey decoherence analytically, and compute T_2^* as a sum of the couplings between the NV and the weakly coupled P1 centers. The Hahn echo signal is instead simulated at the CCE4 level of theory (see Methods for more details).

We validate our theoretical calculations against a reference dataset of NV ensemble coherence times in bulk ^{14}N P1 spin baths. We extract T_2 from the coherence curve by fitting the signal to a stretched exponential function, $\exp\left\{[-(\frac{t}{T_2})^n]\right\}$, as shown in Fig. 10.2(b). Computed ensemble T_2^* and T_2, averaged over a set of random P1 positions, are overlaid in

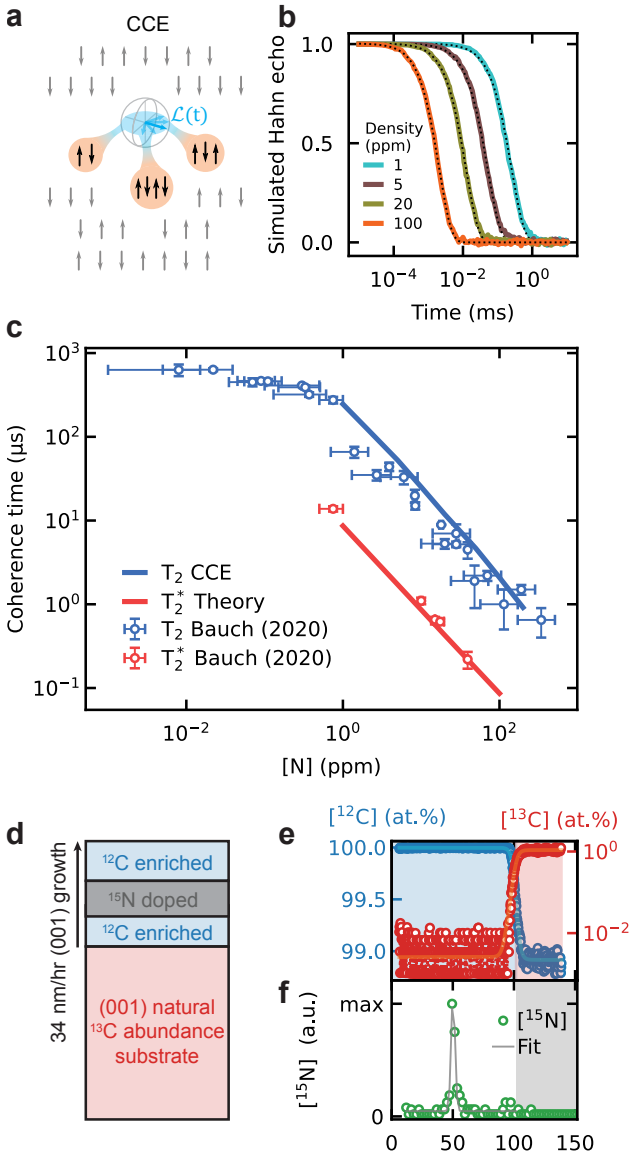

Figure 10.2: Computational and diamond growth methods. (a) Schematic representation of the cluster correlation expansion (CCE) approach. (b) Example of the Hahn-echo coherence calculated using the PyCCE code [108] for various ^{14}N P1 spin baths. The values of T_2 times are extracted from a stretched exponential fit of the form $\exp\left\{[-(\frac{t}{T_2})^n]\right\}$ (dashed line). (c) T_2 and T_2^* coherence times overlaid with corresponding experimental data [174], validating our computational methods. (d) Schematic of isotopically pure (^{12}C) PE-CVD (100) diamond overgrowth with isotopically tagged ^{15}N nitrogen δ-doping. This sample geometry with varying nitrogen incorporation density and thickness is considered throughout this paper. (e,f) Carbon (top) and nitrogen (bottom) isotope concentrations measured via SIMS on characterization sample, demonstrating isotopic purification of host material and isotopically tagged nitrogen incorporation.

Fig. 10.2(c) with experimental data, taken from Ref. [174]. We find excellent agreement with the experimental data, showing that the first-principles calculation with CCE method yields a quantitative description of the decoherence due to P1 spin baths. The stretched exponent parameter of the computed Hahn-echo decay is between $n = 1.2$-1.3, in excellent agreement with the data of Ref. [174].

10.2.2 Diamond growth and defect synthesis

The sample studied in this paper, shown schematically in Fig. 10.2(d) was grown with a 3 min 10 sccm $^{15}N_2$ flow at a time corresponding to a depth of ≈50 nm. Nitrogen δ-doping is achieved by introducing $^{15}N_2$ gas (99.99 % chemical purity, 99.9 at% isotopic purity) during diamond growth. According to the SIMS characterization of a calibration sample, shown in Fig. 10.2(e-f), this creates a 3.8(2) nm thick (compared to $1.3^{+2.2}_{-0}$nm predicted from growth calibrations) ^{15}N-doped layer at a depth of 50.2(1) nm, with a SIMS-quantified [^{15}N] density of 0.39(2) ppm. These values are obtained from a calibration sample, processed and grown identically to the sample studied in this paper.

While SIMS is ideal for detecting low concentrations of dopants in semiconducting materials, sample geometries unique to our application remain difficult to characterize accurately due to experimental trade-offs. Specifically, the trade-off between depth resolution and overall sensitivity is dictated by the analysis/sputtering energy. Under our characterization conditions, the ideal detection limits for $^{15}N_2$ and $^{14}N_2$ densities are 1×10^{15} cm^{-3} (≈0.006 ppm) and 5×10^{15} cm^{-3} (≈0.028 ppm), respectively. However, the obtained densities can vary significantly as a function of sample inhomogeneities, the presence of growth defects, and experimental conditions. While studying samples that were nominally grown under the same conditions, SIMS quantification of [^{15}N] has been observed to regularly vary by at least an order of magnitude, requiring rigorous statistics over growth of multiple samples, a time- and resource-consuming process. A truly local spin-defect materials characterization

method is necessary, motivating the *in-situ* maximum likelihood estimation of the density characterization presented in Sec. 10.2.5, a new capability enabled by our computational results. A different approach with NV ensemble coherence measurements has also recently been developed [241, 242].

10.2.3 Single spin coherence in quasi-2D electron bath

We now turn to investigating single spin coherence properties across the density and thickness parameter space available for the PECVD growth recipe adopted in this work and described in Methods section.

We compute Ramsey coherence time T_2^* (Fig. 10.3(a), left) for 10^4 spin bath configurations with spin bath thickness of 0.5 nm to 12 nm (0.5 nm steps) and density of 0.5 ppm to 12 ppm (0.5 ppm steps) from the coupling between the central NV spin and weakly coupled P1 spins (see Methods). We simulate Hahn-echo measurements (Fig. 10.3(a), right) with spin bath thicknesses of 1 nm to 10 nm (1 nm steps) and densities of 1 ppm to 12 ppm (1 ppm steps) (See SI Sec. IB for justification of CCE order).

We characterize the distributions of the coherence times with the mean $\mu = 10^{\langle \log T_2/[1\text{ms}] \rangle}$ and the variance $\sigma^2 = \langle \log^2 T_2 \rangle - \langle \log T_2 \rangle^2$ of the logarithm of the coherence times at each density and thickness (Fig. 10.3). Using the logarithm of the coherence we can directly compare the coherence distributions at different timescales.

Figs. 10.3(b,c) and (d,e) depict μ and σ over the chosen range of parameters for T_2^* and T_2, respectively. In each case, the computed average coherence time decreases with increasing spin density and/or increasing thickness, as expected. In the three-dimensional limit, the average coherence time is independent of bath thickness. Observed decrease in μ as a function of thickness (Fig. 10.3(b) and (d)) suggests the presence a low-dimensional spin bath regime in the chosen range of parameters.

We analytically derive the distribution of the interaction strength between the central

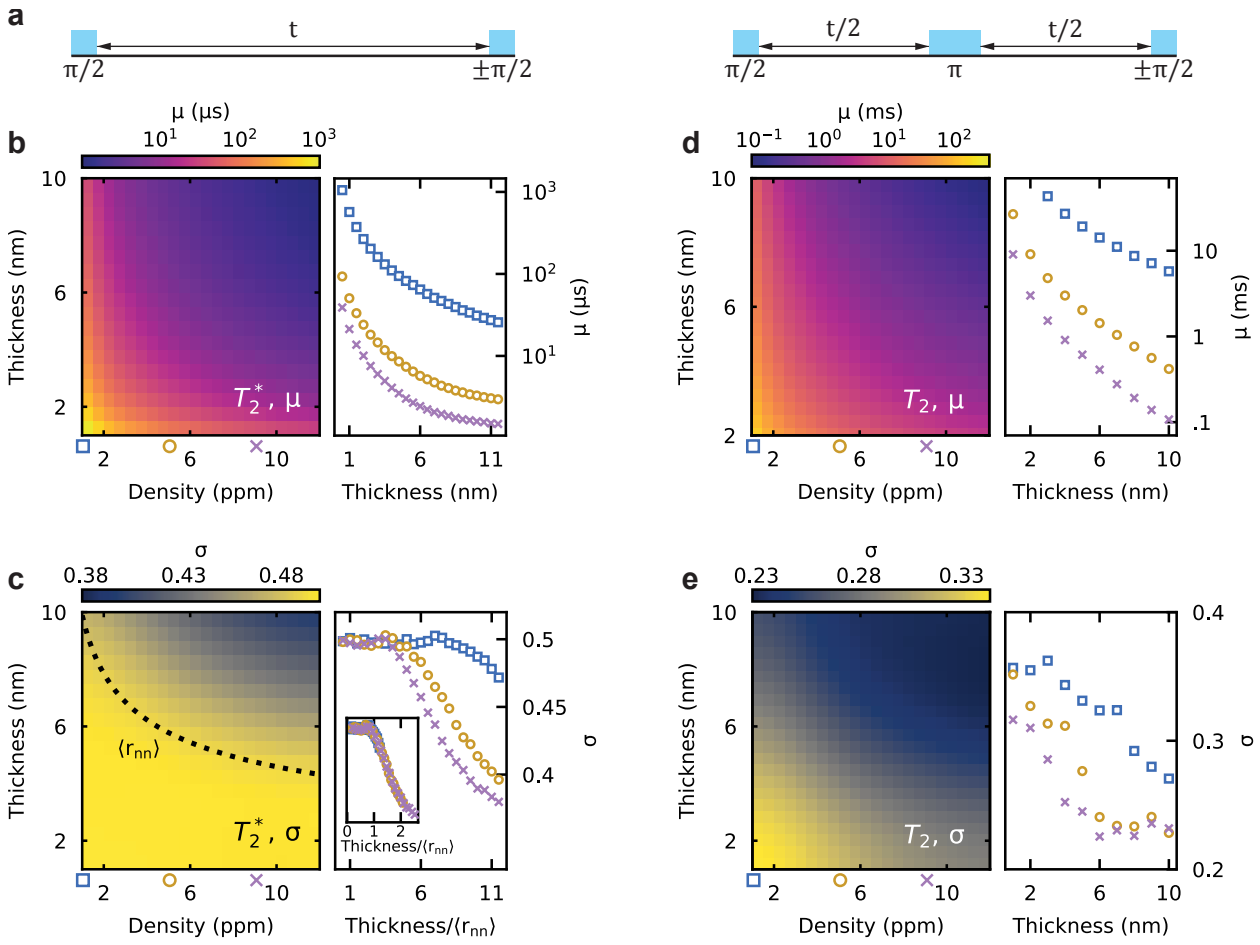

Figure 10.3: Single spin coherence in low-dimensional spin baths. (a) Ramsey (left) and Hahn echo (right) microwave measurement pulse sequences. (b,c) Mean of $\log T_2^*$ distributions $\mu = 10^{\langle \log T_2^* \rangle}$ (b) and variance $\sigma^2 = \langle \log^2 T_2^* \rangle - \langle \log T_2^* \rangle^2$ (c) as a function of P1 density and layer thickness. Values are linearly interpolated between datapoints. The black dashed line in (c) indicates the thickness equal to the average nearest-neighbor bath spin distance $\langle r_{nn} \rangle = 0.554\rho^{-1/3}$ for each density ρ (see text, Sec. 10.2.6), demonstrating a boundary between dimensionalities. At right in (b,c) are line-cuts of μ and σ at densities of 1, 5, and 9 ppm. Inset in (c) is σ at multiple densities with thickness normalized by $\langle r_{nn} \rangle$, demonstrating universal behavior versus dimensionality. (d,e) Same data as (b,c) presented for T_2 coherence times.

spin and bath spins in low-dimensional baths in Sec. 10.2.6. In the case of T_2, we predict times >1 ms, beyond what is generally observed in experiment. This suggests that experimental T_2 times in thin, low density spin baths are limited by noise sources not captured in our model, as suggested previously [174]. However, our calculations predict that, in principle, low dimensional lightly doped samples can realize T_1 limited coherence times at room temperature.

Bath dimensionality further impacts the relative distribution of coherence times, described by the standard deviation σ. Focusing on the inhomogeneous dephasing time T_2^* (Fig. 10.3(c), right), σ exhibits unexpected behavior in the region where the thickness equals the average nearest neighbor distance in three dimensions, $\langle r_{nn} \rangle$, plotted as a function of density in the left plot. σ plateaus when the thickness is smaller than $\langle r_{nn} \rangle$ and decreases when thicknesses are larger. The inset in Fig. 10.3(c), right, demonstrates universal behavior of coherence times relative to the bath dimensionality. The x-axis is normalized to $\langle r_{nn} \rangle$. This indicates that two-dimensional spin baths naturally have a wider spread of NV coherence times. While thin and less dense samples may optimize coherence times, they typically also lead to greater fluctuations in single-qubit coherence properties.

We see similar trends in Hahn-echo T_2 times (Fig. 10.3(e), right). We find in general that $\sigma_{T_2^*} > \sigma_{T_2}$. In the SI Sec. IC, we find convergence for T_2^* and T_2 at twelve and 100 bath spins, respectively, suggesting heuristically that Ramsey measurements are sensitive to the variation of a fewer number of spins. In general, one expects a smaller standard deviation in physical quantities that are sensitive to larger numbers of randomly placed spins due to the central limit theorem. We thus expect a larger impact of the stochasticity in P1 position on the T_2^* distributions. These results inform solid-state qubit synthesis characterization, where both T_2^* and T_2 are standard measurements performed on multiple NV centers.

Our theoretical results constitute a full computational characterization of spin-bath induced coherence times across a range of bath geometries and densities. Our computational

strategy is not limited to NV centers in diamond and can be applied to other spin defect systems, as well as other spin bath measurements, as long as the appropriate pulse sequence can be simulated using the PyCCE code. Additionally, our approach will inform future diamond growth and NV synthesis. Rather than extrapolating from bulk data [174] or measurements on single δ-doped NV centers, growth may now be informed by the theoretical predictions of coherence times distributions.

10.2.4 Sample characterization

We now characterize the coherence of an exemplar sample grown under the conditions outlined in Sec. 10.4.2. Fig. 10.4(a) presents frequency-dependent double electron-electron resonance measurements of a single NV center in a P1 center bath. This measurement essentially performs electron spin resonance (ESR) spectroscopy on target spins by recoupling their dipolar interactions to the NV probe spin, which are otherwise decoupled by the Hahn-echo sequence. At the experimental magnetic field of 311 G, and given ^{15}N P1 hyperfine couplings, we expect, based on the possible P1 Jahn-Teller axis directions and ^{15}N nuclear spin states (see Methods), transitions near 935 MHz and 954 MHz for the three misaligned and one aligned axes, respectively, and the nitrogen nuclear spin state $+1/2$ probed here (only half the bath is probed in this data). We observe resonances at mircowave light frequencies f_{P1} of 934.8 MHz ($f_{P1,3/8}$) and 953.1 MHz ($f_{P1,1/8}$). The subscripts indicate the fraction of the bath probed at that frequency. This confirms the presence of ^{15}N P1 centers in our sample.

We measure T_2^* times for a set of eight single NV centers in the same test sample. Fig. 10.4(b) shows characteristic Ramsey interferometry data for the one of these NV centers. Data is fit to an exponential decay with oscillations capturing coupling to single nearby P1 centers, as in the Ramsey analysis in Sec. 10.2. While the ^{15}NV center exhibits a $\approx$3 MHz splitting from its nitrogen nuclear spin, CCE calculations do not account for the central spin's

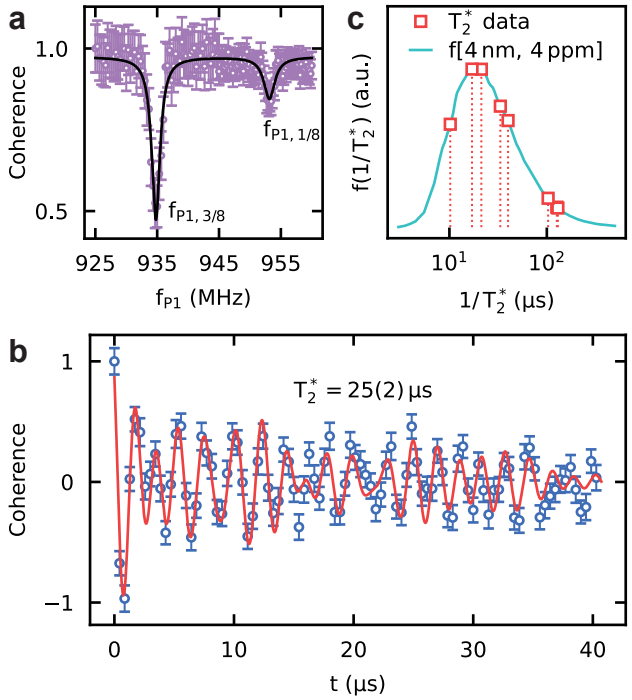

Figure 10.4: NV center measurements. (a) DEER spectroscopy with NV center confirming the presence of a P1 center electron spin bath. Marked values of f_{P1} correspond to P1 ESR transitions corresponding to the static magnetic field and internal P1 hyperfine parameters. (b) Ramsey interferometry measurement to extract T_2^* coherence time. (c) Compiled decoherence rates for eight measured NV centers overlaid with the best calculated distribution fit. The height of each data point indicates the PDF value for that time, and is not extracted from the measurement.

nuclear spin. We are careful to drive with 909 kHz Rabi rate pulses to avoid mixing nuclear hyperfine effects into our measurement. This NV exhibits T_2^*=25(2) μs (see SI Sec. III for details of NV measurements). This process is followed for the remaining NV centers.

Decoherence rates for the set of measured NV centers are plotted in Fig. 10.4(c) along with the calculated probability distribution function (PDF) that best fits the measured distribution as determined via MLE, discussed in the next section. The aim in the following section will be to determine which calculated distribution best fits this dataset.

10.2.5 Maximum likelihood estimation

Using the theoretical dependence of the coherence time distributions on thickness and P1 density, in this section we develop the maximum likelihood model (MLE) to recover the growth parameters of the given sample. Taking interpolated distributions $f(T_2^*)$, recovered from the numerical data, the likelihood of a given bath configuration is calculated as the joint probability of the $\{T_2^*\}$ dataset for each pair of bath thickness t and density ρ as [248]

$$L(t,\rho) = \prod_i f(t,\rho,T_{2,i}^*). \tag{10.1}$$

The MLE procedure determines what coherence distribution best predicts the measured distribution in Fig. 10.4(c). In Fig. 10.5(a) we plot $L(t,\rho)$ over the computational phase space for the coherence times in Fig. 10.4(c). We find a band of potential bath geometries that satisfy the observed coherence time distribution, rather than uniquely predicting a single set of values. Based on the CVD growth discussed in Sec. 10.4.2, we estimate the bath thickness at t_{SIMS} =4 nm and plot the linecut of L in Fig. 10.5(b). This provides a measure of the bath density of 3.6(7) ppm, where the error is found by fitting $L(t_{SIMS},\rho)$ to a normal distribution.

We now benchmark the error in the MLE procedure versus the number of coherence time samples in Fig. 10.5(c). For each number of samples, N, and set of bath parameters, 200 random T_2^* datasets of N coherence times are chosen from the numerical datasets used in Sec. 10.2. Then, the likelihood is calculated for a fixed thickness t_0, and the relative error for one dataset is calculated as $\epsilon_{\rho_0}^2 = (\rho_{mle}-\rho_0)^2/\rho_0^2$, where ρ_{mle} is the density such that $L(t_0,\rho_{mle}) = \max[L(t_0,\rho)]$. This is averaged over a range of tested densities, plotted in Fig. 10.5(c). We calculate the error for eight samples to be 25%, corresponding to an uncertainty of 0.9 ppm for the density estimate from Fig. 10.5(a). This is similar to the error from fitting L, and is stable when the thickness is varied. We fit the average error as $A\cdot N^{-p}$, shown over the calculated error in Fig. 10.5(c), finding a $N^{-1.6}$ trend.

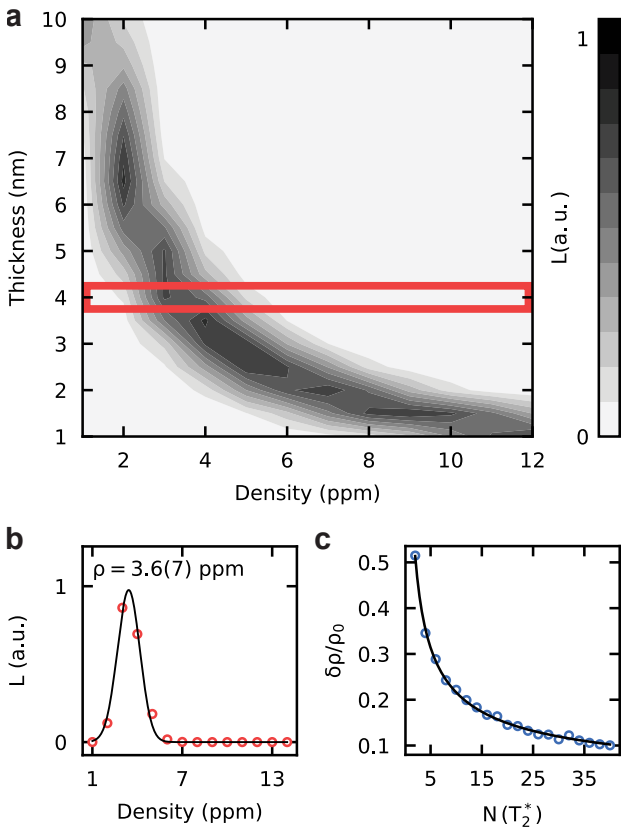

Figure 10.5: Maximum likelihood estimation. (a) Likelihood of dataset in Fig. 10.4(c) calculated for each set of bath parameters, from theoretical results. (b) Likelihood restricted to a thickness of $t_{SIMS} = 4\,\text{nm}$ (from Fig. 10.2(e)), from which we extract a density of $3.6(7)\,\text{ppm}$. (c) Calculated error of density estimation across full density range with fixed thickness, calculated for 200 random datasets at each density.

10.2.6 Strong coupling yield

Entangled qubit-based sensors promise to greatly enhance quantum sensing capabilities as compared to the current state-of-the-art [214]. The applicability of these schemes is enabled by high-yield synthesis of strongly coupled quantum systems, e.g. NV center spins and multiple single bath spins. We consider the impact of growth dimensionality on the yield of such systems analytically, quantifying our results with numerical predictions. In our calculations we consider central NV spins and P1 bath spins, but our approach is easily generalized to other spin systems.

Each bath spin couples to the NV with a dipolar coupling strength A_z^i. The NV coherence in the absence of dynamical protocols and coupled to a bath of many weakly coupled spins can be described as a product of individual coupling contributions (see Methods).

We aim to describe how likely the coupling to the nearest spin, A_0, is to be greater than the dephasing from the rest of the bath, A_{bath}. The distributions of nearest neighbor distance r_{nn} in two and three dimensions are

$$g_{2D} = \exp\Big(-\pi r_{nn}^2 \varsigma\Big) \varsigma \, 2\pi r_{nn}, \tag{10.2}$$

$$g_{3D} = \exp\Big(-4\pi r_{nn}^3 \rho/3\Big) \rho \, 4\pi r_{nn}^2, \tag{10.3}$$

where ρ is the 3D density and $\varsigma = \rho t$ is the 2D density for bath thickness t nominally less than the average nearest neighbor distance. Notably, the distributions depend on the bath dimensionality. The bath decoherence can be estimated as follows

$$\Gamma_{2D}^{\text{bath}} \propto \sqrt{\sum_{2D} |1/r^3|^2} \quad = \sqrt{\textstyle\int_0^\infty dr 2\pi r \varsigma r^{-6}}, \tag{10.4}$$

$$\Gamma_{3D}^{\text{bath}} \propto \sqrt{\sum_{3D} |1/r^3|^2} \quad = \sqrt{\textstyle\int_0^\infty dr 4\pi r^2 \rho r^{-6}}. \tag{10.5}$$

We now define the visibility ν of the nearest neighbour spin as a ratio between its coupling

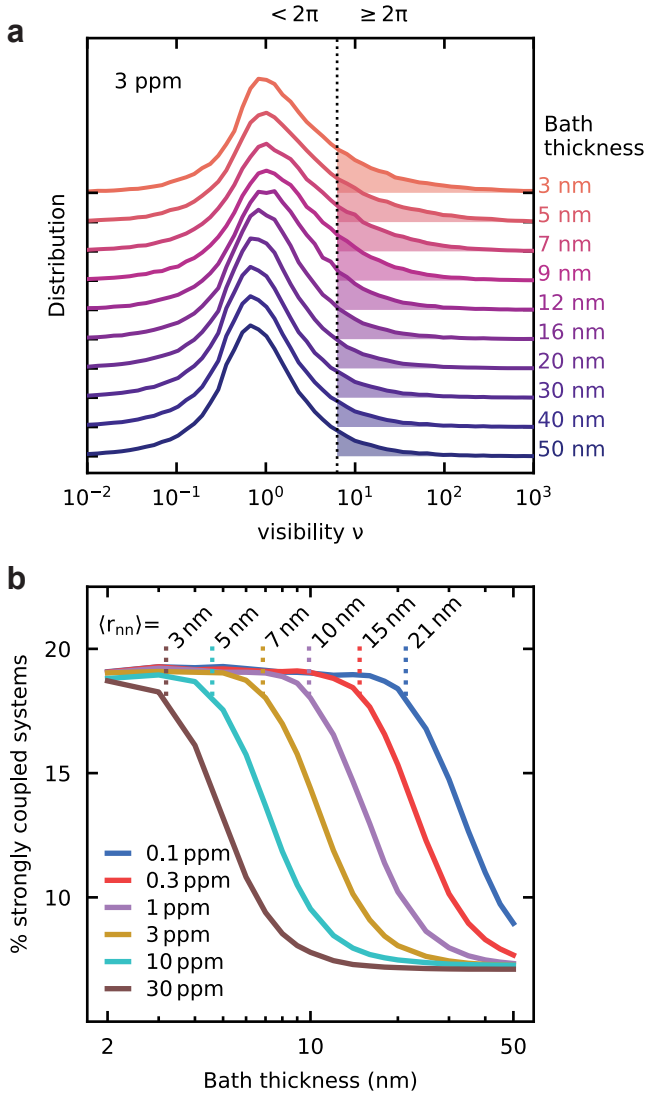

Figure 10.6: Dimensionality dependence of strong coupling. (a) Computed distribution (using PyCCE) of ratio of nearest-neighbor P1 coupling to background decoherence rate for 10^5 3 ppm density P1 bath configurations with varying thickness. Curves are offset for clarity. Shaded regions right of the dashed line indicate coupling ratio $\geq 2\pi$. (b) Percentage of NV-P1 bath systems with at least one strongly coupled bath spin for varying bath density and thickness. Average spin-spin distance is marked atop curves for each density.

to the central spin A_0 and the decoherence rate induced by all other spins A_{bath}

$$\nu = \frac{|A_0|}{\sqrt{2}A_{\text{bath}}}, \tag{10.6}$$

and evaluate average ν over many bath configurations. Assuming the point dipole approximation to compute the coupling between central and bath spins, we find the average visibility at the given dimensionality as $\langle \nu_{kD} \rangle = \langle |A_0|/\sqrt{2}A_{\text{bath}} \rangle \simeq \langle r_{nn}^{-3}/\sqrt{2}\Gamma_{kD} \rangle$, where the distributions Γ_{kD} ($k = \{2, 3\}$) are given by Eqs. (10.2) and (10.3). We note here that averaging Γ_{kD} assumes the dephasing rate due to the rest of the spin bath follows a highly peaked distribution. We then ask if this average is larger for lower dimensional spin baths by evaluating

$$\frac{\nu_{2D}}{\nu_{3D}} = \frac{\langle r_{nn}^{-3}/\Gamma_{2D} \rangle}{\langle r_{nn}^{-3}/\Gamma_{3D} \rangle} = \sqrt{2}. \tag{10.7}$$

We find that the visibility of the nearest neighbour spin is $\sqrt{2}$ larger in the 2D case, pointing at the fact that yield of strongly coupled bath spins is significantly higher in the low dimensional systems.

We confirm these analytical predictions with numerical simulations. Using the PyCCE code we generate 10^5 50 nm-thick P1 electron spin baths in a (001)-oriented diamond lattice whose densities range over two orders of magnitude, and divide each bath into slices of varying thickness. For each density and thickness we compute visibility ν (Eq. (10.6)). Representative histograms for 3 ppm spin baths are shown in Fig. 10.6(a). As the bath thickness decreases, the visibility distribution shifts to higher values, in line with the prediction from Eq. (10.7). We follow the criterion laid out in the Methods and Eq. (10.11) below to identify strongly coupled bath spins. We set a threshold for the visibility at $\nu \geq 2\pi$. At this value coherence goes through a full oscillation period when the signal contrast reaches $1/e$.

We plot the resulting probability of obtaining strongly coupled spins in Fig. 10.6(b) for each density. At all densities, the likelihood of finding a NV-spin bath configuration with

the desired coupling ratio is almost three times as high in the thin bath limit. Furthermore, there is a crossover transition for each density from three-dimensional to two-dimensional behavior, which intersects with the average nearest neighbor spacing $\langle r_{nn} \rangle = 0.554\rho^{-1/3}$, obtained from Eq. (10.3). Heuristically, as the thickness reduces below $\langle r_{nn} \rangle$, there are no spins proximal to the central spin in the out-of-plane direction, only in the plane of the central spin. In SI Sec. IV we present a point of comparison between the analytical and numerical approaches, finding agreement between calculated coupling distributions and the result in Eq. (10.7).

10.3 Outlook

Point-defects in diamond and other wide-bandgap semiconductors are promising platforms for qubit-based sensors. Deterministic synthesis of such systems will benefit from feed-forward techniques that optimize host crystal parameters for specific outcomes and applications. Additionally, such systems pave the way for entangled qubit-based sensors which hold great promise to enhance current quantum sensing capabilities. In this paper, we have demonstrated holistic quantum simulations of NV center coherence (with techniques applicable to other spin defects) as a tool for quantum system coherence characterization driven synthesis, minimizing the need for large-scale and destructive materials characterization. Practically, we showed how our approach allows, with basic prior sample knowledge, for the use of rudimentary T_2^* measurements to approximate *in-situ* doping densities. Specifically, we have demonstrated a MLE model based on a CCE-generated distribution library as an aid to process calibration and sample characterization. This method is non-destructive and operates at the density scales relevant for quantum technologies.

Additionally, the coherence distribution results presented in this paper explore the expected sample properties in low-dimensional spin baths. By going beyond approximate analytical treatments and sampling over a wide distribution of random bath configurations with

a range of central spin-bath couplings, the CCE calculations quantitatively capture the connection between bath geometries and coherence time distributions, providing an invaluable analytical tool for experimental design.

While in this work we focus on a single dominant spin bath species in low-dimensional geometries, our MLE method is not limited to this regime. CCE methods can readily be extended to additional spin bath species in diamond, as well as mixed nuclear and electronic spin baths. By calculating coherence times in these other situations, dopant densities in samples with multiple dominant noise sources can be characterized. Furthermore, the strategy presented here can be applied to other solid state hosts where qubit coherence is limited by spin bath noise.

10.4 Methods

Our work builds on two previously established techniques, CCE calculations and PECVD synthesis of NV centers in diamond as described below and in Fig. 10.2. We focus on the ^{15}N isotope of nitrogen for the majority of the calculations as this allows us to experimentally distinguish intentionally doped defects from background occurring defects.

10.4.1 Theory

The dynamics of the systems are simulated using the following Hamiltonian:

$$\begin{aligned}\hat{H} = &-\gamma_e B_z \hat{S}_z + D\hat{S}_z^2 + \textstyle\sum_i a(m_i)\hat{P}_{z,i} - \gamma_e B_z \hat{P}_{z,i} \\ &+ \textstyle\sum_i \mathbf{S}\mathbf{A}^i\mathbf{P}_i + \sum_{i\neq j} \mathbf{P}_i\mathbf{J}^{ij}\mathbf{P}_j,\end{aligned} \tag{10.8}$$

where γ_e is the electron spin gyromagnetic ratio, B_z is the magnetic field aligned with the z-axis, $\mathbf{S} = (\hat{S}_x, \hat{S}_y, \hat{S}_z)$ are NV spin operators, D is the NV zero field splitting, $\mathbf{P} =$

$(\hat{P}_x, \hat{P}_y, \hat{P}_z)$ are spin operators of the P1 center, and $a(m_i)$ is the hyperfine coupling between the P1 ^{15}N nuclear spin and the P1 electron spin, dependent on the random orientation of the Jahn-Teller axis along one of four crystal directions and the nuclear spin state for each P1 (m_i), where i runs over all the simulated P1 centers [249]. $\mathbf{A}^i$ are dipolar couplings between the NV center and P1 centers, and $\mathbf{J}^{ij}$ is the coupling between two P1 electron spins. The applied 50 G is sufficiently past the high field limit and these calculations translate over to measurements at higher fields as well (see SI Sec. IA).

In the SI (Sec. IB and IC) we show convergence tests for Ramsey and Hahn echo simulations versus both CCE order and total number of simulated bath spins. We use CCE methods with bath state sampling [53] to achieve convergence for the electron spin bath. For each pure electron bath state the state of ^{15}N spin and the P1 orientation is chosen at random. More details about the method are available in [108].

The CCE approach [47, 48] approximates the coherence function $\mathcal{L}(t) = \frac{\langle\sigma_-(t)\rangle}{\langle\sigma_-(0)\rangle} = \frac{\langle 0|\hat{\rho}(t)|1\rangle}{\langle 0|\hat{\rho}(0)|1\rangle}$, the normalized off-diagonal element of the density matrix $\rho_{m,n}$ of the qubit, where m and n are either the ground or excited spin states $|0\rangle$ and $|1\rangle$, respectively. $\mathcal{L}(t)$ is approximated as a product of cluster contributions:

$$\mathcal{L}(t) = \prod_i \tilde{L}^{\{i\}} \prod_{i,j} \tilde{L}^{\{ij\}} ..., \tag{10.9}$$

where $\tilde{L}^{\{i\}}$ is the contribution of a single bath spin, $\tilde{L}^{\{ij\}}$ is the contribution of spin pairs, and so on for higher order clusters (Fig. 10.2(a)). The maximum size of the cluster n included in the expansion denotes the order of CCEn approximation.

The Ramsey signal is converged at the first order of CCE. As such, we can represent the high-field Ramsey coherence function in the rotating frame for a bath in a fully mixed state

as [52]:

$$\mathcal{L}(t) \approx \prod_j^N \cos\tfrac{A_z^j t}{2} \approx \exp\left[-\tfrac{A_{\text{bath}}^2}{2} t^2\right] \prod_i^n \cos\tfrac{A_z^i t}{2} \tag{10.10}$$

$$= \exp\left[-(\tfrac{t}{T_2^*})^2\right] \prod_i^n \cos\tfrac{A_z^i t}{2}$$

where $A_{\text{bath}}^2 = \frac{\sum_j (A_z^j)^2}{4}$, $T_2^* = \frac{\sqrt{2}}{A_{\text{bath}}}$ index i goes over only n the strongly coupled P1 centers, and index j goes over all other P1s. We define strongly coupled bath spins as those distinguishable from the background decoherence, setting threshold for its visibility (Eq. (10.6)) as:

$$\nu_i = \frac{\left|A_z^i\right|}{2} \geq 2\pi \cdot \frac{A_{\text{bath}}}{\sqrt{2}}, \tag{10.11}$$

so that at least one full period of oscillation of the coherence function is visible when the signal contrast reaches $1/e$. For each random bath configuration we order the P1 spins by strength of the coupling, and one-by-one select out the strongly coupled spins until the condition (10.11) is violated. T_2^* is then recovered from the coupling to the remaining bath spins.

Ref. [245] shows that CCE at second order can be used to qualitatively recover the behaviour of T_2 coherence times in the P1 bath. We further extend this approach, and converge CCE Hahn echo calculations at 4th order with bath-state sampling (see SI Sec. IB and Fig. S1(c)).

10.4.2 Materials growth

All defects studied in this work are doped *in-situ* during diamond PECVD with subsequent electron irradiation and annealing for NV^- activation. This recipe constitutes our standard PECVD process for growing isotopically pure diamond with isotopically tagged NV centers, as shown in Fig. 10.2(d). High purity electronic grade ($\leq$10 ppb) diamond substrates 2 mm by 2 mm by 0.5 mm, with $\langle 001 \rangle$ growth face and $\langle 110 \rangle$ sides (Element Six) were

used as starting substrates. The as-received substrates were Chemical-Mechanical Polished (CMP) to a surface roughness of $R_q \leq 0.4\,\mathrm{pm}$ by Syntek, LLC. Subsequently, these substrates were inductively coupled plasma reactive ion etched (ICP-RIE) down to remove $\approx 2.5\,\mu\mathrm{m}$ of damaged diamond surface using a composite, cycled Ar/Cl_2 and O_2 plasma etching recipe. Pre-growth, the samples were annealed at $1200\,^{\circ}\mathrm{C}$ and tri-acid cleaned to mobilize/annihilate vacancy clusters and remove any amorphous/sp^2 carbon, respectively. See SI Sec. II for a more detailed description of sample processing.

Homoepitaxial growth of diamond was performed in a custom-configured PECVD reactor [250] (Seki Diamond). The growth chamber was pumped down to $8 \times 10^{-8}\,\mathrm{Torr}$ to minimize background contamination. Thereafter, high purity H_2 (99.999 99 %) was introduced into the chamber, with the process microwave power of $11.5\,\mathrm{W\,mm^{-2}}$ and pressure of 25 Torr maintained throughout. The substrate temperature was maintained in the range of $800(27)\,^{\circ}\mathrm{C}$ as tracked by an IR pyrometer. Before introduction of the diamond growth precursor, the sample was submitted to a H_2 & O_2 etch (4 % of O_2) for 5 min and a subsequent 20 min etch using H_2 only, to etch away any residual surface contaminants and defects, and expose the growth surface atomic step edges [227, 251]. Thereafter, $^{12}CH_4$ (99.9999 % chemical purity, 99.99 at % isotopic purity) is introduced as the carbon precursor. Isotopic growth, demonstrated in Fig. 10.2(e), enables the study of electron spins in the absence of the natural ^{13}C nuclear spin bath. The methane-to-hydrogen ratio is maintained constant at 0.1 % (H_2:$^{12}CH_4$ = 400 sccm : 0.4 sccm) as to ensure step-flow growth [227, 250]. Growth rates for the obtained films were determined to be $38(10)\,\mathrm{nm\,h^{-1}}$ via ex-situ secondary ion mass spectroscopy (SIMS) analysis averaged over six calibration substrates (e.g., ^{12}C overgrowth shown in Fig. 10.2(e)).

Post-growth and nitrogen incorporation, bulk electron irradiation with a $2 \times 10^{14}\,\mathrm{cm^{-2}}$ dose at 2 MeV and a 2 h anneal at $850\,^{\circ}\mathrm{C}$ under an Ar atmosphere converts a fraction of doped nitrogen into NV centers with $[^{15}NV] \approx 0.01$ ppb to 0.1 ppb, with the remaining

nitrogen sites remaining as N_s (P1 centers). NV activation is intentionally performed in a vacancy diffusion-limited regime [234] in order to reliably obtain optically resolvable single NV centers. As the nitrogen doping is buried 50 nm below the diamond surface, we do not expect band-bending effects on the defect charge states [252, 253].

CHAPTER 11

ENTANGLEMENT AND CONTROL OF SINGLE NUCLEAR SPINS IN ISOTOPICALLY ENGINEERED SILICON CARBIDE

This chapter is adapted from the publication [1].

Nuclear spins in the solid state are both a cause of decoherence and a valuable resource for spin qubits [254]. In this work, we demonstrate control of isolated ^{29}Si nuclear spins in silicon carbide (SiC) to create an entangled state between an optically active divacancy spin and a strongly coupled nuclear register. We then show how isotopic engineering of SiC unlocks control of single weakly coupled nuclear spins and present an ab initio method to predict the optimal isotopic fraction which maximizes the number of usable nuclear memories. We bolster these results by reporting high-fidelity electron spin control (F=99.984(1)%), alongside extended coherence times (T_2 = 2.3 ms, $T_2^{DD} > 14.5$ ms), and a > 40 fold increase in dephasing time (T_2^*) from isotopic purification. Overall, this work underlines the importance of controlling the nuclear environment in solid-state systems and provides milestone demonstrations that link single photon emitters with nuclear registers in an industrially scalable material.

11.1 Introduction

Nuclear spins are one of the most robust quantum systems, displaying relaxation times that can exceed hours or days[255–257]. This makes them exciting candidates for quantum technologies requiring long memory times. In particular, nuclear spins are attractive quantum registers for optically active spin defects in the solid-state [211]. For example, nuclear registers can be used for repetitive quantum non-demolition (QND) optical readout[258], to enhance the signal-to-noise in quantum sensing[259], to implement quantum error correction schemes[135], or as vital components of quantum repeater [80] and

quantum communications[204] nodes. Additionally, electron-nuclear hybrid systems provide a platform for studying measurement back-action[260] and the emergence of classicality in quantum mechanics [261].

Recently, commercial SiC has been shown to provide a technologically mature semiconductor host for multiple defect spin qubits [4, 85, 86, 262–264]. In particular, this material allows the integration of isolated color centers into classical electronic devices which can be used to engineer and tune the spin-photon interface[100]. Combining such a tunable near-infrared emitter[88, 265] with a long-lived quantum memory is a promising basis for quantum network nodes fabricated at wafer scale by the semiconductor industry. To realize these quantum memories, SiC provides both carbon and silicon isotopes with non-zero nuclear spin. These isotopes have been shown to couple to various electronic spin defects[85, 266]; however, the control of single nuclear spins[186] in SiC has remained an outstanding challenge.

In this work, we report coherent control and entanglement of nuclear spin quantum registers strongly coupled to a single neutral divacancy spin (VV^0) in naturally abundant SiC. We then extend this control to weakly coupled nuclear spins, where isotopic purification enables the selective control of these registers with high fidelity. Using isotopic engineering, we also report both record coherence times and record single qubit gate fidelities[267] for electronic spins in SiC. Throughout this work, we present both experiment and ab initio theory that explores the inherent tradeoffs between spin coherence and nuclear memory availability which are involved when isotopically engineering materials. These results develop a full suite of nuclear spin controls in SiC and provide a guide for future materials design of spin-based quantum technologies.

11.2 Strongly coupled nuclear registers

In natural SiC, 1.1% of the carbon atoms and 4.7% of silicon atoms possess an $I = 1/2$ nuclear spin. Thus, about a third of all single c-axis oriented (hh and kk) divacancies will have a ^{29}Si

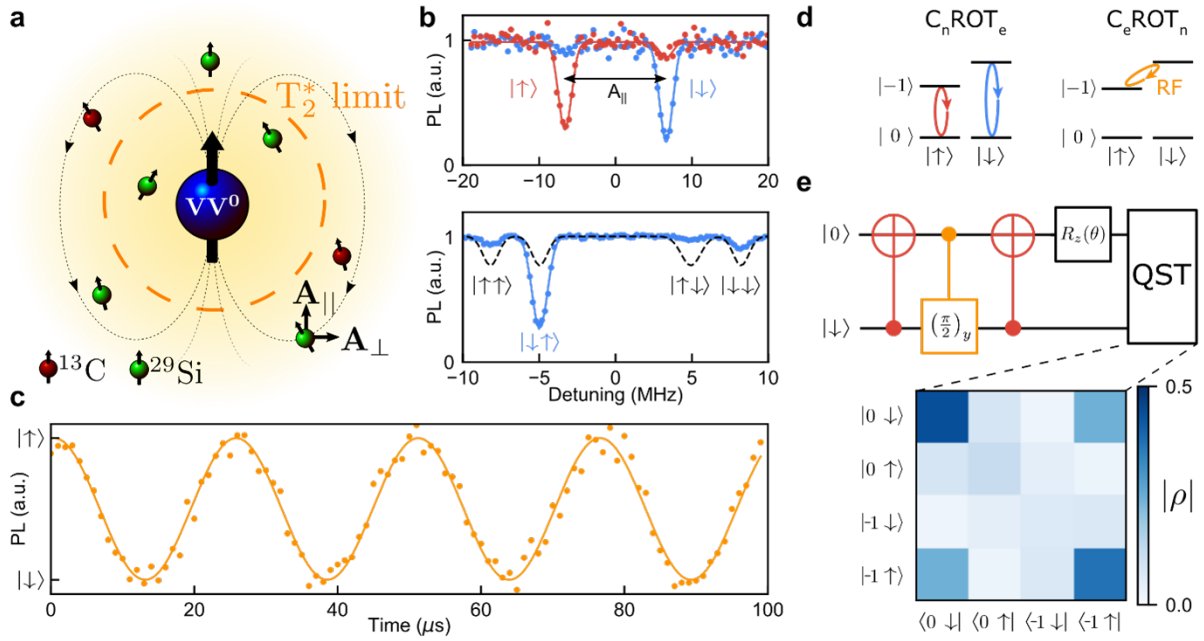

Figure 11.1: Initializing, controlling and entangling strongly coupled nuclear spins. (a) Schematic of a single divacancy with surrounding nuclear spins. (b) Optically detected magnetic resonance of a single (kk) VV^0 after initialization of both the electron and either 1 (top) or 2 (bottom) strongly coupled nuclear spins. Top: initialization in either the $|\uparrow\rangle$ (red) or $|\downarrow\rangle$ (blue) nuclear spin states. Detuning is from 1.139 GHz. Bottom: dashed line (black) represents the expected results from an uninitialized state, blue line is the experimental initialized state. Detuning is from 2.153 GHz. (c) Nuclear Rabi oscillations (between $|-1\uparrow\rangle$ and $|-1\downarrow\rangle$) obtained by driving an RF tone implementing a C_eROT_n. (d) level structure schematic of a divacancy spin coupled to a single nuclear register. The $|+1\rangle$ electron spin state is not shown. (left) C_nROT_e transitions correspond to the peaks seen in b. (right) C_eROT_n RF transition corresponds to the oscillations in c. (e) (top) Quantum circuit used to generate a bipartite entangled state between an electron and nuclear spin. (bottom) Resulting density matrix ($|\rho|$). The third initialized qubit is omitted. All data are taken at $T = 5$ K

register on one of the nearest-neighbor lattice sites (denoted Si_I, Si_{IIa} or Si_{IIb})[268]. When the hyperfine coupling exceeds the linewidth (order $1/\!/T_2^*$) of the electronic state (Fig. 11.1a), oscillations due to these nuclear spins are observable in Ramsey experiments. We refer to such nuclear spins as strongly coupled. This strong coupling splits the $m_s = \pm 1$ electronic ground state levels, which results in pairs of resolved transitions that enables direct selective control of this two-qubit state using external radio frequency (RF) magnetic fields.

Here, we demonstrate such a strongly coupled system by isolating a single c-axis (kk) VV0 with a nearby ^{29}Si at theSi_{IIa} site (parallel hyperfine $A_\parallel = 2\pi \cdot 13.2$ MHz) in natural 4H-SiC. In this case, because the electron spin linewidth (1 MHz) is much lower than the hyperfine splitting $A_\parallel$, we observe two individually addressable transitions corresponding to the two nuclear spin states (Fig. 11.1b). To polarize this nuclear register, we make use of two iterations of algorithmic cooling in which we optically polarize the electron spin and then swap this polarized state to the nuclear spin[269]. Using this method, we can achieve a high initialization fidelity (93%) as measured by the peak asymmetry in the optically detected magnetic resonance spectrum shown in Fig. 11.1b.

After nuclear initialization, we prepare the electron spin in the $m_s = -1$ state and use a 13.2 MHz RF magnetic field to drive nuclear Rabi oscillations (Fig. 11.1c), which we read out by projecting onto the electron spin. Since these oscillations are only driven in the $m_s = \pm 1$ states, this allows us to demonstrate a $C_{\pm 1}NOT_n$ gate[85, 270] which can be performed in 12.7 μs. Throughout these measurements, we also make use of fast (limited only by the hyperfine splitting of the lines) C_nNOT_e gates by applying microwave pulses at one of the two frequencies shown in Fig. 11.1d.

Having demonstrated control over a single nuclear spin, we then increase the number of registers by finding a (kk) divacancy which is strongly coupled to two ^{29}Si spins (with 6% probability for naturally abundant SiC). For this defect, we show that by using both algorithmic cooling and dynamical nuclear polarization[85, 271] (DNP), we can polarize

the full three-qubit system (Fig. 11.1b). We then demonstrate individual control of these registers and calibrate gates operating on either register.

In this three-qubit spin system, we apply the quantum circuit in Fig. 11.1e on the electron and one of the two coupled nuclear spins to create an electron-nuclear entangled state, and measure its full density matrix using quantum state tomography[85] (QST). We evaluate this density matrix using the positive partial transpose test, confirming unambiguously the entanglement in this system with an estimated entangled state fidelity of 81%.

These results demonstrate that single, strongly coupled nuclear spins can be used as quantum registers in SiC with relatively fast gate times. This type of register is useful for QND measurement of the nuclear spin and more generally for any applications that require fast operations[272] on ancilla qubits [273, 274]. However, the number of available nearby nuclear sites which can be controlled in this way is limited. Additionally, the high coupling strength makes these nuclear registers more sensitive to stochastic noise from the electron spin and limit applications where repeated electron initialization and control is necessary[80, 275], such as in long-distance quantum communications[276] or entanglement distillation[204].

11.3 Weakly coupled nuclear memories

To complement these strongly coupled registers, we therefore investigate nuclear spins which are weakly coupled to divacancy electron spins. In order to access these memories and go beyond the $1/T_2^*$ limit, we use an XY8-based dynamical decoupling sequence to perform nanoscale NMR[140, 186, 277, 278] of the nuclear environment of a (kk) divacancy (Fig. 11.2a). This sequence (Fig. 11.2b) not only protects the electron spin from decoherence, but also allows for selective control of nuclear spins even when their hyperfine coupling is lower than the electron spin linewidth. In this measurement, each nuclear spin produces a series of dips in the coherence function at a pulse spacings[186] $\tau_k \approx \frac{(2k+1)\pi}{2\omega_L + A_{||}}$ at integer order k and

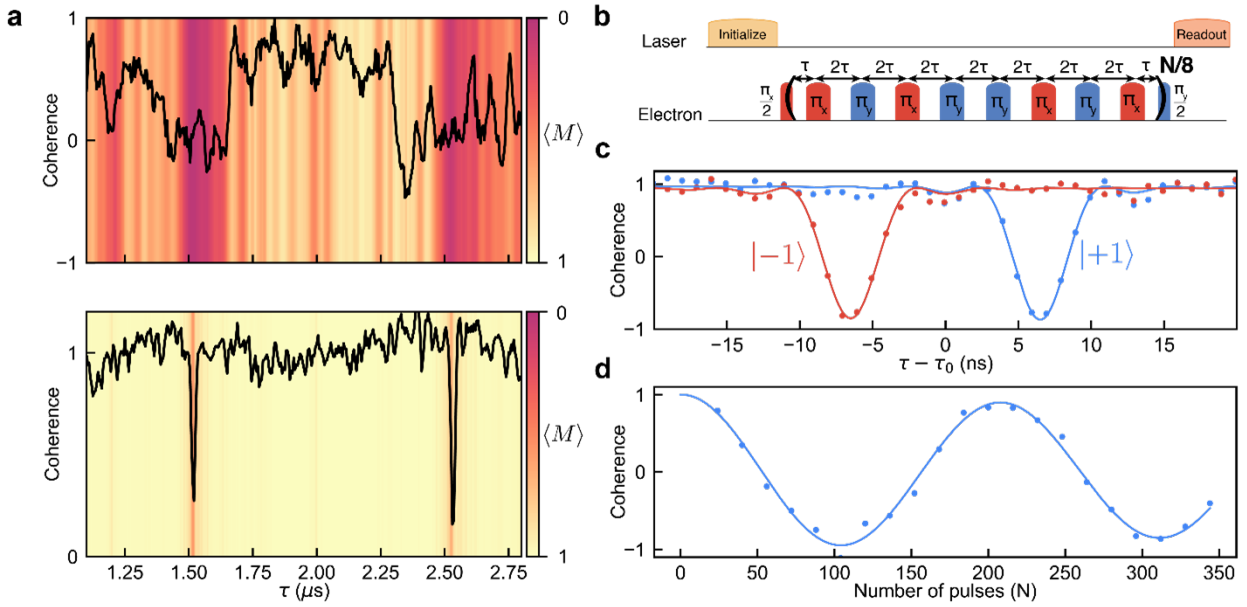

Figure 11.2: Spectroscopy and control of weakly coupled nuclear spins. (a) CPMG based NMR spectroscopy of the nuclear environment of an example *kk* divacancy in a natural (top) and isotopically purified (bottom) sample. The data is shown as a black solid line. The background gradient represents the calculated average coherence function obtained over many nuclear configurations M, which represents the expected density of coherence dips. (b) Schematic of the XY8 pulse sequence. (c) Coherence dips (8th order (k=8), $\tau_0 = 6.125\mu$s) using either the $|-1\rangle$ (red) or $|+1\rangle$ (blue) electron spin state, providing a measure of $A_{\|} \approx 2\pi \cdot 650$ Hz. (d) A $C_e\text{ROT}_{x,n}(\pm\Theta)$ oscillation demonstrated on the 6th order ($k = 6$) of the isolated nuclear spin and achieved by varying the number of XY8 subsequence repetitions. After seven XY8 repetitions (total pulse number$N = 56$), a conditional $\pi/2$ rotation is achieved with a fidelity of $F = 97(1)\%$. All data are taken at $T = 5$ K and $B = 584$ G.

Larmor frequency ω_L, corresponding to its specific nuclear precession frequency. With this spectroscopy, we observe that natural SiC has a crowded nuclear resonance spectrum due to the relatively abundant ^{29}Si, making it difficult to isolate single spins with low hyperfine coupling[204] (defined here to be $< 2\pi \cdot 60$ kHz). This spectrum, along with *ab initio* cluster-correlation-expansion[5] (CCE) simulations of various possible nuclear spin configurations (Fig. 11.2a), demonstrates that natural SiC is not well suited for isolating single weakly coupled nuclear spins with low hyperfine values.

To address this issue, we use isotopically purified gases to grow 4H-SiC with 99.85% ^{28}Si and 99.98% ^{12}C. In this sample, we once again measure the nuclear environment of a few (kk) divacancies and identify one with a single isolated dip in the coherence function (Fig. 11.2a). We find that the dip positions very closely match the different orders (k) of the Larmor frequency of a ^{29}Si (differing only through the hyperfine value[186]). We further confirm the gyromagnetic ratio for this nuclear spin species by repeating the experiment at a different magnetic field.

Having confirmed that the dips correspond to a ^{29}Si nuclear spin, we perform spectroscopy in both the $\{m_s = 0, m_s = +1\}$ and the $\{m_s = 0, m_s = -1\}$ basis (Fig. 11.2c), and measure a small $A_\parallel \approx 2\pi \cdot 650$ Hz[186], which would not be resolvable in a Ramsey experiment. Low $A_\parallel$ nuclear spins are especially useful as robust quantum memories because the dephasing of the nuclear spin caused by stochastic noise from the electron is particularly sensitive to the parallel component of the hyperfine tensor ($A_\parallel$)[80].

Fixing the pulse spacing (2τ) to a specific coherence dip ($k = 6$), we then vary the number of pulses (N) to coherently control this weakly coupled single nuclear spin[135, 186]. The corresponding $C_e\text{ROT}_{x,n}(\pm\Theta)$ oscillations observed (Fig. 11.2d) allow us to measure the perpendicular hyperfine component $A_\perp \approx 2\pi \cdot 11.45$ kHz (where $\theta \approx \frac{A_\perp \cdot N}{\omega_L}$) and confirm the successful application of a maximally entangling two-qubit gate [135]. If no other nuclear spins were present, one could choose any resonance order (k) to perform the two-qubit gate.

In practice however, as k increases, the resonance of the isolated nuclear spin separates from the rest of the bath which drastically increases the two-qubit gate fidelity. Here, even in the isotopically purified sample where the nuclear spectrum is sparse, the electron-nuclear gate fidelity increases greatly at higher orders (k) as the resonance separates from the bath (up to 97(1)% at $k = 6$). These results demonstrate the importance of reducing the nuclear spin bath for high fidelity control of isolated nuclear registers with weak hyperfine interactions.

11.4 Isotopic engineering of weakly coupled nuclear memories

With these results in mind, we now turn our attention to estimating the optimal isotopic fraction required to maximize the number of isolated and controllable nuclear memories. Here, we need to strike a balance between too much purification which removes most usable nuclear spins and too little which results in a crowded and unresolvable spectrum. Limiting the gate time to a regime where nuclear-nuclear interactions are negligible, we developed a method to predict the average number of resolvable nuclear memories as a function of isotopic concentration. This is achieved by considering both the intrinsic gate fidelity from the electron-nuclear interaction and the average effect of unwanted rotations from all other nuclear species.

11.4.1 Theoretical system

We consider a system consisting of a central electron with spin-1 and impurities with spin $\frac{1}{2}$ in an external magnetic field; the Hamiltonian is given by:

$$\hat{H} = D\left(\hat{S}_z^2 - \frac{1}{3}S\left(S+1\right)\right) - \gamma_e B_z\ \hat{S}_z - \sum_i \gamma_n B_z\ \hat{I}_{iz} + \sum_i \mathbf{S}\mathbf{A}\ \mathbf{I_i} + \sum_{i\neq j} \mathbf{I_i}\mathbf{P}\mathbf{I_j} \qquad (11.1)$$

where $\mathbf{S}$ is the central spin, S is the total spin quantum number of the central spin, and $\mathbf{I_i}$

are the bath (nuclear or electron) spins. The **A** tensor denotes the hyperfine interaction (spin dipole-dipole interaction) between the central spin and the nuclear (or electronic) baths. The **P** tensor denotes the spin dipole-dipole interaction between the spins belonging to the bath. We assume that the diagonal elements of the density matrix of the central electron do not change in time; hence the terms in the Hamiltonian containing $\hat{S}_x$ and $\hat{S}_y$ are negligible (secular approximation). Under this approximation, we can rewrite Eq.(11.1) for the spin bath driven by the $m_s = 0$ ($|0\rangle$ qubit state) ($\hat{H}_0$) or $m_s = -1$ ($|1\rangle$ qubit state) ($\hat{H}_1$) levels of the central electron spin[47]:

$$\hat{H}_0 = -\gamma_n B_z \hat{I}_z + \sum_{i,j} \mathbf{I}_i \mathbf{P} \mathbf{I}_j \tag{11.2}$$

$$\hat{H}_1 = -\sum_i \gamma_n B_z \ \hat{I}_{iz} - \sum_i \left[A_{zz} \hat{S}_z \hat{I} + A_{zx} \hat{S}_z \hat{I}_x + A_{zy} \hat{S}_z \hat{I}_y \right] + \sum_{i,j} \mathbf{I}_i \mathbf{P} \mathbf{I}_j \tag{11.3}$$

The hyperfine tensors of the nuclear spins were predicted using two levels of approximation, depending on the proximity of the spin to the central defect. For those nuclei located within a distance of up to 10-15 Åof the central defect, the hyperfine tensors were computed using Density Functional Theory (DFT) and the PBE functional[161] with the GIPAW code. We used a supercell with 1438 atoms with Γ-point sampling of the Brilloun zone. Electronic structure calculations were carried out with the Quantum Espresso code[63], and with a kinetic energy cutoff of 40 Ry. GIPAW pseudopotentials were used to model electron-ion interactions. For those nuclei located at a distance larger than 10-15 Å, hyperfine tensors were estimated using the dipolar approximation.

For a given delay between pulses (τ) and number of pulses (N), the total time of the

experiment is $t = N2\tau$, and the coherence function of the qubit is given by:

$$L(t) = \frac{Tr\left[\hat{\rho}(t)\,\hat{S}^{+}\right]}{Tr\left[\hat{\rho}(0)\,\hat{S}^{+}\right]} \tag{11.4}$$

Where $\hat{\rho}$ is the density matrix of the qubit. If the qubit is prepared in a state $|+x\rangle = \frac{1}{\sqrt{2}}(|0\rangle + |1\rangle)$, the coherence function at time t is given by:

$$L(t) = Tr\left[\hat{U}_0\hat{U}_1^{\dagger}\right] \tag{11.5}$$

The conditional propagators $\hat{U}_0$ and $\hat{U}_1$ are defined differently depending on the experiment. For free induction decay (FID, $N = 0$, $t = \tau$):

$$\hat{U}_0 = \exp\left\{\left[-i\hat{H}_0\tau\right]\right\} \tag{11.6}$$

$$\hat{U}_1 = \exp\left\{\left[-i\hat{H}_1\tau\right]\right\} \tag{11.7}$$

For the Hahn-echo experiment ($N = 1$):

$$\hat{U}_0 = \exp\left\{\left[-i\hat{H}_0\tau\right]\right\}\exp\left\{\left[-i\hat{H}_1\tau\right]\right\} \tag{11.8}$$

$$\hat{U}_1 = \exp\left\{\left[-i\hat{H}_1\tau\right]\right\}\exp\left\{\left[-i\hat{H}_0\tau\right]\right\} \tag{11.9}$$

In experiments with number of pulses ≥ 2, the propagators are given by $\hat{U}_0 = \hat{V}_0^{N/2}$ and $\hat{U}_1 = \hat{V}_1^{N/2}$, where:

$$\hat{V}_0 = \exp\left\{\left[-i\hat{H}_0\tau\right]\right\}\exp\left\{\left[-i\hat{H}_1 2\tau\right]\right\}\exp\left\{\left[-i\hat{H}_0\tau\right]\right\} \tag{11.10}$$

$$\hat{V}_1 = \exp\left\{\left[-i\hat{H}_1\tau\right]\right\}\exp\left\{\left[-i\hat{H}_0 2\tau\right]\right\}\exp\left\{\left[-i\hat{H}_1\tau\right]\right\} \tag{11.11}$$

For a system of one electron and one nuclear spin, we can write the Hamiltonian (11.1)

as follows:

$$\hat{H} = D\ \left(\hat{S}_z^2 - \frac{1}{3}S\left(S+1\right)\right) - \gamma_e B_z \hat{S}_z - \gamma_n B_z \hat{I}_z + A_{zz}\hat{S}_z\hat{I}_z + A_{zx}\hat{S}_z\hat{I}_x + A_{zy}\hat{S}_z\hat{I}_y \quad (11.12)$$

Using the notation for coupling parameters adopted previously, we then rewrite Hamiltonian (11.12) as:

$$\hat{H} = D\left(\hat{S}_z^2 - \frac{1}{3}S\left(S+1\right)\right) - \gamma_e B_z \hat{S}_z - \gamma_n B_z \hat{I}_z + A_{||}\hat{S}_z\hat{I}_z + A_{\perp}\hat{S}_z\hat{I}_x \quad (11.13)$$

With $A_{||} = A_{zz}$, being the parallel hyperfine coupling, and $A_{\perp} = \sqrt{A_{zx}^2 + A_{zy}^2}$ the perpendicular hyperfine coupling. The magnetization of the qubit along the x-axis can be computed as the real part of the coherence function L:

$$M = Re\ L\left(t\right) = Re\ Tr\left[\hat{U}_0\hat{U}_1^{\dagger}\right] \quad (11.14)$$

11.4.2 Average fidelity of weakly coupled nuclear memory

In order to understand how many nuclei on average can be used as memory units at a given nuclear spin concentration, we proceed as follows. A given nuclear spin i can be used as a memory unit if the state of the electron spin can be preserved, following a rotation induced by the nuclear spin. For an electron qubit initially prepared in the $|+x\rangle$ state, the fidelity function F measures how well its state is preserved:

$$F\left(|-x\rangle, \hat{\rho}\right) = \langle -x|\hat{\rho}|-x\rangle \quad (11.15)$$

where $\hat{\rho}$ is the density matrix of the qubit. If the fidelity of the qubit rotation induced by nucleus i is higher than a chosen threshold value, then the nucleus is considered a usable memory unit. The threshold value is chosen depending on the purpose of the memory unit,

and typical values are in the range $0.9 - 0.99$. The fidelity of the electron spin is related to the electron magnetization M at given $N,\ \tau$:

$$F_{N\tau}(|\ -x\ |,\rangle\ \rho)\ =\ \sqrt{\frac{1}{2} - \frac{M}{2}} \tag{11.16}$$

At short time scales (compared to the decay of the coherence function), the interaction between different nuclei can be neglected. Then the electron spin magnetization can be written as a product of conditional magnetizations[186] given by the magnetization of the electron interacting with a single isolated nuclear spin. As a function of delay between pulses (2τ) and number of pulses (N) the magnetization is given by:

$$M\left(N,\tau\right) = \prod_{i} M_i\left(N,\tau\right) \tag{11.17}$$

To determine if a given nucleus i in the lattice is available as a memory unit, we consider the magnetization of the electron when the given nucleus is present. The expectation value of the magnetization when the nucleus i is present is:

$$\widetilde{M_i} = E\left(M|M_i \in M\right) = M_i \prod_{j \neq i} E(M_j) \tag{11.18}$$

Where j runs over all other possible nuclear positions. Then M_j is given as:

$$M_j = \begin{cases} M_j & \text{if } j \text{ is present} \\ 1 & \text{otherwise} \end{cases} \tag{11.19}$$

At a given nuclear spin concentration c_j, the expectation value $E(M_j)$ is:

$$E(M_j) = 1 \cdot (1 - c_j)\ +\ M_j \cdot c_j \tag{11.20}$$

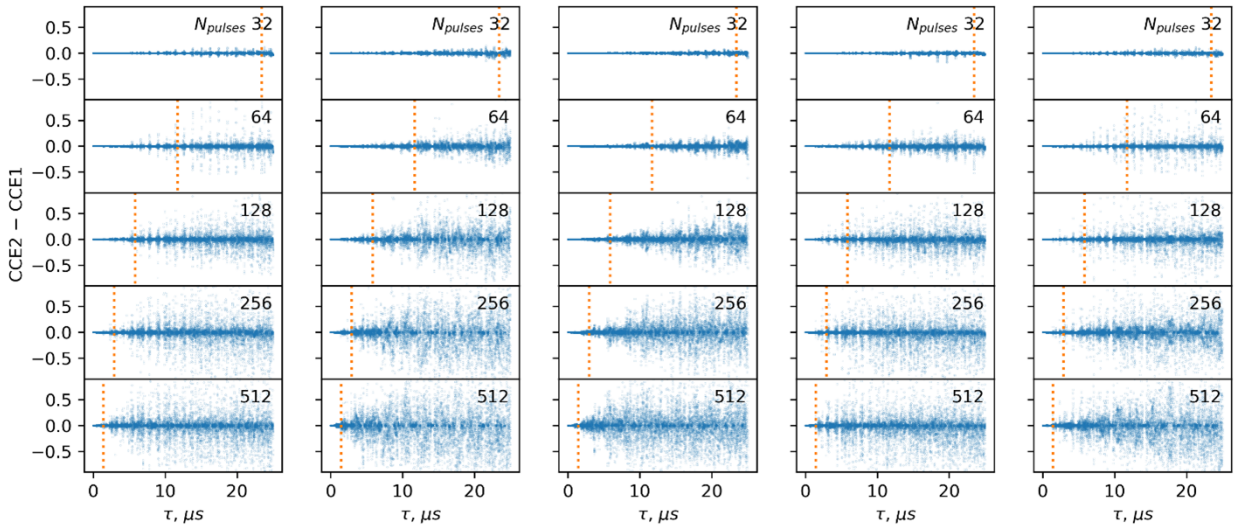

Figure 11.3: Difference in coherence function predicted using the CCE2 and CCE1 approximations. Blue dots show the difference between the coherence functions obtained from CCE1 and CCE2 calculations, and the orange line shows the total gate time (equal to $N2\tau$) of 1.5 ms for six different nuclear configurations at a natural concentration of nuclear spins.

A given nucleus is considered usable as a memory unit if the fidelity of the electron spin after rotation at $\widetilde{M}_i$ is higher than a certain threshold F_{min}. The average number of nuclei i present at this lattice site is equal to the concentration of the isotope c_i. Therefore, the total number of usable memory units can be computed as the sum of c_i for all i that meet the fidelity criterion for at least one set of $N,\ \tau$:

$$N_{mem} = \sum_{i}^{F\left(\widetilde{M}_i\right) \geq F_{min}} c_i \tag{11.21}$$

11.4.3 Limitations of the approach

The method adopted here assumes that the nuclei-nuclei interactions are negligible in determining the electron magnetization. The assumption can be verified by comparing coherence functions obtained at different orders of cluster-correlation expansion (CCE) for random nuclear configurations. A significant difference between the spectra obtained with the CCE1

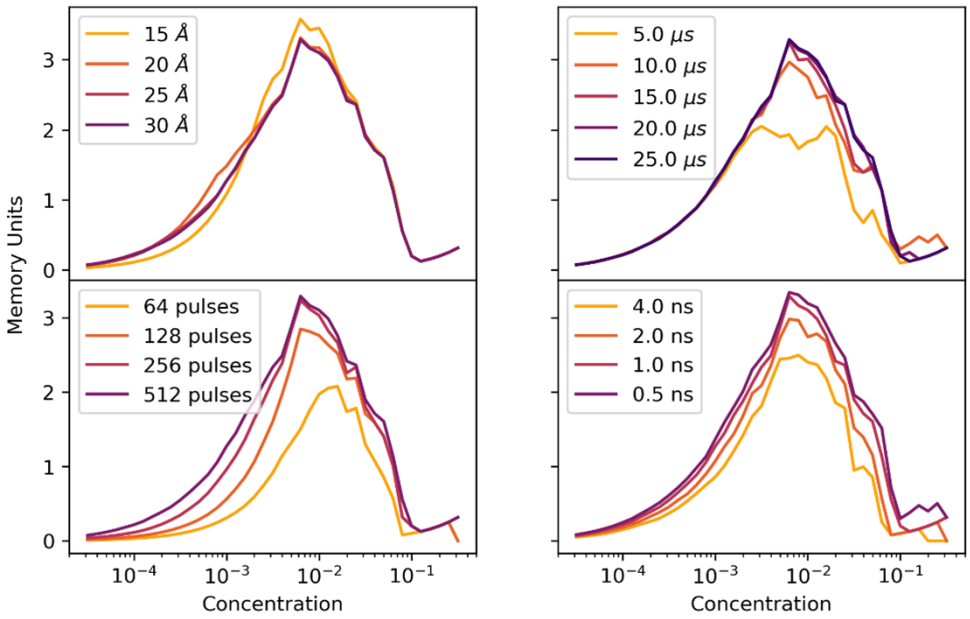

Figure 11.4: Convergence tests for the calculation of usable memory units. Left to right, top to bottom: computed number of usable memory units as a function of nuclear concentrations at a maximum gate time of 2 ms for different bath sizes, maximum τ, number of pulses, and timestep. For each plot, the parameters that are not varied have the following values: bath size = 30 Å, maximum $\tau = 25\mu$s, number of pulses = 512, and timestep = 1 ns.

and CCE2 approximations would indicate nonnegligible nuclei-nuclei interactions. Figure 11.3 shows the difference between the results of CCE2 and CCE1 for 6 different nuclear spin configurations at natural concentration (c(^{29}Si) = 4.7%, c(^{13}C) = 1.1%) for the magnetic field of 500 G. We can see that at long delay times there are significant differences between coherence functions obtained with CCE2 and CCE1. The delay at which the deviations occur is inversely proportional to the number of pulses. Therefore, the maximum available gate time (equal to $N2\tau$) can be found from the value of the delay for a given number of pulses at which significant deviations occur. From the analysis of the CCE spectra for natural isotopic concentrations, the maximum gate time was established to be between $1-2$ ms before significant deviations occur. This theoretical limit determines the maximum gate time, after which the fidelity of the rotation becomes limited by nuclear-nuclear interactions.

Having established the theoretical maximum gate time, we checked the convergence of the

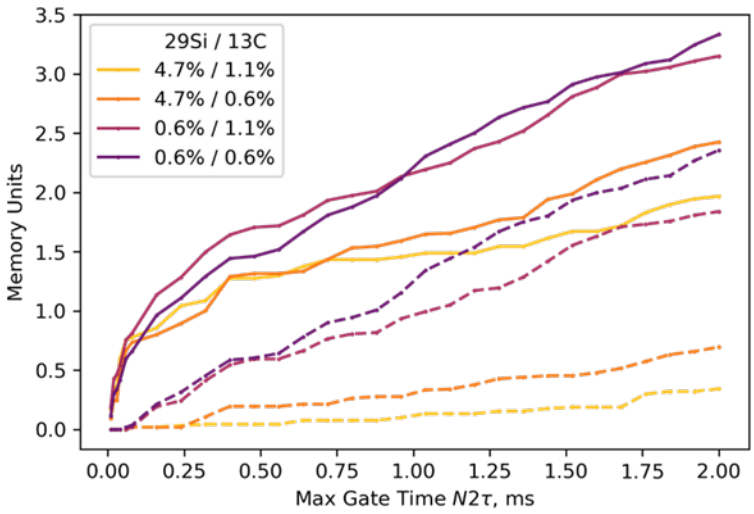

Figure 11.5: Number of usable memory units as a function of the gate time. The different color of the lines denotes different isotopic concentrations, indicated in the inset. Dotted lines show the number of memory units with parallel hyperfine terms below $2\pi \cdot 60$ kHz. The minimum fidelity is equal to 0.95.

number of memory units with respect to the size of the bath, timestep resolution, number of pulses, and the range of the delays between pulses. The convergence is shown in Figure 11.4. It was found that the number of memory units at the magnetic field of 500 G is converged at bath size 30 Å, maximum τ of 25 μs, timestep of 0.5 ns, number of pulses of 512.

11.4.4 Nuclear memory units as a function of isotopic concentration

Figure 11.5 shows the increase of an average number of memory units as a function of the maximum gate time. We can see that the total number is proportional to the square root of the gate time. Furthermore, the purification of Si leads to two-fold increase in the number of available memory units at long gate times, while the isotopic purification of carbon does not lead to any significant improvement. It is interesting to note that the initial part of the curve corresponds to the nuclei with strong hyperfine coupling, and further increase in the number of usable nuclei include those with weak hyperfine coupling. The number of available memory units with weak hyperfine varies linearly with the maximum gate time within the

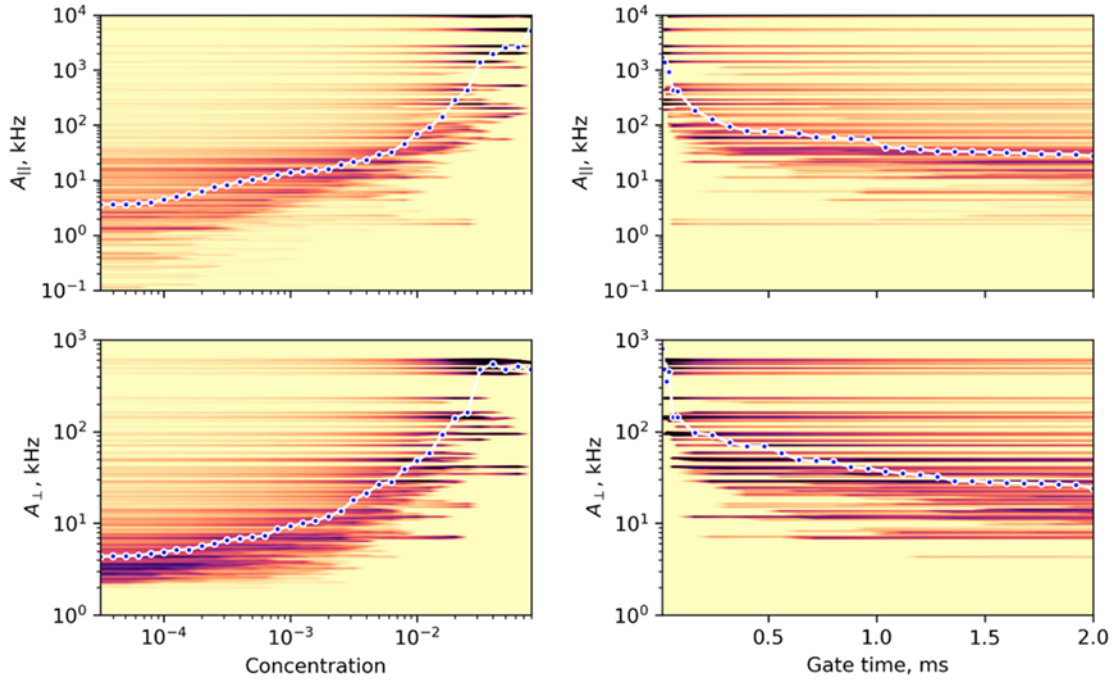

Figure 11.6: Number of usable memory units as a function of the gate time. The different color of the lines denotes different isotopic concentrations, indicated in the in set. Dotted lines show the number of memory units with parallel hyperfine terms below $2\pi \cdot 60$ kHz. The minimum fidelity is equal to 0.95.

chosen timescale.

Hyperfine distribution Figure 11.6 shows the distribution of hyperfine couplings for memory units, available at different isotopic concentration / gate time. The gate time dependence further proves a point outlined above: usage of most of the nuclei with strong hyperfine coupling occurs at small timescales, and extended gate time allows one to access weakly coupled nuclei. Figure 11.7 shows the distribution for different minimum fidelities. Interestingly, the shape of the distribution is the same, albeit shifted towards higher concentrations at lower F_{min}.

Our analysis demonstrates several important aspects of nuclear availability in SiC. First, there exists an optimal nuclear spin concentration (Fig. 11.8a) that maximizes the average number of available nuclear memories which can be controlled within a maximum gate time and at a given minimum gate fidelity. Here, we find that naturally abundant SiC has a pro-

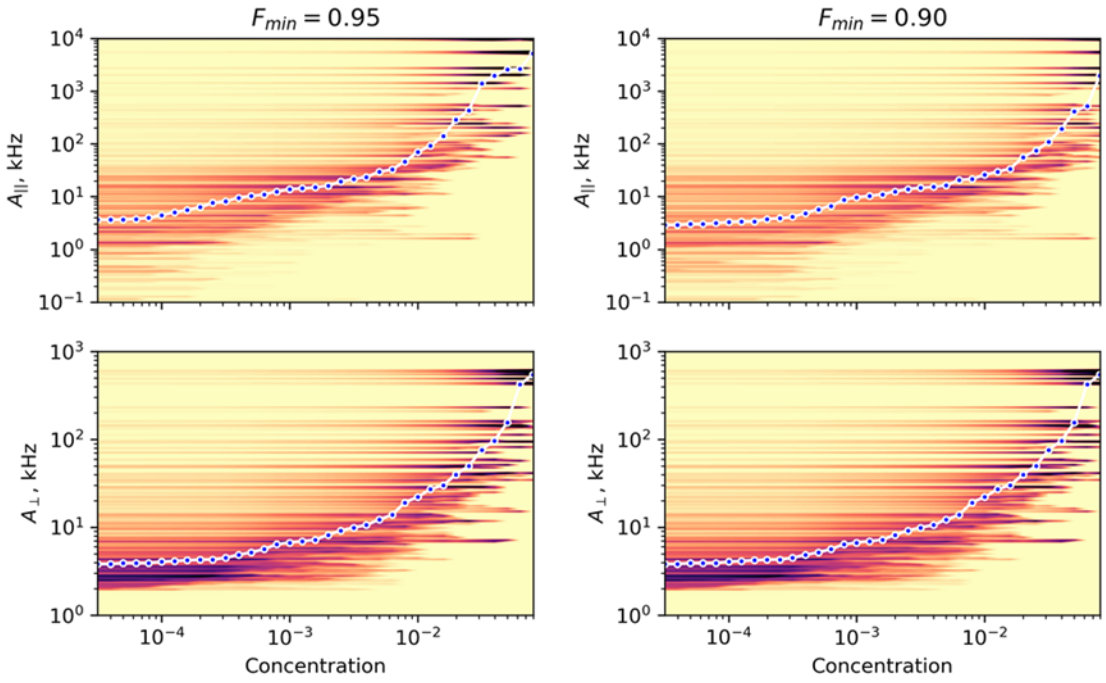

Figure 11.7: Most plausible hyperfine values for memory units at different fidelities. Color corresponds to the probability that memory units in the sample with given nuclear concentration will have the corresponding hyperfine term. The maximum gate time $N2\tau$ 1.5 ms, On the left the minimum fidelity of 0.95 is shown, on the right $F_{\text{min}} = 0.90$. Blue circles show the median of hyperfine values at the given concentration.

hibitively high concentration of ^{29}Si, which prevents the isolation of nuclear memories with low hyperfine coupling ($\leq 2\pi \cdot 60$ kHz). This reinforces the importance of isotopic engineering for nuclear memories in SiC and explains the spectrum observed in Fig. 11.2a. Second, the hyperfine values of the resulting controllable memories vary with isotopic concentration (Fig. 11.8b). At high concentration, nuclei with moderate hyperfine ($> 2\pi \cdot 60$ kHz) contribute to most of the available memories, while low hyperfine nuclear spins are unresolvable. On the other hand, a lower isotopic concentration results in a less crowded spectrum and allows for the isolation of nuclei with lower hyperfine. The choice of nuclear concentration thus not only determines the total number of available quantum memories, but also the distribution of hyperfine values for these controllable nuclei.

Furthermore, we note that there is a tradeoff between the maximum allowable gate time

and the number of available nuclear memories. While longer gate times allow for the resolution of more distant nuclei, this increase is shown to be only sublinear. Additionally, when both nuclear species are utilized, the SiC binary lattice may provide roughly double the number of resolvable nuclear registers compared to a monoatomic crystal.

While the range of desired hyperfine values may differ depending on the particular application, a careful selection of the isotopic fraction is critical to maximizing the number of nuclear spins available in this range. This careful selection also determines the resulting average gate speeds and fidelities, allowing further optimization for the application at hand. These results therefore constitute not only a proof-of-principle demonstration of single weakly coupled nuclear spin control in SiC, but also provide guidance for future isotopic growth of materials for a variety of spin-based quantum technologies.

11.5 High-fidelity qubit control and extended coherences

Broadly, these experiments are all predicated on the divacancy electronic spin being a controllable and long-lived qubit. In this section, we discuss in detail the main factors that limit the coherence of divacancies in SiC and quantify our ability to perform single-qubit manipulation.

We begin by measuring both T_2^* (Ramsey spin dephasing time) and T_2 (Hahn-echo coherence time) of both c-axis (kk) and basally (kh) oriented defects in isotopically purified material. We measure the c-axis defects at $B = 48.8$ G and the basal defects at $B = 0$ G (to benefit from the magnetic insensitivity arising from a clock-like transition[82, 90]).

We report (Fig. 11.9a and 11.9b) T_2^* times of 48.4(7) μs and 375(12) μs for the c-axis (kk) and basal (kh) defects in isotopically purified SiC, compared to 1.1 μs[87] and 70-160 μs [82, 90] in naturally abundant material. These numbers correspond to record dephasing times for spin qubits in SiC[266]. Additionally, despite only moderate isotopic purity, these results are very competitive with NV centers in diamond with much lower nuclear spin

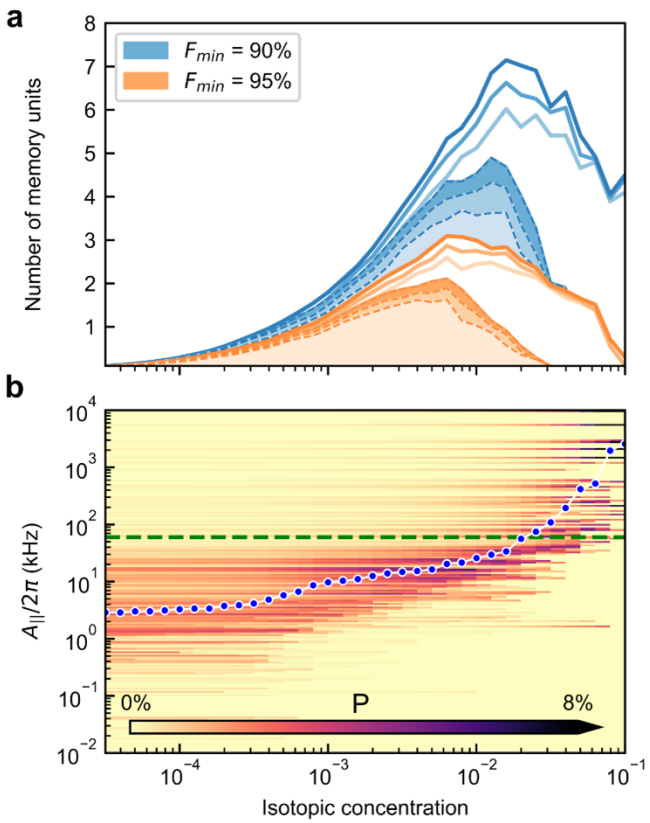

Figure 11.8: Isotopic optimization of nuclear memories. (a) Calculated average number of memory units as a function of isotopic concentration where $[^{13}\mathrm{C}] = [^{29}\mathrm{Si}]$. A memory unit is defined as a nuclear spin that can be isolated and controlled above a given gate fidelity (F_{min}) within the maximum gate time. Solid lines correspond to all memory units whereas the dotted lines with shaded areas correspond to only memories with $A_{||} \leq 2\pi \cdot 60$ kHz. Three different maximum allowable gate times are represented (lightest to darkest: 1 ms, 1.5 ms and 2 ms). (b) Distribution of the hyperfine values for usable memory units as a function of isotopic concentration. Darker colors correspond to a higher probability (P) that memory units, if present and usable, will have the corresponding hyperfine value (maximum gate time = 1.5 ms, $F_{\mathrm{min}} = 0.9$). Blue circles show the median of the distribution at the given concentration. The green dotted line corresponds to $A_{||} = 2\pi \cdot 60$. The values are computed at the magnetic field of 500 G.

concentration[279–281]. This favorable scaling most likely arises from the SiC binary lattice and longer bond length, which results in reduced nuclear flip-flops[5]. These improvements in T_2^* are vital for DC quantum sensing schemes and for achieving strong coupling in hybrid systems[89, 282].

The significant increase in dephasing times arising from the isotopic purification for the c-axis defects shows that magnetic field noise from the nuclear environment is by far the main limiting factor to T_2^* for these defects. We provide further evidence of this by investigating the dephasing in isotopically purified SiC with *ab initio* cluster-correlation-expansion (CCE) simulations. Taking into account the remaining nuclear spin bath, these calculations predict average T_2^* values which are consistent with our experimental observations (Fig. 11.9a).

On the other hand, while basal divacancies benefit from first-order insensitivity to magnetic field noise at $B = 0$ G, this magnetic noise protection comes at the cost of increased sensitivity to electrical fields[99]. Since charge fluctuations can cause significant electric field noise[100], this may explain why the increase in T_*^2 obtained from isotopic purification (Fig. 11.9b) is less pronounced than that of the c-axis divacancies. Furthermore, this magnetic protection also makes nuclear control difficult in the basal (kh) divacancies. This underlines the tradeoffs involved when choosing a defect species to work with.

Next, we perform Hahn-echo experiments to measure T_2 in isotopically purified SiC (Fig. 4c). Although we find a factor of 2 improvement in the coherence time for (kk) defects in this material (2.32(3) ms versus 1.1 ms[87]), we remark that this is a more modest improvement than that of T_2^*. Nevertheless, this T_2 is comparable to the longest observed Hahn-echo coherence time in isotopically purified diamond samples with much greater isotopic purity[73, 240]. Interestingly, the measured T_2 deviates from the predictions of nuclear spin induced decoherence obtained with CCE calculations, which yield an average coherence time of 37 ms. To understand these results, we carried out second order CCE simulations to study the effect of non-interacting electron spin pairs on the coherence time[57]. At the esti-

mated paramagnetic density (impurities and radiation induced defects in the $3 \cdot 10^{14}$–$3 \cdot 10^{15}$ cm^{-3} range, see the next section for details) we find good agreement with experiment (Fig. 11.9d), thus confirming both the accuracy of our theoretical model and the important role of paramagnetic defects in limiting coherence. Our results are consistent with magnetic noise from a weak, but quickly fluctuating paramagnetic spin bath combined with noise from a strong, but slowly fluctuating, nuclear spin bath[283]. As a consequence, T_2^* is limited by nuclear spins, while T_2 is limited by paramagnetic impurities for the c-axis defects. On the other hand, differences in the basal divacancy's coherence compared to other reports[82, 90] likely stems not only from the isotopic purification, but also from sample-to-sample variations in electric field noise, which could be mitigated using charge depletion techniques[100].

11.5.1 Computational details

The coupling tensors of the electron impurity were computed using only dipolar-dipolar interactions, as exchange interactions between electrons are negligible at average distance between impurities of 0.1 μm for paramagnetic density of 10^{15} cm^{-3}, of interest here.

The coherence time is obtained by fitting the coherence function to the form $L(t) = exp\left[\left(\frac{t}{T_i}\right)^n\right]$, where T_i is the coherence time.

Cluster expansion (CCE) calculations for nuclear spins were carried out following Yang and Liu[47] and convergence with respect to the order of the CCE was carefully checked in each case. The clusters were chosen according to the procedure described by Seo et al[5]. In the case of electron spins, the strength of interactions between spins belonging to the bath is comparable to the coupling of the bath spins to the central spin, and the perturbative approach on which the cluster expansion is based upon is not justified. The break-down of the perturbative approach leads to CCE calculations of order 3 or higher to diverge[57]. We can however use an approximate description by assuming that CCE2 is sufficient to correctly estimate electron-electron interactions. This approximation likely

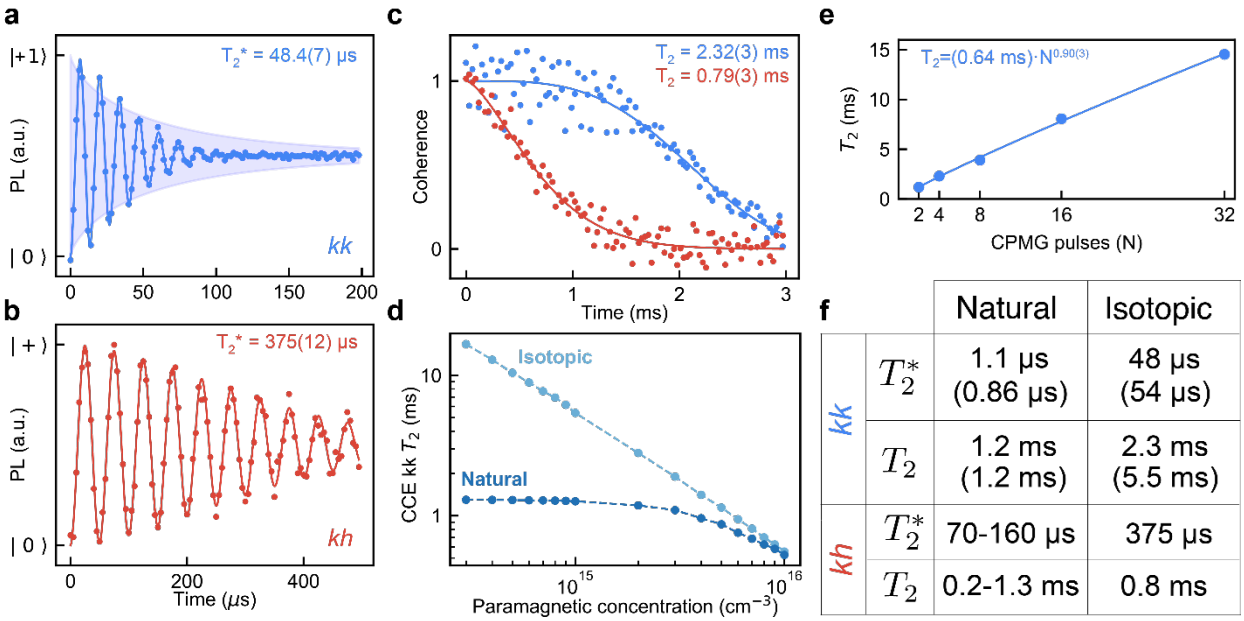

		Natural	Isotopic
kk	T_2^*	1.1 μs (0.86 μs)	48 μs (54 μs)
	T_2	1.2 ms (1.2 ms)	2.3 ms (5.5 ms)
kh	T_2^*	70-160 μs	375 μs
	T_2	0.2-1.3 ms	0.8 ms

Figure 11.9: Divacancy dephasing and decoherence times in isotopically purified material. (a) Dephasing of a c-axis (kk) defect in the isotopic sample at $B = 48.8$ G. The shaded region represents the predicted average results from CCE ($B = 50G$ and paramagnetic density of 10^{15} cm^{-3}). (b) Dephasing of a basal (kh) defect at $B = 0$ G. (c) Coherence function under a Hahn echo sequence for kk (blue) and kh (red) single defects. (d) CCE calculations (including the effects of paramagnetic traps) for a kk defect showing that the expected average Hahn echo T_2 varies greatly based on paramagnetic spin density for both natural (dark blue) and isotopic (light blue) material (at $B = 500$ G). (e) Coherence time for a (kk) defect in the isotopic sample under a varying number of CPMG pulses (N) shows that T_2 increases roughly linearly ($N^{0.90(3)}$) with pulse number ($B = 48.8$ G). (f) Table summarizing representative numbers for T_2^* and T_2 (Hahn echo) in kk and kh defects in both natural and isotopic samples. Natural SiC coherences are taken from literature[82, 85, 90]. Numbers in parentheses are the theoretical numbers obtained by CCE (at $B = 50$ G) with both the nuclear spin bath and a paramagnetic spin bath of 10^{15} cm^{-3}. All data are taken at $T = 5$ K.

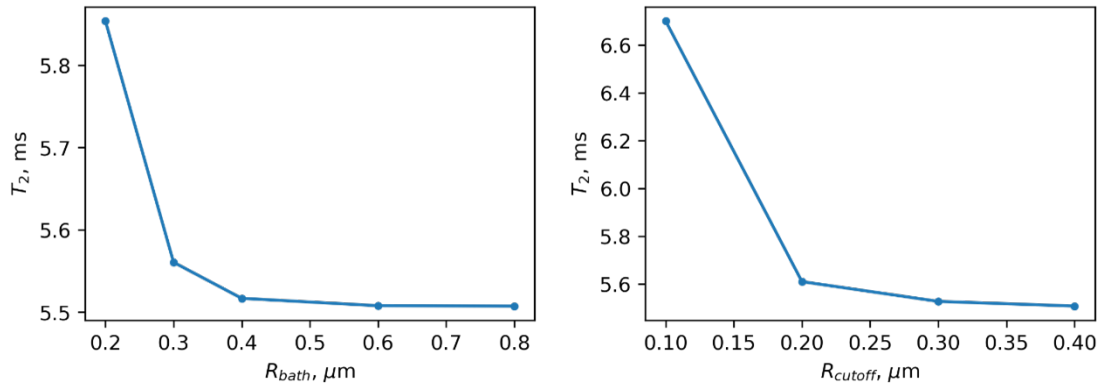

Figure 11.10: Convergence of the coherence time, computed for the electron bath only. On the left panel the coherence time T_2 is reported as a function of bath size (R_{bath}), and on the right panel as a function of the cutoff distance (R_{cutoff}) between electron spins

yields underestimated coherence times at a given concentration of impurity electron spins, as in real systems the flip rate of electron pairs is reduced due to non-pair-wise interactions with other electrons. But at small electron spin concentration, high order effects are expected to be insignificant to determine the qualitative impact of electron spins on coherence times. To compute the impact of electron spins on coherence times, we randomly placed the electron spins at a distance between 0–2 μm from the qubit. Following a procedure to choose the clusters similar to the one used for nuclear spins, in the calculation of coherence functions we only included the pairs of electron spins with distance smaller than a given cutoff distance, and we only considered clusters of spins in a finite bath. Both the pair distance cutoff and the bath size were chosen to be large enough to obtain converge of the coherence function as shown in Fig. 11.10.

Due to different spatial scales of the nuclear-electron and electron-electron interactions, the two baths (electron and nuclear) can be considered as decoupled. Therefore, the total coherence function can be factorized into contributions from electron and nuclear spins, respectively:

$$L\left(t\right) = L_{electron} L_{nuclear} \tag{11.22}$$

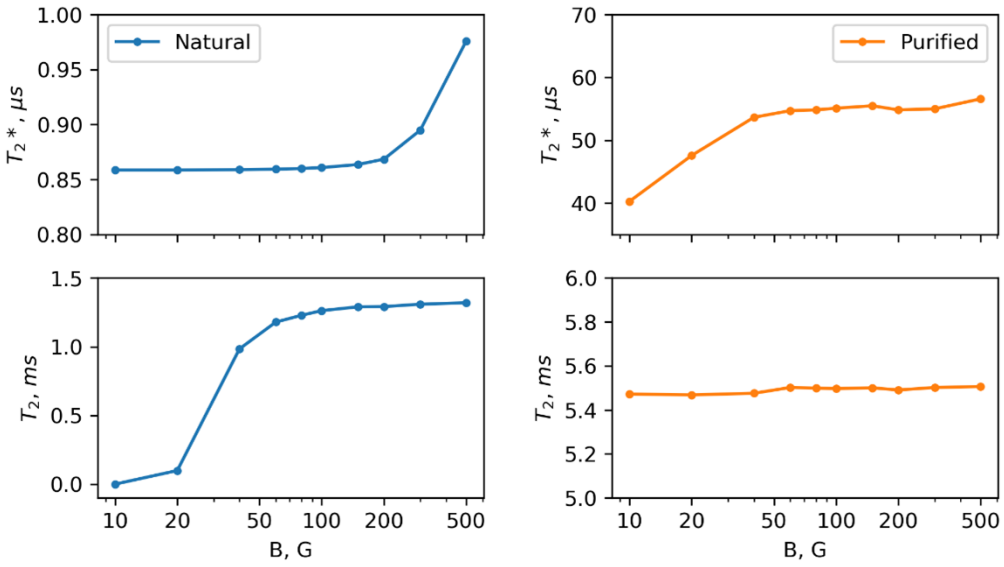

Figure 11.11: Coherence times as a function of magnetic field (B). The coherence time T_2 of the natural material is shown on the left-hand side, and that of the isotopically purified material is on the right-hand side.

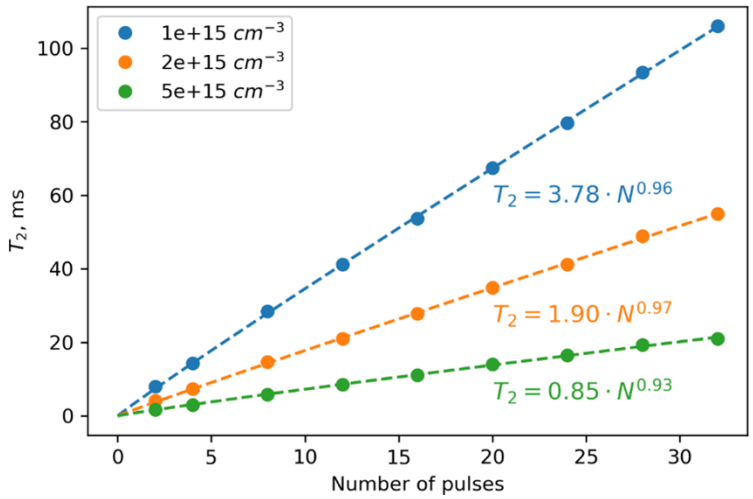

Figure 11.12: Theoretical CPMG scaling. The coherence time, limited by paramagnetic impurities, as a function of number of pulses in a CPMG sequence for three different paramagnetic densities. The dashed lines correspond to the power law fits with the scaling shown in picture. Simulation is for a (kk) divacancy.

The coherence function was obtained by averaging over the results of 200 (1000) calculations for different configurations of electron or nuclear spins, in the presence of a magnetic field of 50 G (500 G). In the experimental measurement, the pulse bandwidth used to control the qubit state allows to simultaneously excite only a small subpopulation of the divacancies in the SiC sample. In this subpopulation, the energy splitting of the qubit levels does not deviate significantly from that of isolated divacancies. Hence, when computing the average coherence time to be compared with experiments, we need to exclude from the calculation the nuclear configurations whose hyperfine coupling would lead to significant deviation in energy splitting from that of an isolated divacancy. Therefore, only nuclear configurations with maximum parallel Hyperfine coupling < 1 MHz were considered. However, we note that when including all the configurations, irrespective of their hyperfine coupling, we obtained very similar T_2 values and T_2^* values within 5-10%, for natural concentration.

The computed values of T_2 and T_2^* for both isotopically purified and natural materials (with free electron concentration of 10^{15} cm^{-3}) as a function of magnetic field are shown in Figure 11.11. In both cases, the T_2^* is not significantly impacted by changes in the magnetic field, while T_2 is impacted: in particular in the natural material we observed a considerable increase in nuclei-limited coherence time. Instead, in the case of electron-limited decoherence, the effect of magnetic field in the range studied here (see Fig. 11.11) is negligible.

We also compute the average scaling of the coherence time with increasing pulse number in a CPMG sequence. The result is shown in Fig. 11.12. A free power fit shows a scaling exponent between 0.93-0.97 depending on the density of paramagnetic impurities. This is consistent with our observed scaling of 0.90(3) observed in experiment (Fig. 11.9e).

11.5.2 Randomized benchmarking of gate fidelities

Finally, we characterize our single qubit gate fidelities through randomized benchmarking experiments and obtain an average gate fidelity of 99.984(1)% (Fig. 11.13). These bare

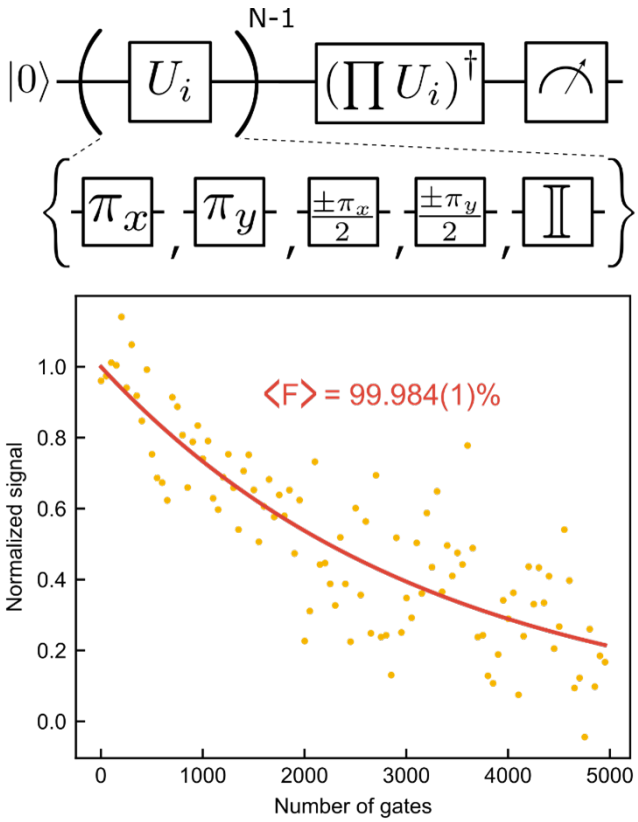

Figure 11.13: Average single qubit gate fidelity as measured by randomized benchmarking. Results obtained by applying N Clifford gates (as represented by the quantum circuit) on the electronic spin of a *kh* defect in the isotopically purified material at $T = 5$ K, $B = 0$ G. From this decay, we extract an average gate fidelity of 99.984(1)%.

fidelities are amongst the highest for single spins in the solid state [267, 284, 285] and exceed the threshold for error correction codes [286–288]. Furthermore, high-fidelity control of the electron spin is crucial to prevent reduced coherence in nuclear spin memories[275]. The long coherence ($T_2^{DD} > 14.5$ ms) and high-fidelity control (99.984(1)%), combined with a >99% initialization and readout fidelity demonstrated in this work establishes the divacancy in SiC as a promising system for future solid-state quantum devices.

11.6 Conclusions

Defect spins in SiC are exciting candidates for wafer-scale quantum technologies requiring stationary qubits and a photonic quantum communication channel. In this work, we provide milestone demonstrations of control for both strongly and weakly coupled nuclear spins in a technologically mature semiconductor material. This work also examines, both experimentally and theoretically, the tradeoffs that are inherent to isotopic purification and offers a pathway towards optimizing nuclear spin concentration to maximize the number of usable nuclear memories.

Our results underline the importance of isotopic engineering in designing materials for solid-state quantum applications. Such engineering can provide a two-fold benefit for quantum memories: it enables control of more nuclear spins by unlocking access to memories with low hyperfine coupling, while also drastically increasing the coherence of these nuclear spins[289]. Moreover, isotopic engineering enables the selection of a hyperfine distribution that can optimally trade off the effect of the "frozen core"[290] against the electron spin induced noise inherent in realistic quantum communications protocols[275]. Further optimization may also be achieved by considering differing nuclear control methods[211, 291]. Additionally, the demonstrated proof-of-principle nanoscale NMR detection of a single nuclear spin (at a distance of 1.2 nm) in SiC provides a route for a functionalizable, biocompatible platform for quantum sensing with polarization and readout in the biological

near-infrared window[292]. Overall, these results cement defects in SiC as attractive systems for the development of quantum communication nodes and underline the importance of isotopic control in material design for future quantum technologies.

CHAPTER 12

BATH-LIMITED DYNAMICS OF NUCLEAR SPINS IN SOLID-STATE SPIN PLATFORMS

This chapter is adapted from the submitted work [9].

Nuclear spins in the proximity of electronic spin defects in solids are promising platforms for quantum information processing due to their ability to preserve quantum states for a remarkably long time. Here we report a comprehensive *ab initio* study of the nuclear spin dynamics in solid-state systems. First, we characterize spin exchange-dependent oscillations of the Hahn-echo signal of the single nuclear spins in iso-nuclear spin baths as a new sensing modality of dynamical-decoupling spectroscopy. Using first-principles simulations, we then quantify the enhancement in the coherence of nuclear spins as a function of distance and state of the electron spin and validate our results with experimental data for the nitrogen vacancy in diamond. Finally, we describe how hybridization of the electronic states suppresses the coherence time of strongly coupled nuclear spins and how dynamical changes of the electron spin state may deteriorate nuclear coherence. The computational framework developed in our work is general and can be broadly applied to predict the dynamical properties of nuclear spins in a wide variety of systems. Overall, our results elucidate many pitfalls that should be avoided to preserve the nuclear spin state in solid-state systems.

12.1 Introduction

Nuclear spins in solids and molecules can preserve their quantum state for a remarkably long time, exceeding seconds [258, 293] and even hours [294, 295], compared to the typical millisecond timescale of electronic spin defects [3, 24], due to their low magnetic moment. Hence nuclear spins are valuable resources for quantum information processing, including memory registers in quantum networks [46, 207, 293, 296], nuclei-assisted quantum sensors

[297, 298] and components of fault-tolerant quantum processors [267, 299]. In particular, in the presence of electron spin qubits in semiconductors and insulators, the hyperfine interactions between the electron and nuclear spins allow for electron-spin assisted initialization and read-out [300–302], enabling full quantum control over the nuclear spin states.

Yet it still remains unclear what is limiting the coherence time of nuclear spins. While the coherence properties of the spin defects have been extensively investigated both experimentally [99, 99, 174, 239, 283, 303–305] and theoretically [52, 245, 306–308], our understanding of the nuclear spin qubit dynamics is minimal. Acquiring a fundamental understanding of nuclear spin coherence in the proximity of electron spin qubits is crucial, e.g., to guide the design of nuclear spin environments for optimal performance of memory registers in quantum network applications [3, 293, 309].

First principles simulations represent promising techniques to investigate decoherence of the spin qubits in solids. From predicting bath spin-induced relaxation [83, 310], identifying new host materials [55, 56], and sensing modalities [51, 179, 185, 311] to engineering spin environments [54, 224, 312], simulations have proved to be crucial in understanding spin-bath interactions in realistic systems. However to date, no attempt has been made to quantitatively characterize nuclear spin coherence processes in the presence of a spin defect using accurate computational methods. Such a characterization is challenging as one needs to account for weak correlated fluctuations of numerous bath spins, where the dominant interaction arises from the electron-nuclear spin coupling.

In this work, we use large-scale cluster-correlation expansion (CCE) calculations in conjunction with density functional theory (DFT) results to perform an *ab initio* study of nuclear spin coherence dynamics. We consider nuclear spins in the proximity of a state-of-the-art spin qubit platform, the negatively charged nitrogen vacancy in diamond (NV) [313, 314]. Our computational results for nuclear spin Hahn-echo and Ramsey coherence times are in excellent agreement with experimental data, bridging the gap between theory and experi-

ment. Our calculations enable the precise mapping of the coherence times to the geometric positions of the nuclear spins, relative to the spin defect, and the identification of the primary sources of nuclear spin decoherence in a wide range of conditions. The decoherence channels identified in our work are general and our conclusions may be applied to any nuclear-electron spin coupled platforms. Overall, our work provides a robust approach to predict nuclear spin coherence dynamics for a variety of systems.

12.2 Nuclear spin in a nuclear spin bath

We begin by investigating the coherence properties of a single nuclear spin coupled to an iso-nuclear spin bath. As an example, we consider a ^{13}C nucleus in diamond with natural isotopic abundance (Fig. 1a). We adopt two theoretical frameworks - the CCE approach [47], which assumes that decoherence arises only from dephasing, and the generalized CCE approach (gCCE) [53], which accounts for both relaxation and dephasing of the central spin (see Appendix 12.6 for in-depth discussion on the methods).

Figure 12.1b shows the computed coherence time of the nuclear spins corresponding to Ramsey and Hahn-echo measurements. We find an excellent agreement between theory and experiment [211]. Ramsey calculations (Fig. 12.1c) converge at the 2nd order of the CCE (CCE2) and Hahn-echo results (Fig. 12.1d) converge at the 4th order (see Section A). The difference between Ramsey signals computed at the first and second order is small, indicating that the single bath spin dynamics dominates the decoherence process, as expected [52]. The order at which the Hahn-echo signal converges is significantly higher than that typically required to investigate the coherence time of electron spins (CCE2) [5, 315, 316], highlighting the need to account for higher-order correlations of the bath dynamics to accurately predict nuclear spin coherence times.

We note that the distributions of the inhomogeneous T_2^* and homogeneous spin dephasing times T_2 overlap in Fig. 1b, and the coherence enhancement from the refocusing pulse is on

average small, a characteristic behavior of a broad noise spectrum [15].

However, the behaviour of the coherence function turns out to be much more complex than one might expect from classical stochastic noise models, where inter-nuclear interactions are simply treated as an effective nuclear spin field [317]. Only with a complete quantum-mechanical treatment can we uncover the complex oscillatory dynamics of the Hahn-echo signal (Fig 12.1d). The oscillations arise from the direct spin-exchange interactions with single spins in the environment: if one neglects the spin exchange (CCE framework), the coherent oscillations are not present in the Hahn-echo signal (Fig. 12.1d). Similar effects have been observed in the electron spin-echo modulation (ESEEM) of electron-radical pairs in organic molecules [318, 319]. Contrary to the ESEEM arising from perpendicular hyperfine couplings [5], these oscillatory features do not disappear with increasing magnetic field.

One can use the spin-echo sequences to extract the spin-exchange couplings between nuclear spins. Here, we derive an analytical expression for the Hahn-echo coherence function $\mathcal{L}(t) = \frac{1}{\mathcal{L}(0)}\left(\langle \hat{I}_{x,0}(t)\rangle + i\langle \hat{I}_{y,0}(t)\rangle\right)$ of a central spin coupled to a single bath spin. We consider the following simplified Hamiltonian of the system:

$$\hat{H} = w_0 \hat{I}_{z,0} + w_1 \hat{I}_{z,1} + \frac{1}{2}\sigma(\hat{I}_{+,0}\hat{I}_{-,1} + h.c.) \tag{12.1}$$

where $\hat{I}_{i,0}$ and $\hat{I}_{i,1}$ are spin operators for the central spin and the bath spin respectively, w_0, w_1 are Larmor frequencies, and σ is the spin-exchange coupling. The presence of $\hat{I}_{z,0}\hat{I}_{z,1}$ type of couplings in the Hamiltonian leads to the same expression for the spin magnetization (see Eq. 12.2 and 12.3 below) and hence they were omitted in Eq. 12.1. Assuming the initial state of the central spin is $|+X\rangle = \frac{1}{\sqrt{2}}(|\uparrow\rangle + |\downarrow\rangle)$ and the π-pulse applies a rotation around the x-axis, we obtain the following expressions for the spin magnetization:

$$\begin{aligned}\langle \hat{I}_{x,0}(t)\rangle = \frac{1}{2} - \frac{\sigma^2}{4\Omega^2}(1 - \cos(\frac{\Omega t}{2}) - \cos(\frac{(w_0+w_1)t}{2}) \\ + \cos(\frac{(w_0+w_1)t}{2})\cos\frac{\Omega t}{2})),\end{aligned} \tag{12.2}$$

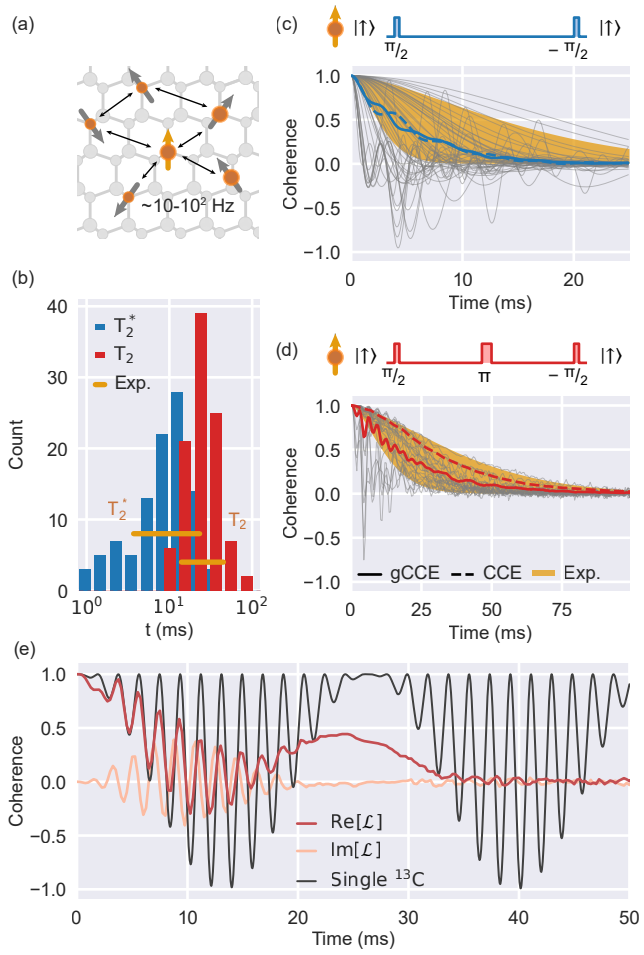

Figure 12.1: (a) Schematic representation of a nuclear spin in a nuclear spin bath. (b) Distribution of Ramsey (T_2^*) and Hahn-echo (T_2) coherence times for nuclear spins computed with the gCCE approach. Horizontal bars show the range of experimental values[211]. (c (d)) Computed Ramsey (Hahn-echo) signals of the nuclear spins. The top diagram represents the sequence of pulses for each type of experiment. Each grey trace was obtained for a single random configuration and computed at the gCCE level of theory. Colored lines show ensemble-averaged coherence curve computed with the CCE (dashed line) and gCCE (solid line) methods. The applied magnetic field is 50 mT. (e) Real (red) and imaginary (orange) part of the Hahn-echo coherence function for a random bath configuration which contains a bath spin coupled to a central spin with $\sigma = 151$ Hz (Eq. 12.1) at a magnetic field of 0.05 mT. Analytical expression for $\langle \hat{I}_x \rangle$ of the system with only the central spin and a single bath spin shown in black (Eq. 12.2).

and

$$\langle \hat{I}_{y,0}(t) \rangle = \frac{\sigma^2}{2\Omega^2} \sin^2 (\frac{\Omega t}{4}) \sin ((w_0 + w_1)\frac{t}{2}), \tag{12.3}$$

where $\Omega = \sqrt{(w_1 - w_0)^2 + \sigma^2}$. For a ^{13}C nuclear spin in a ^{13}C spin bath, Larmor frequencies are equal, $w_0 = w_1 = -\gamma_n B_z$, and the spin-exchange coupling arises from the dipolar interactions $\sigma = -P_{zz}$ (see Appendix 12.6).

Hence, one can observe a strong out-of-phase signal $\langle \hat{I}_y(t) \rangle$ (Eq. (12.3) and Fig. 12.1e), which should be easily detectable in the experiment, providing a new way to directly measure spin-exchange coupling between spins in solids. In contrast to existing methods that probe the nuclear spin pair dynamics with the sensor spin [78, 320], the echo oscillations characterized here require selective π-pulses and readout on one of the spins, but do not necessitate an auxiliary probing qubit.

In addition, our calculations show that the role of longitudinal relaxation in determining the decoherence processes is highly dependent on the given nuclear spin configuration. Relaxation is negligible for some nuclear spins; for others, it completely determines the decoherence rate (see Section A). On average, the spin exchange with the environment accounts for about 40% of the decoherence rate for the ensemble of nuclear spins (gCCE ensemble T_2 22.4(2) ms vs. CCE 36.66(9) ms) and 30% for single ones. Thus, for each specific electronic spin defect present in a solid, one should perform a detailed search within all experimentally available nuclear spins to identify the ones best suited for quantum memories.

12.3 Nuclear spins in the presence of an electron spin

Now we turn our attention to the properties of nuclear spins in the presence of an electron spin.

The CCE method up to the second order was previously used to qualitatively investigate the properties of the nuclear spins in proximity of shallow donors in Si [290]. Here

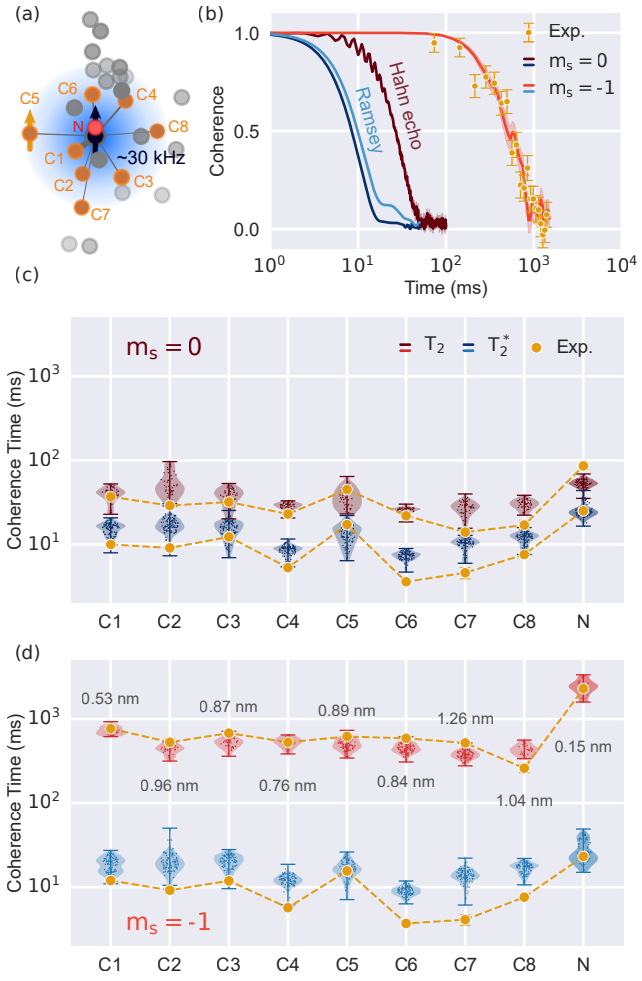

Figure 12.2: (a) Graphical representation of the experimentally determined positions of 27 ^{13}C nuclear spins in proximity of an NV center in diamond from ref. [140]. Orange circles show nuclear spins with measured coherence times. (b) Coherence signals for the nuclear spin C5. Solid lines are theoretical predictions; yellow points are experimental data. (c (d)) T_2 and T_2^* of the nine nuclear spin registers measured by Bradley et al. [211] and represented by yellow lines when the NV is in the $m_s = 0$ ($m_s = -1$) state. Distributions correspond to computed coherence times in 50 random nuclear spin configurations around the 27 nuclear spins, identified in the experiment (see text). The Hahn echo is computed at the 4th (5th) order of the cluster expansion for the ^{13}C (^{14}N) nuclear spins.

we apply the fully converged CCE [47] and generalized CCE [53] schemes with so called "externally aware" cluster corrections [57] (See Appendix 12.6) to quantitatively reproduce the experimental data.

We consider the NV center in diamond as a prototypical example of an electronic spin defect. With a total spin of 1, the NV center can be initialized in three eigenstates, which differ by the projection of the magnetic moment along the [111] axis of diamond ($m_s = -1, 0, 1$). By preparing the NV in the $m_s = 0$ state, one can, up to first order, eliminate the electron spin coupling to the spin bath and recover the same coherence time that nuclear spins exhibit in a pure nuclear spin bath (i.e, free nuclear spins). In the $m_s = -1, 1$ states, the NV center induces a strong hyperfine field on the nuclear spins, which dominates the inter-nuclear interactions. The hyperfine field gradient greatly suppresses the polarization transfer between different nuclei, leading to a significant change in the nuclear spin dynamics - an effect known as frozen core [290, 321].

12.3.1 Experimental validation of the computational protocol

We validate the predictions of our calculations by comparing our results with the experimental measurements of coherence times reported by T. H. Taminiau and coworkers [140, 211, 302]. The data for NV in $m_s = 0$ presents a new and previously unpublished data set obtained on the same NV center as used in these studies [322]. To apply π-pulses to the separate nuclear spins in the experiment, one has to include a short period of time during which the electron spin is in $m_s = -1$ state (see Section A), which might lead to small discrepancies between the theoretical predictions and the experimental data.

We prepare a set of random configurations of nuclear spins placed around a cluster of 27 nuclear spins with experimentally identified positions [140] and compute the coherence of nine selected nuclear spins (C1-C8 and N in Fig. 12.2a). Using *ab initio* computed hyperfine parameters for randomly placed nuclear spins (see Appendix 12.6), we obtain both

Hahn-echo and Ramsey coherence times of all nine nuclear registers.

Our calculations show that the presence of the electronic defect center greatly affects the nuclear spin qubit dynamics under the dynamical decoupling protocol. For example, in Fig. 12.2b, we show that the Hahn-echo coherence time of the C5 nuclear register is enhanced by a factor of 18 when the electron spin is in the $m_s = -1$ state. We also find a clear correlation between distance from the NV and the T_2 of the nuclear spins. Maximum T_2 values are achieved for the ^{14}N nuclear spin, which is located in the center of the frozen core and has a lower gyromagnetic ratio than that of ^{13}C.

The electron-nuclear spin interactions dominate the dynamics of the nuclear spin bath; thus, an accurate description of the nuclear spin's decoherence processes requires accounting for numerous weak correlated fluctuations of the bath spins. For the CCE calculations to converge, it was necessary to include on the order of 10^6 clusters of three and four nuclear spins in our Hahn-echo calculations for ^{13}C nuclear spins, and additionally 10^6 clusters of five for ^{14}N. In contrast to the results obtained for the free nuclear spin bath ($m_s = 0$), the Hahn echoes for the NV center in the $m_s = -1$ state are identical with both the CCE and gCCE methods (see Section A), indicating a complete suppression of the spin relaxation process.

Unlike the Hahn echo, the Ramsey signal remains mostly unchanged when the electron is in the $m_s = -1$, compared to that of the free nuclear spins. The T_2^* is limited by the interactions with the small number of nearest bath spins [52]. We note that each experimental data falls well within the computed distribution (Fig. 12.1b); however the computed T_2^* is overestimated for specific nuclear spins, likely due to the exclusion radius around the experimental cluster used to set up our model (see Appendix 12.6). Our results point at an amount of nuclear spins in the proximity of each of the registers which is larger than expected based on the number of experimentally identified positions [140].

Overall we find excellent agreement between experimental and computed values, thus val-

idating the applicability and accuracy of our computational framework, even in the presence of the dominating hyperfine field of the electron spin.

12.3.2 Coherence time of nuclear spins as a function of position

Having validated our computational framework, we now turn to investigating the dependence of the nuclear coherence time on the position and orientation of the nuclear spins inside the frozen core of the electron spin (Fig. 12.3a).

In Figure 12.3b, we report a complete map of the nuclear spins ensemble averaged T_2, computed as a function of the polar angle Θ and the distance from the electron spin d, for the NV center in the $m_s = -1$ state. We find that T_2 in the limit of high magnetic field ranges from more than 600 ms for nuclear spins within 0.5 nm of the electron spin to less than 50 ms for nuclear spins at distances larger than 4 nm. Figure 12.3c reports cuts along several polar angles, showing a strong dependence of the coherence time on the orientation of the nuclear spin with respect to the NV center. The coherence time reaches its maximum for equatorial nuclear spins in the (111) plane, $\Theta = 90°$. In the vicinity of the NV, the distribution of computed T_2 values matches that of the spin density of the defect (Fig. 12.3a), and the nuclear spins located where the spin density is the highest exhibit the maximum coherence time. In contrast, the axial nuclear spins along the [111] axis have longer T_2 times at larger distances. Interestingly, our calculations show that at about 4 to 5 nm from the NV center, T_2 is the same as in the absence of the electronic spin. This distance is smaller than the one ($d \geq 6$ nm) at which the average strength of the inter-nuclear interactions (~ 60 kHz) exceeds that of the mean hyperfine coupling.

12.3.3 Frozen core size of the electron spin

To quantify the spatial extent of the frozen core of the electron spin, we propose a simplified spin pair-only model, where the size of the bath and spin-pair cutoff radii are obtained in the

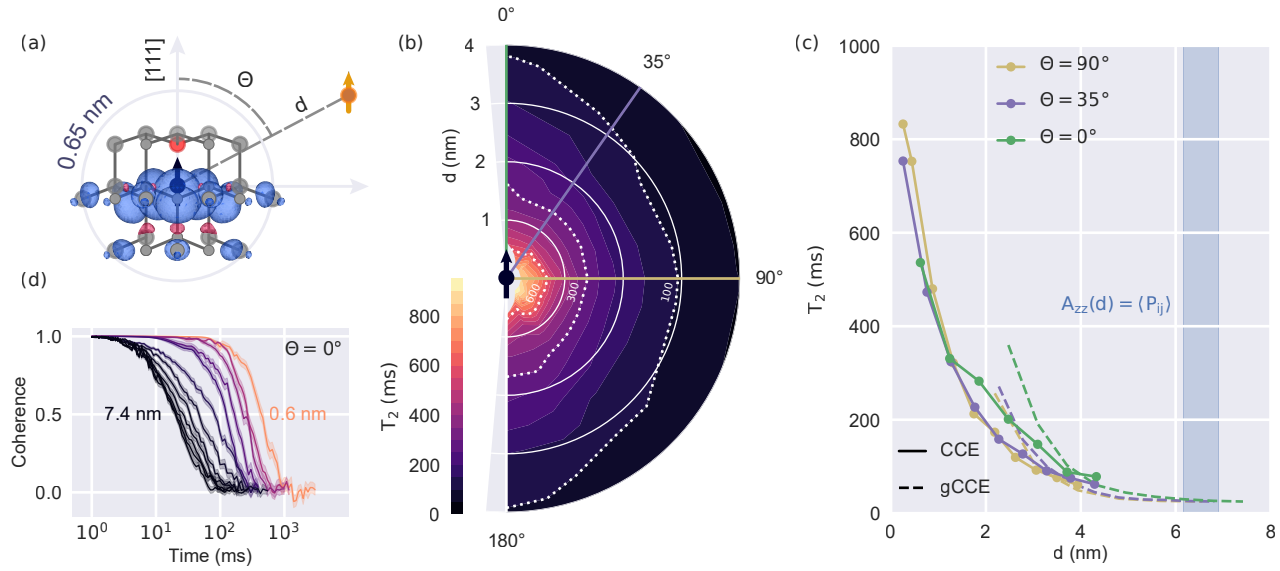

Figure 12.3: (a) Spin density distribution around the NV center in diamond computed using DFT and the PBE functional. d is the distance from the NV center, the polar angle Θ is the angle between the NV axis and the position of the nuclei. (b) Computed ensemble-averaged T_2 as a function of the distance d from the NV center and the polar angle Θ. The coherence time of the nuclear spins at distances ≤ 0.5 nm computed at the magnetic field of 1 T to decouple electron and nuclear spin, for all others distances $B = 50$ mT. Dashed white lines show distances at which the T_2 is (from left to right) 600, 300, and 100 ms. (c) Computed T_2 of the nuclear spin at three polar angles $\Theta = 0°, 35°, 90°$. The generalized cluster expansion (gCCE) simulations (dashed line) were carried out using a smaller number of clusters than CCE, converged for free nuclear spin (see Section A). The value of d where the mean hyperfine coupling is equal to the mean internuclear coupling $A_{zz}(d) = \langle P_{ij} \rangle$ was computed as $\left| \frac{\gamma_e}{\gamma_n} \overline{r}_{ij}^3 \right|^{1/3}$ where $\overline{r}_{ij}$ is the mean internuclear distance (0.45-0.5 nm). (d) Computed ensemble-averaged Hahn echo as a function of the distance from the NV center for nuclear spins aligned along the [111] direction.

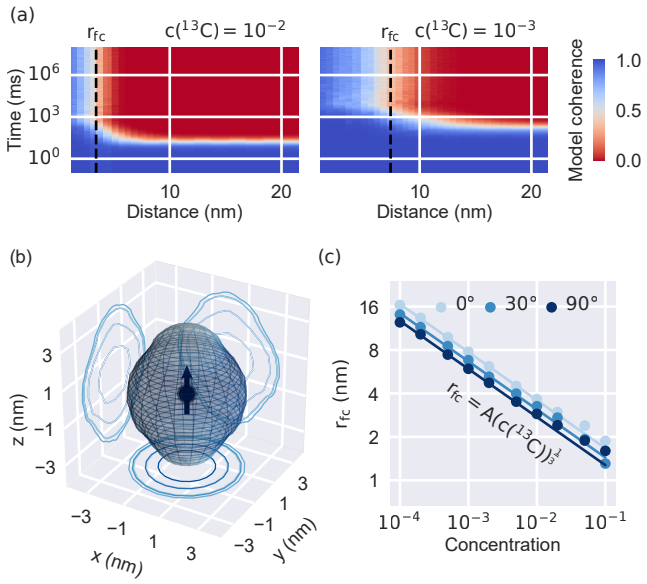

Figure 12.4: (a) Spin-pair coherence function as a function of distance from the NV for two different isotopic concentrations. The frozen core radius r_{fc} is computed as the distance at which the model coherence function at time $\geq 10^6$ ms decreases to $1/e$ (b) Shape of the NV frozen core at natural isotopic concentration. (c) Scaling of the r_{fc} with ^{13}C concentrations at different polar angles Θ (See Fig. 12.3). Solid lines show fits to the function $r_{fc} = Ac^{-1/3}$.

absence of the electron spin (See Appendix 12.6). We find that within this approximation, the computed Hahn echo of the nuclear spins in the vicinity of the electron spin persists indefinitely. In the opposite limit of large distances between nuclear and electron spins, the model yields a coherence function decaying to zero, as expected (Fig. 12.4a). The distance from the electron at which the model coherence function changes its behavior from constant to decaying determines the boundary of the frozen core. Specifically, we define the frozen core radius (r_{fc}) as the distance at which the model coherence at an infinite time decreases to $1/e$.

Using this definition, we find that the frozen core of the NV center is asymmetrical and elongated along the z-axis (Fig. 12.4b). The radius r_{fc} varies from 2.7 nm at $\Theta = 55^\circ$ to 3.8 nm at $\Theta = 180^\circ$, matching the coherence time behavior shown in Fig 12.3c: the computed T_2 decays below 100 ms at 3.8 nm for axial and at 2.9 nm for equatorial spins nuclear spins. In contrast, the r_{fc} dependence on the azimuthal angle is negligible. The total volume of the frozen core is 165 nm^3, which corresponds to about 300 ^{13}C nuclear spins on average.

The frozen core size is correlated with the strength of the parallel component of the hyperfine interaction with the electron spin. Within the point-dipole approximation, this interaction can be written as [323]:

$$A_{zz} = -\frac{\mathcal{G}}{r^3}(3\cos^2\Theta - 1) \tag{12.4}$$

Where $\mathcal{G} = \frac{\mu_0 \gamma_e \gamma_n \hbar}{4\pi} = 7.60$ Hz nm^3 for ^{13}C nuclear spins. We note that for different systems (such as quantum dots in Si [290]), other terms might dominate the hyperfine interactions, and one can expect different shapes of the frozen core. Interestingly, at the angle $\arccos(1/\sqrt{3}) \approx 55^\circ$ where the dipolar coupling vanishes, the value of $r_{fc} = 2.7$ nm is only slightly smaller than 2.8 nm, obtained for $\Theta = 90^\circ$.

We find that the isotopic purification of the system leads to an increased size of the frozen core, where r_{fc} scales as the cubic root of the isotopic concentration in a wide range of spin

densities (Fig. 12.4c). The ratio between r_{fc} at different polar angles remains constant. Such scaling means that the average number of nuclear spins inside the frozen core remains constant for most isotopic concentrations. Only at high concentrations (above two percent of ^{13}C), the scaling deviates from cubic, and then the actual electron spin density distribution and discrete lattice site positions should be taken into account.

12.3.4 Nuclear spin coherence in a strongly coupled hybrid electron-nuclear spins system

The results of the Sec. 12.3.2 are valid when electron spin and nuclear spin states are fully decoupled (i.e., $\hat{S}_z$ and $\hat{I}_z$ commute with the total Hamiltonian). However, at ambient magnetic fields, this condition can be violated when nuclear spin is strongly coupled to the electron, significantly altering the nuclear spin dynamics.

As an example, we consider ^{13}C (Fig. 12.5a) belonging to the first shell of the NV center. We write the central spins Hamiltonian as:

$$\begin{aligned} \hat{H}_{en} = D\hat{S_z}^2 + \gamma_e B_z \hat{S}_z + \gamma_n B_z \hat{I}_z + A_{zz}\hat{S}_z\hat{I}_z + \\ A_{xx}\hat{S}_x\hat{I}_x + A_{yy}\hat{S}_y\hat{I}_y + A_{xz}(\hat{S}_x\hat{I}_z + \hat{S}_z\hat{I}_x) \end{aligned} \tag{12.5}$$

Where $\hat{S}_i$, $\hat{I}_i$ are electron and nuclear spin operators, $D = 2.88$ GHz is the NV center zero-field splitting, γ_e, γ_n are electron and ^{13}C nuclear spin gyromagnetic ratios respectively (see Appendix 12.6 for the full description). $A_{xx} = 99.8$ MHz, $A_{yy} = 176.8$ MHz, $A_{zz} = 108.0$ MHz, $A_{xz} = 25.5$ MHz are hyperfine couplings obtained from DFT calculations and are in good agreement with experimental data [324]. The energy levels of the combined electron-nuclear spins system are shown in Figure 12.5b.

We find that to obtain saturation of the coherence time of the first shell ^{13}C, a much higher magnetic field is required than in the case of free nuclear spins (Fig. 12.5c). Strikingly,

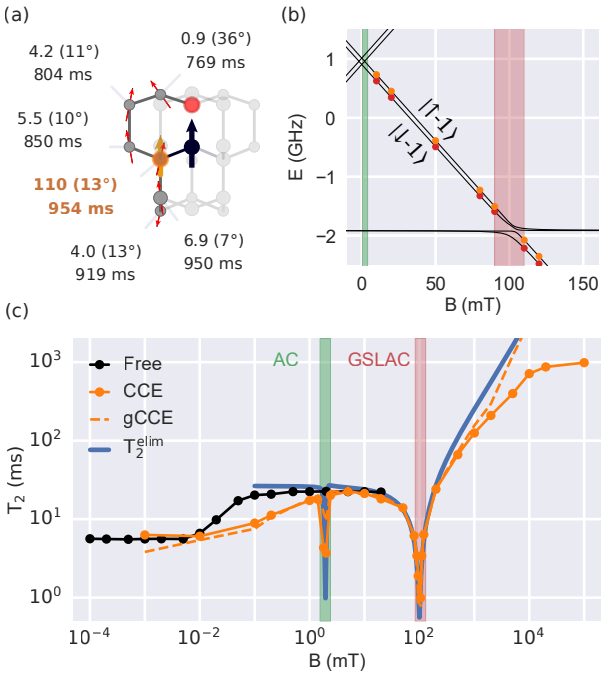

Figure 12.5: (a) Computed first and second shell ensemble-averaged nuclear spin coherence times. For each nuclear spin, we also report the hyperfine coupling $\tilde{A}_{zz} = \sqrt{A_{xz}^2 + A_{zz}^2}$ in MHz, the angle Θ_A between the [111] axis of diamond and the hyperfine quantization axis, and T_2 computed in the limit of a large magnetic field. For the first shell nuclear spin (highlighted in orange), the coherence time is computed at 10 T, and for all others at 1T. Red arrows show hyperfine quantization axes. (b) Energy levels of the hybrid electron-nuclear spins system for NV and first shell nuclear spin as a function of an applied magnetic field along the [111] direction. Orange and red dots correspond to $|0_a\rangle$ and $|1_a\rangle$ levels respectively (see text). (c) Coherence time of the first-shell ^{13}C as a function of the applied magnetic field along the [111] axis, computed with CCE (solid orange line), gCCE (dashed orange line), and hybridization-limited T_2^{elim} (blue line, see text). T_2 for the free nuclear spin (black) is shown as a comparison. The green shaded region denotes avoided crossing (AC) in the electronic levels due to the hyperfine interactions; the red shaded region denotes ground state level anticrossing (GSLAC) of the electronic levels.

at all other applied fields, the nuclear spin T_2 is severely affected by the partial hybridization of the electronic spin levels induced by the hyperfine coupling. To analyze this effect, we express the two energy levels $|0_a\rangle$ and $|1_a\rangle$ of the hybrid electron-spin nuclear spin system as:

$$|1_a\rangle = |-1\uparrow\rangle + \alpha^{1a}_{-1\downarrow}|-1\downarrow\rangle + \alpha^{1a}_{0\uparrow}|0\uparrow\rangle + \alpha^{1a}_{0\downarrow}|0\downarrow\rangle \tag{12.6}$$

$$|0_a\rangle = |-1\downarrow\rangle + \alpha^{0a}_{-1\uparrow}|-1\uparrow\rangle + \alpha^{0a}_{0\uparrow}|0\uparrow\rangle + \alpha^{0a}_{0\downarrow}|0\downarrow\rangle \tag{12.7}$$

In the limit of $B_z \to \infty$, the amplitudes α_i vanish. The latter can be computed by directly diagonalizing the Hamiltonian or from perturbation theory and are expected to be significantly smaller than one. If the reduced density matrices of the electron spin in states $|0_a\rangle$ and $|1_a\rangle$ differ substantially, we expect a significant impact of the mixing of electron spin levels on the nuclear spin coherence time. To estimate the effect on T_2 of the difference in hybridization between the $|0_a\rangle$ and $|1_a\rangle$ levels, we use a modified approximate model first suggested in Ref. [49]. The model was proposed to predict the T_2 of two electron-spin states with similar magnetization in the high-field regime, when slow oscillations of nuclear spin pairs dominate the decoherence process. Using such a model, the contribution to the *nuclear spin* coherence time arising only from the electronic hybridization (which we denote as electron-limited, (elim)) can be expressed as:

$$T_2^{\text{elim}}(B) \approx \mathcal{C}\frac{||P_{0a}(B)|| + ||P_{1a}(B)||}{||P_{0a}(B) - P_{1a}(B)||}, \tag{12.8}$$

where $P_{0a}(B) = \langle 0_a|\,\mathbf{S}\,|0_a\rangle$, $P_{1a}(B) = \langle 1_a|\,\mathbf{S}\,|1_a\rangle$ are the effective magnetization of the electron spin in the $|0_a\rangle$ and $|1_a\rangle$ states respectively, $\mathcal{C}$ is a magnetic field-independent constant, specific to a given system. We find $\mathcal{C}$ to be equal to 0.31 ms for the parameter range appropriate for the system under study (see Section A). The electron-limited coherence obtained from the model agrees well with the predictions of the full quantum mechanical

treatment over a wide range of magnetic fields, thus confirming the significant impact of the hybridization of the electron spin levels on the coherence time of nuclear spins.

Using perturbation theory, we obtain an approximate expression for the electron spin-limited coherence time (see Section A):

$$T_2^{\text{elim}}(B) \approx \frac{4\mathcal{C}(D+\gamma_e B)(A_{zz}+\gamma_n B)}{A_{xz}(A_{xx}+2A_{zz}+2\gamma_n B)} \tag{12.9}$$

We find that T_2^{elim} is proportional to $\tan^{-1}(\Theta_A)$ at intermediate magnetic fields, where Θ_A is the angle between the hyperfine quantization axis $\mathbf{n} = A_{xz}\mathbf{i} + A_{yz}\mathbf{j} + A_{zz}\mathbf{k}$ and the [111] direction of the diamond lattice. Hence our results show that the T_2 of any nuclear spin with a substantial perpendicular component of the hyperfine coupling requires a significantly higher magnetic field to achieve saturation when the electron spin is in $m_s = -1$ state. One can use Eq. 12.9 to estimate the conditions at which the impact of the hybridization of the electron spin levels on nuclear spin T_2 becomes insignificant.

The effect of the partial hybridization of electron spin levels has the highest impact near avoided crossings of energy levels. In the case of electron spins, avoided crossings originating from hyperfine interactions lead to a decoherence-protected subspace [325]. Instead, the effect of these transitions on the T_2 of nuclear spins is extremely detrimental. At each of the avoided crossings, our calculations show a sharp dip in the coherence time of strongly coupled nuclear spins, highlighting the important trade-off one faces in utilizing nuclear spins as memory qubits at avoided crossings [300].

12.4 Effect of electron spin control on nuclear spin coherence

Having analyzed the characteristics of nuclear spin coherence times in the vicinity of an electron spin as a function of m_s, we now investigate how nuclear spin coherence is affected by *changes* in the state of the electronic spin. The dynamical change of the state of the

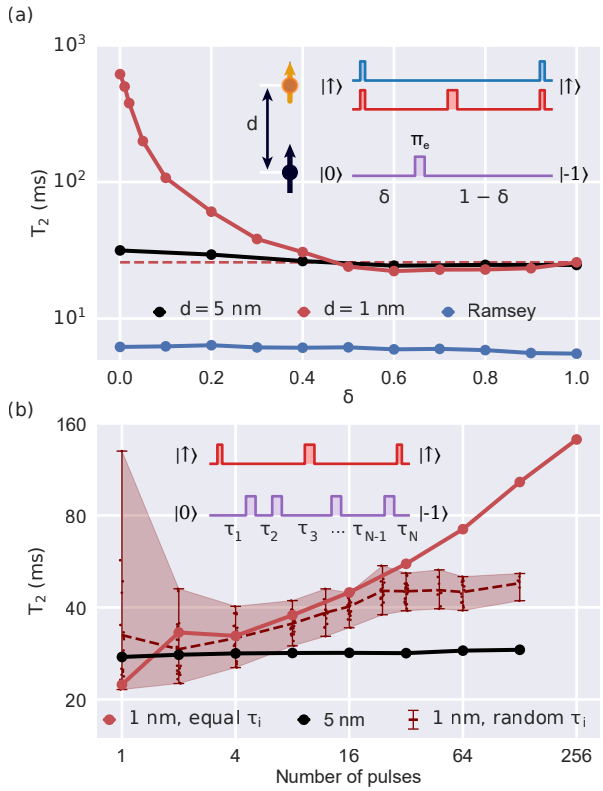

Figure 12.6: (a) Pulse sequences and the corresponding computed nuclear spin T_2 (black and red) and T_2^* (blue) for a single nuclear spin at distances 1 nm and 5 nm from the NV center when a single π_e pulse is applied to the electron spin. The dark blue (orange) arrow represents an electron (nuclear) spin. T_2^* is shown for d = 1 nm.(b) Pulse sequence and the nuclear spin T_2 when many π_e pulses are applied to the electron spin. Red color shows T_2 of the nuclear spin at 1 nm. Spacing between the pulses (τ_i) is either random (points inside shaded area) or constant (solid line). Black line shows T_2 of the nuclear spin at 5 nm.

electron spin has been shown to be a valuable tool for improving nuclear spin coherence. For example, one can use unbalanced echo [326] by applying control pulses to the electron spin to enhance the protection of the nuclear spin ensembles against lattice strain noise.

We analyze the effect of the central spin coherent control on nuclear spin coherence by applying a sequence of π_e-pulses (here, the index e denotes electron spin) to the NV center and we compute the dynamics of nuclear spins at two distances from the electron.

Figure 12.6a shows the nuclear spin coherence when a single π_e-pulse is applied to the electron spin at different fractions of the total time $0 \leq \delta \leq 1$. The electron spin is initialized in the $m_s = 0$ state; after the π_e-pulse is applied, the electron spin rotates into the $m_s = -1$ state. Before the π_e pulse, the nuclear spin precesses with frequency $w_L^{(0)} = -\gamma_n B$; upon the application of the pulse, the frequency is $w_L^{(-1)} = -\gamma_n B - A_{zz}$, leading to the emergence of a nonzero phase of the Hahn-echo signal. In our calculations, we obtain the decay of the coherence time from the absolute value of the coherence function $|\mathcal{L}|$.

We find that the coherence time of the nuclear spins outside the frozen core does not change significantly with the state of the central spin. However, within the frozen core, the change is drastic: when $\delta > 0.5$, the nuclear spin coherence time reaches a local minimum and we observe a 15% drop in T_2, compared to that of the spin in the $m_s = 0$ state, indicating a destructive interference between nuclear and electron control pulses.

Figure 12.6b shows the T_2 of the nuclear spin as a function of the number of applied π_e pulses. The electron spin is initialized in the $m_s = 0$ state. In this case, one can achieve a so-called motional narrowing of the hyperfine field [300]: as the number of π_e pulses increases, the electron-induced field rapidly oscillates and its overall effect can be described by an average field. The motional narrowing leads to a significant enhancement in coherence time. We obtain the highest increase in T_2 for a constant spacing between π_e pulses; however, T_2 is still much smaller than the coherence time achieved when the electron spin remains in the $m_s = -1$ state (620 ms).

12.5 Discussion and Outlook

In this work, we presented and validated a robust computational protocol to describe the nuclear spin dynamics in a nuclear spin bath. Using the proposed protocol, we determined the main noise channels affecting the coherent lifetime of nuclear memories in spin defect systems. In the absence of electron spins, nuclear spin coherence is limited almost equally by dephasing and relaxation processes. However, the interplay between these two processes greatly varies depending on the specific spatial configuration of nuclear spins. This finding indicates that the geometrical arrangements of the nuclear spin environment of spin defects should be carefully characterized [140], in order to identify the optimal nuclear spins to store nuclear quantum states as long as possible.

Our calculations showed that the Hahn echo of single nuclear spins exhibit complex oscillatory features emerging from the spin exchange interactions with the bath. These oscillations arise from the direct interactions between a single bath spin and the central spin, and they can be used to identify and characterize spin exchange interactions with the single spins in the bath.

In the presence of electron spins, we characterized the shape of the frozen core of nuclear spins around the defect with a spin-pair model. The core turns out to be oblong and elongated along the z-axis, matching the dependence of the dipolar hyperfine coupling on the polar angle. The volume of the frozen core is inversely proportional to the concentration of nuclear spins; thus, the total number of nuclear spins inside the frozen core is constant and equal to about 300 ^{13}C, irrespective of any isotopic purification. This value sets a precise boundary on how many ^{13}C nuclear spins it is possible to interact with and, therefore, sense or control using a single NV center.

We analyzed the frozen core effect on coherence time and found that the Hahn-echo T_2 of the nuclear spins can be enhanced by up to 36 times for the closest nuclear spins, when an electron is in the $m_s = -1$ state. Near an NV center, the highest T_2 is attained by equatorial

nuclear spins, closely matching the spin density distribution of the NV center. Further away from the electronic spin defect, it is the polar nuclear spins that retain the highest T_2.

However, in strongly coupled nuclear-electron spin systems, the hyperfine-induced hybridization of electron spin levels acts as a major source of decoherence at commonly used range of magnetic fields. This decoherence channel is most prominent near avoided crossings between energy levels. We find that the prohibitively high magnetic fields would be necessary to suppress the impact of partial hybridization of electron spin states on coherence time in the strong coupling regime.

Finally, we uncovered that the coherent control of the electron magnetic states severely impacts the nuclear spin coherence time inside the frozen core. Even with no noise affecting the electron spin, we find that the nuclear T_2 is dramatically decreased as soon as the state of the electron is changed.

Overall, the validated computational framework proposed here for the study of nuclear spin registers is general and applicable to broad classes of systems and problems. For example, one can use the proposed platform to study the impact of the total spin of an electron qubit on the frozen core effect. In particular, one could investigate the difference in coherence times in the presence of electron spin-$1/2$ qubits, exhibiting a hyperfine field in any state, and NV centers, where one of the magnetic states does not exert a hyperfine field. Importantly, using our computational platform one may screen materials for optimal nuclear spin coherence times [56].

Another interesting avenue of research is the exploration of the predicted frozen core size and shape as an engineering tool for the bottom-up design of spin qubits in molecular systems [327]. With each frozen core corresponding to a computational domain of a specific electron spin, one can envision a nanoscale network of spin processors, with electron spins as processing units and nuclear spins acting as memory qubits.

Finally, our results tell a series of cautionary tales for the applications of nuclear spins

for quantum technologies. From the applied magnetic field to the electron spin control, we elucidated the various noise channels that may adversely affect the quantum state of the nuclear spins.

12.6 Computational framework

The quantum evolution of the combined electron spin-nuclear register is described by the model Hamiltonian:

$$\hat{H} = \hat{H}_{en} + \hat{H}_{en\text{-}b} + H_b \tag{12.10}$$

The central spin Hamiltonian $\hat{H}_{en}$ includes:

$$\hat{H}_{en} = D\hat{S}_z + \gamma_e \mathbf{B} \cdot \mathbf{S} + \gamma_n \mathbf{B} \cdot \mathbf{I}_0 + \mathbf{S} \cdot \mathbf{A}_0 \cdot \mathbf{I}_0 \tag{12.11}$$

Here D is the zero field splitting of the electron spin, $\mathbf{B} = (B_x, B_y, B_z)$ is the magnetic field, γ_n is the gyromagnetic ratio of the ^{13}C nuclear spin, $\mathbf{S} = (\hat{S}_x, \hat{S}_y, \hat{S}_z)$ and $\mathbf{I}_i = (\hat{I}_{x,i}, \hat{I}_{y,i}, \hat{I}_{z,i})$ denote electron and the i-th nuclear spin operators, respectively. The zero index denotes a given nuclear spin chosen as a qubit.

The bath-central spins Hamiltonian $\hat{H}_{en\text{-}b}$ and the bath Hamiltonian $\hat{H}_b$ are defined as follows:

$$\hat{H}_{en\text{-}b} = \sum_i \mathbf{S} \cdot \mathbf{A}_i \cdot \mathbf{I}_i + \mathbf{I}_0 \cdot \mathbf{P}_{0i} \cdot \mathbf{I}_i, \tag{12.12}$$

and

$$\hat{H}_b = \sum_i -\gamma_n \mathbf{B} \cdot \mathbf{I}_i + \sum_{i \geq j} \mathbf{I}_i \cdot \mathbf{P}_{ij} \cdot \mathbf{I}_j \tag{12.13}$$

.

Here $\mathbf{A}_i$ is the hyperfine coupling tensor of the i-th nuclear spin, and $\mathbf{P}_{ij}$ is the dipole-

dipole coupling between spins i and j.

We use the cluster-correlation expansion (CCE) to compute the coherence function of the nuclear spin, defined as:

$$\mathcal{L}(t) = \frac{\langle \hat{I}_-(t) \rangle}{\langle \hat{I}_-(0) \rangle} = \frac{\langle \uparrow | \, \hat{\rho}(t) \, | \downarrow \rangle}{\langle \uparrow | \, \hat{\rho}(0) \, | \downarrow \rangle} \tag{12.14}$$

where $|\uparrow\rangle$ and $|\downarrow\rangle$ are nuclear spin-up and spin-down states and $\hat{I}_-$ are nuclear lowering spin operators, $\hat{\rho}(t)$ is the density matrix of the central spin. In the presence of an NV center we define off-diagonal elements between eigenstates of $\hat{H}_{en}$ corresponding to the diabatic levels $|\uparrow 0\rangle$, $|\downarrow -1\rangle$ for $m_s = 0$, and to $|\uparrow -1\rangle$, $|\downarrow -1\rangle$ for $m_s = -1$ cases.

Within the CCE scheme, the coherence function $\mathcal{L}(t)$ is factorized into the contributions of bath spin clusters with different size [47]:

$$\mathcal{L}(t) = \prod_i \tilde{L}^{\{i\}} \prod_{i,j} \tilde{L}^{\{ij\}} ... \tag{12.15}$$

The contributions are computed recursively from the coherence function of the central spin, interacting with only a given cluster C as $\tilde{L}_C = \frac{L_C}{\prod_{C'} \tilde{L}_{C' \subset C}}$, where the subscript C' indicates all sub-clusters of C.

Depending on the framework, the L_C are computed as follows. In conventional CCE [47, 48] (referred throughout the text as CCE), the relaxation processes of the central spin are discarded, and the coherence function is computed as an overlap in the cluster evolution, dependent on the central spins state:

$$L_C = \langle C | \, \hat{U}_C^{(0)}(t) \hat{U}_C^{(1)\dagger}(t) \, | C \rangle \tag{12.16}$$

Where $|C\rangle$ is the initial state of the cluster C. $\hat{U}_C^{(\alpha)}(t)$ is the time propagator defined in terms of the effective Hamiltonian $\hat{H}_C^{(\alpha)}$ conditioned on the qubit levels. Up to the second

order of perturbation theory it can be written as:

$$\hat{H}_C^{(\alpha)} = \langle\alpha|\,\hat{H}_C\,|\alpha\rangle + \sum_{i\neq\alpha} \frac{\langle\alpha|\,\hat{H}_b\,|i\rangle\,\langle i|\,\hat{H}_b\,|\alpha\rangle}{E_\alpha - E_i} \tag{12.17}$$

Where $|\alpha\rangle$, $|i\rangle$ are eigenstates of the central spins Hamiltonian $\hat{H}_{en}$, $\hat{H}_C$ is the Hamiltonian in Eq. (12.11) including only the bath spins in the cluster C:

$$\hat{H}_C = \hat{H}_{en} + \hat{H}_{en\text{-}b}^{(i\in C)} + \hat{H}_b^{(i,j\in C)} \tag{12.18}$$

In contrast, in the generalized CCE (gCCE) we compute the cluster contributions from the respective elements of the reduced density matrix of the central spin as [53]:

$$L_C = \langle a|\,\mathrm{Tr}_C[\hat{\rho}_{en\otimes C}(t)]\,|b\rangle\,, \tag{12.19}$$

where $\rho_{en\otimes C}(t)$ is the density matrix of the system, which includes bath spins in the cluster C and all central spins. The evolution is computed using the full cluster Hamiltonian $\hat{H}_C$.

All π-pulses are assumed to be ideal, instantaneous, and selective to the spin chosen as a central one.

The strength of interactions between central nuclear spin and bath spins is very similar in the system under study, making the convergence of the expansion order particularly challenging. Here, we use Monte Carlo sampling of bath states [53], and for each pure bath state, we use "externally aware" cluster expansion by adding Izing-type coupling with the bath spins outside of the given cluster in a mean-field way. This approach has been shown to improve the convergence of the CCE method in the all-dipolar spin systems [57].

We use the PyCCE module [108] to carry out all CCE simulations. To approximate the dipolar coupling parameters, we use the actual spin density of the NV center in diamond, computed with density functional theory at the PBE [161] level in a 1000 atoms supercell

using the Quantum Espresso package [63]. The dipolar coupling is then computed as [32]:

$$A_{ab} = \frac{1}{2}\frac{\mu_0}{4\pi}\gamma_e\gamma_n\hbar^2 \int \frac{|\mathbf{r}|^2\delta_{ab} - 3\mathbf{r}_a\mathbf{r}_b}{|\mathbf{r}|^5}\rho_s(\mathbf{r})d\mathbf{r} \tag{12.20}$$

Where $\mathbf{r}$ is the position relative to a given nuclear spin, ρ_s is the electron spin density.

The contact terms of the nuclear spins at distances under 1 nm were computed using the GIPAW module of Quantum Espresso. For every other nuclear spin we assumed the contact terms to be vanishing.

To approximate the experimental nuclear spin bath we generated 50 random bath configurations around the experimental cluster. Assuming that all closest nuclear spins were identified in the experiment, we imposed a cutoff of 0.56 nm around each of the identified nuclear spins. This cutoff is chosen so that the exclusion volume on average contains 27 nuclear spins.

To characterize the extent of the frozen core, we used the CCE2 (spin-pair approximation) with the number of pairs converged in the absence of the electron spin. Using the same number of pairs, we computed the hypothetical coherence signal at various distances from the NV center.

CHAPTER 13

CONCLUSIONS AND OUTLOOK

"It is a dream" — David D. Awschalom

Starting as a simple mathematical model, the cluster correlation expansion method became a powerful tool for quantitatively predicting the spin qubits' dynamics in realistic media. In this thesis, I presented a unified computational framework to conduct such simulations. Within this framework, we've made several improvements to the CCE method to relax some constraints. The method improvements enabled a successful series of papers estimating the coherence enhancement of the spin qubits at avoided crossings. We studied several types of the spin defects in wide-band-gap semiconductors as well as molecular hosts. What we found here is quite insightful: irrespectively of the type of the solid state host, the guiding principles of spin qubit coherence protection at clock transitions stay the same.

I further expanded the boundaries of applicability of the proposed framework as a tool to aid in the experimental characterization of spin qubits. We showed how the qualitative predictions of the model allow one to use it to characterize the material growth on the example of nitrogen doping in diamond. We next used the first principle simulations to guide the experiments in sensing the polarization of the bath around spin qubits, and characterized the difference in bath-induced decoherence in the vicinity of low dimensional materials.

Finally, we used the *ab initio* predictions to flip the script and look at the properties of the bath spins themselves. We investigated how we can improve the applicability of nuclear spins in the vicinity of electron spins and found that there is an optimal concentration of nuclear spins (conveniently located at about 0.5-1%), and that there exists a lot of pitfalls one needs to avoid to preserve the coherence of nuclear spins.

But the good work never stops. There are quite a few avenues one would want to explore with first principles to ensure the practical applicability of spin defects as solid-state qubit platforms.

Understanding the surface spins noise from the first principles

In chapter 10, I have shown that the CCE method can efficiently predict the properties of the electron spin qubit in the electron spin bath in the bulk materials. However, the defects must be placed near the surface for sensing applications. In this regime, a dominating effect comes from the surface noise. And it is well known that the surface spins have very short T_1 lifetimes, dominated by the other noise sources, usually Markovian in nature. Accounting for the classical noise environment of the bath spins would require substantial theoretical developments in addition to the computational effort. Here I envision a thrust to derive the cluster expansion, starting with the master equation instead of the von Neumann equation.

Nuclear spin memories

Using CCE, one can obtain excellent agreement with the experimental data for the nuclear spin dynamics in the most basic spin coherence experiments, as shown in chapter 12. However, all experiments in this chapter are assumed to be completely coherent, and no noise is introduced when one changes the state with the electron spin. The natural next question to ask is how the *incoherent* reset of the electron spin (for example, in the entangling attempts for quantum networking applications) will affect the memory properties of the nuclear spin. I expect the effect to be severe for strongly coupled nuclear spins.

The other thing left to address is to look at the instantaneous diffusion on the weakly coupled nuclear spins. The decoupling pulses on the nuclear spins are not ideal and can recouple spins with similar hyperfine couplings, inducing the decoherence channel known as instantaneous diffusion. This channel should be straightforward to address with CCE simulations and is worth exploring.

Material growth characterization

Another avenue I want to see expanded is a continued effort to use the simulations in the material synthesis presented in chapter 10. Building an automated framework in collaboration with the experiment to characterize single spin defects would help solve the scaling of spin defect-based technologies.

APPENDIX A

BATH-LIMITED DYNAMICS OF NUCLEAR SPINS IN SOLID-STATE SPIN PLATFORMS: ADDITIONAL INFORMATION

A.1 Note on experimental Hahn-echo measurements of single nuclear spins

In the experiment, to make the π-pulses selective to a specific nuclear spin, one has to rotate NV into $m_s = -1$ state for a short period of time, regardless of the NV state of interest. This means that even the data for $m_s = 0$ state includes a small fraction of time during which the NV is in $m_s = -1$ state. Depending on the nuclear spin, this time is between 0.3-1.6 ms (See ref. [211] Table S3 for specific gate times), which can lead to the nuclear spin acquiring an additional phase, not present in the simulations.

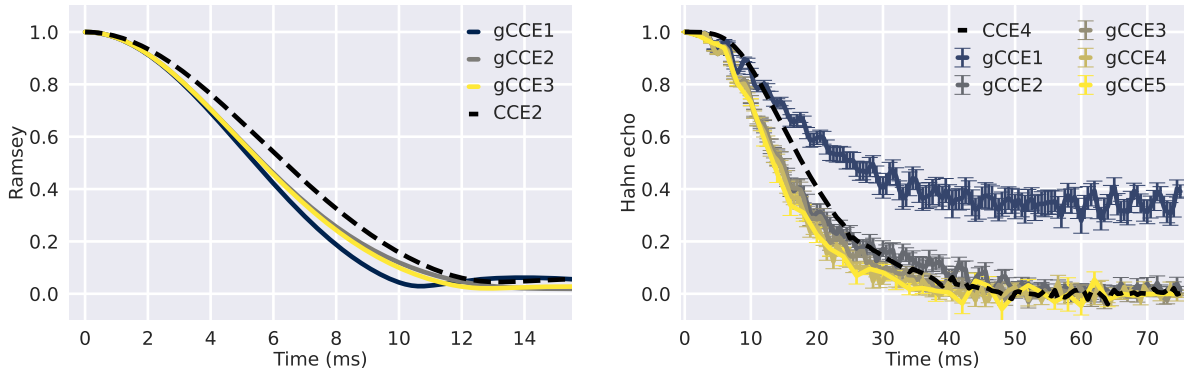

Figure A.1: Coherence function convergence with CCE order for the free nuclear spin in a single random bath configuration. Left: Ramsey signal, right: Hahn-echo signal.The black dash line represents CCE predictions, and all other lines show the results of gCCE calculations. Error bars show 1 SE.

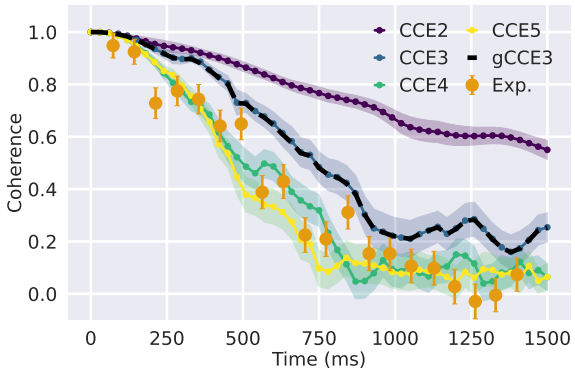

Figure A.2: Coherence function convergence for the C5 memory register from the main text. The shaded area for each coherence curve represents errorbars of 1SE, where SE was obtained from the coherence curves for random bath states. The dashed black line shows gCCE prediction and all other lines show the results of CCE calculations.

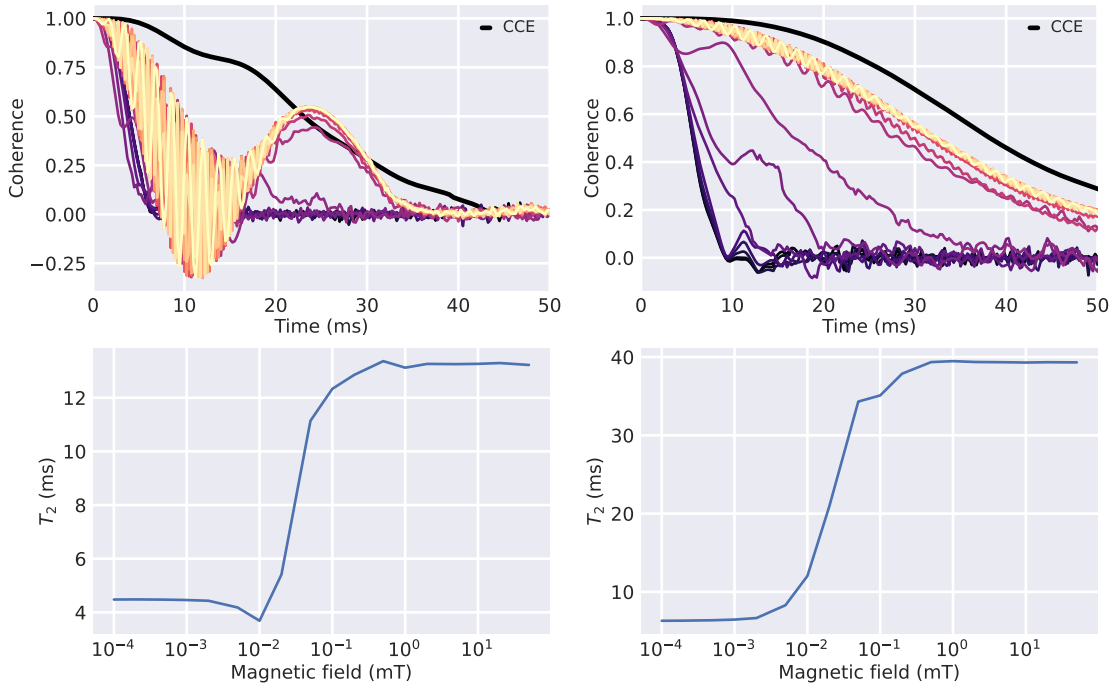

Figure A.3: Hahn-echo coherence function and T_2 as a function of magnetic field for the free nuclear spin in two random bath configurations. Colored lines correspond to the coherence function computed with gCCE at different magnetic fields. Black solid lines show CCE predictions for the high field limit (10 mT).

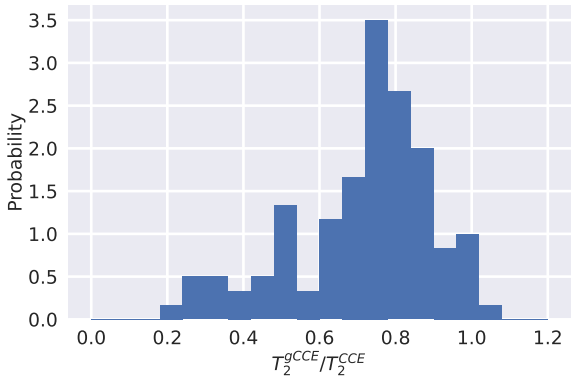

Figure A.4: Histogram of the ratio between T_2 computed at gCCE and CCE level for a free nuclear spin in 100 random bath configurations.

A.2 Convergence of the coherence function calculations

Convergence of the coherence function calculations of the free nuclear spin is achieved with ≈ 1000 bath nuclear spins at distances up to 5 nm. Cluster expansion includes approximately $2 \cdot 10^4$ pairs, $8 \cdot 10^4$ clusters of three, and $8 \cdot 10^4$ clusters of 4.

Figure A.1 shows the convergence of the coherence curve with CCE order for Ramsey (left) and Hahn-echo (right) signals for a random nuclear spin bath configuration. The dashed line shows CCE predictions, and the solid lines show gCCE ones.

The convergence of the nuclear spin coherence time in the presence of an NV center is particularly challenging. Due to the gradient of the hyperfine couplings, the flip-flop interactions between nuclear spins are almost completely suppressed, and a significant number of the nuclear spin clusters contributes to the decoherence rate. The converged calculations at CCE4 order for the Hahn echo of nuclear spins in the vicinity of an NV includes about 1000 bath spins (the same size of the bath as for the free nuclear spins), $2 \cdot 10^5$ pairs, $2 \cdot 10^6$ clusters of three and $2 \cdot 10^6$ clusters of four. The calculations at CCE5 order for the nitrogen nuclear spin include additionally 10^6 clusters of five.

Figure A.2 shows the convergence of the coherence curve with CCE order for Hahn echo of the C5 memory register from the main text in a single random nuclear spin bath

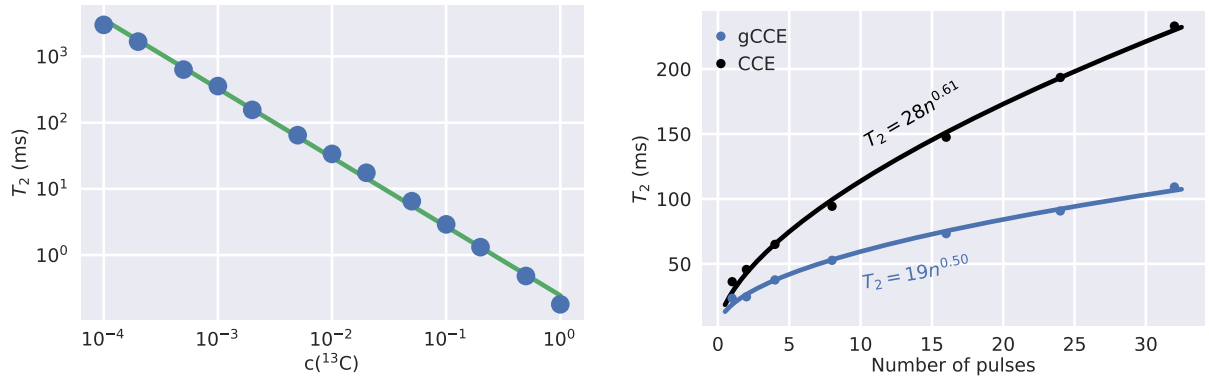

Figure A.5: Left: Ensemble-averaged coherence time T_2 for the free nuclear spin as a function of isotopic ^{13}C concentration in diamond. The coherence is computed with gCCE4. The number of clusters used for each datapoint is equal to the one used at the natural isotopic concentration. Right: Ensemble-averaged coherence time T_2^n of the free nuclear spin as a function of applied pulses n in Carr-Purcell-Meiboom-Gill (CPMG) sequence. Solid lines show a fit to the points.

configuration. The gCCE predictions at third order exactly match the CCE3 curve.

In the bath state sampling method, a small subset of computed coherence values is prone to numerical instabilities due to some cluster contributions being very close to zero. Therefore, a number of divisions by a very small number occurs, which may lead to a significant numerical error. The nonphysical computed coherence function values where $|\mathcal{L}| > 1$ were renormalized as $\tilde{\mathcal{L}} = \frac{\mathcal{L}}{|\mathcal{L}|}$.

A.3 Additional data for the free nuclear spin

Figure A.3 shows the coherence function of the nuclear spin in two random bath configurations. The left configuration is the same one as shown in the main text, Figure 1d. In the gCCE results, we observe rapid oscillations that persist throughout the full range of the magnetic fields studied here. The oscillations frequency scales linearly with the applied magnetic field. The coherence time is converged at a magnetic field of about 0.1 mT.

Figure A.4 shows the distribution of the ratio between T_2, obtained with gCCE and CCE methods. We observe a broad distribution, with the most probable value of the ratio T_2^{gCCE} :

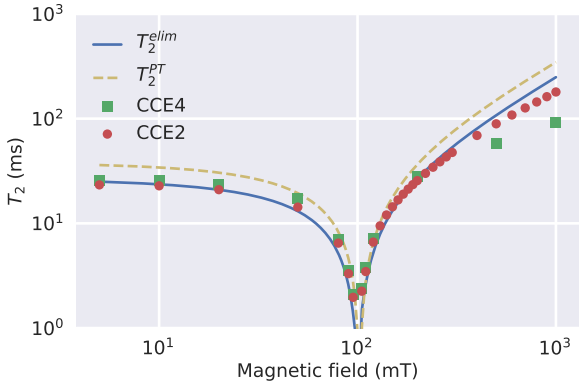

Figure A.6: Ensemble-averaged electron spin-limited coherence time T_2 of the hybrid electron-first shell ^{13}C system computed at CCE4 (squares) and CCE2 (circles) levels as a function of an applied magnetic field. T_2^{elim} is the coherence time computed with Eq. (8) from the main text. T_2^{PT} is the coherence time obtained with Eq. (9) from the main text.

$T_2^{CCE} = 0.72 : 1$. For a few bath configurations, the direct spin exchange completely dominates the decoherence such that T_2 obtained with gCCE is five times smaller than the one computed with the CCE method.

Figure A.5 shows the scaling of the free nuclear spin T_2 as a function of isotopic purification computed with gCCE. We find the T_2 inversely proportional to the nuclear spin concentration, $T_2 = 0.245c^{-1}$. This dependence is the same as the scaling of the electron spin coherence time.

Figure A.5 shows the computed scaling of the coherence time with the number of dynamical decoupling pulses in the CPMG sequence. The coherence was computed at the fourth order of the expansion. We find a significant difference between CCE and gCCE scaling and between the magnitudes of coherence time. However, with an increase in the number of pulses, we expect higher-order correlations to play an even more significant role; thus, the scaling obtained with gCCE4 might be unreliable.

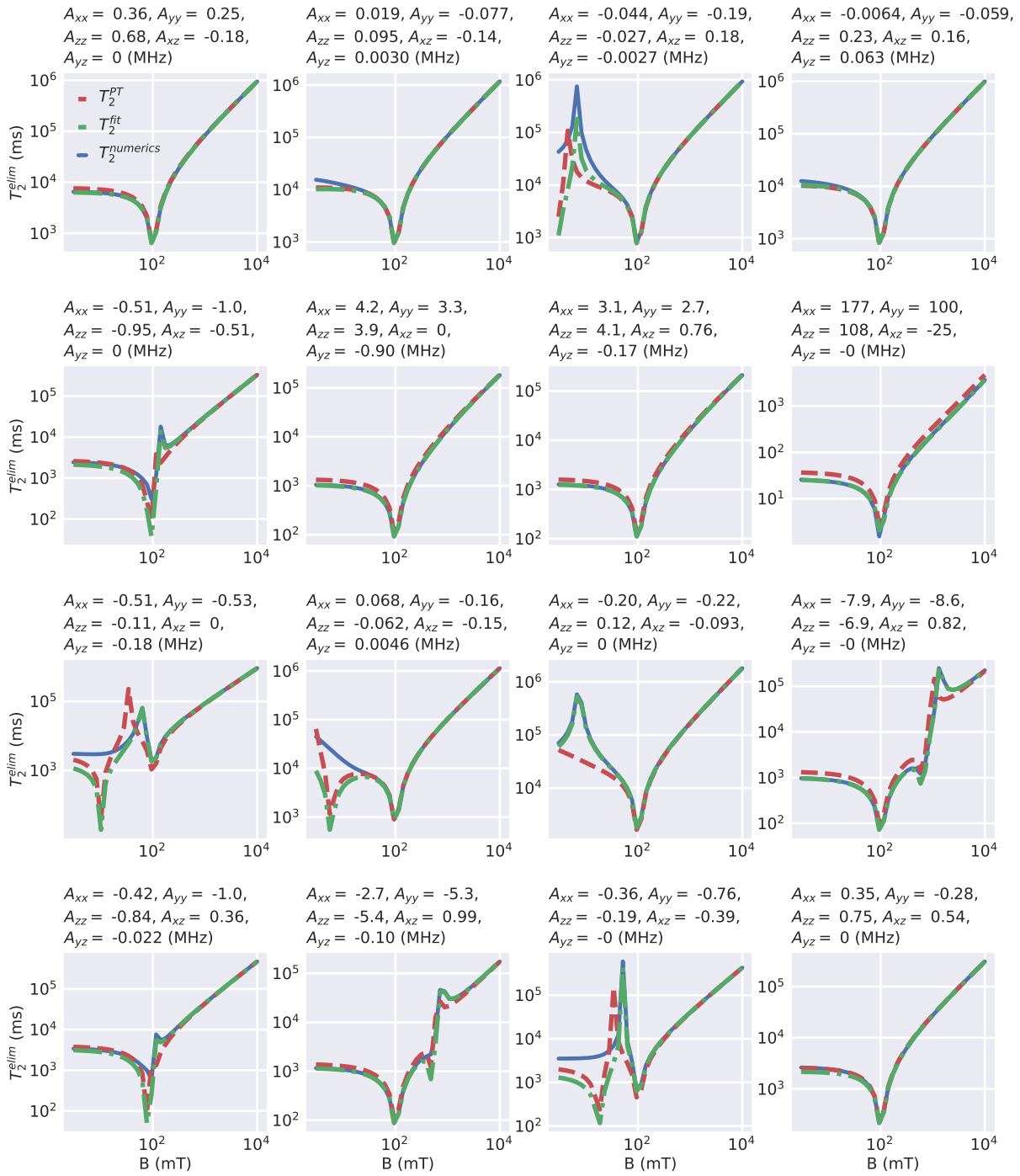

Figure A.7: Electron-limited coherence time T_2^{elim} when electron is in the $m_s = -1$ state for 16 strongly coupled nuclear spins.

A.4 Electron-limited coherence

To recover the value of the $\mathcal{C}$ constant, we run a set of CCE simulations of an electron coupled to the first-shell ^{13}C in the spin bath, setting all interactions between the first-shell ^{13}C and nuclear spin bath to zero. We thus recover the decoherence induced only by the electron spin levels. We then fit the T_2 obtained in this way to Eq. (12.8). We find that for B between 1-500 mT the constant is $\mathcal{C} = 0.31$ ms (Fig. A.6).

The electron spin magnetization for $|0_a\rangle$ and $|1_a\rangle$ can be written in terms of the amplitudes of the spin levels, following the notation in the main text:

$$P_{1a} = (\frac{1}{\sqrt{2}}(\alpha_{0\uparrow}^{1a} + \alpha_{0\uparrow}^{1a*} + \alpha_{0\downarrow}^{1a*}\alpha_{-1\downarrow}^{1a} + \alpha_{0\downarrow}^{1a}\alpha_{-1\downarrow}^{1a*}), 0, -1) \tag{A.1}$$

$$P_{0a} = (\frac{1}{\sqrt{2}}(\alpha_{0\downarrow}^{0a} + \alpha_{0\downarrow}^{0a*} + \alpha_{0\uparrow}^{0a*}\alpha_{-1\uparrow}^{0a} + \alpha_{0\uparrow}^{0a}\alpha_{-1\uparrow}^{0a*}), 0, -1) \tag{A.2}$$

Using first-order perturbation theory, we can approximate the amplitudes of the hybridized states $|0_a\rangle$ and $|1_a\rangle$ as:

$$\alpha_{0\uparrow}^{1a} = -\frac{A_{xz}}{\sqrt{2}(A_{zz} - 2(D + \gamma_e B_z)} \tag{A.3}$$

$$\alpha_{0\downarrow}^{1a} = -\frac{A_{xx} + A_{yy}}{\sqrt{2}(A_{zz} - 2(D + (\gamma_e - \gamma_n)B_z)} \tag{A.4}$$

$$\alpha_{-1\downarrow}^{1a} = \frac{A_{xz}}{(2A_{zz} + 2\gamma_n B_z)} \tag{A.5}$$

and

$$\alpha_{0\uparrow}^{0a} = \frac{A_{xx} - A_{yy}}{\sqrt{2}(A_{zz} + 2(D + (\gamma_e + \gamma_n)B_z)} \tag{A.6}$$

$$\alpha_{0\downarrow}^{0a} = -\frac{A_{xz}}{\sqrt{2}(A_{zz} + 2(D + \gamma_e B_z)} \tag{A.7}$$

$$\alpha_{-1\uparrow}^{0a} = -\frac{A_{xz}}{(2A_{zz} + 2\gamma_n B_z)} \tag{A.8}$$

Leading to the final expression in the main text. In a similar fashion, we can derive the equation when both A_{xz} and A_{yz} are non-zero and obtain the following expression:

$$T_2^{\mathrm{PT}}(B) \approx \frac{4\mathcal{C}(D + \gamma_e B)(A_{zz} + \gamma_n B)}{\sqrt{A_{xz}^2 a_x^2 + A_{yz}^2 a_y^2}} \tag{A.9}$$

Where $a_x = A_{xx} + 2A_{zz} + 2\gamma_n B$, and $a_y = A_{yy} + 2A_{zz} + 2\gamma_n B$

We also find that we can empirically correct the perturbation theory-based equation to obtain a significantly better agreement with the T_2^{elim} from magnetic projections, computed numerically, by adding a factor of two in front of A_{xx} and A_{yy} (Fig. A.7):

$$T_2^{\mathrm{fit}}(B) \approx \frac{4\mathcal{C}(D + \gamma_e B)(A_{zz} + \gamma_n B)}{\sqrt{A_{xz}^2 \tilde{a}_x^2 + A_{yz}^2 \tilde{a}_y^2}} \tag{A.10}$$

With $\tilde{a}_x = 2A_{xx} + 2A_{zz} + 2\gamma_n B$, and $\tilde{a}_y = 2A_{yy} + 2A_{zz} + 2\gamma_n B$. The physical meaning of such a factor remains, however, unclear.

A.5 Shape of the frozen core

Figure A.8 shows the dependence of the frozen core radius as a function of radial Θ and azimuthal ϕ angles for the natural isotopic concentration in diamond. The minimum of the frozen core radius is located at $\arccos(1/\sqrt{3}) \approx 54.7^\circ$, where the dipolar hyperfine coupling A_{zz} vanishes.

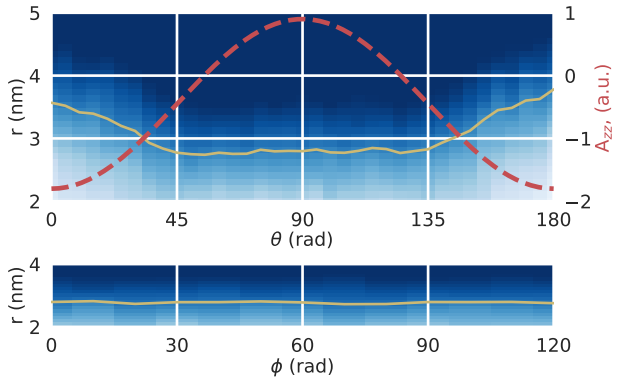

Figure A.8: Spin-pair coherence at an infinite time (see main text) as a function of distance r from the NV center, radial Θ, and azimuthal ϕ angles. The yellow line shows the frozen core radius, and the red line shows the dipolar hyperfine coupling in the arbitrary units. Darker colors correspond to zero values of the model coherence.

APPENDIX B

DESIGN DOCUMENT OF PYCCE

PyCCE has been rather successful, with the number of downloads exceeding 600 as of May 2023 (see Fig. B.1). However, currently, I am the only developer actively supporting it; thus, below are the general guidelines I follow in the development process.

Specifically, I discuss the design philosophy behind the core decisions I made during the PyCCE development. This section is aimed at the people who want to modify and tailor PyCCE to their own needs or, simply put, developers. It is not intended as a usage guide; see the section 5 and online documentation at `https://pycce.readthedocs.io/` for the user documentation.

The properties of the spin bath are stored in the objects of the `BathArray` class. `BathArray` is a subclass of the `numpy.array` with a fixed datatype. Such a choice was made to ensure fast and reliable access for the user to the properties of hundreds or even thousands of bath spins. Properties of the spins are stored either as a property of an individual spin (and stored inside the underlying `numpy.array`) or properties of the spin *type*.

The assumption is the following: it is very much guaranteed that all bath spins will have different positions and different coupling parameters with the central spin. Hence, we need to ensure easy generation and storage of a large number of these values. The coupling to the magnetic field or the total spin of the particles, for the most part, will be the same for the significant portion of the bath, so storing it as a single value makes sense. A shortcoming is that if one needs to have a bath with a magnetic field gradient, the code might significantly underperform compared to a unified magnetic field.

The spin type of a particular bath spin is determined by its name, stored in the `BathArray.N` attribute. The properties of the spin type are stored in the `SpinType` object, invisible to the user. All spin types of the given bath array are stored in the `SpinDict` object, available as a `BathArray.types` attribute. Most of the `SpinType` attributes are directly accessible as the

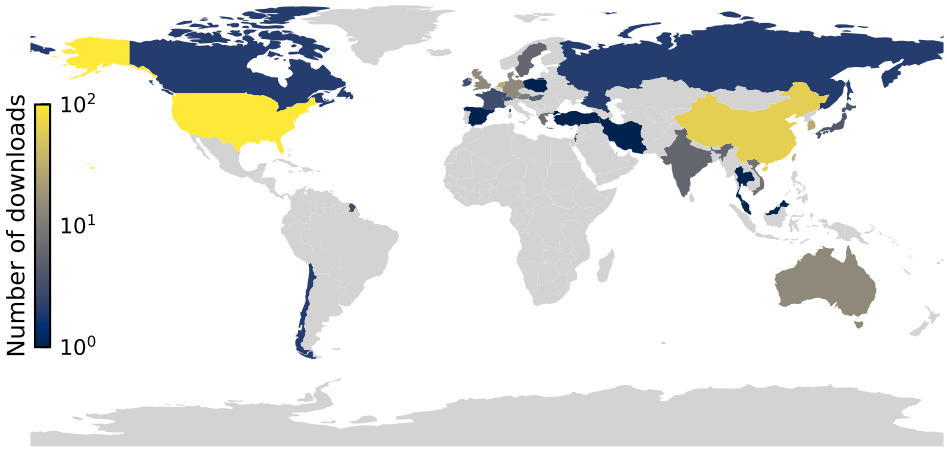

Figure B.1: Distribution of the PyCCE downloads per country. Courtesy of Google BigQuery.

attributes of `BathArray`, so usually, one doesn't need to work with it directly.

Adding properties of the spin *type* is way easier for a developer than trying to change the fixed datatype of the class; thus, it should be the first option to add new terms to the bath spin Hamiltonian. If there is a need to create a bath with each spin having a unique parameter stored in its type, it is recommended to name the bath spins with different indexes (e.g., `"e1"`...`"en"` for a set of n electron spins), and create a unique `SpinType` object for each.

In comparison, the `CenterArray` class is intended to store a few (up to 3-4) spins, each with its own completely unique parameters. Therefore, the `CenterArray` class significantly differs from the bath - it does not directly inherit from `numpy.array` and is written from scratch. Each element of the `CenterArray` is an instance of the `Center` class, which contains all the properties of the bath spins and the center-specific ones. It is still in active development, and the backend of the `Center` class might significantly change in the future.

The main interface between the user and the calculation of interest is done via the objects of the `Simulator` class. On the backend, when the `Simulator` objects are initialized, they do the following steps:

- Prepare a spin bath by choosing a subset of the `BathArray` according to the `r_bath` parameter and generating the hyperfine couplings from the `hyperfine` keywords.
- Generate a set of clusters to be used in the cluster expansion calculation.

The CCE calculations themselves are carried out by the objects of various subclasses of `BaseRunner` class, called during the `Simulator.compute` call. Each of the `BaseRunner` has the following attributes, by overriding which the developer can easily create a new type of CCE simulation:

- `.kerner` defines the subroutine, which is run to compute the result for each cluster. If not defined, it calls `.generate_hamiltonian` and `.compute_result` methods.
- `.preprocess` defines the code block which will run before the given CCE runs or before each of the bath states calculations.
- `.postprocess` defines the code block which will be run *after* given CCE run or after each of the bath states calculations.

These attributes are used by the `cluster_expansion_decorator` to do a CCE calculation.

REFERENCES

[1] S. A. Zargaleh, H. J. von Bardeleben, J. L. Cantin, U. Gerstmann, S. Hameau, B. Eblé, and Weibo Gao. Electron paramagnetic resonance tagged high-resolution excitation spectroscopy of nv-centers in 4h-sic. *Phys. Rev. B*, 98:214113, December 2018. doi:10.1103/PhysRevB.98.214113. URL `https://link.aps.org/doi/10.1103/PhysRevB.98.214113`.

[2] A. Csóré, H. J. von Bardeleben, J. L. Cantin, and A. Gali. Characterization and formation of nv centers in 3c, 4h, and \$6h\$ sic: An ab initio study. *Phys. Rev. B*, 96: 085204, August 2017. doi:10.1103/PhysRevB.96.085204. URL `https://link.aps.org/doi/10.1103/PhysRevB.96.085204`.

[3] Alexandre Bourassa, Christopher P. Anderson, Kevin C. Miao, Mykyta Onizhuk, He Ma, Alexander L. Crook, Hiroshi Abe, Jawad Ul-Hassan, Takeshi Ohshima, Nguyen T. Son, Giulia Galli, and David D. Awschalom. Entanglement and control of single nuclear spins in isotopically engineered silicon carbide. *Nature Materials*, pages 1–7, September 2020. ISSN 1476-4660. doi:10.1038/s41563-020-00802-6. URL `https://doi.org/10.1038/s41563-020-00802-6`.

[4] William F. Koehl, Bob B. Buckley, F. Joseph Heremans, Greg Calusine, and David D. Awschalom. Room temperature coherent control of defect spin qubits in silicon carbide. *Nature*, 479(7371):84–87, November 2011. ISSN 1476-4687. doi:10.1038/nature10562. URL `https://doi.org/10.1038/nature10562`.

[5] Hosung Seo, Abram L. Falk, Paul V. Klimov, Kevin C. Miao, Giulia Galli, and David D. Awschalom. Quantum decoherence dynamics of divacancy spins in silicon carbide. *Nature Communications*, 7(1):12935, September 2016. ISSN 2041-1723. doi:10.1038/ncomms12935. URL `https://doi.org/10.1038/ncomms12935`. Article.

[6] Michael A. Nielsen and Isaac L. Chuang. *Quantum Computation and Quantum Information: 10th Anniversary Edition*. Cambridge University Press, New York, NY, USA, 10th edition, 2011. ISBN 1107002176, 9781107002173.

[7] Kevin C. Miao, Matt McEwen, Juan Atalaya, Dvir Kafri, Leonid P. Pryadko, Andreas Bengtsson, Alex Opremcak, Kevin J. Satzinger, Zijun Chen, Paul V. Klimov, Chris Quintana, Rajeev Acharya, Kyle Anderson, Markus Ansmann, Frank Arute, Kunal Arya, Abraham Asfaw, Joseph C. Bardin, Alexandre Bourassa, Jenna Bovaird, Leon Brill, Bob B. Buckley, David A. Buell, Tim Burger, Brian Burkett, Nicholas Bushnell, Juan Campero, Ben Chiaro, Roberto Collins, Paul Conner, Alexander L. Crook, Ben Curtin, Dripto M. Debroy, Sean Demura, Andrew Dunsworth, Catherine Erickson, Reza Fatemi, Vinicius S. Ferreira, Leslie Flores Burgos, Ebrahim Forati, Austin G. Fowler, Brooks Foxen, Gonzalo Garcia, William Giang, Craig Gidney, Marissa Giustina, Raja Gosula, Alejandro Grajales Dau, Jonathan A. Gross, Michael C. Hamilton, Sean D. Harrington, Paula Heu, Jeremy Hilton, Markus R. Hoffmann, Sabrina Hong, Trent Huang, Ashley Huff, Justin Iveland, Evan Jeffrey, Zhang

Jiang, Cody Jones, Julian Kelly, Seon Kim, Fedor Kostritsa, John Mark Kreikebaum, David Landhuis, Pavel Laptev, Lily Laws, Kenny Lee, Brian J. Lester, Alexander T. Lill, Wayne Liu, Aditya Locharla, Erik Lucero, Steven Martin, Anthony Megrant, Xiao Mi, Shirin Montazeri, Alexis Morvan, Ofer Naaman, Matthew Neeley, Charles Neill, Ani Nersisyan, Michael Newman, Jiun How Ng, Anthony Nguyen, Murray Nguyen, Rebecca Potter, Charles Rocque, Pedram Roushan, Kannan Sankaragomathi, Christopher Schuster, Michael J. Shearn, Aaron Shorter, Noah Shutty, Vladimir Shvarts, Jindra Skruzny, W. Clarke Smith, George Sterling, Marco Szalay, Douglas Thor, Alfredo Torres, Theodore White, Bryan W. K. Woo, Z. Jamie Yao, Ping Yeh, Juhwan Yoo, Grayson Young, Adam Zalcman, Ningfeng Zhu, Nicholas Zobrist, Hartmut Neven, Vadim Smelyanskiy, Andre Petukhov, Alexander N. Korotkov, Daniel Sank, and Yu Chen. Overcoming leakage in scalable quantum error correction, 2022.

[8] Daniel Sank. See the reply at https://physics.stackexchange.com/questions/458654/rotating-wave-approximation-and-classical-rabi-oscillations-why-dont-the-fast, 2019.

[9] Daniel Manzano. A short introduction to the lindblad master equation. *AIP Advances*, 10(2):025106, 2020. doi:10.1063/1.5115323. URL https://doi.org/10.1063/1.5115323.

[10] C. L. Degen, F. Reinhard, and P. Cappellaro. Quantum sensing. *Rev. Mod. Phys.*, 89:035002, July 2017. ISSN 0034-6861. doi:10.1103/RevModPhys.89.035002. URL https://link.aps.org/doi/10.1103/RevModPhys.89.035002.

[11] A. A. Clerk, M. H. Devoret, S. M. Girvin, Florian Marquardt, and R. J. Schoelkopf. Introduction to quantum noise, measurement, and amplification. *Rev. Mod. Phys.*, 82: 1155–1208, April 2010. doi:10.1103/RevModPhys.82.1155. URL https://link.aps.org/doi/10.1103/RevModPhys.82.1155.

[12] E. L. Hahn. Spin echoes. *Phys. Rev.*, 80:580–594, November 1950. doi:10.1103/PhysRev.80.580. URL https://link.aps.org/doi/10.1103/PhysRev.80.580.

[13] Kevin C. Young and K. Birgitta Whaley. Qubits as spectrometers of dephasing noise. *Phys. Rev. A*, 86:012314, July 2012. doi:10.1103/PhysRevA.86.012314. URL https://link.aps.org/doi/10.1103/PhysRevA.86.012314.

[14] Łukasz Cywiński, Roman M. Lutchyn, Cody P. Nave, and S. Das Sarma. How to enhance dephasing time in superconducting qubits. *Phys. Rev. B*, 77:174509, May 2008. doi:10.1103/PhysRevB.77.174509. URL https://link.aps.org/doi/10.1103/PhysRevB.77.174509.

[15] Wen Yang, Wen-Long Ma, and Ren-Bao Liu. Quantum many-body theory for electron spin decoherence in nanoscale nuclear spin baths. *Reports on Progress in Physics*, 80(1):016001, November 2016. ISSN 00344885. doi:10.1088/0034-4885/80/1/016001. URL https://doi.org/10.1088/0034-4885/80/1/016001.

[16] Kenta Takeda, Akito Noiri, Takashi Nakajima, Jun Yoneda, Takashi Kobayashi, and Seigo Tarucha. Quantum tomography of an entangled three-qubit state in silicon. *Nature Nanotechnology*, 16(9):965–969, June 2021. doi:10.1038/s41565-021-00925-0. URL https://doi.org/10.1038/s41565-021-00925-0.

[17] Guido Burkard, Thaddeus D. Ladd, John M. Nichol, Andrew Pan, and Jason R. Petta. Semiconductor spin qubits, 2021.

[18] Shannon P. Harvey. Quantum dots/spin qubits, February 2022. URL https://doi.org/10.1093%2Facrefore%2F9780190871994.013.83.

[19] Anasua Chatterjee, Paul Stevenson, Silvano De Franceschi, Andrea Morello, Nathalie P. de Leon, and Ferdinand Kuemmeth. Semiconductor qubits in practice. *Nature Reviews Physics*, 3(3):157–177, February 2021. doi:10.1038/s42254-021-00283-9. URL https://doi.org/10.1038/s42254-021-00283-9.

[20] Andrea Morello, Jarryd J. Pla, Patrice Bertet, and David N. Jamieson. Donor spins in silicon for quantum technologies. *Advanced Quantum Technologies*, 3(11):2000005, July 2020. doi:https://doi.org/10.1002/qute.202000005. URL https://onlinelibrary.wiley.com/doi/abs/10.1002/qute.202000005.

[21] Belita Koiller, R. B. Capaz, Xuedong Hu, and S. Das Sarma. Shallow-donor wave functions and donor-pair exchange in silicon: Ab initio theory and floating-phase heitler-london approach. *Phys. Rev. B*, 70:115207, Sep 2004. doi:10.1103/PhysRevB.70.115207. URL https://link.aps.org/doi/10.1103/PhysRevB.70.115207.

[22] Michael W. Swift, Hartwin Peelaers, Sai Mu, John J. L. Morton, and Chris G. Van de Walle. First-principles calculations of hyperfine interaction, binding energy, and quadrupole coupling for shallow donors in silicon. *npj Computational Materials*, 6(1), November 2020. doi:10.1038/s41524-020-00448-7. URL https://doi.org/10.1038/s41524-020-00448-7.

[23] C. Zu, F. Machado, B. Ye, S. Choi, B. Kobrin, T. Mittiga, S. Hsieh, P. Bhattacharyya, M. Markham, D. Twitchen, A. Jarmola, D. Budker, C. R. Laumann, J. E. Moore, and N. Y. Yao. Emergent hydrodynamics in a strongly interacting dipolar spin ensemble. *Nature*, 597(7874):45–50, September 2021. doi:10.1038/s41586-021-03763-1. URL https://doi.org/10.1038/s41586-021-03763-1.

[24] Gary Wolfowicz, F. Joseph Heremans, Christopher P. Anderson, Shun Kanai, Hosung Seo, Adam Gali, Giulia Galli, and David D. Awschalom. Quantum guidelines for solid-state spin defects. *Nature Reviews Materials*, 6(10):906–925, April 2021. ISSN 2058-8437. doi:10.1038/s41578-021-00306-y. URL https://doi.org/10.1038/s41578-021-00306-y.

[25] Christopher Paul Anderson. *Spin Qubits in Silicon Carbide Electronic Devices*. PhD thesis, The University of Chicago, 2020.

[26] Nan Sheng, Christian Vorwerk, Marco Govoni, and Giulia Galli. Green's function formulation of quantum defect embedding theory. *Journal of Chemical Theory and Computation*, 18(6):3512–3522, June 2022. doi:10.1021/acs.jctc.2c00240. URL https://doi.org/10.1021/acs.jctc.2c00240.

[27] Denis R. Candido and Michael E. Flatté. Interplay between charge and spin noise in the near-surface theory of decoherence and relaxation of c_{3v} symmetry qutrit spin-1 centers. *Preprint at arXiv:2303.13370*, 2023.

[28] R. McWeeny. *Methods of Molecular Quantum Mechanics*. Elsevier Science, 1992. ISBN 9780124865525. URL https://books.google.com/books?id=gyHAQgAACAAJ.

[29] Frank Neese. Prediction of electron paramagnetic resonance g values using coupled perturbed hartree–fock and kohn–sham theory. *The Journal of Chemical Physics*, 115 (24):11080–11096, 2001. doi:10.1063/1.1419058. URL https://doi.org/10.1063/1.1419058.

[30] Carole Duboc, Dmitry Ganyushin, Kantharuban Sivalingam, Marie-Noëlle Collomb, and Frank Neese. Systematic theoretical study of the zero-field splitting in coordination complexes of mn(iii). density functional theory versus multireference wave function approaches. *The Journal of Physical Chemistry A*, 114(39):10750–10758, October 2010. ISSN 1089-5639. doi:10.1021/jp107823s. URL https://doi.org/10.1021/jp107823s.

[31] Stefan Stoll and Arthur Schweiger. Easyspin, a comprehensive software package for spectral simulation and analysis in epr. *Journal of Magnetic Resonance*, 178(1):42–55, 2006. ISSN 1090-7807. doi:https://doi.org/10.1016/j.jmr.2005.08.013. URL https://www.sciencedirect.com/science/article/pii/S1090780705002892.

[32] Krishnendu Ghosh, He Ma, Vikram Gavini, and Giulia Galli. All-electron density functional calculations for electron and nuclear spin interactions in molecules and solids. *Phys. Rev. Materials*, 3:043801, April 2019. doi:10.1103/PhysRevMaterials.3.043801. URL https://link.aps.org/doi/10.1103/PhysRevMaterials.3.043801.

[33] Julio C. Facelli. Chemical shift tensors: Theory and application to molecular structural problems. *Progress in Nuclear Magnetic Resonance Spectroscopy*, 58(3):176–201, 2011. ISSN 0079-6565. doi:https://doi.org/10.1016/j.pnmrs.2010.10.003. URL http://www.sciencedirect.com/science/article/pii/S007965651000110X.

[34] M.H. Levitt. *Spin Dynamics: Basics of Nuclear Magnetic Resonance*. Wiley, 2001. ISBN 9780471489221. URL https://books.google.com/books?id=_1wZXxz1TIQC.

[35] Daniel Loss and David P. DiVincenzo. Quantum computation with quantum dots. *Phys. Rev. A*, 57:120–126, January 1998. doi:10.1103/PhysRevA.57.120. URL https://link.aps.org/doi/10.1103/PhysRevA.57.120.

[36] N. W. Hendrickx, D. P. Franke, A. Sammak, G. Scappucci, and M. Veldhorst. Fast two-qubit logic with holes in germanium. *Nature*, 577(7791):487–491, January 2020. ISSN 1476-4687. doi:10.1038/s41586-019-1919-3. URL https://doi.org/10.1038/s41586-019-1919-3.

[37] Hendrik Bluhm, Sandra Foletti, Izhar Neder, Mark Rudner, Diana Mahalu, Vladimir Umansky, and Amir Yacoby. Dephasing time of gaas electron-spin qubits coupled to a nuclear bath exceeding 200 μs. *Nature Physics*, 7(2):109–113, February 2011. ISSN 1745-2481. doi:10.1038/nphys1856. URL https://doi.org/10.1038/nphys1856.

[38] T. F. Watson, S. G. J. Philips, E. Kawakami, D. R. Ward, P. Scarlino, M. Veldhorst, D. E. Savage, M. G. Lagally, Mark Friesen, S. N. Coppersmith, M. A. Eriksson, and L. M. K. Vandersypen. A programmable two-qubit quantum processor in silicon. *Nature*, 555(7698):633–637, March 2018. ISSN 1476-4687. doi:10.1038/nature25766. URL https://doi.org/10.1038/nature25766.

[39] J. R. Petta, A. C. Johnson, J. M. Taylor, E. A. Laird, A. Yacoby, M. D. Lukin, C. M. Marcus, M. P. Hanson, and A. C. Gossard. Coherent manipulation of coupled electron spins in semiconductor quantum dots. *Science*, 309(5744):2180–2184, 2005. ISSN 0036-8075. doi:10.1126/science.1116955. URL https://science.sciencemag.org/content/309/5744/2180.

[40] Gary Wolfowicz, Alexei M. Tyryshkin, Richard E. George, Helge Riemann, Nikolai V. Abrosimov, Peter Becker, Hans-Joachim Pohl, Mike L. W. Thewalt, Stephen A. Lyon, and John J. L. Morton. Atomic clock transitions in silicon-based spin qubits. *Nature Nanotechnology*, 8(8):561–564, August 2013. ISSN 1748-3395. doi:10.1038/nnano.2013.117. URL https://doi.org/10.1038/nnano.2013.117.

[41] Alexei M. Tyryshkin, Shinichi Tojo, John J. L. Morton, Helge Riemann, Nikolai V. Abrosimov, Peter Becker, Hans-Joachim Pohl, Thomas Schenkel, Michael L. W. Thewalt, Kohei M. Itoh, and S. A. Lyon. Electron spin coherence exceeding seconds in high-purity silicon. *Nature Materials*, 11(2):143–147, February 2012. ISSN 1476-4660. doi:10.1038/nmat3182. URL https://doi.org/10.1038/nmat3182.

[42] Stephanie Simmons, Richard M. Brown, Helge Riemann, Nikolai V. Abrosimov, Peter Becker, Hans-Joachim Pohl, Mike L. W. Thewalt, Kohei M. Itoh, and John J. L. Morton. Entanglement in a solid-state spin ensemble. *Nature*, 470(7332):69–72, February 2011. ISSN 1476-4687. doi:10.1038/nature09696. URL https://doi.org/10.1038/nature09696.

[43] N. Bar-Gill, L. M. Pham, A. Jarmola, D. Budker, and R. L. Walsworth. Solid-state electronic spin coherence time approaching one second. *Nature Communications*, 4(1):1743, April 2013. ISSN 2041-1723. doi:10.1038/ncomms2771. URL https://doi.org/10.1038/ncomms2771.

[44] H. Bernien, B. Hensen, W. Pfaff, G. Koolstra, M. S. Blok, L. Robledo, T. H. Taminiau, M. Markham, D. J. Twitchen, L. Childress, and R. Hanson. Heralded entanglement between solid-state qubits separated by three metres. *Nature*, 497(7447):86–90, May 2013. ISSN 1476-4687. doi:10.1038/nature12016. URL https://doi.org/10.1038/nature12016.

[45] Sébastien Pezzagna and Jan Meijer. Quantum computer based on color centers in diamond. *Applied Physics Reviews*, 8(1):011308, 2021. doi:10.1063/5.0007444. URL https://doi.org/10.1063/5.0007444.

[46] M. Pompili, S. L. N. Hermans, S. Baier, H. K. C. Beukers, P. C. Humphreys, R. N. Schouten, R. F. L. Vermeulen, M. J. Tiggelman, L. dos Santos Martins, B. Dirkse, S. Wehner, and R. Hanson. Realization of a multinode quantum network of remote solid-state qubits. *Science*, 372(6539):259–264, 4 2021. ISSN 0036-8075. doi:10.1126/science.abg1919. URL https://science.sciencemag.org/content/372/6539/259.

[47] Wen Yang and Ren-Bao Liu. Quantum many-body theory of qubit decoherence in a finite-size spin bath. *Phys. Rev. B*, 78:085315, August 2008. doi:10.1103/PhysRevB.78.085315. URL https://link.aps.org/doi/10.1103/PhysRevB.78.085315.

[48] Wen Yang and Ren-Bao Liu. Quantum many-body theory of qubit decoherence in a finite-size spin bath. ii. ensemble dynamics. *Phys. Rev. B*, 79:115320, March 2009. doi:10.1103/PhysRevB.79.115320. URL https://link.aps.org/doi/10.1103/PhysRevB.79.115320.

[49] S. J. Balian, Gary Wolfowicz, John J. L. Morton, and T. S. Monteiro. Quantum-bath-driven decoherence of mixed spin systems. *Phys. Rev. B*, 89:045403, January 2014. doi:10.1103/PhysRevB.89.045403. URL https://link.aps.org/doi/10.1103/PhysRevB.89.045403.

[50] S. J. Balian, Ren-Bao Liu, and T. S. Monteiro. Keeping a spin qubit alive in natural silicon: Comparing optimal working points and dynamical decoupling. *Phys. Rev. B*, 91:245416, June 2015. doi:10.1103/PhysRevB.91.245416. URL https://link.aps.org/doi/10.1103/PhysRevB.91.245416.

[51] Wen-Long Ma, Gary Wolfowicz, Nan Zhao, Shu-Shen Li, John J.L. Morton, and Ren-Bao Liu. Uncovering many-body correlations in nanoscale nuclear spin baths by central spin decoherence. *Nature Communications*, 5(1):4822, September 2014. ISSN 2041-1723. doi:10.1038/ncomms5822. URL https://doi.org/10.1038/ncomms5822.

[52] Nan Zhao, Sai-Wah Ho, and Ren-Bao Liu. Decoherence and dynamical decoupling control of nitrogen vacancy center electron spins in nuclear spin baths. *Phys. Rev. B*, 85:115303, March 2012. ISSN 10980121. doi:10.1103/PhysRevB.85.115303. URL https://link.aps.org/doi/10.1103/PhysRevB.85.115303.

[53] Mykyta Onizhuk, Kevin C. Miao, Joseph P. Blanton, He Ma, Christopher P. Anderson, Alexandre Bourassa, David D. Awschalom, and Giulia Galli. Probing the coherence of solid-state qubits at avoided crossings. *PRX Quantum*, 2:010311, January 2021. ISSN 26913399. doi:10.1103/PRXQuantum.2.010311. URL https://link.aps.org/doi/10.1103/PRXQuantum.2.010311.

[54] Mykyta Onizhuk and Giulia Galli. Substrate-controlled dynamics of spin qubits in low dimensional van der waals materials. *Applied Physics Letters*, 118(15):154003, April 2021. ISSN 00036951. doi:10.1063/5.0048399. URL https://doi.org/10.1063/5.0048399.

[55] Meng Ye, Hosung Seo, and Giulia Galli. Spin coherence in two-dimensional materials. *npj Computational Materials*, 5(1):44, April 2019. ISSN 2057-3960. doi:10.1038/s41524-019-0182-3. URL https://doi.org/10.1038/s41524-019-0182-3.

[56] Shun Kanai, F. Joseph Heremans, Hosung Seo, Gary Wolfowicz, Christopher P. Anderson, Sean E. Sullivan, Giulia Galli, David D. Awschalom, and Hideo Ohno. Generalized scaling of spin qubit coherence in over 12,000 host materials, 4 2021. ISSN 0027-8424. URL https://pnas.org/doi/full/10.1073/pnas.2121808119.

[57] Wayne M. Witzel, Malcolm S. Carroll, Łukasz Cywiński, and S. Das Sarma. Quantum decoherence of the central spin in a sparse system of dipolar coupled spins. *Phys. Rev. B*, 86:035452, July 2012. doi:10.1103/PhysRevB.86.035452. URL https://link.aps.org/doi/10.1103/PhysRevB.86.035452.

[58] Wayne M. Witzel, Kevin Young, and Sankar Das Sarma. Converting a real quantum spin bath to an effective classical noise acting on a central spin. *Phys. Rev. B*, 90:115431, September 2014. doi:10.1103/PhysRevB.90.115431. URL https://link.aps.org/doi/10.1103/PhysRevB.90.115431.

[59] Wen-Long Ma, Gary Wolfowicz, Shu-Shen Li, John J. L. Morton, and Ren-Bao Liu. Classical nature of nuclear spin noise near clock transitions of bi donors in silicon. *Phys. Rev. B*, 92:161403, October 2015. doi:10.1103/PhysRevB.92.161403. URL https://link.aps.org/doi/10.1103/PhysRevB.92.161403.

[60] Ask Hjorth Larsen, Jens Jørgen Mortensen, Jakob Blomqvist, Ivano E Castelli, Rune Christensen, Marcin Dułak, Jesper Friis, Michael N Groves, Bjørk Hammer, Cory Hargus, Eric D Hermes, Paul C Jennings, Peter Bjerre Jensen, James Kermode, John R Kitchin, Esben Leonhard Kolsbjerg, Joseph Kubal, Kristen Kaasbjerg, Steen Lysgaard, Jón Bergmann Maronsson, Tristan Maxson, Thomas Olsen, Lars Pastewka, Andrew Peterson, Carsten Rostgaard, Jakob Schiøtz, Ole Schütt, Mikkel Strange, Kristian S Thygesen, Tejs Vegge, Lasse Vilhelmsen, Michael Walter, Zhenhua Zeng, and Karsten W Jacobsen. The atomic simulation environment—a python library for working with atoms. *Journal of Physics: Condensed Matter*, 29(27):273002, June 2017. doi:10.1088/1361-648x/aa680e. URL https://doi.org/10.1088/1361-648x/aa680e.

[61] Paul Bourke. Gaussian cube file format. http://paulbourke.net/dataformats/cube/, 2003. Accessed: 2023.

[62] Frank Neese. The orca program system. *WIREs Computational Molecular Science*, 2 (1):73–78, 2012. doi:https://doi.org/10.1002/wcms.81. URL https://onlinelibrary.wiley.com/doi/abs/10.1002/wcms.81.

[63] Paolo Giannozzi, Stefano Baroni, Nicola Bonini, Matteo Calandra, Roberto Car, Carlo Cavazzoni, Davide Ceresoli, Guido L Chiarotti, Matteo Cococcioni, Ismaila Dabo, Andrea Dal Corso, Stefano de Gironcoli, Stefano Fabris, Guido Fratesi, Ralph Gebauer, Uwe Gerstmann, Christos Gougoussis, Anton Kokalj, Michele Lazzeri, Layla Martin-Samos, Nicola Marzari, Francesco Mauri, Riccardo Mazzarello, Stefano Paolini, Alfredo Pasquarello, Lorenzo Paulatto, Carlo Sbraccia, Sandro Scandolo, Gabriele Sclauzero, Ari P Seitsonen, Alexander Smogunov, Paolo Umari, and Renata M Wentzcovitch. Quantum espresso: a modular and open-source software project for quantum simulations of materials. *J. Phys.: Condens. Matter*, 21(39):395502, September 2009. doi:10.1088/0953-8984/21/39/395502.

[64] Mykyta Onizhuk. See the full pycce documentation at read the docs. https://pycce.readthedocs.io/en/latest/, 2023. Accessed: 2023.

[65] Arthur Schweiger and Gunnar Jeschke. *Principles of pulse electron paramagnetic resonance*. Oxford University Press, London, England, October 2001.

[66] L. T. Hall, J. H. Cole, and L. C. L. Hollenberg. Analytic solutions to the central-spin problem for nitrogen-vacancy centers in diamond. *Phys. Rev. B*, 90:075201, August 2014. doi:10.1103/PhysRevB.90.075201. URL https://link.aps.org/doi/10.1103/PhysRevB.90.075201.

[67] Davide Ceresoli. https://github.com/dceresoli/qe-gipaw, 2023. Accessed: 2023.

[68] Eisuke Abe, Alexei M. Tyryshkin, Shinichi Tojo, John J. L. Morton, Wayne M. Witzel, Akira Fujimoto, Joel W. Ager, Eugene E. Haller, Junichi Isoya, Stephen A. Lyon, Mike L. W. Thewalt, and Kohei M. Itoh. Electron spin coherence of phosphorus donors in silicon: Effect of environmental nuclei. *Phys. Rev. B*, 82:121201, September 2010. doi:10.1103/PhysRevB.82.121201. URL https://link.aps.org/doi/10.1103/PhysRevB.82.121201.

[69] Rogerio de Sousa and S. Das Sarma. Theory of nuclear-induced spectral diffusion: Spin decoherence of phosphorus donors in si and gaas quantum dots. *Phys. Rev. B*, 68:115322, September 2003. doi:10.1103/PhysRevB.68.115322. URL https://link.aps.org/doi/10.1103/PhysRevB.68.115322.

[70] L. Bergeron, C. Chartrand, A. T. K. Kurkjian, K. J. Morse, H. Riemann, N. V. Abrosimov, P. Becker, H.-J. Pohl, M. L. W. Thewalt, and S. Simmons. Silicon-integrated telecommunications photon-spin interface. *PRX Quantum*, 1:020301, October 2020.

doi:10.1103/PRXQuantum.1.020301. URL https://link.aps.org/doi/10.1103/PRXQuantum.1.020301.

[71] Muhandis Shiddiq, Dorsa Komijani, Yan Duan, Alejandro Gaita-Ariño, Eugenio Coronado, and Stephen Hill. Enhancing coherence in molecular spin qubits via atomic clock transitions. *Nature*, 531(7594):348–351, March 2016. ISSN 1476-4687. doi:10.1038/nature16984. URL https://doi.org/10.1038/nature16984.

[72] S. L. Bayliss, D. W. Laorenza, P. J. Mintun, B. D. Kovos, D. E. Freedman, and D. D. Awschalom. Optically addressable molecular spins for quantum information processing. *Science*, 370(6522):1309–1312, 2020. ISSN 0036-8075. doi:10.1126/science.abb9352. URL https://science.sciencemag.org/content/370/6522/1309.

[73] E. D. Herbschleb, H. Kato, Y. Maruyama, T. Danjo, T. Makino, S. Yamasaki, I. Ohki, K. Hayashi, H. Morishita, M. Fujiwara, and N. Mizuochi. Ultra-long coherence times amongst room-temperature solid-state spins. *Nature Communications*, 10(1):3766, August 2019. ISSN 2041-1723. doi:10.1038/s41467-019-11776-8. URL https://doi.org/10.1038/s41467-019-11776-8.

[74] Lucio Robledo, Lilian Childress, Hannes Bernien, Bas Hensen, Paul F. A. Alkemade, and Ronald Hanson. High-fidelity projective read-out of a solid-state spin quantum register. *Nature*, 477(7366):574–578, September 2011. ISSN 1476-4687. doi:10.1038/nature10401. URL https://doi.org/10.1038/nature10401.

[75] J. R. Weber, W. F. Koehl, J. B. Varley, A. Janotti, B. B. Buckley, C. G. Van de Walle, and D. D. Awschalom. Quantum computing with defects. *Proceedings of the National Academy of Sciences*, 107(19):8513–8518, April 2010. ISSN 0027-8424. doi:10.1073/pnas.1003052107. URL https://www.pnas.org/content/107/19/8513.

[76] Richard E. George, James P. Edwards, and Arzhang Ardavan. Coherent spin control by electrical manipulation of the magnetic anisotropy. *Phys. Rev. Lett.*, 110:027601, January 2013. doi:10.1103/PhysRevLett.110.027601. URL https://link.aps.org/doi/10.1103/PhysRevLett.110.027601.

[77] W. M. Witzel and S. Das Sarma. Quantum theory for electron spin decoherence induced by nuclear spin dynamics in semiconductor quantum computer architectures: Spectral diffusion of localized electron spins in the nuclear solid-state environment. *Phys. Rev. B*, 74:035322, July 2006. doi:10.1103/PhysRevB.74.035322. URL https://link.aps.org/doi/10.1103/PhysRevB.74.035322.

[78] M. H. Abobeih, J. Cramer, M. A. Bakker, N. Kalb, M. Markham, D. J. Twitchen, and T. H. Taminiau. One-second coherence for a single electron spin coupled to a multi-qubit nuclear-spin environment. *Nature Communications*, 9(1):2552, June 2018. ISSN 2041-1723. doi:10.1038/s41467-018-04916-z. URL https://doi.org/10.1038/s41467-018-04916-z.

[79] T. van der Sar, Z. H. Wang, M. S. Blok, H. Bernien, T. H. Taminiau, D. M. Toyli, D. A. Lidar, D. D. Awschalom, R. Hanson, and V. V. Dobrovitski. Decoherence-protected quantum gates for a hybrid solid-state spin register. *Nature*, 484(7392):82–86, April 2012. ISSN 1476-4687. doi:10.1038/nature10900. URL https://doi.org/10.1038/nature10900.

[80] Andreas Reiserer, Norbert Kalb, Machiel S. Blok, Koen J. M. van Bemmelen, Tim H. Taminiau, Ronald Hanson, Daniel J. Twitchen, and Matthew Markham. Robust quantum-network memory using decoherence-protected subspaces of nuclear spins. *Phys. Rev. X*, 6:021040, June 2016. doi:10.1103/PhysRevX.6.021040. URL https://link.aps.org/doi/10.1103/PhysRevX.6.021040.

[81] M. H. Mohammady, G. W. Morley, and T. S. Monteiro. Bismuth qubits in silicon: The role of epr cancellation resonances. *Phys. Rev. Lett.*, 105:067602, August 2010. doi:10.1103/PhysRevLett.105.067602. URL https://link.aps.org/doi/10.1103/PhysRevLett.105.067602.

[82] Kevin C. Miao, Joseph P. Blanton, Christopher P. Anderson, Alexandre Bourassa, Alexander L. Crook, Gary Wolfowicz, Hiroshi Abe, Takeshi Ohshima, and David D. Awschalom. Universal coherence protection in a solid-state spin qubit. *Science*, 369 (6510):1493–1497, 2020. ISSN 0036-8075. doi:10.1126/science.abc5186. URL https://science.sciencemag.org/content/369/6510/1493.

[83] Viktor Ivády. Longitudinal spin relaxation model applied to point-defect qubit systems. *Phys. Rev. B*, 101:155203, April 2020. doi:10.1103/PhysRevB.101.155203. URL https://link.aps.org/doi/10.1103/PhysRevB.101.155203.

[84] A. Jarmola, V. M. Acosta, K. Jensen, S. Chemerisov, and D. Budker. Temperature- and magnetic-field-dependent longitudinal spin relaxation in nitrogen-vacancy ensembles in diamond. *Phys. Rev. Lett.*, 108:197601, May 2012. doi:10.1103/PhysRevLett.108.197601. URL https://link.aps.org/doi/10.1103/PhysRevLett.108.197601.

[85] Paul V. Klimov, Abram L. Falk, David J. Christle, Viatcheslav V. Dobrovitski, and David D. Awschalom. Quantum entanglement at ambient conditions in a macroscopic solid-state spin ensemble. *Science Advances*, 1(10), November 2015. doi:10.1126/sciadv.1501015. URL https://advances.sciencemag.org/content/1/10/e1501015.

[86] Nguyen T. Son, Christopher P. Anderson, Alexandre Bourassa, Kevin C. Miao, Charles Babin, Matthias Widmann, Matthias Niethammer, Jawad Ul Hassan, Naoya Morioka, Ivan G. Ivanov, Florian Kaiser, Joerg Wrachtrup, and David D. Awschalom. Developing silicon carbide for quantum spintronics. *Applied Physics Letters*, 116(19):190501, 2020. doi:10.1063/5.0004454. URL https://doi.org/10.1063/5.0004454.

[87] David J. Christle, Abram L. Falk, Paolo Andrich, Paul V. Klimov, Jawad Ul Hassan, Nguyen T. Son, Erik Janzén, Takeshi Ohshima, and David D. Awschalom. Isolated electron spins in silicon carbide with millisecond coherence times. *Nature Materials*, 14(2):160–163, February 2015. ISSN 1476-4660. doi:10.1038/nmat4144. URL https://doi.org/10.1038/nmat4144.

[88] Alexander L. Crook, Christopher P. Anderson, Kevin C. Miao, Alexandre Bourassa, Hope Lee, Sam L. Bayliss, David O. Bracher, Xingyu Zhang, Hiroshi Abe, Takeshi Ohshima, Evelyn L. Hu, and David D. Awschalom. Purcell enhancement of a single silicon carbide color center with coherent spin control. *Nano Letters*, 20(5):3427–3434, May 2020. ISSN 1530-6984. doi:10.1021/acs.nanolett.0c00339. URL https://doi.org/10.1021/acs.nanolett.0c00339.

[89] Samuel J. Whiteley, Gary Wolfowicz, Christopher P. Anderson, Alexandre Bourassa, He Ma, Meng Ye, Gerwin Koolstra, Kevin J. Satzinger, Martin V. Holt, F. Joseph Heremans, Andrew N. Cleland, David I. Schuster, Giulia Galli, and David D. Awschalom. Spin–phonon interactions in silicon carbide addressed by gaussian acoustics. *Nature Physics*, 15(5):490–495, May 2019. ISSN 1745-2481. doi:10.1038/s41567-019-0420-0. URL https://doi.org/10.1038/s41567-019-0420-0.

[90] Kevin C. Miao, Alexandre Bourassa, Christopher P. Anderson, Samuel J. Whiteley, Alexander L. Crook, Sam L. Bayliss, Gary Wolfowicz, Gergő Thiering, Péter Udvarhelyi, Viktor Ivády, Hiroshi Abe, Takeshi Ohshima, Ádám Gali, and David D. Awschalom. Electrically driven optical interferometry with spins in silicon carbide. *Science Advances*, 5(11):eaay0527, 2019. doi:10.1126/sciadv.aay0527. URL https://advances.sciencemag.org/content/5/11/eaay0527.

[91] Davide Ceresoli. https://sites.google.com/site/dceresoli/pseudopotentials, 2023. Accessed:2023.

[92] Jiwon Yun, Kiho Kim, and Dohun Kim. Strong polarization of individual nuclear spins weakly coupled to nitrogen-vacancy color centers in diamond. *New Journal of Physics*, 21(9):093065, September 2019. doi:10.1088/1367-2630/ab43aa. URL https://doi.org/10.1088%2F1367-2630%2Fab43aa.

[93] A. Dréau, J.-R. Maze, M. Lesik, J.-F. Roch, and V. Jacques. High-resolution spectroscopy of single nv defects coupled with nearby ^{13}c nuclear spins in diamond. *Phys. Rev. B*, 85:134107, April 2012. doi:10.1103/PhysRevB.85.134107. URL https://link.aps.org/doi/10.1103/PhysRevB.85.134107.

[94] Zhi-Sheng Yang, Yan-Xiang Wang, Ming-Jie Tao, Wen Yang, Mei Zhang, Qing Ai, and Fu-Guo Deng. Longitudinal relaxation of a nitrogen-vacancy center in a spin bath by generalized cluster-correlation expansion method. *Annals of Physics*, 413:168063, 2020. ISSN 0003-4916. doi:https://doi.org/10.1016/j.aop.2019.168063. URL http://www.sciencedirect.com/science/article/pii/S0003491619303185.

[95] Geng-Li Zhang, Wen-Long Ma, and Ren-Bao Liu. Cluster-correlation expansion for studying decoherence of clock transitions in spin baths, 2020.

[96] G. de Lange, Z. H. Wang, D. Ristè, V. V. Dobrovitski, and R. Hanson. Universal dynamical decoupling of a single solid-state spin from a spin bath. *Science*, 330(6000): 60–63, 2010. ISSN 0036-8075. doi:10.1126/science.1192739. URL https://science.sciencemag.org/content/330/6000/60.

[97] Swathi S. Hegde, Jingfu Zhang, and Dieter Suter. Efficient quantum gates for individual nuclear spin qubits by indirect control. *Phys. Rev. Lett.*, 124:220501, June 2020. doi:10.1103/PhysRevLett.124.220501. URL https://link.aps.org/doi/10.1103/PhysRevLett.124.220501.

[98] Abram L. Falk, Bob B. Buckley, Greg Calusine, William F. Koehl, Viatcheslav V. Dobrovitski, Alberto Politi, Christian A. Zorman, Philip X.-L. Feng, and David D. Awschalom. Polytype control of spin qubits in silicon carbide. *Nature Communications*, 4(1):1819, May 2013. ISSN 2041-1723. doi:10.1038/ncomms2854. URL https://doi.org/10.1038/ncomms2854.

[99] P. Jamonneau, M. Lesik, J. P. Tetienne, I. Alvizu, L. Mayer, A. Dréau, S. Kosen, J.-F. Roch, S. Pezzagna, J. Meijer, T. Teraji, Y. Kubo, P. Bertet, J. R. Maze, and V. Jacques. Competition between electric field and magnetic field noise in the decoherence of a single spin in diamond. *Phys. Rev. B*, 93:024305, January 2016. doi:10.1103/PhysRevB.93.024305. URL https://link.aps.org/doi/10.1103/PhysRevB.93.024305.

[100] Christopher P. Anderson, Alexandre Bourassa, Kevin C. Miao, Gary Wolfowicz, Peter J. Mintun, Alexander L. Crook, Hiroshi Abe, Jawad Ul Hassan, Nguyen T. Son, Takeshi Ohshima, and David D. Awschalom. Electrical and optical control of single spins integrated in scalable semiconductor devices. *Science*, 366(6470):1225–1230, 2019. ISSN 0036-8075. doi:10.1126/science.aax9406. URL https://science.sciencemag.org/content/366/6470/1225.

[101] Gary Wolfowicz, Christopher P. Anderson, Andrew L. Yeats, Samuel J. Whiteley, Jens Niklas, Oleg G. Poluektov, F. Joseph Heremans, and David D. Awschalom. Optical charge state control of spin defects in 4h-sic. *Nature Communications*, 8(1):1876, November 2017. ISSN 2041-1723. doi:10.1038/s41467-017-01993-4. URL https://doi.org/10.1038/s41467-017-01993-4.

[102] I. A. Merkulov, Al. L. Efros, and M. Rosen. Electron spin relaxation by nuclei in semiconductor quantum dots. *Phys. Rev. B*, 65:205309, April 2002. doi:10.1103/PhysRevB.65.205309. URL https://link.aps.org/doi/10.1103/PhysRevB.65.205309.

[103] Bing Gu and Ignacio Franco. When can quantum decoherence be mimicked by classical noise? *The Journal of Chemical Physics*, 151(1):014109, 2019. doi:10.1063/1.5099499. URL https://doi.org/10.1063/1.5099499.

[104] Daniel Stanek, Carsten Raas, and Götz S. Uhrig. From quantum-mechanical to classical dynamics in the central-spin model. *Phys. Rev. B*, 90:064301, August 2014. doi:10.1103/PhysRevB.90.064301. URL https://link.aps.org/doi/10.1103/PhysRevB.90.064301.

[105] Pu Huang, Xi Kong, Nan Zhao, Fazhan Shi, Pengfei Wang, Xing Rong, Ren-Bao Liu, and Jiangfeng Du. Observation of an anomalous decoherence effect in a quantum bath at room temperature. *Nature Communications*, 2(1):570, December 2011. ISSN 2041-1723. doi:10.1038/ncomms1579. URL https://doi.org/10.1038/ncomms1579.

[106] Li-Ping Yang, Christian Burk, Matthias Widmann, Sang-Yun Lee, Jörg Wrachtrup, and Nan Zhao. Electron spin decoherence in silicon carbide nuclear spin bath. *Phys. Rev. B*, 90:241203, December 2014. doi:10.1103/PhysRevB.90.241203. URL https://link.aps.org/doi/10.1103/PhysRevB.90.241203.

[107] Abram L. Falk, Paul V. Klimov, Bob B. Buckley, Viktor Ivády, Igor A. Abrikosov, Greg Calusine, William F. Koehl, Ádám Gali, and David D. Awschalom. Electrically and mechanically tunable electron spins in silicon carbide color centers. *Phys. Rev. Lett.*, 112(18):187601, May 2014. doi:10.1103/PhysRevLett.112.187601. URL https://link.aps.org/doi/10.1103/PhysRevLett.112.187601.

[108] Mykyta Onizhuk and Giulia Galli. Pycce: A python package for cluster correlation expansion simulations of spin qubit dynamics. *Advanced Theory and Simulations*, 4: 2100254, 11 2021. ISSN 2513-0390. doi:10.1002/adts.202100254. URL https://onlinelibrary.wiley.com/doi/10.1002/adts.202100254.

[109] Fazhan Shi, Qi Zhang, Pengfei Wang, Hongbin Sun, Jiarong Wang, Xing Rong, Ming Chen, Chenyong Ju, Friedemann Reinhard, Hongwei Chen, Jörg Wrachtrup, Junfeng Wang, and Jiangfeng Du. Single-protein spin resonance spectroscopy under ambient conditions. *Science*, 347(6226):1135–1138, March 2015. doi:10.1126/science.aaa2253. URL https://doi.org/10.1126/science.aaa2253.

[110] Karolina Janicka, Aleksander L. Wysocki, and Kyungwha Park. Computational insights into electronic excitations, spin–orbit coupling effects, and spin decoherence in cr(IV)-based molecular qubits. *The Journal of Physical Chemistry A*, 126(43):8007–8020, October 2022. doi:10.1021/acs.jpca.2c06854. URL https://doi.org/10.1021/acs.jpca.2c06854.

[111] Daniel W. Laorenza, Arailym Kairalapova, Sam L. Bayliss, Tamar Goldzak, Samuel M. Greene, Leah R. Weiss, Pratiti Deb, Peter J. Mintun, Kelsey A. Collins, David D. Awschalom, Timothy C. Berkelbach, and Danna E. Freedman. Tunable cr^{4+} molecular color centers. *Journal of the American Chemical Society*, 143(50):21350–21363, November 2021. doi:10.1021/jacs.1c10145. URL https://doi.org/10.1021/jacs.1c10145.

[112] Krishnendu Ghosh, He Ma, Mykyta Onizhuk, Vikram Gavini, and Giulia Galli. Spin-spin interactions in solids from mixed all-electron and pseudopotential calculations − a path to screening materials for spin qubits, 2021.

[113] Jun-Feng Wang, Fei-Fei Yan, Qiang Li, Zheng-Hao Liu, He Liu, Guo-Ping Guo, Li-Ping Guo, Xiong Zhou, Jin-Ming Cui, Jian Wang, Zong-Quan Zhou, Xiao-Ye Xu, Jin-Shi Xu, Chuan-Feng Li, and Guang-Can Guo. Coherent control of nitrogen-vacancy center spins in silicon carbide at room temperature. *Phys. Rev. Lett.*, 124:223601, June 2020. doi:10.1103/PhysRevLett.124.223601. URL `https://link.aps.org/doi/10.1103/PhysRevLett.124.223601`.

[114] Zhao Mu, Soroush Abbasi Zargaleh, Hans Jürgen von Bardeleben, Johannes E. Fröch, Milad Nonahal, Hongbing Cai, Xinge Yang, Jianqun Yang, Xingji Li, Igor Aharonovich, and Weibo Gao. Coherent manipulation with resonant excitation and single emitter creation of nitrogen vacancy centers in 4h silicon carbide. *Nano Letters*, 20(8):6142–6147, 2020. doi:10.1021/acs.nanolett.0c02342. URL `https://doi.org/10.1021/acs.nanolett.0c02342`. Pmid: 32644809.

[115] Chris G. Van de Walle and P. E. Blöchl. First-principles calculations of hyperfine parameters. *Phys. Rev. B*, 47:4244–4255, February 1993.

[116] S. Blügel, H. Akai, R. Zeller, and P. H. Dederichs. Hyperfine fields of 3d and 4d impurities in nickel. *Phys. Rev. B*, 35:3271–3283, March 1987.

[117] Harald Overhof and Uwe Gerstmann. Ab initio calculation of hyperfine and superhyperfine interactions for shallow donors in semiconductors. *Phys. Rev. Lett.*, 92:087602, February 2004.

[118] Mohammad Saeed Bahramy, Marcel HF Sluiter, and Yoshiyuki Kawazoe. Pseudopotential hyperfine calculations through perturbative core-level polarization. *Phys. Rev. B*, 76(3):035124, 2007.

[119] MJ Rayson and PR Briddon. First principles method for the calculation of zero-field splitting tensors in periodic systems. *Phys. Rev. B*, 77(3):035119, 2008.

[120] Zoltán Bodrog and Adam Gali. The spin–spin zero-field splitting tensor in the projector-augmented-wave method. *J. Phys.: Condens. Matter*, 26(1):015305, 2013.

[121] Timur Biktagirov, Wolf Gero Schmidt, and Uwe Gerstmann. Calculation of spin-spin zero-field splitting within periodic boundary conditions: Towards all-electron accuracy. *Phys. Rev. B*, 97(11):115135, 2018.

[122] Lars Olsen, Ove Christiansen, Lars Hemmingsen, Stephan PA Sauer, and Kurt V Mikkelsen. Electric field gradients of water: A systematic investigation of basis set, electron correlation, and rovibrational effects. *J. Chem. Phys.*, 116(4):1424–1434, 2002.

[123] Sebastian Sinnecker and Frank Neese. Spin- spin contributions to the zero-field splitting tensor in organic triplets, carbenes and biradicals a density functional and ab initio study. *J. Phys. Chem. A*, 110(44):12267–12275, 2006.

[124] Frank Neese. Efficient and accurate approximations to the molecular spin-orbit coupling operator and their use in molecular g-tensor calculations. *J. Chem. Phys.*, 122 (3):034107, 2005.

[125] Roman Reviakine, Alexei V Arbuznikov, Jean-Christophe Tremblay, Christian Remenyi, Olga L Malkina, Vladimir G Malkin, and Martin Kaupp. Calculation of zero-field splitting parameters: Comparison of a two-component noncolinear spin-density-functional method and a one-component perturbational approach. *J. Chem. Phys.*, 125(5):054110, 2006.

[126] Simone Kossmann, Barbara Kirchner, and Frank Neese. Performance of modern density functional theory for the prediction of hyperfine structure: meta-GGA and double hybrid functionals. *Mol. Phys.*, 105(15-16):2049–2071, 2007.

[127] Frank Neese. Calculation of the zero-field splitting tensor on the basis of hybrid density functional and Hartree-Fock theory. *J. Chem. Phys.*, 127(16):164112, 2007.

[128] Eugene S. Kadantsev and Tom Ziegler. Implementation of a density functional theory-based method for the calculation of the hyperfine a-tensor in periodic systems with the use of numerical and Slater type atomic orbitals: Application to paramagnetic defects. *J. Phys. Chem. A*, 112(19):4521–4526, 2008.

[129] Karlheinz Schwarz and Peter Blaha. Solid state calculations using WIEN2k. *Comput. Mater. Sci.*, 28(2):259–273, 2003.

[130] G. H. O. Daalderop, P. J. Kelly, and M. F. H. Schuurmans. Magnetocrystalline anisotropy of yco_5 and related $reco_5$ compounds. *Phys. Rev. B*, 53:14415–14433, June 1996.

[131] Roberto Dovesi, Alessandro Erba, Roberto Orlando, Claudio M Zicovich-Wilson, Bartolomeo Civalleri, Lorenzo Maschio, Michel Rérat, Silvia Casassa, Jacopo Baima, Simone Salustro, and Bernard Kirtman. Quantum-mechanical condensed matter simulations with crystal. *Wiley Interdiscip. Rev.: Comput. Mol. Sci.*, page e1360, 2018.

[132] P. E. Blöchl. Projector augmented-wave method. *Phys. Rev. B*, 50:17953–17979, December 1994.

[133] Krishnendu Ghosh, He Ma, Vikram Gavini, and Giulia Galli. All-electron density functional calculations for electron and nuclear spin interactions in molecules and solids. *Phys. Rev. Mater.*, 3(4):043801, 2019.

[134] Phani Motamarri, Sambit Das, Shiva Rudraraju, Krishnendu Ghosh, Denis Davydov, and Vikram Gavini. Dft-fe – a massively parallel adaptive finite-element code for large-scale density functional theory calculations. *Computer Physics Communications*, 246: 106853, 2020. ISSN 0010-4655. doi:https://doi.org/10.1016/j.cpc.2019.07.016. URL `https://www.sciencedirect.com/science/article/pii/S0010465519302309`.

[135] T. H. Taminiau, J. Cramer, T. van der Sar, V. V. Dobrovitski, and R. Hanson. Universal control and error correction in multi-qubit spin registers in diamond. *Nature Nanotechnology*, 9(3):171–176, February 2014. doi:10.1038/nnano.2014.2. URL https://doi.org/10.1038/nnano.2014.2.

[136] IA Merkulov, Al L Efros, and M Rosen. Electron spin relaxation by nuclei in semiconductor quantum dots. *Phys. Rev. B*, 65(20):205309, 2002.

[137] John F Barry, Jennifer M Schloss, Erik Bauch, Matthew J Turner, Connor A Hart, Linh M Pham, and Ronald L Walsworth. Sensitivity optimization for nv-diamond magnetometry. *Reviews of Modern Physics*, 92(1):015004, 2020.

[138] Joseph M. Zadrozny, Audrey T. Gallagher, T. David Harris, and Danna E. Freedman. A porous array of clock qubits. *Journal of the American Chemical Society*, 139(20): 7089–7094, May 2017. ISSN 0002-7863. doi:10.1021/jacs.7b03123. URL https://doi.org/10.1021/jacs.7b03123.

[139] Viktor Ivády, Igor A. Abrikosov, and Adam Gali. First principles calculation of spin-related quantities for point defect qubit research. *npj Comput. Mater.*, 4(1), December 2018. doi:10.1038/s41524-018-0132-5.

[140] M. H. Abobeih, J. Randall, C. E. Bradley, H. P. Bartling, M. A. Bakker, M. J. Degen, M. Markham, D. J. Twitchen, and T. H. Taminiau. Atomic-scale imaging of a 27-nuclear-spin cluster using a quantum sensor. *Nature*, 576(7787):411–415, December 2019. ISSN 1476-4687. doi:10.1038/s41586-019-1834-7. URL https://doi.org/10.1038/s41586-019-1834-7.

[141] Xiaolong Liu and Mark C. Hersam. 2d materials for quantum information science. *Nature Reviews Materials*, 4(10):669–684, October 2019. ISSN 2058-8437. doi:10.1038/s41578-019-0136-x. URL https://doi.org/10.1038/s41578-019-0136-x.

[142] Moritz Fuchs, Valentin Rychkov, and Björn Trauzettel. Spin decoherence in graphene quantum dots due to hyperfine interaction. *Phys. Rev. B*, 86:085301, August 2012. doi:10.1103/PhysRevB.86.085301. URL https://link.aps.org/doi/10.1103/PhysRevB.86.085301.

[143] Christian Volk, Christoph Neumann, Sebastian Kazarski, Stefan Fringes, Stephan Engels, Federica Haupt, André Müller, and Christoph Stampfer. Probing relaxation times in graphene quantum dots. *Nature Communications*, 4(1):1753, April 2013. ISSN 2041-1723. doi:10.1038/ncomms2738. URL https://doi.org/10.1038/ncomms2738.

[144] Nathan Chejanovsky, Mohammad Rezai, Federico Paolucci, Youngwook Kim, Torsten Rendler, Wafa Rouabeh, Felipe Fávaro de Oliveira, Patrick Herlinger, Andrej Denisenko, Sen Yang, Ilja Gerhardt, Amit Finkler, Jurgen H. Smet, and Jörg Wrachtrup. Structural attributes and photodynamics of visible spectrum quantum

emitters in hexagonal boron nitride. *Nano Letters*, 16(11):7037–7045, November 2016. ISSN 1530-6984. doi:10.1021/acs.nanolett.6b03268. URL https://doi.org/10.1021/acs.nanolett.6b03268.

[145] M. Koperski, K. Nogajewski, A. Arora, V. Cherkez, P. Mallet, J.-Y. Veuillen, J. Marcus, P. Kossacki, and M. Potemski. Single photon emitters in exfoliated wse2 structures. *Nature Nanotechnology*, 10(6):503–506, June 2015. ISSN 1748-3395. doi:10.1038/nnano.2015.67. URL https://doi.org/10.1038/nnano.2015.67.

[146] K. Barthelmi, J. Klein, A. Hötger, L. Sigl, F. Sigger, E. Mitterreiter, S. Rey, S. Gyger, M. Lorke, M. Florian, F. Jahnke, T. Taniguchi, K. Watanabe, V. Zwiller, K. D. Jöns, U. Wurstbauer, C. Kastl, A. Weber-Bargioni, J. J. Finley, K. Müller, and A. W. Holleitner. Atomistic defects as single-photon emitters in atomically thin mos2. *Applied Physics Letters*, 117(7):070501, 2020. doi:10.1063/5.0018557. URL https://doi.org/10.1063/5.0018557.

[147] Annemarie L. Exarhos, David A. Hopper, Raj N. Patel, Marcus W. Doherty, and Lee C. Bassett. Magnetic-field-dependent quantum emission in hexagonal boron nitride at room temperature. *Nature Communications*, 10(1):222, January 2019. ISSN 2041-1723. doi:10.1038/s41467-018-08185-8. URL https://doi.org/10.1038/s41467-018-08185-8.

[148] Andreas Gottscholl, Mehran Kianinia, Victor Soltamov, Sergei Orlinskii, Georgy Mamin, Carlo Bradac, Christian Kasper, Klaus Krambrock, Andreas Sperlich, Milos Toth, Igor Aharonovich, and Vladimir Dyakonov. Initialization and read-out of intrinsic spin defects in a van der waals crystal at room temperature. *Nature Materials*, 19(5):540–545, May 2020. ISSN 1476-4660. doi:10.1038/s41563-020-0619-6. URL https://doi.org/10.1038/s41563-020-0619-6.

[149] Andreas Gottscholl, Matthias Diez, Victor Soltamov, Christian Kasper, Andreas Sperlich, Mehran Kianinia, Carlo Bradac, Igor Aharonovich, and Vladimir Dyakonov. Room temperature coherent control of spin defects in hexagonal boron nitride. *Science Advances*, 7(14), 2021. doi:10.1126/sciadv.abf3630. URL https://advances.sciencemag.org/content/7/14/eabf3630.

[150] Kathleen M. McCreary, Aubrey T. Hanbicki, Simranjeet Singh, Roland K. Kawakami, Glenn G. Jernigan, Masa Ishigami, Amy Ng, Todd H. Brintlinger, Rhonda M. Stroud, and Berend T. Jonker. The effect of preparation conditions on raman and photoluminescence of monolayer ws2. *Scientific Reports*, 6(1):35154, October 2016. ISSN 2045-2322. doi:10.1038/srep35154. URL https://doi.org/10.1038/srep35154.

[151] Bong Gyu Shin, Gang Hee Han, Seok Joon Yun, Hye Min Oh, Jung Jun Bae, Young Jae Song, Chong-Yun Park, and Young Hee Lee. Indirect bandgap puddles in monolayer mos2 by substrate-induced local strain. *Advanced Materials*, 28(42):9378–9384, 2016. doi:https://doi.org/10.1002/adma.201602626. URL https://onlinelibrary.wiley.com/doi/abs/10.1002/adma.201602626.

[152] Gianluca Fiori, Francesco Bonaccorso, Giuseppe Iannaccone, Tomás Palacios, Daniel Neumaier, Alan Seabaugh, Sanjay K. Banerjee, and Luigi Colombo. Electronics based on two-dimensional materials. *Nature Nanotechnology*, 9(10):768–779, October 2014. ISSN 1748-3395. doi:10.1038/nnano.2014.207. URL https://doi.org/10.1038/nnano.2014.207.

[153] Eunho Lee, Seung Goo Lee, Wi Hyoung Lee, Hyo Chan Lee, Nguyen Ngan Nguyen, Min Seok Yoo, and Kilwon Cho. Direct cvd growth of a graphene/mos2 heterostructure with interfacial bonding for two-dimensional electronics. *Chemistry of Materials*, 32 (11):4544–4552, June 2020. ISSN 0897-4756. doi:10.1021/acs.chemmater.0c00503. URL https://doi.org/10.1021/acs.chemmater.0c00503.

[154] L. Britnell, R. V. Gorbachev, R. Jalil, B. D. Belle, F. Schedin, A. Mishchenko, T. Georgiou, M. I. Katsnelson, L. Eaves, S. V. Morozov, N. M. R. Peres, J. Leist, A. K. Geim, K. S. Novoselov, and L. A. Ponomarenko. Field-effect tunneling transistor based on vertical graphene heterostructures. *Science*, 335(6071):947–950, 2012. ISSN 0036-8075. doi:10.1126/science.1218461. URL https://science.sciencemag.org/content/335/6071/947.

[155] Simone Bertolazzi, Daria Krasnozhon, and Andras Kis. Nonvolatile memory cells based on mos2/graphene heterostructures. *ACS Nano*, 7(4):3246–3252, April 2013. ISSN 1936-0851. doi:10.1021/nn3059136. URL https://doi.org/10.1021/nn3059136.

[156] Wonbong Choi, Nitin Choudhary, Gang Hee Han, Juhong Park, Deji Akinwande, and Young Hee Lee. Recent development of two-dimensional transition metal dichalcogenides and their applications. *Materials Today*, 20(3):116–130, 2017. ISSN 1369-7021. doi:https://doi.org/10.1016/j.mattod.2016.10.002. URL http://www.sciencedirect.com/science/article/pii/S1369702116302917.

[157] Igor Aharonovich, Dirk Englund, and Milos Toth. Solid-state single-photon emitters. *Nature Photonics*, 10(10):631–641, October 2016. ISSN 1749-4893. doi:10.1038/nphoton.2016.186. URL https://doi.org/10.1038/nphoton.2016.186.

[158] Luca Chirolli and Guido Burkard. Decoherence in solid-state qubits. *Advances in Physics*, 57(3):225–285, 2008. doi:10.1080/00018730802218067. URL https://doi.org/10.1080/00018730802218067.

[159] Zhong Lin, Bruno R Carvalho, Ethan Kahn, Ruitao Lv, Rahul Rao, Humberto Terrones, Marcos A Pimenta, and Mauricio Terrones. Defect engineering of two-dimensional transition metal dichalcogenides. *2D Materials*, 3(2):022002, April 2016. doi:10.1088/2053-1583/3/2/022002. URL https://doi.org/10.1088/2053-1583/3/2/022002.

[160] T. A. Kennedy, J. S. Colton, J. E. Butler, R. C. Linares, and P. J. Doering. Long coherence times at 300 k for nitrogen-vacancy center spins in diamond grown by chemical vapor deposition. *Applied Physics Letters*, 83(20):4190–4192, 2003. doi:10.1063/1.1626791. URL https://doi.org/10.1063/1.1626791.

[161] John P. Perdew, Kieron Burke, and Matthias Ernzerhof. Generalized gradient approximation made simple. *Phys. Rev. Lett.*, 77(18):3865–3868, October 1996. doi:10.1103/PhysRevLett.77.3865. URL https://link.aps.org/doi/10.1103/PhysRevLett.77.3865.

[162] Matěj Velický, Gavin E. Donnelly, William R. Hendren, Stephen McFarland, Declan Scullion, William J. I. DeBenedetti, Gabriela Calinao Correa, Yimo Han, Andrew J. Wain, Melissa A. Hines, David A. Muller, Kostya S. Novoselov, Héctor D. Abruña, Robert M. Bowman, Elton J. G. Santos, and Fumin Huang. Mechanism of gold-assisted exfoliation of centimeter-sized transition-metal dichalcogenide monolayers. *ACS Nano*, 12(10):10463–10472, October 2018. ISSN 1936-0851. doi:10.1021/acsnano.8b06101. URL https://doi.org/10.1021/acsnano.8b06101.

[163] Kapildeb Dolui, Ivan Rungger, and Stefano Sanvito. Origin of the n-type and p-type conductivity of mos$_2$ monolayers on a sio$_2$ substrate. *Phys. Rev. B*, 87:165402, April 2013. doi:10.1103/PhysRevB.87.165402. URL https://link.aps.org/doi/10.1103/PhysRevB.87.165402.

[164] Yan Wang, Jong Chan Kim, Ryan J. Wu, Jenny Martinez, Xiuju Song, Jieun Yang, Fang Zhao, Andre Mkhoyan, Hu Young Jeong, and Manish Chhowalla. Van der waals contacts between three-dimensional metals and two-dimensional semiconductors. *Nature*, 568(7750):70–74, April 2019. ISSN 1476-4687. doi:10.1038/s41586-019-1052-3. URL https://doi.org/10.1038/s41586-019-1052-3.

[165] Jianping Shi, Donglin Ma, Gao-Feng Han, Yu Zhang, Qingqing Ji, Teng Gao, Jingyu Sun, Xiuju Song, Cong Li, Yanshuo Zhang, Xing-You Lang, Yanfeng Zhang, and Zhongfan Liu. Controllable growth and transfer of monolayer mos2 on au foils and its potential application in hydrogen evolution reaction. *ACS Nano*, 8(10):10196–10204, October 2014. ISSN 1936-0851. doi:10.1021/nn503211t. URL https://doi.org/10.1021/nn503211t.

[166] Ryan E. Wood, Lawson T. Lloyd, Fauzia Mujid, Lili Wang, Marco A. Allodi, Hui Gao, Richard Mazuski, Po-Chieh Ting, Saien Xie, Jiwoong Park, and Gregory S. Engel. Evidence for the dominance of carrier-induced band gap renormalization over biexciton formation in cryogenic ultrafast experiments on mos2 monolayers. *The Journal of Physical Chemistry Letters*, 11(7):2658–2666, April 2020. doi:10.1021/acs.jpclett.0c00169. URL https://doi.org/10.1021/acs.jpclett.0c00169.

[167] Jianping Shi, Rui Tong, Xiebo Zhou, Yue Gong, Zhepeng Zhang, Qingqing Ji, Yu Zhang, Qiyi Fang, Lin Gu, Xina Wang, Zhongfan Liu, and Yanfeng Zhang. Temperature-mediated selective growth of mos2/ws2 and ws2/mos2 vertical stacks on au foils for direct photocatalytic applications. *Advanced Materials*, 28(48):10664–10672, 2016. doi:https://doi.org/10.1002/adma.201603174. URL https://onlinelibrary.wiley.com/doi/abs/10.1002/adma.201603174.

[168] Amirhossein Hasani, Quyet Van Le, Mahider Tekalgne, Min-Ju Choi, Seokhoon Choi, Tae Hyung Lee, Hayeong Kim, Sang Hyun Ahn, Ho Won Jang, and Soo Young Kim. Fabrication of a ws2/p-si heterostructure photocathode using direct hybrid thermolysis. *ACS Applied Materials & Interfaces*, 11(33):29910–29916, August 2019. ISSN 1944-8244. doi:10.1021/acsami.9b08654. URL https://doi.org/10.1021/acsami.9b08654.

[169] Daniel Rhodes, Sang Hoon Chae, Rebeca Ribeiro-Palau, and James Hone. Disorder in van der waals heterostructures of 2d materials. *Nature Materials*, 18(6):541–549, June 2019. ISSN 1476-4660. doi:10.1038/s41563-019-0366-8. URL https://doi.org/10.1038/s41563-019-0366-8.

[170] Riccardo Pisoni, Andor Kormányos, Matthew Brooks, Zijin Lei, Patrick Back, Marius Eich, Hiske Overweg, Yongjin Lee, Peter Rickhaus, Kenji Watanabe, Takashi Taniguchi, Atac Imamoglu, Guido Burkard, Thomas Ihn, and Klaus Ensslin. Interactions and magnetotransport through spin-valley coupled landau levels in monolayer mos_2. *Phys. Rev. Lett.*, 121:247701, December 2018. doi:10.1103/PhysRevLett.121.247701. URL https://link.aps.org/doi/10.1103/PhysRevLett.121.247701.

[171] Fang Zhang, Wei Li, Yaqiang Ma, Yanan Tang, and Xianqi Dai. Tuning the schottky contacts at the graphene/ws2 interface by electric field. *RSC Adv.*, 7:29350–29356, 2017. doi:10.1039/c7ra00589j. URL http://dx.doi.org/10.1039/C7RA00589J.

[172] Zilu Wang, Qian Chen, and Jinlan Wang. Electronic structure of twisted bilayers of graphene/mos2 and mos2/mos2. *The Journal of Physical Chemistry C*, 119(9):4752–4758, March 2015. ISSN 1932-7447a. doi:10.1021/jp507751p. URL https://doi.org/10.1021/jp507751p.

[173] Bruno Schuler, Katherine A. Cochrane, Christoph Kastl, Edward S. Barnard, Edward Wong, Nicholas J. Borys, Adam M. Schwartzberg, D. Frank Ogletree, F. Javier García de Abajo, and Alexander Weber-Bargioni. Electrically driven photon emission from individual atomic defects in monolayer ws2. *Science Advances*, 6(38), 2020. doi:10.1126/sciadv.abb5988. URL https://advances.sciencemag.org/content/6/38/eabb5988.

[174] Erik Bauch, Swati Singh, Junghyun Lee, Connor A. Hart, Jennifer M. Schloss, Matthew J. Turner, John F. Barry, Linh M. Pham, Nir Bar-Gill, Susanne F. Yelin, and Ronald L. Walsworth. Decoherence of ensembles of nitrogen-vacancy centers in diamond. *Phys. Rev. B*, 102:134210, October 2020. ISSN 24699969. doi:10.1103/PhysRevB.102.134210. URL https://link.aps.org/doi/10.1103/PhysRevB.102.134210.

[175] V. V. Dobrovitski, A. E. Feiguin, D. D. Awschalom, and R. Hanson. Decoherence dynamics of a single spin versus spin ensemble. *Phys. Rev. B*, 77:245212, June 2008.

doi:10.1103/PhysRevB.77.245212. URL https://link.aps.org/doi/10.1103/PhysRevB.77.245212.

[176] J. R. Klauder and P. W. Anderson. Spectral diffusion decay in spin resonance experiments. *Phys. Rev.*, 125:912–932, February 1962. doi:10.1103/PhysRev.125.912. URL https://link.aps.org/doi/10.1103/PhysRev.125.912.

[177] Rogerio de Sousa and S. Das Sarma. Electron spin coherence in semiconductors: Considerations for a spin-based solid-state quantum computer architecture. *Phys. Rev. B*, 67:033301, January 2003. doi:10.1103/PhysRevB.67.033301. URL https://link.aps.org/doi/10.1103/PhysRevB.67.033301.

[178] Wang Yao, Ren-Bao Liu, and L. J. Sham. Theory of electron spin decoherence by interacting nuclear spins in a quantum dot. *Phys. Rev. B*, 74:195301, November 2006. doi:10.1103/PhysRevB.74.195301. URL https://link.aps.org/doi/10.1103/PhysRevB.74.195301.

[179] Nan Zhao, Jian-Liang Hu, Sai-Wah Ho, Jones T. K. Wan, and R. B. Liu. Atomic-scale magnetometry of distant nuclear spin clusters via nitrogen-vacancy spin in diamond. *Nature Nanotechnology*, 6(4):242–246, April 2011. ISSN 1748-3395. doi:10.1038/nnano.2011.22. URL https://doi.org/10.1038/nnano.2011.22.

[180] I. Lovchinsky, J. D. Sanchez-Yamagishi, E. K. Urbach, S. Choi, S. Fang, T. I. Andersen, K. Watanabe, T. Taniguchi, A. Bylinskii, E. Kaxiras, P. Kim, H. Park, and M. D. Lukin. Magnetic resonance spectroscopy of an atomically thin material using a single-spin qubit. *Science*, 355(6324):503–507, 2017. ISSN 0036-8075. doi:10.1126/science.aal2538. URL https://science.sciencemag.org/content/355/6324/503.

[181] Brian B. Zhou, Paul C. Jerger, Kan-Heng Lee, Masaya Fukami, Fauzia Mujid, Jiwoong Park, and David D. Awschalom. Spatiotemporal mapping of a photocurrent vortex in monolayer mos_2 using diamond quantum sensors. *Phys. Rev. X*, 10:011003, January 2020. doi:10.1103/PhysRevX.10.011003. URL https://link.aps.org/doi/10.1103/PhysRevX.10.011003.

[182] Junqing Xu, Adela Habib, Sushant Kumar, Feng Wu, Ravishankar Sundararaman, and Yuan Ping. Spin-phonon relaxation from a universal ab initio density-matrix approach. *Nature Communications*, 11(1):2780, June 2020. ISSN 2041-1723. doi:10.1038/s41467-020-16063-5. URL https://doi.org/10.1038/s41467-020-16063-5.

[183] Zhe Wang, Dong-Keun Ki, Hua Chen, Helmuth Berger, Allan H. MacDonald, and Alberto F. Morpurgo. Strong interface-induced spin–orbit interaction in graphene on ws2. *Nature Communications*, 6(1):8339, September 2015. ISSN 2041-1723. doi:10.1038/ncomms9339. URL https://doi.org/10.1038/ncomms9339.

[184] Luyi Yang, Nikolai A. Sinitsyn, Weibing Chen, Jiangtan Yuan, Jing Zhang, Jun Lou, and Scott A. Crooker. Long-lived nanosecond spin relaxation and spin coherence of

electrons in monolayer mos2 and ws2. *Nature Physics*, 11(10):830–834, October 2015. ISSN 1745-2481. doi:10.1038/nphys3419. URL https://doi.org/10.1038/nphys3419.

[185] Damian Kwiatkowski, Piotr Szańkowski, and Łukasz Cywiński. Influence of nuclear spin polarization on the spin-echo signal of an nv-center qubit. *Phys. Rev. B*, 101: 155412, April 2020. doi:10.1103/PhysRevB.101.155412. URL https://link.aps.org/doi/10.1103/PhysRevB.101.155412.

[186] T. H. Taminiau, J. J. T. Wagenaar, T. van der Sar, F. Jelezko, V. V. Dobrovitski, and R. Hanson. Detection and control of individual nuclear spins using a weakly coupled electron spin. *Phys. Rev. Lett.*, 109:137602, September 2012. doi:10.1103/PhysRevLett.109.137602. URL https://link.aps.org/doi/10.1103/PhysRevLett.109.137602.

[187] Shimon Kolkowitz, Quirin P. Unterreithmeier, Steven D. Bennett, and Mikhail D. Lukin. Sensing distant nuclear spins with a single electron spin. *Phys. Rev. Lett.*, 109: 137601, Sep 2012. doi:10.1103/PhysRevLett.109.137601. URL https://link.aps.org/doi/10.1103/PhysRevLett.109.137601.

[188] Laima Busaite, Reinis Lazda, Andris Berzins, Marcis Auzinsh, Ruvin Ferber, and Florian Gahbauer. Dynamic ^{14}N nuclear spin polarization in nitrogen-vacancy centers in diamond. *Phys. Rev. B*, 102:224101, Dec 2020. doi:10.1103/PhysRevB.102.224101. URL https://link.aps.org/doi/10.1103/PhysRevB.102.224101.

[189] Yu-Xin Wang and Aashish A. Clerk. Intrinsic and induced quantum quenches for enhancing qubit-based quantum noise spectroscopy. *Nature Communications*, 12(1), November 2021. doi:10.1038/s41467-021-26868-7. URL https://doi.org/10.1038/s41467-021-26868-7.

[190] A. Henstra and W. Th. Wenckebach. The theory of nuclear orientation via electron spin locking (novel). *Mol. Phys.*, 106(7):859–871, 2008. doi:10.1080/00268970801998262. URL https://www.tandfonline.com/doi/abs/10.1080/00268970801998262.

[191] Dominik B. Bucher, David R. Glenn, Hongkun Park, Mikhail D. Lukin, and Ronald L. Walsworth. Hyperpolarization-enhanced nmr spectroscopy with femtomole sensitivity using quantum defects in diamond. *Phys. Rev. X*, 10:021053, Jun 2020. doi:10.1103/PhysRevX.10.021053. URL https://link.aps.org/doi/10.1103/PhysRevX.10.021053.

[192] D. R. Glenn, D. B. Bucher, J. Lee, M. D. Lukin, H. Park, and R. L. Walsworth. High-resolution magnetic resonance spectroscopy using a solid-state spin sensor. *Nature (London)*, 555:351, Mar 2018. doi:10.1038/nature25781. URL https://doi.org/10.1038/nature25781.

[193] Marcus W. Doherty, Neil B. Manson, Paul Delaney, Fedor Jelezko, Jörg Wrachtrup, and Lloyd C.L. Hollenberg. The nitrogen-vacancy colour centre in diamond. *Phys.*

Rep., 528(1):1–45, 7 2013. ISSN 03701573. doi:10.1016/j.physrep.2013.02.001. URL https://linkinghub.elsevier.com/retrieve/pii/S0370157313000562.

[194] Carlo Bradac, Weibo Gao, Jacopo Forneris, Matthew E. Trusheim, and Igor Aharonovich. Quantum nanophotonics with group iv defects in diamond. *Nat. Commun.*, 10:5625, 12 2019. ISSN 20411723. doi:10.1038/s41467-019-13332-w.

[195] Gopalakrishnan Balasubramanian, I. Y. Chan, Roman Kolesov, Mohannad Al-Hmoud, Julia Tisler, Chang Shin, Changdong Kim, Aleksander Wojcik, Philip R. Hemmer, Anke Krueger, Tobias Hanke, Alfred Leitenstorfer, Rudolf Bratschitsch, Fedor Jelezko, and Jörg Wrachtrup. Nanoscale imaging magnetometry with diamond spins under ambient conditions. *Nature*, 455:648–651, 10 2008. ISSN 14764687. doi:10.1038/nature07278.

[196] J. R. Maze, P. L. Stanwix, J. S. Hodges, S. Hong, J. M. Taylor, P. Cappellaro, L. Jiang, M. V. Gurudev Dutt, E. Togan, A. S. Zibrov, A. Yacoby, R. L. Walsworth, and M. D. Lukin. Nanoscale magnetic sensing with an individual electronic spin in diamond. *Nature*, 455:644–647, 10 2008. ISSN 14764687. doi:10.1038/nature07279.

[197] B. J. Maertz, A. P. Wijnheijmer, G. D. Fuchs, M. E. Nowakowski, and D. D. Awschalom. Vector magnetic field microscopy using nitrogen vacancy centers in diamond. *Appl. Phys. Lett.*, 96:092504, 2010. ISSN 00036951. doi:10.1063/1.3337096.

[198] D. Le Sage, K. Arai, D. R. Glenn, S. J. DeVience, L. M. Pham, L. Rahn-Lee, M. D. Lukin, A. Yacoby, A. Komeili, and R. L. Walsworth. Optical magnetic imaging of living cells. *Nature*, 496:486–489, 4 2013. ISSN 0028-0836. doi:10.1038/nature12072. URL http://www.nature.com/articles/nature12072.

[199] L Rondin, J-P Tetienne, T Hingant, J-F Roch, P Maletinsky, and V Jacques. Magnetometry with nitrogen-vacancy defects in diamond. *Rep. Prog. Phys.*, 77:056503, 5 2014. ISSN 0034-4885. doi:10.1088/0034-4885/77/5/056503. URL https://iopscience.iop.org/article/10.1088/0034-4885/77/5/056503.

[200] H. J. Mamin, M. Kim, M. H. Sherwood, C. T. Rettner, K. Ohno, D. D. Awschalom, and D. Rugar. Nanoscale nuclear magnetic resonance with a nitrogen-vacancy spin sensor. *Science*, 339:557–560, 2 2013. ISSN 0036-8075. doi:10.1126/science.1231540. URL https://www.science.org/doi/10.1126/science.1231540.

[201] T. Staudacher, F. Shi, S. Pezzagna, J. Meijer, J. Du, C. A. Meriles, F. Reinhard, and J. Wrachtrup. Nuclear magnetic resonance spectroscopy on a (5-nanometer)^3 sample volume. *Science*, 339:561–563, 2 2013. ISSN 10959203. doi:10.1126/science.1231675.

[202] Francesco Casola, Toeno van der Sar, and Amir Yacoby. Probing condensed matter physics with magnetometry based on nitrogen-vacancy centres in diamond. *Nat. Rev. Mater.*, 3:17088, 1 2018. ISSN 2058-8437. doi:10.1038/natrevmats.2017.88. URL http://www.nature.com/articles/natrevmats201788.

[203] Zhiyuan Zhao, Xiangyu Ye, Shaoyi Xu, Pei Yu, Zhiping Yang, Xi Kong, Ya Wang, Tianyu Xie, Fazhan Shi, and Jiangfeng Du. Sub-nanotesla sensitivity at the nanoscale with a single spin. *arXiv*, page 2205.04415, 5 2022. URL http://arxiv.org/abs/2205.04415.

[204] N. Kalb, A. A. Reiserer, P. C. Humphreys, J. J. W. Bakermans, S. J. Kamerling, N. H. Nickerson, S. C. Benjamin, D. J. Twitchen, M. Markham, and R. Hanson. Entanglement distillation between solid-state quantum network nodes. *Science*, 356 (6341):928–932, June 2017. ISSN 0036-8075. doi:10.1126/science.aan0070. URL https://doi.org/10.1126/science.aan0070.

[205] C. T. Nguyen, D. D. Sukachev, M. K. Bhaskar, B. Machielse, D. S. Levonian, E. N. Knall, P. Stroganov, R. Riedinger, H. Park, M. Lončar, and M. D. Lukin. Quantum network nodes based on diamond qubits with an efficient nanophotonic interface. *Phys. Rev. Lett.*, 123:183602, October 2019. doi:10.1103/PhysRevLett.123.183602. URL https://link.aps.org/doi/10.1103/PhysRevLett.123.183602.

[206] C. T. Nguyen, D. D. Sukachev, M. K. Bhaskar, B. Machielse, D. S. Levonian, E. N. Knall, P. Stroganov, C. Chia, M. J. Burek, R. Riedinger, H. Park, M. Lončar, and M. D. Lukin. An integrated nanophotonic quantum register based on silicon-vacancy spins in diamond. *Phys. Rev. B*, 100:165428, October 2019. doi:10.1103/PhysRevB.100.165428. URL https://link.aps.org/doi/10.1103/PhysRevB.100.165428.

[207] S. L. N. Hermans, M. Pompili, H. K. C. Beukers, S. Baier, J. Borregaard, and R. Hanson. Qubit teleportation between non-neighbouring nodes in a quantum network. *Nature*, 605(7911):663–668, May 2022. ISSN 0028-0836. doi:10.1038/s41586-022-04697-y. URL https://doi.org/10.1038/s41586-022-04697-y.

[208] D. M. Toyli, D. J. Christle, A. Alkauskas, B. B. Buckley, C. G. Van de Walle, and D. D. Awschalom. Measurement and control of single nitrogen-vacancy center spins above 600 k. *Phys. Rev. X*, 2:031001, 2012. ISSN 21603308. doi:10.1103/PhysRevX.2.031001.

[209] F. Joseph Heremans, Christopher G. Yale, and David D. Awschalom. Control of spin defects in wide-bandgap semiconductors for quantum technologies. *Proc. IEEE*, 104: 2009–2023, 10 2016. ISSN 00189219. doi:10.1109/jproc.2016.2561274. URL https://ieeexplore.ieee.org/document/7478018/.

[210] Matthias Pfender, Nabeel Aslam, Hitoshi Sumiya, Shinobu Onoda, Philipp Neumann, Junichi Isoya, Carlos A. Meriles, and Jörg Wrachtrup. Nonvolatile nuclear spin memory enables sensor-unlimited nanoscale spectroscopy of small spin clusters. *Nat. Commun.*, 8:834, 12 2017. ISSN 20411723. doi:10.1038/s41467-017-00964-z.

[211] C. E. Bradley, J. Randall, M. H. Abobeih, R. C. Berrevoets, M. J. Degen, M. A. Bakker, M. Markham, D. J. Twitchen, and T. H. Taminiau. A ten-qubit solid-state spin register with quantum memory up to one minute. *Phys. Rev. X*, 9:031045, September 2019. ISSN 21603308. doi:10.1103/PhysRevX.9.031045. URL https://link.aps.org/doi/10.1103/PhysRevX.9.031045.

[212] M. J. Degen, S. J.H. Loenen, H. P. Bartling, C. E. Bradley, A. L. Meinsma, M. Markham, D. J. Twitchen, and T. H. Taminiau. Entanglement of dark electron-nuclear spin defects in diamond. *Nat. Commun.*, 12:3470, 12 2021. ISSN 20411723. doi:10.1038/s41467-021-23454-9.

[213] Tianyu Xie, Zhiyuan Zhao, Xi Kong, Wenchao Ma, Mengqi Wang, Xiangyu Ye, Pei Yu, Zhiping Yang, Shaoyi Xu, Pengfei Wang, Ya Wang, Fazhan Shi, and Jiangfeng Du. Beating the standard quantum limit under ambient conditions with solid-state spins. *Sci. Adv.*, 7:eabg9204, 8 2021. ISSN 2375-2548. doi:10.1126/sciadv.abg9204. URL `https://www.science.org/doi/10.1126/sciadv.abg9204`.

[214] Tian-Xing Zheng, Anran Li, Jude Rosen, Sisi Zhou, Martin Koppenhöfer, Ziqi Ma, Frederic T. Chong, Aashish A. Clerk, Liang Jiang, and Peter C. Maurer. Preparation of metrological states in dipolar-interacting spin systems. *npj Quantum Inf.*, 8:150, December 2022. doi:10.1038/s41534-022-00667-4. URL `https://doi.org/10.1038/s41534-022-00667-4`.

[215] R. Hanson, F. M. Mendoza, R. J. Epstein, and D. D. Awschalom. Polarization and readout of coupled single spins in diamond. *Phys. Rev. Lett.*, 97:087601, 8 2006. ISSN 0031-9007. doi:10.1103/PhysRevLett.97.087601. URL `https://link.aps.org/doi/10.1103/PhysRevLett.97.087601`.

[216] Helena S. Knowles, Dhiren M. Kara, and Mete Atatüre. Demonstration of a coherent electronic spin cluster in diamond. *Phys. Rev. Lett.*, 117:1–5, 2016. ISSN 10797114. doi:10.1103/PhysRevLett.117.100802.

[217] J. Meijer, B. Burchard, M. Domhan, C. Wittmann, T. Gaebel, I. Popa, F. Jelezko, and J. Wrachtrup. Generation of single color centers by focused nitrogen implantation. *Appl. Phys. Lett.*, 87:1–3, 2005. ISSN 00036951. doi:10.1063/1.2103389.

[218] J. R. Rabeau, P. Reichart, G. Tamanyan, D. N. Jamieson, S. Prawer, F. Jelezko, T. Gaebel, I. Popa, M. Domhan, and J. Wrachtrup. Implantation of labelled single nitrogen vacancy centers in diamond using 15n. *Appl. Phys. Lett.*, 88:1–3, 2006. ISSN 00036951. doi:10.1063/1.2158700.

[219] Torsten Gaebel, Michael Domhan, Iulian Popa, Christoffer Wittmann, Philipp Neumann, Fedor Jelezko, James R. Rabeau, Nikolas Stavrias, Andrew D. Greentree, Steven Prawer, Jan Meijer, Jason Twamley, Philip R. Hemmer, and Jörg Wrachtrup. Room-temperature coherent coupling of single spins in diamond. *Nat. Phys.*, 2:408–413, 2006. ISSN 17452481. doi:10.1038/nphys318.

[220] P. Neumann, R. Kolesov, B. Naydenov, J. Beck, F. Rempp, M. Steiner, V. Jacques, G. Balasubramanian, M. L. Markham, D. J. Twitchen, S. Pezzagna, J. Meijer, J. Twamley, F. Jelezko, and J. Wrachtrup. Quantum register based on coupled electron spins in a room-temperature solid. *Nat. Phys.*, 6:249–253, 2010. ISSN 17452473. doi:10.1038/nphys1536. URL `http://dx.doi.org/10.1038/nphys1536`.

[221] F. Dolde, I. Jakobi, B. Naydenov, N. Zhao, S. Pezzagna, C. Trautmann, J. Meijer, P. Neumann, F. Jelezko, and J. Wrachtrup. Room-temperature entanglement between single defect spins in diamond. *Nat. Phys.*, 9:139–143, 3 2013. ISSN 1745-2473. doi:10.1038/nphys2545. URL http://www.nature.com/articles/nphys2545.

[222] E. L. Rosenfeld, L. M. Pham, M. D. Lukin, and R. L. Walsworth. Sensing coherent dynamics of electronic spin clusters in solids. *Phys. Rev. Lett.*, 120:243604, 2018. ISSN 10797114. doi:10.1103/PhysRevLett.120.243604. URL https://doi.org/10.1103/PhysRevLett.120.243604.

[223] Alexandre Cooper, Won Kyu Calvin Sun, Jean Christophe Jaskula, and Paola Cappellaro. Identification and control of electron-nuclear spin defects in diamond. *Phys. Rev. Lett.*, 124:083602, 2 2020. ISSN 10797114. doi:10.1103/PhysRevLett.124.083602.

[224] Jaewook Lee, Huijin Park, and Hosung Seo. First-principles theory of extending the spin qubit coherence time in hexagonal boron nitride. *npj 2D Materials and Applications*, 6(1):2203.07610, September 2022. doi:10.1038/s41699-022-00336-2. URL https://doi.org/10.1038/s41699-022-00336-2.

[225] T. Yamamoto, T. Umeda, K. Watanabe, S. Onoda, M. L. Markham, D. J. Twitchen, B. Naydenov, L. P. McGuinness, T. Teraji, S. Koizumi, F. Dolde, H. Fedder, J. Honert, J. Wrachtrup, T. Ohshima, F. Jelezko, and J. Isoya. Extending spin coherence times of diamond qubits by high-temperature annealing. *Phys. Rev. B*, 88:075206, 8 2013. ISSN 10980121. doi:10.1103/PhysRevB.88.075206.

[226] H. Okushi, H. Watanabe, S. Ri, S. Yamanaka, and D. Takeuchi. Device-grade homoepitaxial diamond film growth. *J. Cryst. Growth*, 237-239:1269–1276, 4 2002. ISSN 00220248. doi:10.1016/s0022-0248(01)02144-3. URL https://linkinghub.elsevier.com/retrieve/pii/S0022024801021443.

[227] K. Ohno. *Nanometer-scale engineering of shallow spins in diamond*. PhD thesis, University of California, Santa Barbara, 2014.

[228] Tim R. Eichhorn, Claire A. McLellan, and Ania C. Bleszynski Jayich. Optimizing the formation of depth-confined nitrogen vacancy center spin ensembles in diamond for quantum sensing. *Phys. Rev. Mater.*, 3:113802, 11 2019. ISSN 2475-9953. doi:10.1103/PhysRevMaterials.3.113802. URL https://link.aps.org/doi/10.1103/PhysRevMaterials.3.113802.

[229] Priyadharshini Balasubramanian, Christian Osterkamp, Ovidiu Brinza, Maxime Rollo, Isabelle Robert-Philip, Philippe Goldner, Vincent Jacques, Fedor Jelezko, Jocelyn Achard, and Alexandre Tallaire. Enhancement of the creation yield of nv ensembles in a chemically vapour deposited diamond. *Carbon*, 194:282–289, 7 2022. ISSN 00086223. doi:10.1016/j.carbon.2022.04.005. URL https://linkinghub.elsevier.com/retrieve/pii/S0008622322002755.

[230] Kenichi Ohno, F. Joseph Heremans, Lee C. Bassett, Bryan A. Myers, David M. Toyli, Ania C. Bleszynski Jayich, Christopher J. Palmstrøm, and David D. Awschalom. Engineering shallow spins in diamond with nitrogen delta-doping. *Appl. Phys. Lett.*, 101: 082413, 8 2012. ISSN 0003-6951. doi:10.1063/1.4748280. URL `http://aip.scitation.org/doi/10.1063/1.4748280`.

[231] Claire A. McLellan, Bryan A. Myers, Stephan Kraemer, Kenichi Ohno, David D. Awschalom, and Ania C. Bleszynski Jayich. Patterned formation of highly coherent nitrogen-vacancy centers using a focused electron irradiation technique. *Nano Lett.*, 16: 2450–2454, 4 2016. ISSN 1530-6984. doi:10.1021/acs.nanolett.5b05304. URL `https://pubs.acs.org/doi/10.1021/acs.nanolett.5b05304`.

[232] David M. Toyli, Christoph D. Weis, Gregory D. Fuchs, Thomas Schenkel, and David D. Awschalom. Chip-scale nanofabrication of single spins and spin arrays in diamond. *Nano Lett.*, 10:3168–3172, 8 2010. ISSN 15306984. doi:10.1021/nl102066q.

[233] P. Spinicelli, A. Dréau, L. Rondin, F. Silva, J. Achard, S. Xavier, S. Bansropun, T. Debuisschert, S. Pezzagna, J. Meijer, V. Jacques, and J. F. Roch. Engineered arrays of nitrogen-vacancy color centers in diamond based on implantation of cn^- molecules through nanoapertures. *New J. Phys.*, 13:025014, 2 2011. ISSN 13672630. doi:10.1088/1367-2630/13/2/025014.

[234] Kenichi Ohno, F. Joseph Heremans, Charles F. De Las Casas, Bryan A. Myers, Benjamín J. Alemán, Ania C. Bleszynski Jayich, and David D. Awschalom. Three-dimensional localization of spins in diamond using 12c implantation. *Appl. Phys. Lett.*, 105:052406, 8 2014. ISSN 00036951. doi:10.1063/1.4890613.

[235] S. Sangtawesin, T. O. Brundage, Z. J. Atkins, and J. R. Petta. Highly tunable formation of nitrogen-vacancy centers via ion implantation. *Appl. Phys. Lett.*, 105:063107, 8 2014. ISSN 00036951. doi:10.1063/1.4892971.

[236] I. Jakobi, S. A. Momenzadeh, F. Fávaro De Oliveira, J. Michl, F. Ziem, M. Schreck, P. Neumann, A. Denisenko, and J. Wrachtrup. Efficient creation of dipolar coupled nitrogen-vacancy spin qubits in diamond. *J. Phys.: Conf. Ser.*, 752:012001, 9 2016. ISSN 17426596. doi:10.1088/1742-6596/752/1/012001.

[237] Igal Bayn, Edward H. Chen, Matthew E. Trusheim, Luozhou Li, Tim Schröder, Ophir Gaathon, Ming Lu, Aaron Stein, Mingzhao Liu, Kim Kisslinger, Hannah Clevenson, and Dirk Englund. Generation of ensembles of individually resolvable nitrogen vacancies using nanometer-scale apertures in ultrahigh-aspect ratio planar implantation masks. *Nano Lett.*, 15:1751–1758, 3 2015. ISSN 1530-6984. doi:10.1021/nl504441m. URL `https://pubs.acs.org/doi/10.1021/nl504441m`.

[238] Tae-Yeon Hwang, Junghyun Lee, Seung-Woo Jeon, Yong-Su Kim, Young-Wook Cho, Hyang-Tag Lim, Sung Moon, Sang-Wook Han, Yong-Ho Choa, and Hojoong Jung. Sub-10 nm precision engineering of solid-state defects via nanoscale aperture array mask. *Nano Lett.*, 22:1672–1679, 2 2022. ISSN 15306992. doi:10.1021/acs.nanolett.1c04699.

[239] N. Mizuochi, P. Neumann, F. Rempp, J. Beck, V. Jacques, P. Siyushev, K. Nakamura, D. J. Twitchen, H. Watanabe, S. Yamasaki, F. Jelezko, and J. Wrachtrup. Coherence of single spins coupled to a nuclear spin bath of varying density. *Phys. Rev. B*, 80: 041201, July 2009. ISSN 10980121. doi:10.1103/PhysRevB.80.041201. URL `https://link.aps.org/doi/10.1103/PhysRevB.80.041201`.

[240] Gopalakrishnan Balasubramanian, Philipp Neumann, Daniel Twitchen, Matthew Markham, Roman Kolesov, Norikazu Mizuochi, Junichi Isoya, Jocelyn Achard, Johannes Beck, Julia Tissler, Vincent Jacques, Philip R. Hemmer, Fedor Jelezko, and Jörg Wrachtrup. Ultralong spin coherence time in isotopically engineered diamond. *Nature Materials*, 8(5):383–387, April 2009. ISSN 1476-1122. doi:10.1038/nmat2420. URL `https://doi.org/10.1038/nmat2420`.

[241] E. J. Davis, B. Ye, F. Machado, S. A. Meynell, W. Wu, T. Mittiga, W. Schenken, M. Joos, B. Kobrin, Y. Lyu, Z. Wang, D. Bluvstein, S. Choi, C. Zu, A. C. Bleszynski Jayich, and N. Y. Yao. Probing many-body dynamics in a two-dimensional dipolar spin ensemble. *Nat. Phys.*, 3 2023. ISSN 1745-2473. doi:10.1038/s41567-023-01944-5. URL `https://www.nature.com/articles/s41567-023-01944-5`.

[242] Lillian B. Hughes, Zhiran Zhang, Chang Jin, Simon A. Meynell, Bingtian Ye, Weijie Wu, Zilin Wang, Emily J. Davis, Thomas E. Mates, Norman Y. Yao, Kunal Mukherjee, and Ania C. Bleszynski Jayich. Two-dimensional spin systems in pecvd-grown diamond with tunable density and long coherence for enhanced quantum sensing and simulation. *APL Mater.*, 11(2):021101, 2023. doi:10.1063/5.0133501. URL `https://doi.org/10.1063/5.0133501`.

[243] Tobias Lühmann, Roger John, Ralf Wunderlich, Jan Meijer, and Sébastien Pezzagna. Coulomb-driven single defect engineering for scalable qubits and spin sensors in diamond. *Nat. Commun.*, 10:4956, 12 2019. ISSN 20411723. doi:10.1038/s41467-019-12556-0.

[244] Riku Kawase, Hiroyuki Kawashima, Hiromitsu Kato, Norio Tokuda, Satoshi Yamasaki, Masahiko Ogura, Toshiharu Makino, , and Norikazu Mizuochi. n-type diamond synthesized with tert-butylphosphine for long spin coherence times of perfectly aligned nv centers. *arXiv*, page 2205.15539, 5 2022. URL `http://arxiv.org/abs/2205.15539`.

[245] Huijin Park, Junghyun Lee, Sangwook Han, Sangwon Oh, and Hosung Seo. Decoherence of nitrogen-vacancy spin ensembles in a nitrogen electron-nuclear spin bath in diamond. *npj Quantum Information*, 8(1):95, August 2022. ISSN 20566387. doi:10.1038/s41534-022-00605-4. URL `https://doi.org/10.1038/s41534-022-00605-4`.

[246] Nathalie P. de Leon, Kohei M. Itoh, Dohun Kim, Karan K. Mehta, Tracy E. Northup, Hanhee Paik, B. S. Palmer, N. Samarth, Sorawis Sangtawesin, and D. W. Steuerman. Materials challenges and opportunities for quantum computing hardware. *Science*,

372:eabb2823, 4 2021. ISSN 0036-8075. doi:10.1126/science.abb2823. URL https://www.science.org/doi/10.1126/science.abb2823.

[247] Chikara Shinei, Yuta Masuyama, Masashi Miyakawa, Hiroshi Abe, Shuya Ishii, Seiichi Saiki, Shinobu Onoda, Takashi Taniguchi, Takeshi Ohshima, and Tokuyuki Teraji. Nitrogen related paramagnetic defects: Decoherence source of ensemble of nv^- center. *J. Appl. Phys.*, 132:214402, 12 2022. ISSN 0021-8979. doi:10.1063/5.0103332. URL https://aip.scitation.org/doi/10.1063/5.0103332.

[248] M. Annis, W. Cheston, and H. Primakoff. On statistical estimation in physics. *Rev. Mod. Phys.*, 25:818–830, 10 1953. ISSN 0034-6861. doi:10.1103/RevModPhys.25.818. URL https://link.aps.org/doi/10.1103/RevModPhys.25.818.

[249] A Cox, M E Newton, and J M Baker. 13c, 14n and 15n endor measurements on the single substitutional nitrogen centre (pl) in diamond. *J. Phys.: Condens. Matter*, 6: 551–563, 1994. doi:10.1088/0953-8984/6/2/025.

[250] Xinghan Guo, Nazar Delegan, Jonathan C. Karsch, Zixi Li, Tianle Liu, Robert Shreiner, Amy Butcher, David D. Awschalom, F. Joseph Heremans, and Alexander A. High. Tunable and transferable diamond membranes for integrated quantum technologies. *Nano Lett.*, 21:10392–10399, 12 2021. ISSN 1530-6984. doi:10.1021/acs.nanolett.1c03703. URL https://pubs.acs.org/doi/10.1021/acs.nanolett.1c03703.

[251] A. Tallaire, M. Kasu, K. Ueda, and T. Makimoto. Origin of growth defects in cvd diamond epitaxial films. *Diam. Relat. Mater.*, 17:60–65, 1 2008. ISSN 09259635. doi:10.1016/j.diamond.2007.10.003.

[252] D. A. Broadway, N. Dontschuk, A. Tsai, S. E. Lillie, C. T.-K. Lew, J. C. McCallum, B. C. Johnson, M. W. Doherty, A. Stacey, L. C. L. Hollenberg, and J.-P. Tetienne. Spatial mapping of band bending in semiconductor devices using in situ quantum sensors. *Nat. Electron.*, 1:502–507, 9 2018. ISSN 2520-1131. doi:10.1038/s41928-018-0130-0. URL http://www.nature.com/articles/s41928-018-0130-0.

[253] Jeffrey Neethi Neethirajan, Toni Hache, Domenico Paone, Dinesh Pinto, Andrej Denisenko, Rainer Stöhr, Péter Udvarhelyi, Anton Pershin, Adam Gali, Joerg Wrachtrup, Klaus Kern, and Aparajita Singha. Controlled surface modification to revive shallow nv–centers. *Nano Lett.*, 03 2023. doi:10.1021/acs.nanolett.2c04733. URL https://doi.org/10.1021/acs.nanolett.2c04733.

[254] Kohei M. Itoh and Hideyuki Watanabe. Isotope engineering of silicon and diamond for quantum computing and sensing applications. *MRS Communications*, 4(4):143–157, 2014. doi:10.1557/mrc.2014.32.

[255] J. Stephen Hartman, Bob Berno, Paul Hazendonk, Christopher W Kirby, Eric Ye, Josef W. Zwanziger, and Alex D. Bain. Nmr studies of nitrogen doping in the 4h

polytype of silicon carbide: Site assignments and spin-lattice relaxation. *Journal of Physical Chemistry C*, 113:15024–15036, 2009.

[256] Peter Niedbalski, Qing Wang, Christopher Parish, Fatemeh Khashami, Andhika Kiswandhi, and Lloyd Lumata. Magnetic-field-dependent lifetimes of hyperpolarized ^{13}c spins at cryogenic temperature. *The Journal of Physical Chemistry B*, 122(6): 1898–1904, February 2018. doi:10.1021/acs.jpcb.8b00630. URL https://doi.org/10.1021/acs.jpcb.8b00630.

[257] Cornelis J. Terblanche, Eduard C. Reynhardt, and Jan A. van Wyk. 13c spin–lattice relaxation in natural diamond: Zeeman relaxation at 4.7 t and 300 k due to fixed paramagnetic nitrogen defects. *Solid State Nuclear Magnetic Resonance*, 20(1-2):1–22, August 2001. doi:10.1006/snmr.2001.0026. URL https://doi.org/10.1006/snmr.2001.0026.

[258] P. C. Maurer, G. Kucsko, C. Latta, L. Jiang, N. Y. Yao, S. D. Bennett, F. Pastawski, D. Hunger, N. Chisholm, M. Markham, D. J. Twitchen, J. I. Cirac, and M. D. Lukin. Room-temperature quantum bit memory exceeding one second. *Science*, 336(6086): 1283–1286, June 2012. ISSN 0036-8075. doi:10.1126/science.1220513. URL https://science.sciencemag.org/content/336/6086/1283.

[259] Sebastian Zaiser, Torsten Rendler, Ingmar Jakobi, Thomas Wolf, Sang-Yun Lee, Samuel Wagner, Ville Bergholm, Thomas Schulte-Herbrüggen, Philipp Neumann, and Jörg Wrachtrup. Enhancing quantum sensing sensitivity by a quantum memory. *Nature Communications*, 7(1), August 2016. doi:10.1038/ncomms12279. URL https://doi.org/10.1038/ncomms12279.

[260] K. S. Cujia, J. M. Boss, K. Herb, J. Zopes, and C. L. Degen. Tracking the precession of single nuclear spins by weak measurements. *Nature*, 571(7764):230–233, June 2019. doi:10.1038/s41586-019-1334-9. URL https://doi.org/10.1038/s41586-019-1334-9.

[261] T. K. Unden, D. Louzon, M. Zwolak, W. H. Zurek, and F. Jelezko. Revealing the emergence of classicality using nitrogen-vacancy centers. *Phys. Rev. Lett.*, 123:140402, October 2019. doi:10.1103/PhysRevLett.123.140402. URL https://link.aps.org/doi/10.1103/PhysRevLett.123.140402.

[262] Matthias Widmann, Sang-Yun Lee, Torsten Rendler, Nguyen Tien Son, Helmut Fedder, Seoyoung Paik, Li-Ping Yang, Nan Zhao, Sen Yang, Ian Booker, Andrej Denisenko, Mohammad Jamali, S. Ali Momenzadeh, Ilja Gerhardt, Takeshi Ohshima, Adam Gali, Erik Janzén, and Jörg Wrachtrup. Coherent control of single spins in silicon carbide at room temperature. *Nature Materials*, 14(2):164–168, December 2014. doi:10.1038/nmat4145. URL https://doi.org/10.1038/nmat4145.

[263] Berk Diler, Samuel J. Whiteley, Christopher P. Anderson, Gary Wolfowicz, Marie E. Wesson, Edward S. Bielejec, F. Joseph Heremans, and David D. Awschalom. Coherent

control and high-fidelity readout of chromium ions in commercial silicon carbide. *npj Quantum Information*, 6(1):11, January 2020. ISSN 2056-6387. doi:10.1038/s41534-020-0247-7. URL https://doi.org/10.1038/s41534-020-0247-7.

[264] Gary Wolfowicz, Christopher P. Anderson, Berk Diler, Oleg G. Poluektov, F. Joseph Heremans, and David D. Awschalom. Vanadium spin qubits as telecom quantum emitters in silicon carbide. *Science Advances*, 6(18):eaaz1192, May 2020. doi:10.1126/sciadv.aaz1192. URL https://advances.sciencemag.org/content/6/18/eaaz1192.

[265] David J. Christle, Paul V. Klimov, Charles F. de las Casas, Krisztián Szász, Viktor Ivády, Valdas Jokubavicius, Jawad Ul Hassan, Mikael Syväjärvi, William F. Koehl, Takeshi Ohshima, Nguyen T. Son, Erik Janzén, Ádám Gali, and David D. Awschalom. Isolated spin qubits in sic with a high-fidelity infrared spin-to-photon interface. *Phys. Rev. X*, 7:021046, June 2017. doi:10.1103/PhysRevX.7.021046. URL https://link.aps.org/doi/10.1103/PhysRevX.7.021046.

[266] Roland Nagy, Matthias Niethammer, Matthias Widmann, Yu-Chen Chen, Péter Udvarhelyi, Cristian Bonato, Jawad Ul Hassan, Robin Karhu, Ivan G. Ivanov, Nguyen Tien Son, Jeronimo R. Maze, Takeshi Ohshima, Öney O. Soykal, Ádám Gali, Sang-Yun Lee, Florian Kaiser, and Jörg Wrachtrup. High-fidelity spin and optical control of single silicon-vacancy centres in silicon carbide. *Nature Communications*, 10 (1), April 2019. doi:10.1038/s41467-019-09873-9. URL https://doi.org/10.1038/s41467-019-09873-9.

[267] Xing Rong, Jianpei Geng, Fazhan Shi, Ying Liu, Kebiao Xu, Wenchao Ma, Fei Kong, Zhen Jiang, Yang Wu, and Jiangfeng Du. Experimental fault-tolerant universal quantum gates with solid-state spins under ambient conditions. *Nature Communications*, 6 (1), November 2015. doi:10.1038/ncomms9748. URL https://doi.org/10.1038/ncomms9748.

[268] N. T. Son, P. Carlsson, J. ul Hassan, E. Janzén, T. Umeda, J. Isoya, A. Gali, M. Bockstedte, N. Morishita, T. Ohshima, and H. Itoh. Divacancy in 4h-sic. *Phys. Rev. Lett.*, 96:055501, February 2006. doi:10.1103/PhysRevLett.96.055501. URL https://link.aps.org/doi/10.1103/PhysRevLett.96.055501.

[269] G. Waldherr, Y. Wang, S. Zaiser, M. Jamali, T. Schulte-Herbrüggen, H. Abe, T. Ohshima, J. Isoya, J. F. Du, P. Neumann, and J. Wrachtrup. Quantum error correction in a solid-state hybrid spin register. *Nature*, 506(7487):204–207, February 2014. doi:10.1038/nature12919. URL https://doi.org/10.1038/nature12919.

[270] F. Jelezko, T. Gaebel, I. Popa, M. Domhan, A. Gruber, and J. Wrachtrup. Observation of coherent oscillation of a single nuclear spin and realization of a two-qubit conditional quantum gate. *Phys. Rev. Lett.*, 93:130501, September 2004. doi:10.1103/PhysRevLett.93.130501. URL https://link.aps.org/doi/10.1103/PhysRevLett.93.130501.

[271] Abram L. Falk, Paul V. Klimov, Viktor Ivády, Krisztián Szász, David J. Christle, William F. Koehl, Ádám Gali, and David D. Awschalom. Optical polarization of nuclear spins in silicon carbide. *Phys. Rev. Lett.*, 114:247603, June 2015. doi:10.1103/PhysRevLett.114.247603. URL https://link.aps.org/doi/10.1103/PhysRevLett.114.247603.

[272] G. D. Fuchs, G. Burkard, P. V. Klimov, and D. D. Awschalom. A quantum memory intrinsic to single nitrogen–vacancy centres in diamond. *Nature Physics*, 7(10):789–793, June 2011. doi:10.1038/nphys2026. URL https://doi.org/10.1038/nphys2026.

[273] Wolfgang Pfaff, Tim H. Taminiau, Lucio Robledo, Hannes Bernien, Matthew Markham, Daniel J. Twitchen, and Ronald Hanson. Demonstration of entanglement-by-measurement of solid-state qubits. *Nature Physics*, 9(1):29–33, October 2012. doi:10.1038/nphys2444. URL https://doi.org/10.1038/nphys2444.

[274] M. V. Gurudev Dutt, L. Childress, L. Jiang, E. Togan, J. Maze, F. Jelezko, A. S. Zibrov, P. R. Hemmer, and M. D. Lukin. Quantum register based on individual electronic and nuclear spin qubits in diamond. *Science*, 316(5829):1312–1316, June 2007. doi:10.1126/science.1139831. URL https://doi.org/10.1126/science.1139831.

[275] N. Kalb, P. C. Humphreys, J. J. Slim, and R. Hanson. Dephasing mechanisms of diamond-based nuclear-spin memories for quantum networks. *Phys. Rev. A*, 97:062330, June 2018. doi:10.1103/PhysRevA.97.062330. URL https://link.aps.org/doi/10.1103/PhysRevA.97.062330.

[276] B. Hensen, H. Bernien, A. E. Dréau, A. Reiserer, N. Kalb, M. S. Blok, J. Ruitenberg, R. F. L. Vermeulen, R. N. Schouten, C. Abellán, W. Amaya, V. Pruneri, M. W. Mitchell, M. Markham, D. J. Twitchen, D. Elkouss, S. Wehner, T. H. Taminiau, and R. Hanson. Loophole-free bell inequality violation using electron spins separated by 1.3 kilometres. *Nature*, 526(7575):682–686, October 2015. doi:10.1038/nature15759. URL https://doi.org/10.1038/nature15759.

[277] Nabeel Aslam, Matthias Pfender, Philipp Neumann, Rolf Reuter, Andrea Zappe, Felipe Fávaro de Oliveira, Andrej Denisenko, Hitoshi Sumiya, Shinobu Onoda, Junichi Isoya, and Jörg Wrachtrup. Nanoscale nuclear magnetic resonance with chemical resolution. *Science*, 357(6346):67–71, July 2017. doi:10.1126/science.aam8697. URL https://doi.org/10.1126/science.aam8697.

[278] C. Müller, X. Kong, J.-M. Cai, K. Melentijević, A. Stacey, M. Markham, D. Twitchen, J. Isoya, S. Pezzagna, J. Meijer, J. F. Du, M. B. Plenio, B. Naydenov, L. P. McGuinness, and F. Jelezko. Nuclear magnetic resonance spectroscopy with single spin sensitivity. *Nature Communications*, 5(1), August 2014. doi:10.1038/ncomms5703. URL https://doi.org/10.1038/ncomms5703.

[279] C. Bonato, M. S. Blok, H. T. Dinani, D. W. Berry, M. L. Markham, D. J. Twitchen, and R. Hanson. Optimized quantum sensing with a single electron spin using real-

time adaptive measurements. *Nature Nanotechnology*, 11(3):247–252, November 2015. doi:10.1038/nnano.2015.261. URL https://doi.org/10.1038/nnano.2015.261.

[280] Erik Bauch, Connor A. Hart, Jennifer M. Schloss, Matthew J. Turner, John F. Barry, Pauli Kehayias, Swati Singh, and Ronald L. Walsworth. Ultralong dephasing times in solid-state spin ensembles via quantum control. *Phys. Rev. X*, 8:031025, July 2018. doi:10.1103/PhysRevX.8.031025. URL https://link.aps.org/doi/10.1103/PhysRevX.8.031025.

[281] Toyofumi Ishikawa, Kai-Mei C. Fu, Charles Santori, Victor M. Acosta, Raymond G. Beausoleil, Hideyuki Watanabe, Shinichi Shikata, and Kohei M. Itoh. Optical and spin coherence properties of nitrogen-vacancy centers placed in a 100 nm thick isotopically purified diamond layer. *Nano Letters*, 12(4):2083–2087, March 2012. doi:10.1021/nl300350r. URL https://doi.org/10.1021/nl300350r.

[282] A. A. Clerk, K. W. Lehnert, P. Bertet, J. R. Petta, and Y. Nakamura. Hybrid quantum systems with circuit quantum electrodynamics. *Nature Physics*, 16(3):257–267, March 2020. doi:10.1038/s41567-020-0797-9. URL https://doi.org/10.1038/s41567-020-0797-9.

[283] N. Bar-Gill, L. M. Pham, C. Belthangady, D. Le Sage, P. Cappellaro, J. R. Maze, M. D. Lukin, A. Yacoby, and R. Walsworth. Suppression of spin-bath dynamics for improved coherence of multi-spin-qubit systems. *Nature Communications*, 3(1):858, May 2012. ISSN 2041-1723. doi:10.1038/ncomms1856. URL https://doi.org/10.1038/ncomms1856.

[284] C. H. Yang, K. W. Chan, R. Harper, W. Huang, T. Evans, J. C. C. Hwang, B. Hensen, A. Laucht, T. Tanttu, F. E. Hudson, S. T. Flammia, K. M. Itoh, A. Morello, S. D. Bartlett, and A. S. Dzurak. Silicon qubit fidelities approaching incoherent noise limits via pulse engineering. *Nature Electronics*, 2(4):151–158, April 2019. doi:10.1038/s41928-019-0234-1. URL https://doi.org/10.1038/s41928-019-0234-1.

[285] Jun Yoneda, Kenta Takeda, Tomohiro Otsuka, Takashi Nakajima, Matthieu R. Delbecq, Giles Allison, Takumu Honda, Tetsuo Kodera, Shunri Oda, Yusuke Hoshi, Noritaka Usami, Kohei M. Itoh, and Seigo Tarucha. A quantum-dot spin qubit with coherence limited by charge noise and fidelity higher than 99.9%. *Nature Nanotechnology*, 13(2):102–106, December 2017. doi:10.1038/s41565-017-0014-x. URL https://doi.org/10.1038/s41565-017-0014-x.

[286] E. Knill. Quantum computing with realistically noisy devices. *Nature*, 434(7029):39–44, March 2005. doi:10.1038/nature03350. URL https://doi.org/10.1038/nature03350.

[287] M. Veldhorst, J. C. C. Hwang, C. H. Yang, A. W. Leenstra, B. de Ronde, J. P. Dehollain, J. T. Muhonen, F. E. Hudson, K. M. Itoh, A. Morello, and A. S. Dzurak. An addressable quantum dot qubit with fault-tolerant control-fidelity. *Nature*

Nanotechnology, 9(12):981–985, October 2014. doi:10.1038/nnano.2014.216. URL https://doi.org/10.1038/nnano.2014.216.

[288] Earl T. Campbell, Barbara M. Terhal, and Christophe Vuillot. Roads towards fault-tolerant universal quantum computation. *Nature*, 549(7671):172–179, September 2017. doi:10.1038/nature23460. URL https://doi.org/10.1038/nature23460.

[289] Evan S. Petersen, A. M. Tyryshkin, J. J. L. Morton, E. Abe, S. Tojo, K. M. Itoh, M. L. W. Thewalt, and S. A. Lyon. Nuclear spin decoherence of neutral ^{31}P donors in silicon: Effect of environmental ^{29}Si nuclei. *Phys. Rev. B*, 93:161202, April 2016. doi:10.1103/PhysRevB.93.161202. URL https://link.aps.org/doi/10.1103/PhysRevB.93.161202.

[290] R. Guichard, S. J. Balian, G. Wolfowicz, P. A. Mortemousque, and T. S. Monteiro. Decoherence of nuclear spins in the frozen core of an electron spin. *Phys. Rev. B*, 91: 214303, June 2015. doi:10.1103/PhysRevB.91.214303. URL https://link.aps.org/doi/10.1103/PhysRevB.91.214303.

[291] Wenzheng Dong, F A Calderon-Vargas, and Sophia E Economou. Precise high-fidelity electron–nuclear spin entangling gates in NV centers via hybrid dynamical decoupling sequences. *New Journal of Physics*, 22(7):073059, July 2020. doi:10.1088/1367-2630/ab9bc0. URL https://doi.org/10.1088/1367-2630/ab9bc0.

[292] Alexandra Oliveros, Anthony Guiseppi-Elie, and Stephen E. Saddow. Silicon carbide: a versatile material for biosensor applications. *Biomedical Microdevices*, 15(2):353–368, January 2013. doi:10.1007/s10544-013-9742-3. URL https://doi.org/10.1007/s10544-013-9742-3.

[293] C. E. Bradley, S. W. de Bone, P. F. W. Möller, S. Baier, M. J. Degen, S. J. H. Loenen, H. P. Bartling, M. Markham, D. J. Twitchen, R. Hanson, D. Elkouss, and T. H. Taminiau. Robust quantum-network memory based on spin qubits in isotopically engineered diamond. *npj Quantum Information*, 8(1), October 2022. doi:10.1038/s41534-022-00637-w. URL https://doi.org/10.1038/s41534-022-00637-w.

[294] Kamyar Saeedi, Stephanie Simmons, Jeff Z. Salvail, Phillip Dluhy, Helge Riemann, Nikolai V. Abrosimov, Peter Becker, Hans-Joachim Pohl, John J. L. Morton, and Mike L. W. Thewalt. Room-temperature quantum bit storage exceeding 39 minutes using ionized donors in silicon-28. *Science*, 342(6160):830–833, November 2013. doi:10.1126/science.1239584. URL https://doi.org/10.1126/science.1239584.

[295] Manjin Zhong, Morgan P. Hedges, Rose L. Ahlefeldt, John G. Bartholomew, Sarah E. Beavan, Sven M. Wittig, Jevon J. Longdell, and Matthew J. Sellars. Optically addressable nuclear spins in a solid with a six-hour coherence time. *Nature*, 517(7533): 177–180, January 2015. doi:10.1038/nature14025. URL https://doi.org/10.1038/nature14025.

[296] Maximilian Ruf, Noel H. Wan, Hyeongrak Choi, Dirk Englund, and Ronald Hanson. Quantum networks based on color centers in diamond. *Journal of Applied Physics*, 130 (7):070901, 2021. doi:10.1063/5.0056534. URL https://doi.org/10.1063/5.0056534.

[297] Yuichiro Matsuzaki, Takaaki Shimo-Oka, Hirotaka Tanaka, Yasuhiro Tokura, Kouichi Semba, and Norikazu Mizuochi. Hybrid quantum magnetic-field sensor with an electron spin and a nuclear spin in diamond. *Phys. Rev. A*, 94:052330, November 2016. doi:10.1103/PhysRevA.94.052330. URL https://link.aps.org/doi/10.1103/PhysRevA.94.052330.

[298] Ziwei Qiu, Uri Vool, Assaf Hamo, and Amir Yacoby. Nuclear spin assisted magnetic field angle sensing. *npj Quantum Information*, 7(1), February 2021. doi:10.1038/s41534-021-00374-6. URL https://doi.org/10.1038/s41534-021-00374-6.

[299] J. Casanova, Z.-Y. Wang, and M. B. Plenio. Noise-resilient quantum computing with a nitrogen-vacancy center and nuclear spins. *Phys. Rev. Lett.*, 117:130502, September 2016. doi:10.1103/PhysRevLett.117.130502. URL https://link.aps.org/doi/10.1103/PhysRevLett.117.130502.

[300] Andrei Ruskuc, Chun-Ju Wu, Jake Rochman, Joonhee Choi, and Andrei Faraon. Nuclear spin-wave quantum register for a solid-state qubit. *Nature*, 602(7897):408–413, February 2022. doi:10.1038/s41586-021-04293-6. URL https://doi.org/10.1038/s41586-021-04293-6.

[301] Mateusz T. Madzik, Serwan Asaad, Akram Youssry, Benjamin Joecker, Kenneth M. Rudinger, Erik Nielsen, Kevin C. Young, Timothy J. Proctor, Andrew D. Baczewski, Arne Laucht, Vivien Schmitt, Fay E. Hudson, Kohei M. Itoh, Alexander M. Jakob, Brett C. Johnson, David N. Jamieson, Andrew S. Dzurak, Christopher Ferrie, Robin Blume-Kohout, and Andrea Morello. Precision tomography of a three-qubit donor quantum processor in silicon. *Nature*, 601(7893):348–353, January 2022. doi:10.1038/s41586-021-04292-7. URL https://doi.org/10.1038/s41586-021-04292-7.

[302] M. H. Abobeih, Y. Wang, J. Randall, S. J. H. Loenen, C. E. Bradley, M. Markham, D. J. Twitchen, B. M. Terhal, and T. H. Taminiau. Fault-tolerant operation of a logical qubit in a diamond quantum processor. *Nature*, 606(7916):884–889, May 2022. doi:10.1038/s41586-022-04819-6. URL https://doi.org/10.1038/s41586-022-04819-6.

[303] L. Childress, M. V. Gurudev Dutt, J. M. Taylor, A. S. Zibrov, F. Jelezko, J. Wrachtrup, P. R. Hemmer, and M. D. Lukin. Coherent dynamics of coupled electron and nuclear spin qubits in diamond. *Science*, 314(5797):281–285, 2006. doi:10.1126/science.1131871. URL https://www.science.org/doi/abs/10.1126/science.1131871.

[304] P. L. Stanwix, L. M. Pham, J. R. Maze, D. Le Sage, T. K. Yeung, P. Cappellaro, P. R. Hemmer, A. Yacoby, M. D. Lukin, and R. L. Walsworth. Coherence of nitrogen-vacancy electronic spin ensembles in diamond. *Phys. Rev. B*, 82:201201, November 2010. doi:10.1103/PhysRevB.82.201201. URL https://link.aps.org/doi/10.1103/PhysRevB.82.201201.

[305] J R Maze, A Dréau, V Waselowski, H Duarte, J-F Roch, and V Jacques. Free induction decay of single spins in diamond. *New Journal of Physics*, 14(10):103041, October 2012. doi:10.1088/1367-2630/14/10/103041. URL https://doi.org/10.1088/1367-2630/14/10/103041.

[306] J. R. Maze, J. M. Taylor, and M. D. Lukin. Electron spin decoherence of single nitrogen-vacancy defects in diamond. *Phys. Rev. B*, 78:094303, September 2008. doi:10.1103/PhysRevB.78.094303. URL https://link.aps.org/doi/10.1103/PhysRevB.78.094303.

[307] Zhi-Hui Wang and Susumu Takahashi. Spin decoherence and electron spin bath noise of a nitrogen-vacancy center in diamond. *Phys. Rev. B*, 87:115122, March 2013. doi:10.1103/PhysRevB.87.115122. URL https://link.aps.org/doi/10.1103/PhysRevB.87.115122.

[308] Shigeru Ajisaka and Y. B. Band. Decoherence of three-level systems: Application to nitrogen-vacancy centers in diamond near a surface. *Phys. Rev. B*, 94:134107, October 2016. doi:10.1103/PhysRevB.94.134107. URL https://link.aps.org/doi/10.1103/PhysRevB.94.134107.

[309] Stephanie Wehner, David Elkouss, and Ronald Hanson. Quantum internet: A vision for the road ahead. *Science*, 362(6412), October 2018. doi:10.1126/science.aam9288. URL https://doi.org/10.1126/science.aam9288.

[310] Oscar Bulancea-Lindvall, Nguyen T. Son, Igor A. Abrikosov, and Viktor Ivády. Dipolar spin relaxation of divacancy qubits in silicon carbide. *npj Computational Materials*, 7 (1), December 2021. doi:10.1038/s41524-021-00673-8. URL https://doi.org/10.1038/s41524-021-00673-8.

[311] Ekrem Taha Güldeste and Ceyhun Bulutay. Wavelet resolved coherence beating in the overhauser field of a thermal nuclear spin ensemble. *Phys. Rev. B*, 105:075202, February 2022. doi:10.1103/PhysRevB.105.075202. URL https://link.aps.org/doi/10.1103/PhysRevB.105.075202.

[312] S. L. Bayliss, P. Deb, D. W. Laorenza, M. Onizhuk, G. Galli, D. E. Freedman, and D. D. Awschalom. Enhancing spin coherence in optically addressable molecular qubits through host-matrix control. *Phys. Rev. X*, 12:031028, August 2022. ISSN 21603308. doi:10.1103/PhysRevX.12.031028. URL https://link.aps.org/doi/10.1103/PhysRevX.12.031028.

[313] Marcus W. Doherty, Neil B. Manson, Paul Delaney, Fedor Jelezko, Jörg Wrachtrup, and Lloyd C.L. Hollenberg. The nitrogen-vacancy colour centre in diamond. *Physics Reports*, 528(1):1–45, July 2013. ISSN 0370-1573. doi:https://doi.org/10.1016/j.physrep.2013.02.001. URL https://www.sciencedirect.com/science/article/pii/S0370157313000562. The nitrogen-vacancy colour centre in diamond.

[314] John F. Barry, Jennifer M. Schloss, Erik Bauch, Matthew J. Turner, Connor A. Hart, Linh M. Pham, and Ronald L. Walsworth. Sensitivity optimization for nv-diamond magnetometry. *Rev. Mod. Phys.*, 92:015004, March 2020. doi:10.1103/RevModPhys.92.015004. URL https://link.aps.org/doi/10.1103/RevModPhys.92.015004.

[315] Mantas Šimėnas, James O'Sullivan, Oscar W. Kennedy, Sen Lin, Sarah Fearn, Christoph W. Zollitsch, Gavin Dold, Tobias Schmitt, Peter Schüffelgen, Ren-Bao Liu, and John J. L. Morton. Near-surface ^{125}te^{+} spins with millisecond coherence lifetime. *Phys. Rev. Lett.*, 129:117701, September 2022. doi:10.1103/PhysRevLett.129.117701. URL https://link.aps.org/doi/10.1103/PhysRevLett.129.117701.

[316] Samuel M. Jahn, Elizabeth R. Canarie, and Stefan Stoll. Mechanism of electron spin decoherence in a partially deuterated glassy matrix. *The Journal of Physical Chemistry Letters*, 13(24):5474–5479, June 2022. doi:10.1021/acs.jpclett.2c00939. URL https://doi.org/10.1021/acs.jpclett.2c00939.

[317] Girish Sharma, Torsten Gaebel, Ewa Rej, David J. Reilly, Sophia E. Economou, and Edwin Barnes. Enhancement of nuclear spin coherence times by driving dynamic nuclear polarization at defect centers in solids. *Phys. Rev. B*, 99:205423, May 2019. doi:10.1103/PhysRevB.99.205423. URL https://link.aps.org/doi/10.1103/PhysRevB.99.205423.

[318] K. M. Salikhov, Yu. E. Kandrashkin, and A. K. Salikhov. Peculiarities of free induction and primary spin echo signals for spin-correlated radical pairs. *Applied Magnetic Resonance*, 3(1):199–216, January 1992. doi:10.1007/bf03166790. URL https://doi.org/10.1007/bf03166790.

[319] L.V. Kulik, S.A. Dzuba, I.A. Grigoryev, and Yu.D. Tsvetkov. Electron dipole–dipole interaction in ESEEM of nitroxide biradicals. *Chemical Physics Letters*, 343(3-4):315–324, August 2001. doi:10.1016/s0009-2614(01)00721-7. URL https://doi.org/10.1016/s0009-2614(01)00721-7.

[320] H. P. Bartling, M. H. Abobeih, B. Pingault, M. J. Degen, S. J. H. Loenen, C. E. Bradley, J. Randall, M. Markham, D. J. Twitchen, and T. H. Taminiau. Entanglement of spin-pair qubits with intrinsic dephasing times exceeding a minute. *Phys. Rev. X*, 12:011048, March 2022. doi:10.1103/PhysRevX.12.011048. URL https://link.aps.org/doi/10.1103/PhysRevX.12.011048.

[321] Philipp Neumann and Jörg Wrachtrup. *Quantum Optical Diamond Technologies*. Wiley, March 2013. doi:10.1002/9783527648603.ch9. URL https://doi.org/10.1002/9783527648603.ch9.

[322] C. E. Bradley and T. H. Taminiau, 2023. Private communication.

[323] Charles P. Slichter. *Principles of magnetic resonance*. Springer, 2011.

[324] K. Rama Koteswara Rao and Dieter Suter. Characterization of hyperfine interaction between an nv electron spin and a first-shell ^{13}C nuclear spin in diamond. *Phys. Rev. B*, 94:060101, August 2016. doi:10.1103/PhysRevB.94.060101. URL https://link.aps.org/doi/10.1103/PhysRevB.94.060101.

[325] K Rama Koteswara Rao and Dieter Suter. Level anti-crossings of a nitrogen-vacancy center in diamond: decoherence-free subspaces and 3d sensors of microwave magnetic fields. *New Journal of Physics*, 22(10):103065, October 2020. doi:10.1088/1367-2630/abc083. URL https://doi.org/10.1088/1367-2630/abc083.

[326] Guoqing Wang, Ariel Rebekah Barr, Hao Tang, Mo Chen, Changhao Li, Haowei Xu, Ju Li, and Paola Cappellaro. Characterizing temperature and strain variations with qubit ensembles for their robust coherence protection, 2022. URL https://arxiv.org/abs/2205.02790.

[327] Daniel W. Laorenza and Danna E. Freedman. Could the quantum internet be comprised of molecular spins with tunable optical interfaces? *Journal of the American Chemical Society*, November 2022. doi:10.1021/jacs.2c07775. URL https://doi.org/10.1021/jacs.2c07775.